Investigation of Blood Flow in the Superior Mesenteric Artery and its Potential Influence on Atheroma and Gut Ischaemia

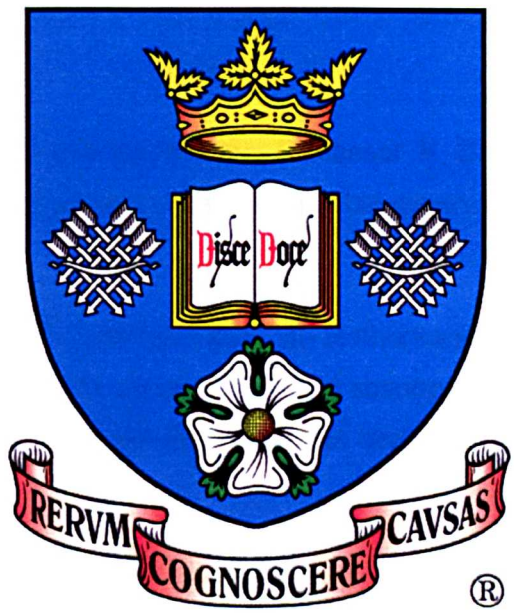

Adam David Jeays

Medical Physics and Clinical Engineering

Submitted for the degree of PhD

Submission Date: January 2006

University of Sheffield, UK

Acknowledgements

I would like to acknowledge the parts that the following people played in this project.

My supervisors Rod Hose and Pat Lawford, for keeping me on the straight and narrow, and hopefully going some way towards turning an engineering graduate into a real scientist.

My third supervisor and paymaster, Professor K D Bardhan, without whom this project wouldn't have existed, for his invaluable insight and his infectious enthusiasm.

Richard Gillott, MRI Superintendent at Rotherham District General Hospital for somehow making time for us on his clinical scanner and for translating all our hand-wavy ideas as to what we wanted to see into beautiful MR images and movies.

Dr Paul Spencer for providing pressure and angiogram data for boundary condition development and for clinical context.

Dr Sam Jacob for allowing me to join his dissection classes to study the cadaveric anatomy of the SMA.

Finally, my beautiful wife Kathy; who, along with two cats, kept me going and looked after me when I needed it, and (completely without the assistance of the cats) sent me out for a run whenever I was unbearable to be in a house with.

Contents

List of Figures

Key to Symbols

Symbol	Meaning	Units
A	State matrix of continuous time system	problem-dependent
B	Bulk modulus	Pa
B (2)	Input vector of continuous time system	problem-dependent
C	Electrical capacitance (or its fluid analog)	Farads (or $m^3 Pa^{-1}$)
C (2)	Output vector of continuous time system	problem-dependent
D	Diameter	M
D (2)	Direct transmission coefficient of continuous time system	problem-dependent
E	Young's modulus	Pa
F	Force density	$N m^{-3}$
F(2)	State matrix of discrete time system	problem-dependent
G	Input vector of discrete time system	problem-dependent
H	Output vector of discrete time system	problem-dependent
J	Direct transmission coefficient of discrete time system	problem-dependent
L	Electrical inertance (or its fluid analog)	Henrys (or $Pa m^{-3} s^2$)
P (also p)	Pressure	Pa
Q	Volume Flow	$m^3 s^{-1}$
R	Radius of cylinder or circle	M
R (2)	Resistance (either electrical or its fluid analog)	Ohms (or $Pa m^{-3} s$)
T	Discretisation timestep (for boundary conditions)	S
V	Through-plane velocity of blood (in MRI)	$m s^{-1}$
V (2)	Volume of CFD element	m^3
a	ratio of tube radius to wall thickness	dimensionless
a (2)	Initial SMA angle of origin measured from a cardiac average	degrees
b	Angle of SMA departure from a sagittal plane	degrees
c	Complex wavespeed	$m^3 s^{-1}$
c (2)	As b but measured 24mm below SMA origin	degrees
h	Wall thickness of tube	m
h (2)	distance from near-wall node to vessel wall	m
k	exponent in power law governing vessel branching	dimensionless
r	Distance from vessel centreline	m

t	Time	s
u	Fluid velocity in x-direction	$m\ s^{-1}$
v	Fluid velocity in y-direction	$m\ s^{-1}$
w	Fluid velocity in z-direction	$m\ s^{-1}$
x	Position in first of three orthogonal spatial dimensions	m
x (2)	distance between AA and SMA centre-lines measured 24mm below SMA origin	m
y	Position in second of three orthogonal spatial dimensions	m
y	Normalised radial position of point in circle (r/R)	dimensionless
z	Position in third of three orthogonal spatial dimensions	m
A^*	Magnitude of pressure gradient	$Pa\ m^{-1}$
C	Arterial compliance in Westerhof model	$m^3\ Pa^{-1}$
E_P	Love's elastic modulus	$Pa\ m^{-1}$
L_n	Inertance of blood in Westerhof model	$Kg\ m^{-4}$
M'_{10}	Magnitude of the spatial pressure gradient	dimensionless
R_i	Internal radius of hollow cylinder	m
R_L	Leakage resistance in Westerhof model	$Pa\ m^{-3}\ s$
R_n	Resitance of blood in Westerhof model	$Pa\ m^{-3}\ s$
R_o	External radius of hollow cylinder	m
R_o (2)	Resistance correction term in Westerhof model	$Pa\ m^{-3}\ s$
TR	Pulse repetition time in TOF MRI	s
V_{ENC}	Blood velocity corresponding to 180 degrees phase shift in PCA	$m\ s^{-1}$
Z_l	Longitudinal impedance of Womersley equations	$Pa\ m^{-4}\ s$
Z_o	Characteristic impedance of Womersley equations	$Pa\ m^{-3}\ s$
Z_p	Terminal impedance of Womersley equations	m
c_m	Modified Moens-Korteweg wavespeed	$m\ s^{-1}$
c_0	Moens-Korteweg wavespeed	$m\ s^{-1}$
c_1	Apperent wavespeed	$m\ s^{-1}$
d_0	Internal diameter of hollow cylinder	m
d_0 (2)	Diameter of parent vessel (in arterial branching)	m
d_1	Diameter of first daughter vessel (in arterial branching)	m
d_2	Diameter of second daughter vessel (in arterial branching)	m
l_{avg}	Average length of CFD element edges	m

l_0	Length of parent vessel (in arterial branching)	m
l_1	Length of first daughter vessel (in arterial branching)	m
l_2	Length of second daughter vessel (in arterial branching)	m
p^*	Pressure estimate in SIMPLE algorithm	Pa
th	Thickness of phase-encoding slice in TOF MRI	m
u^*	x-velocity estimate in SIMPLE algorithm	m
v^*	y-velocity estimate in SIMPLE algorithm	m
w^*	z-velocity estimate in SIMPLE algorithm	m
α	Womersley parameter	dimensionless
α (2)	Asymmetry ratio (in arterial branching)	dimensionless
λ	Damping factor	dimensionless
μ	Dynamic viscosity	Pa s
ν	Poisson ratio	dimensionless
ρ	Density	Kg m^{-3}
σ	Stress	Pa
τ	Shear stress	Pa
ω	Angular velocity	rad s^{-1}
$\mathfrak{I}_n$	An nth order Bessel function	N/A
ε'_{10}	Unit vector with phase equal to that of pressure gradient	dimensionless
θ_1	Bifurcation angle of first daughter vessel (in arterial branching)	degrees
θ_2	Bifurcation angle of second daughter vessel (in arterial branching)	degrees

Key to Abbreviations

Abbreviation	Definition
AA	Abdominal Aorta
AI	Attenuation Index
ALD	Average Linear Displacement
ARCH	Aspect Ratio Change of element
CFD	Computational Fluid Dynamics
CT	x-ray Computer Tomography
ECG	Electrocardiograph
FEA	Finite Element Analysis
FOH	First Order Hold
FSI	Fluid-Structure Interaction
GAR	Generalised Aspect Ratio
IVUS	Intra-Vascular UltraSound
LDL	Low density Lipoprotein
LDS	Linear Displacement Spectrum
MIP	Maximum Intensity Projection
MR	Magnetic Resonance
MRI	Magnetic Resonance Imaging
OSI	Oscillatory Shear Index
PCA	Phase Contrast Angiography
PCMRA	Phase Contrast Magnetic Resonance Angiography
PCR	Preconditioned Conjugate Residual
Re	Reynolds number
RF	Radio-Frequency
SENSE	Sensitivity Encoding
SIMPLE	Semi-Implicit Method for Pressure-Linked Equations
SMA	Superior Mesenteric Artery
TDMA	Tri-Diagonal Matrix Algorithm
TOF	Time Of Flight
TS	TimeStep
VOCH	Volume Change of element
WI	Wavespeed Index
WSS	Wall Shear Stress
ZOH	Zero Order Hold
bpm	beats per minute

Abstract

Atherosclerosis is the underlying process in coronary heart disease leading to myocardial infarction, and in arterial damage leading to cerebrovascular accidents. It accounts for almost 50% of deaths in the western world. Atherosclerosis is characterised by the presence of fibro-lipid plaques (atheroma) within the vessel wall. Whilst the initiation and progression of atheroma are not fully understood, it is generally accepted that the time-varying haemodynamic wall shear stress (WSS) that the vessel wall is exposed to is important in determining the likelihood of development of an atherosclerotic plaque

The superior mesenteric artery (SMA) is the major blood vessel feeding the small intestine; compared to other vessels of similar size, it is largely spared the effects of atherosclerosis.

This project used computational fluid dynamics (CFD) to model the flow in the SMA, so as to characterise the time-varying WSS distributions. In order to achieve this, both the geometry and the boundary conditions for the model had to be characterised.

The first key findings of the project were made during MRI studies to ascertain the geometry of the SMA. The findings were:

- The SMA moved substantially through both the cardiac and respiratory cycles.
- The anatomy of the SMA as seen in cine-MRI images, did not match that described in anatomy textbooks (based on *post mortem* investigation).

Boundary conditions were developed based on both MRI flow measurements and on the basis of impedance matching at the downstream boundary.

Physiologically accurate CFD models of the SMA were created, with static geometry and with cardiac movement included; there was little difference in the results between the models, but both predicted that the SMA would be largely spared the effects of atherosclerosis.

Chapter 1. Introduction and Review of Atherosclerosis

1.1 – The Question

The question posed at the start of this research project was 'Do the haemodynamics of the superior mesenteric artery (SMA) somehow protect it from the effects of atherosclerosis?' To develop an approach to this problem and to back up the question's supposition, the nature of atherosclerosis must be explored a little.

1.2 – Atherosclerosis

Atherosclerosis is a degenerative disease, it is acknowledged by clinicians to be the commonest and most important of vascular diseases. The clinical manifestations of atherosclerosis depend on the vessels involved and the degree of obstruction. Large and medium sized arteries are commonly affected including the aorta and its principal branches, i.e. the coronary, renal, iliac, femoral, carotid, basilar and vertebral arteries.

Atherosclerosis is the underlying process in coronary heart disease leading to myocardial infarction, and in arterial damage leading to cerebrovascular accidents. It accounts for almost 50% of deaths in the western world [1]. In the case of the UK, the incidence of the disease has increased rapidly during the last 50 years [2]; this is likely associated with the increasing age of the population, as well as lifestyle changes.

Atherosclerosis is a disease of the major blood vessels; its pathology must be set in the context of the nature of these vessels, and of the blood flowing in them.

1.2.1 – Blood

Blood is a suspension of erythrocytes (red blood cells), leucocytes (white blood cells) and platelets in plasma. By volume, almost all of the blood is either erythrocytes or plasma, with less than 1% of blood volume being leucocytes or platelets. The percentage of total blood volume (calculated by inspection of a centrifuged blood sample) occupied by red blood cells is called the haematocrit and for normal

volunteers is around 45%; however, the haematocrit can be anywhere in the range 10% to 65% in disease states [3, 4].

Plasma comprises about 55% of the blood volume, and is an aqueous solution of over 100 electrolytes; these include, proteins, buffers, nutrients and waste products. Plasma also contains some non-electrolytes, primarily lipids [3].

Erythrocytes are biconcave disk shaped cells of diameter ~8μm and thickness ~2μm, a scanning electron micrograph showing a number of erythrocytes is shown in Figure 1.1. The biconcave shape of the cells allows them to change shape without stretching or tearing the cell membrane, and to travel through capillaries with internal diameter as small as 4μm. The main function of erythrocytes is to carry oxygen from the lungs to tissues of the body.

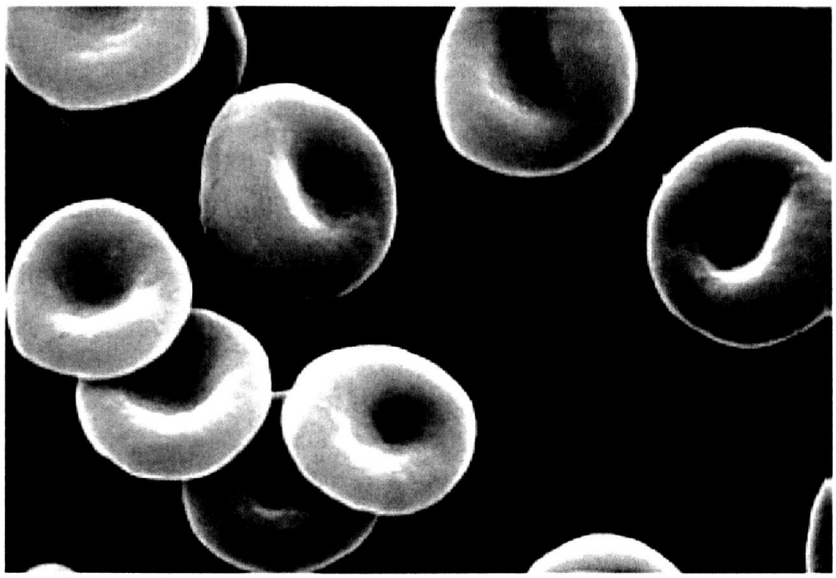

Figure 1.1. Scanning electron microscopy image of erythrocytes. Reproduced from [5].

There are several types of leucocyte, all of which are associated with defending the body against bacteria, viruses, parasites and tumour cells. Leucocytes play an important role in the early development of atherosclerosis.

Platelets (or thrombocytes) are fragments of cytoplasm derived from large cells found in the bone marrow, called megakaryocytes. As will be seen later, platelets play a major role in the clotting process and the progression of atherosclerotic disease.

1.2.2 – The Vessel Wall

All arteries share the same basic structure. The wall comprises three distinct layers; the tunica intima, the tunica media, and the tunica adventitia, as shown in figure 1.2.

The intima consists of two layers; the endothelium and sub-endothelial layer. The endothelium is a monolayer of densely packed, flat cells providing a smooth inner layer to the vessel and minimal disruption to blood flow. The sub-endothelial layer, a loosely packed layer of connective tissue, supports the endothelium.

Surrounding the intima is the media; this is much thicker and, in elastic arteries such as the abdominal aorta (AA) and SMA, consists of concentric sheets of elastin mesh interspersed with sheets of smooth muscle. This smooth muscle controls vasodilatation and vasoconstriction, but is relatively inactive in the large arteries where vessel diameter varies through the cardiac cycle as an elastic response to blood pressure.

External to the media is the adventitia; this connects the vessel to surrounding structures and contains nerve fibres, lymphatic vessels and tiny blood vessels (vasa vasorum) that supply blood to the adventitia and most of the media [6].

Apart from their relative sizes, the major distinguishing factor between different blood vessels is the respective thicknesses and composition of the three tunics.

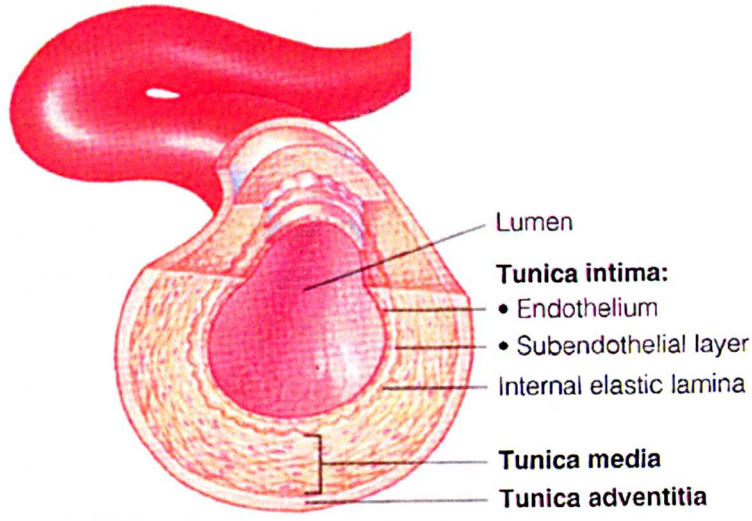

Figure 1.2. Diagram showing the three tunics of a blood vessel. Reproduced from Marieb [7].

1.2.3 – Pathology

Atherosclerosis is characterised by the presence of fibro-lipid plaques (atheroma) within the vessel wall. Whilst the events associated with established lesions are relatively well documented, the processes of initiation and progression are less well-understood and difficult to study clinically; much work is based an animal models fed hypercholesterolemic diets [8]. Present understanding of the initiation of atherosclerosis centres around the work of Ross and Glomset from 1973 onwards [9-11]; one key contention is that atherosclerosis is a 'response to injury': an inflammatory disease.

The lesion first seen in atherosclerosis is the 'fatty streak'; a purely inflammatory lesion consisting of monocyte-derived macrophages and T lymphocytes [12], these are the only inflammatory cells involved in atherosclerosis [13, 14]. This type of lesion is common, even in young children [15].

It has been shown [15, 16] that in those with elevated LDL cholesterol, the inflammatory response is preceded by lipid deposition. Such lipid deposition is one of many factors which may cause endothelial dysfunction – others include; free radicals from cigarette smoke, hypertension, and diabetes mellitus.

Whatever the cause of endothelial dysfunction, many arteries respond through the process of atherogenesis; the fatty streak develops, via an intermediate stage, to become an advanced (or complicated) lesion

Key effects of the injury to the endothelium are to; increase platelet and leucocyte adhesion; to alter the endothelium properties in favour of coagulation; and to encourage the formation of vasoactive molecules, cytokines and growth factors. The inflammatory response will persist until the initial cause of the injury has been dealt with; migration and proliferation of smooth muscle cells into the lesion, during the inflammatory episode, mean that it has reached the stage where it is referred to as an intermediate lesion.

The growth of the lesion thickens the wall of the artery, which slowly dilates or 'remodels' itself, so that up to a point, lumen cross-section is maintained [17].

As the lesion continues to grow, macrophage and lymphocyte numbers increase; their activation leads to the release of hydrolytic enzymes, cytokines, chemokines

and growth factors [18, 19] these can cause further damage, thus increasing the strength of inflammatory response and perpetuating lesion growth.

As the lesion grows, cells in the centre of the lesion become non-viable and die [20], leaving a growing core of lipids and necrotic tissue, this is covered by a fibrous cap of smooth muscle and platelets – it is now a complicated, or advanced, lesion. Eventually, remodelling cannot offset the increase in wall thickness and intrusion of the lesion into the lumen begins to alter blood flow.

Continuing influx of macrophages is thought to lead to thinning of the fibrous cap, which may then rupture leading to rapid thrombosis; such thrombi are the cause of the majority of acute coronary artery syndromes [21]. Rupture of the plaque exposes thrombogenic sub-endothelial tissue to the blood flow; a thrombus of platelets, fibrin and enmeshed red cells quickly forms. This may (depending on flow conditions, plaque make-up and concentrations of other chemical factors); remain non-occlusive, fully occlude the vessel, or break off into the blood stream (embolise) [22].

Figures 1.3 and 1.4 show example histological slides of advanced atherosclerotic plaques. Figure 1.5 illustrates the progression of an atherosclerotic plaque.

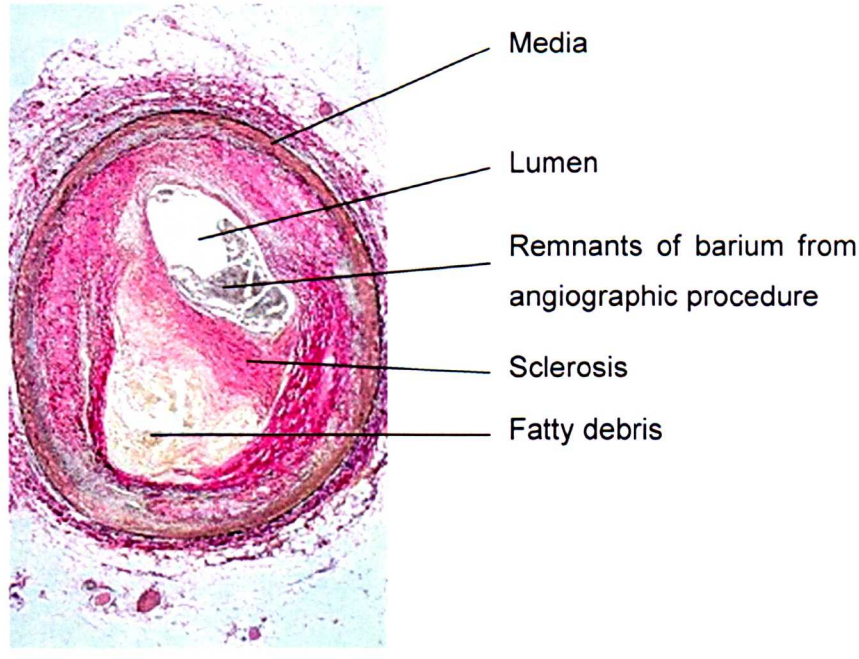

Figure 1.3. Histological section of coronary artery with atherosclerotic lesion composed mainly of fatty debris (media diameter ~3mm). Reproduced from [23].

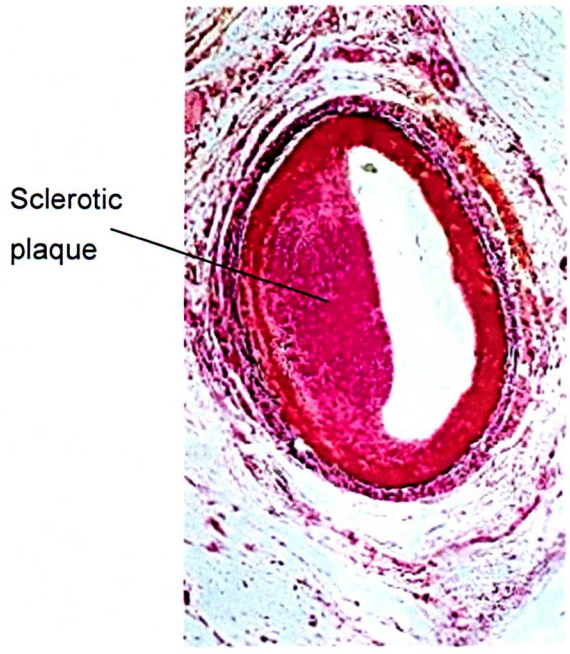

Figure 1.4. Histological section of coronary artery with atherosclerotic lesion composed of dense collagen (media diameter ~3mm). Reproduced from [23].

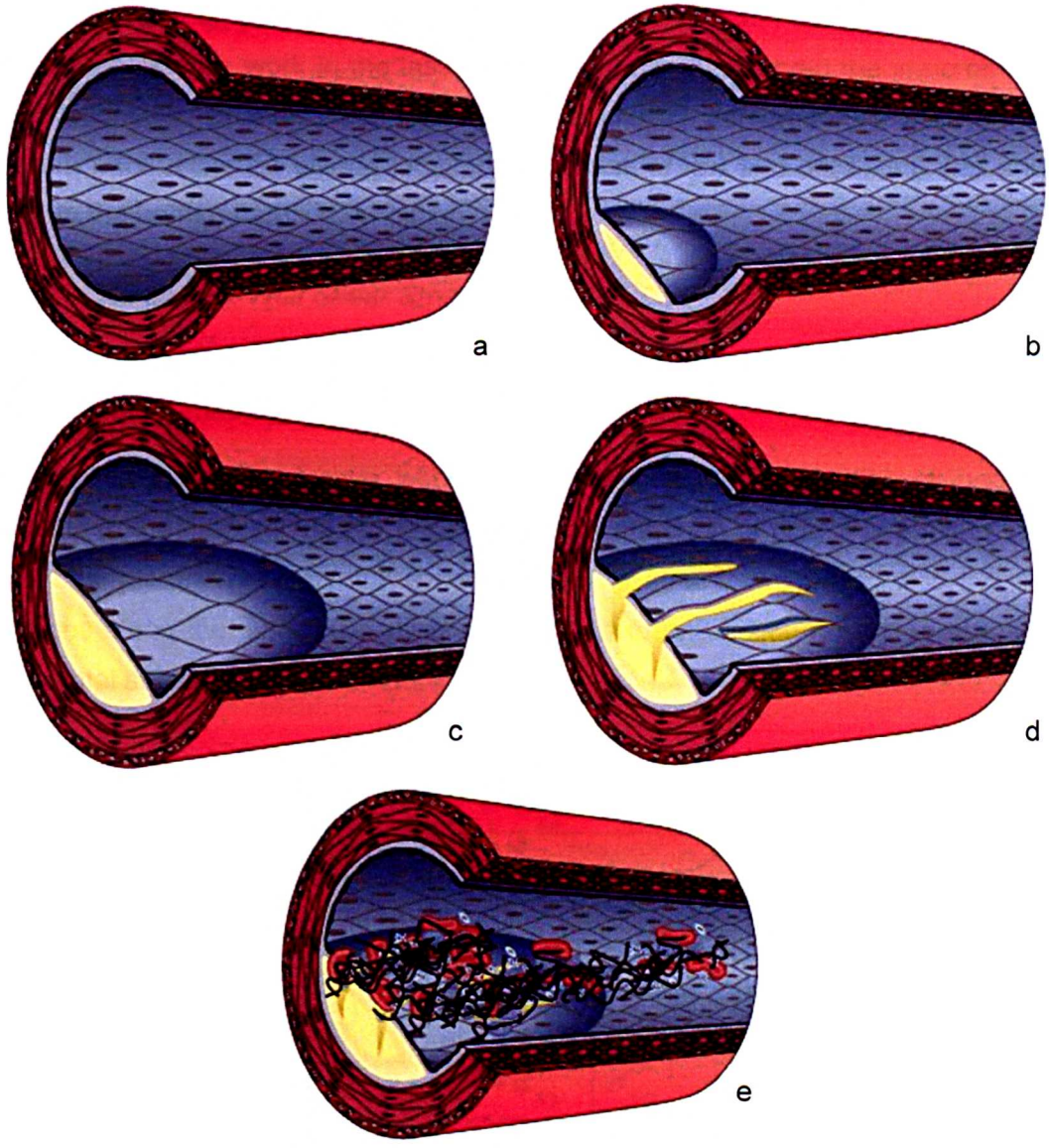

Figure 1.5. Progression of atherosclerotic lesion. Reproduced from [24]: a – normal blood vessel, b – atherosclerotic lesion initiated, c – lesion starts to occlude vessel, d – plaque ruptures (ulceration), e – platelet adherence and activation leading to thrombus composed of layers of platelets, fibrin and erythrocytes (thrombus may detach and embolise).

1.2.4 – Atherosclerosis and Wall Shear Stress

In the clinical situation, the distribution of atheroma is uneven, even in those individuals with extensive atherosclerosis. Post-mortem investigations show that atheroma often forms where arteries curve, narrow or bifurcate. These sites are associated with changes in blood velocity and disturbed patterns of shear stress, thus local haemodynamic factors are believed to be of major significance [25].

In 1969, Caro et al. [26] first suggested a link between local haemodynamic factors and atherosclerosis; work in the last twenty years has highlighted the importance of this relationship. In their 1985 paper, Ku et al [27] demonstrated a correlation between atherosclerotic plaque location and areas of low and oscillating wall shear stress in the human carotid bifurcation.

1.2.4.1 –Definition of Wall Shear Stress

In order to understand wall shear stress (WSS), it is necessary to first consider fluid stresses more generally.

Consider an infinitesimal cube within a volume of fluid. Any motion or pressure gradients in the fluid will lead to forces acting on the cube of fluid. For each of three orthogonal planes there are three components of stress, two acting in orthogonal directions along the plane (the shear stresses), and one acting normal to the plane (the normal stress), as seen in figure 1.6.

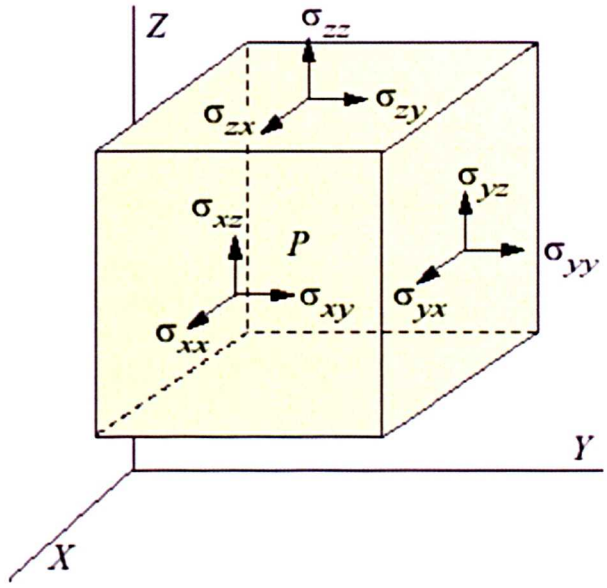

Figure 1.6. Standard notation for stresses.

These stresses are indexed according to plane on which the stress is acting and direction in which the stress is acting, for instance σ_{ij} is the stress acting on the plane normal to the i-axis, in the j-direction. When arranged in the manner shown in 1.1 these nine-components of stress are known as the stress tensor, σ.

$$\sigma_{ij} = \begin{bmatrix} \sigma_{xx} & \sigma_{yx} & \sigma_{zx} \\ \sigma_{xy} & \sigma_{yy} & \sigma_{zy} \\ \sigma_{xz} & \sigma_{yz} & \sigma_{zz} \end{bmatrix} \quad 1.1$$

These fluid stresses contain viscous terms and a hydrostatic pressure term such that the viscous stresses are related to the total stresses by 1.2.

$$\tau_{ij} = \begin{bmatrix} \tau_{xx} & \tau_{yx} & \tau_{zx} \\ \tau_{xy} & \tau_{yy} & \tau_{zy} \\ \tau_{xz} & \tau_{yz} & \tau_{zz} \end{bmatrix} = \begin{bmatrix} \sigma_{xx} - P & \sigma_{yx} & \sigma_{zx} \\ \sigma_{xy} & \sigma_{yy} - P & \sigma_{zy} \\ \sigma_{xz} & \sigma_{yz} & \sigma_{zz} - P \end{bmatrix} \quad 1.2$$

It can be shown through the Navier-Stokes equations (which will be discussed in chapter 2) that for a Newtonian fluid (again discussed later) the viscous shear stresses are given by equations 1.3 to 1.8 [28].

$$\tau_{xx} = 2\mu \frac{\partial u}{\partial x} \quad 1.3$$

$$\tau_{yy} = 2\mu \frac{\partial u}{\partial y} \quad 1.4$$

$$\tau_{zz} = 2\mu \frac{\partial u}{\partial z} \quad 1.5$$

$$\tau_{xy} = \tau_{xy} = \mu \left(\frac{\partial u}{\partial y} + \frac{\partial v}{\partial x} \right) \quad 1.6$$

$$\tau_{xz} = \tau_{zx} = \mu \left(\frac{\partial w}{\partial x} + \frac{\partial u}{\partial z} \right) \quad 1.7$$

$$\tau_{yz} = \tau_{zy} = \mu \left(\frac{\partial v}{\partial z} + \frac{\partial w}{\partial y} \right) \quad 1.8$$

Where u, v and w are fluid velocities (in m s^{-1}) in a three-dimensional cartesian space with dimensions x, y and z; and μ is fluid viscosity (in Pa s).

Now assume that the z vector is the surface normal to the blood vessel at the point of interest, the stresses we are therefore interested in are τ_{zx} and τ_{zy}. Assuming that, in each case, the term in ∂w is negligible (reasonable as w should be close to zero everywhere near to the wall), 1.7 and 1.8 become 1.9 and 1.10 respectively.

$$\tau_{zx} = \mu\left(\frac{\partial u}{\partial z}\right) \quad 1.9$$

$$\tau_{zy} = \mu\left(\frac{\partial v}{\partial z}\right) \quad 1.10$$

These two shear stresses form the two components of the surface traction vector, the force on the vessel wall caused by the viscous drag of the flowing blood. In the haemodynamic literature, the term wall shear stress (WSS) is often used to refer to the surface traction vector or its magnitude; in this thesis, 'WSS' will be used to refer to the surface traction vector, 'WSS magnitude' will be used to refer to the magnitude. Note that, as x and y are an arbitrarily chosen pair of orthogonal vectors on the plane normal to z, they may be aligned in any direction on this plane (with mean flow or with vessel orientation for example) with no loss of generality.

1.2.4.2 – Oscillatory Shear Index

Oscillatory shear index (OSI) was originally defined to deal with specific flow features in a carotid bifurcation [27], however, a more general form of OSI has since been introduced and is widely accepted [29, 30]. OSI is used is to quantify, and allow comparison of, oscillatory shears experienced by endothelial cells.

First, the mean wall shear stress τ_{mean} is calculated as the magnitude of the time-averaged surface traction vector, as in 1.11.

$$\tau_{mean} = \left|\frac{1}{T}\int_0^T t_s dt\right| \quad 1.11$$

Then the absolute shear stress shear stress τ_{abs} is defined as the time-averaged magnitude of the surface traction vector, as in 1.12.

$$\tau_{abs} = \frac{1}{T}\int_0^T |t_s| dt \quad 1.12$$

OSI is then given by 1.13, and is in the range 0-0.5.

$$OSI = \frac{1}{2}\left(1 - \frac{\tau_{mean}}{\tau_{abs}}\right) \quad 1.13$$

Quantitatively, areas prone to atherosclerosis tend to exhibit time-averaged WSS ≤4 dynes/cm^2, compared to ≥ 12 dynes/cm^2 in protected areas of the arterial tree [31].

The clinical threshold for OSI leading to substantially increased risk of atherosclerotic lesions has not been fully established. In a model of the abdominal aorta [32], OSI in the range 0-0.3 was seen along the anterior wall, and 0-0.45 along the posterior wall, although no conclusions were drawn due to the idealised nature of the model geometry.

Animal studies, both considering all the large vessels [33], and concentrating on the aorta [34], agree with the above results (obtained from the carotids). Work in the abdominal aorta has also shown a correlation between the degree of oscillatory shear stress and predisposition towards lesion formation [35, 36].

The mechanisms for the linkage between wall shear stress and atherosclerosis are not yet fully understood. The most visible effect of WSS on the intima is seen in endothelial cell morphology. Exposure to high WSS causes the cells to align with the flow and elongate, whilst those exposed to low WSS remain more rounded without any preferred alignment [37, 38]; this is shown in figure 1.7. Okano and Yoshida [39] produced similar results and suggest that exposure to low WSS may *"functionally activate the endothelial cells, increasing intercellular permeability. These events may increase the vulnerability of these regions of the vessel to atherosclerosis."*

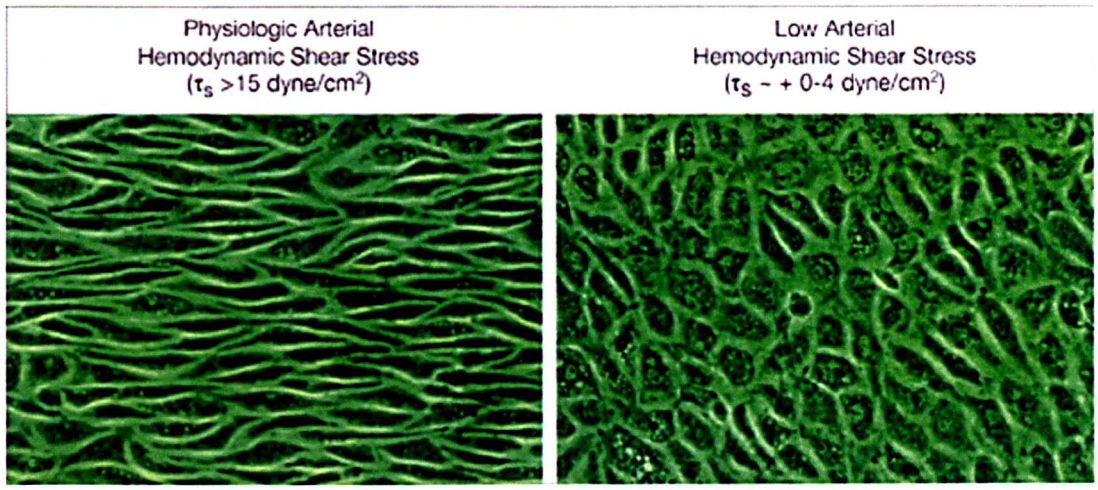

Figure 1.7. (reproduced from [40]). *'Transformation of Endothelial Cell Morphology by Fluid Shear Stress. Bovine aortic endothelial cells exposed to physiologic shear stress (>15 dyne/cm^2, left panel) for 24 hours align in the direction of blood flow while those exposed to low shear stress [magnitude] (right panel) do not (phase contrast; original magnification ×125)'*

1.2.5 – Risk Factors

Many factors have been identified which are believed to increase the risk of developing severe or premature atheroma. These include; a family history of the disease, hypertension, hyperlipidema (in particular, raised low density lipoprotein (LDL) cholesterol levels), diabetes, stress, smoking, obesity, and insufficient exercise. Alcohol (both none and too much) has also been implicated.

Whilst some of these factors can be affected by a change in lifestyle it is clear that these are not the only issues; for some patients presenting with the disease, no obvious risk factor can be identified [25, 41].

1.2.6 – Key sites

Atherosclerosis is most common in the coronary arteries, distal aorta, the proximal internal carotid, the abdominal aorta and the arteries supplying the lower extremities [42].

In a series of three papers from 1959 [43-45]; Roberts, Wilkins et al studied the prevalence of atherosclerosis in various arteries of the body. Their work was separated into three papers covering those dying; without evidence of atherosclerotic catastrophe, with evidence of atherosclerotic catastrophe, and in the presence of other significant cardiovascular disease. They state that in patients dying both with and without morphologic evidence of atherosclerotic catastrophe the SMA and renals rarely showed more than moderate atherosclerosis, with more severe atherosclerosis in the pulmonary, coronary and splenic arteries, coeliac axis, the abdominal aorta and iliacs. The cerebral arteries were also mentioned as interesting in that although they generally exhibited a low degree of atherosclerosis, patterns and severity were extremely variable compared to those in other vessels.

1.3 – The Abdominal Aorta

1.3.1 – Anatomy

The aorta arises from the superior aspect of the left ventricle and, after a few centimetres, arches and descends through the thorax and abdomen. Its posterior aspect is attached, by fascia, to the spinal column. After passing through the diaphragm and entering the abdomen it is referred to as the abdominal aorta. The abdominal aorta gives off many large branches and narrows somewhat, until it

terminates at the iliac bifurcation, at the level of the fourth lumbar vertebra. Figure 1.8 shows the abdominal aorta and its major visceral branches; these include

- The SMA – discussed in 1.4.
- The renal arteries. These arise from each side of the abdominal aorta immediately inferior to the SMA and supply blood to the kidneys
- The coeliac axis. Soon after leaving the aorta, the coeliac axis splits into the gastric, hepatic and splenic arteries, which supply the stomach, liver, spleen, gall bladder, oesophagus, and parts of the duodenum and pancreas.
- The inferior mesenteric artery. This is much smaller than the superior mesenteric and supplies part of the colon.
- The iliac arteries. These are terminal branches of the abdominal aorta and supply blood to the lower limbs.

Other, smaller vessels arising from the aorta are; the 2 inferior phrenics, 4 pairs of lumbar arteries, the middle sacral, middle suprarenals, internal spermatics, and ovarian (in the female).

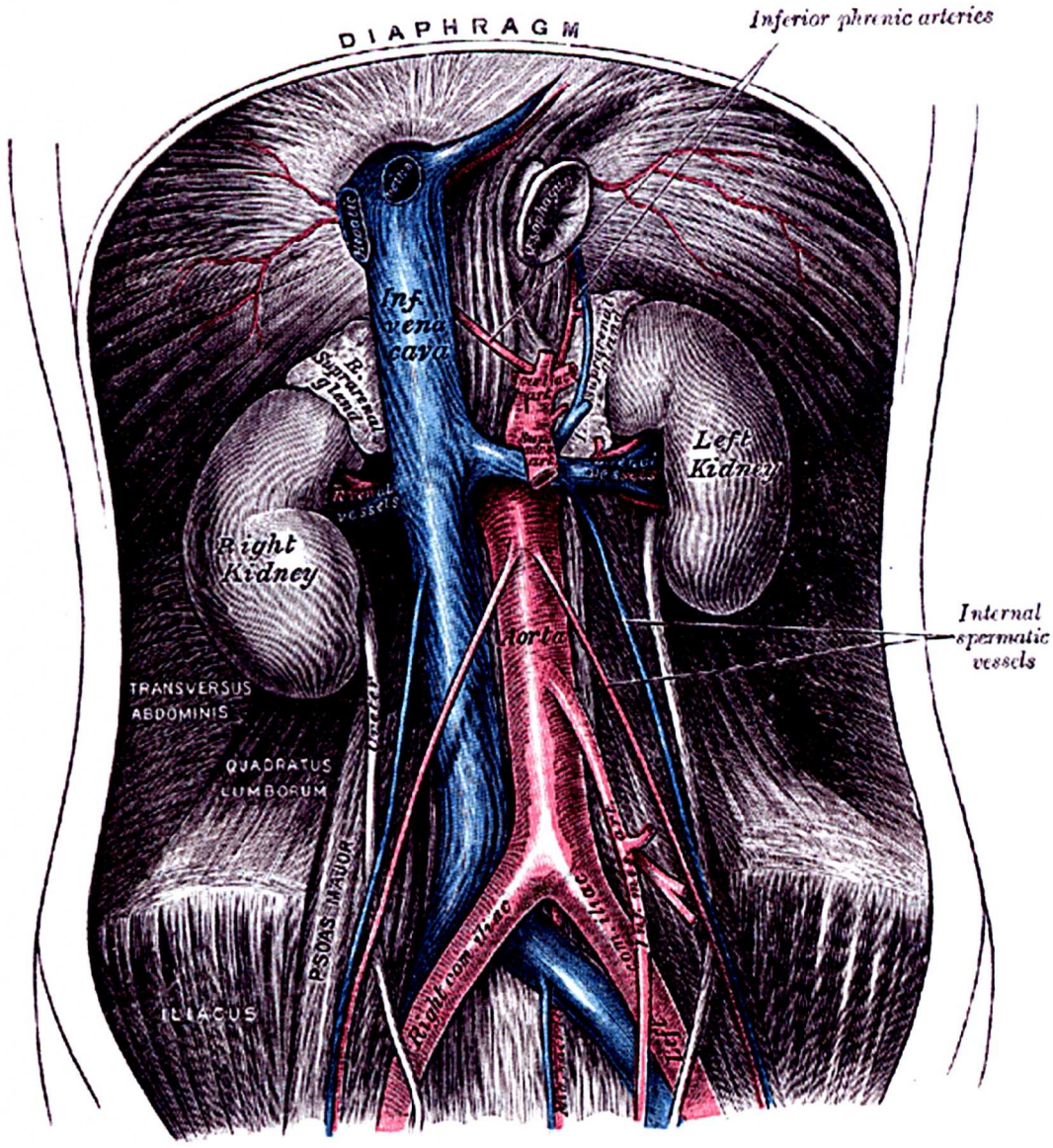

Figure 1.8. The abdominal aorta. Reproduced from [6].

1.3.2 – Incidence of Atheroma

The abdominal aorta is widely considered a prime site for the development of atherosclerotic lesions; in each of Robert's autopsy papers mentioned in section 1.2.6 [43-45], the abdominal aorta was the vessel most heavily affected by atherosclerosis.

Distribution of atheroma within the abdominal aorta is patchy with lesions tending to form on the posterior wall of the aorta inferior to the renals [46]; this is likely due to infra-renal flow reversal, as a large proportion of aortic flow is lost to the SMA, renals and coeliac axis.

1.4 – The Superior Mesenteric Artery

1.4.1 – Anatomy

The SMA leaves the anterior aspect of the abdominal aorta about 1cm below the coeliac axis at the level of the first or second lumbar vertebrae. It supplies the pancreas, duodenum, jejunum, ilium, and ascending and transverse colon. Figure 1.9 shows the SMA and its branches.

The SMA is approximately 6mm in diameter at its origin and is reported to increase in diameter by around 8% postprandially, this increase in diameter occurs alongside a three-fold increase from resting flow to around 20ml s^{-1} [47]. This increase in flow is not only due to the change in diameter of the SMA (for Poiseuille flow an 8% increase in diameter relates to a 36% increase in flow) but also, and more importantly, to an increase in the diameter of the smaller vessels downstream i.e. a decrease in the resistance of the vascular bed (the arterioles and terminal arteries provide a great proportion of the resistance to flow).

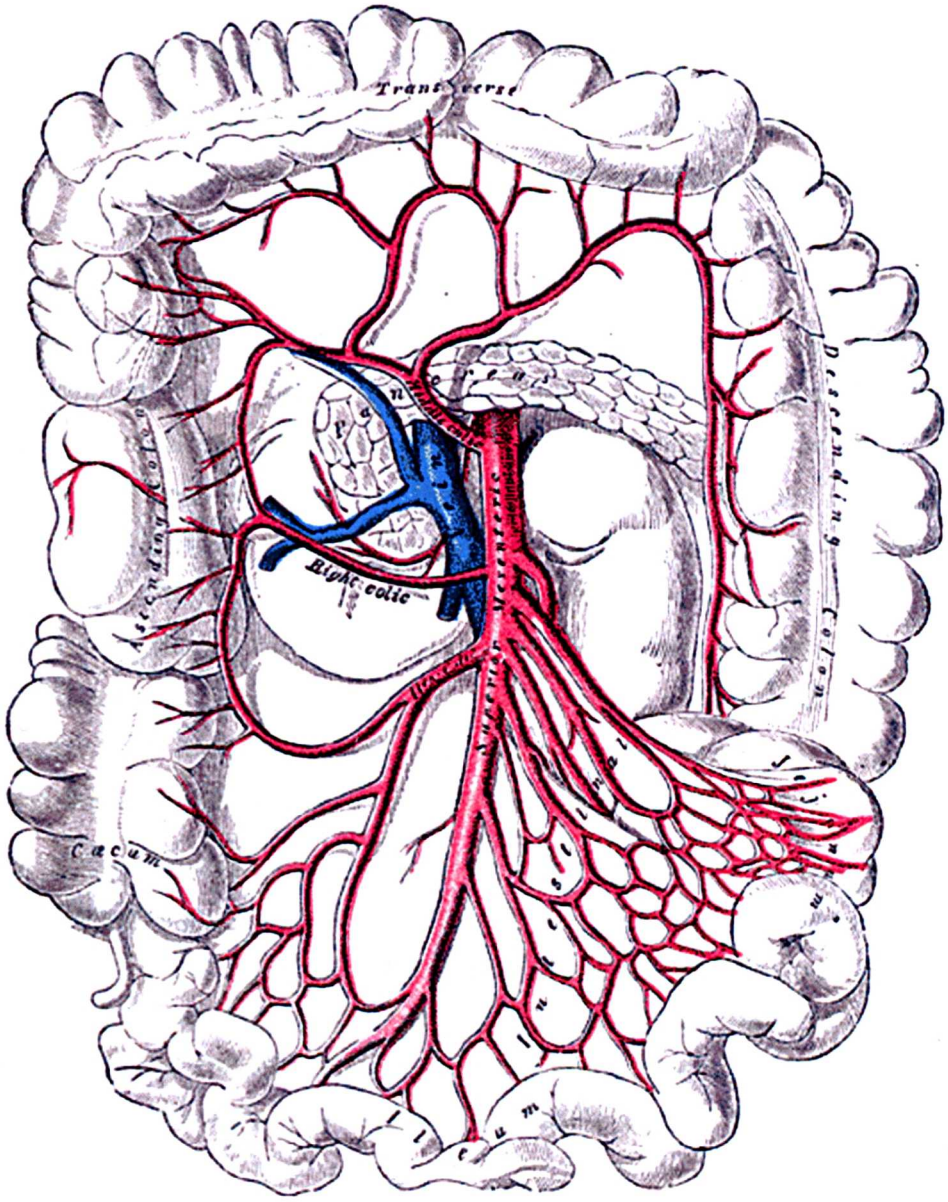

Figure 1.9. The superior mesenteric artery. Reproduced from [6].

1.4.2 – Incidence of Atheroma

Gut ischaemia is uncommon comprising just 0.1% of all hospital admissions [48]; this includes acute mesenteric ischaemia, caused by emboli from elsewhere; and chronic mesenteric ischaemia, caused by atheroma.

Whilst a degree of atheroma in the SMA is not uncommon in older individuals [49], this vessel (together with the thoracic aorta, and internal mammary arteries) is relatively spared compared to many other vessels [42]. Importantly, whilst a minor degree of atherosclerosis in the SMA is not uncommon, chronic mesenteric

ischaemia is rare; this is attributed to slow progression of the atherosclerosis in this location and the frequently mild and subclinical atherosclerotic narrowing.

In one study [50] of 184 asymptomatic subjects, no significant disease (denoted by stenosis ≥70% by diameter) of the SMA was found in any subject under 65 years of age; in the 65 and over age-group 9.1% had significant disease of the SMA while 15.9% had significant disease of the coeliac axis.

Hansen et al. [51] report a study aiming to estimate the prevalence of mesenteric artery stenosis and occlusion in elderly Americans. The study used ultrasound to estimate the prevalence of SMA and coeliac axis stenosis greater than 70% (by diameter) in 533 volunteers (all over the age of 65). The key result of this study, in the context of this thesis, is that while 15% (n=83) of the group had isolated coeliac stenosis, only 1.3% (n=7) had both coeliac and SMA stenoses, and 0.9% (n=5) had isolated SMA stenosis; a further 0.4%(n=2) showed coeliac occlusion. Further to this, SMA stenosis (regardless of coeliac axis disease) was shown to have a significant and independent association with annualised weight loss. This suggests that significant SMA stenosis is rare, and will tend to lead to weight loss.

Heino et al. [52] adopted an alternative approach; they report a series of experiments on anaesthetised pigs. The SMAs of the animals were occluded stepwise by 40%, then 70%, then 100%, to reduce flow. Each occlusion level was maintained for 60 minutes and blood samples were taken at regular intervals; the flow restriction was then removed. They concluded that reduction in blood flow to the organs supplied by the SMA became medically significant at 70% SMA occlusion [by flow]'

1.4.3 – Flow Regulation

Flow in the SMA can vary substantially with demand. A Doppler ultrasound study [47] of 20 volunteers showed a three-fold increase in mean flow rate 30 minutes after a 1000 kcal test meal. Vessel diameter was also seen to increase from 6mm to 6.5mm; it was reasonably surmised that the large proportion of the increase in flow was due to a decrease in downstream (arteriolar) resistance rather than the expansion of the vessel. It has been shown that this flow response can be reduced substantially in patients with chronic mesenteric ischaemia [53].

Work carried out in Rotherham District Hospital by Spencer and Bardhan [54] investigated changes in blood flow in the SMA in response to calorific loading of the gut in groups of young (10 volunteers, mean age 27, 8 men) and old (10 volunteers,

mean age 72, 6 men) volunteers. It had been anticipated that there would be a different pattern of response between the old and the young with elderly subjects showing a reduction of vascular reserve with advancing age. Surprisingly, no differences were recorded and it was concluded that the SMA might be 'protected' in terms of function.

Chapter 2. A Review of Haemodynamic Modelling and the SMA

2.1 – Introduction

In order to answer the question posed in section 1.1, it is necessary to construct a representative physics model of the flow in the SMA as it branches from the AA. For this, a modelling approach must be selected and appropriate data collected; in order to make informed choices about the modelling approach the underlying principles should be understood.

2.2 – Haemodynamics

Haemodynamics is the study of blood flow. Depending on the situation, certain assumptions can be made regarding this flow, and certain models can be used to predict it; this chapter looks to review these modelling techniques.

Before moving onto the substances being modelled and the methods of modelling available, we must consider the frequency content of cardiac pressure (or flow) waveform as this has important consequences for any modelling.

2.2.1 – Frequency Content of the Cardiac Flow Waveform

Many of the models discussed below are defined in either frequency or discrete-time space. In either case, it is necessary to consider the frequency content of the cardiac waveform, as will have an important effect on the applicability and implementation of these models.

Vieli et al. compared ultrasound and magnetic resonance imaging (MRI) to measure the flow in the abdominal aorta (such techniques are discussed in 2.5); they found good agreement between the two methods (as shown in figure 2.1) [55]. The MRI data contained 45 timesteps per cardiac cycle; the ultrasound had a repetition frequency of 10kHz.

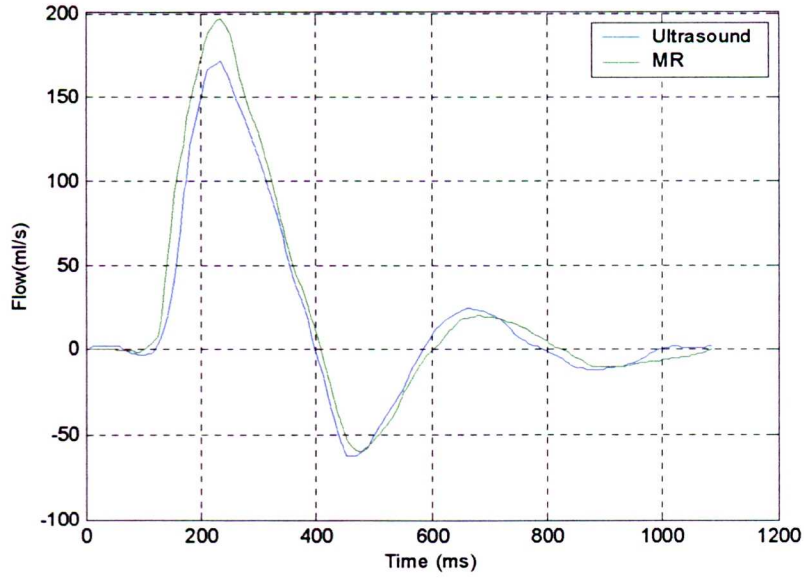

Figure 2.1. Abdominal aortic flow traces based on ultrasound and MRI measurements from [55].

A Fourier transform was applied to the ultrasound trace data in figure 2.1 and reconstruction attempted with various numbers of frequency components. It was found that reconstruction using 10 frequency components (at frequencies of 0.92 to 9.2Hz) recreated the waveform very well, as show in figure 2.2. For this reconstruction, the mean percentage error between the original and reconstructed data was 0.8%.

Even taking a conservative stance, it is reasonable to suggest from this, that the highest frequencies of significance in the resting cardiac flow waveform are of the order of 20Hz; this agrees with McDonald's thinking on the subject [56]. Excluding inter-beat variation, the lowest frequency present will be the cardiac frequency (heart rate in beats per minute/60).

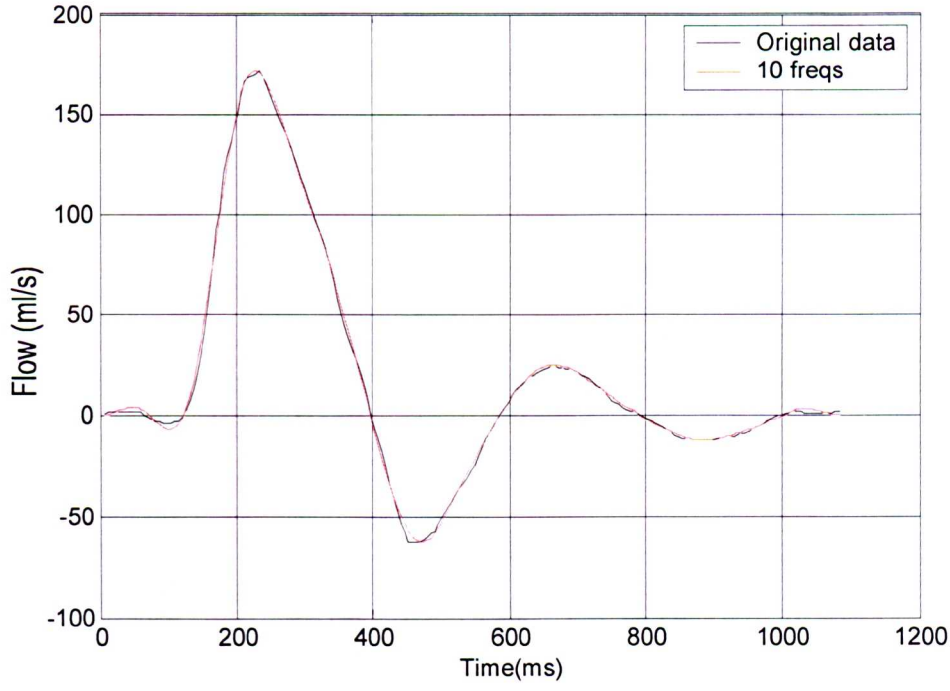

Figure 2.2. Flow profiles for original ultrasound data and reconstruction using the first 10 frequencies.

2.2.2 – Engineering Properties of the Vessel Wall

It has already been stated that the arteries of interest are 'elastic'; they deform as the systolic pressure pulse passes along them. The mechanics of this deformation control the speed of propagation of the pressure pulse, and, based on evidence from the coronaries, may have a significant effect on wall shear stress distributions within the vessel [57]. The dilation is controlled by the stiffness of the material (or materials) involved and shape and thickness of the vessel wall. With its layered, cellular structure, the vessel wall is a complex entity in terms of stiffness; this complexity along with difficulties associated with *in vivo* measurement mean that the mechanical behaviour of human arteries is not yet characterized thoroughly [58]. To couch this complexity in engineering terms, the elastic artery wall is an anisotropic, inhomogeneous, shear-stiffening, viscoelastic structure with elastic modulus that increases with strain and with frequency [59-61].

Zhou and Fung's work on dogs in the late 1990's [62] was probably the most comprehensive to date; they compared the longitudinal and circumferential elastic properties of excised canine aortas post mortem. These properties were recorded and a strain-energy based, two-part stress-strain relationship fitted; the first part is a

linear Hookean model; the second part is a non-linear model, accounting for the difference in strain energy between the linear model and the data. They then define a 'degree of nonlinearity', representing the percentage of total strain energy accounted for by the nonlinear model. Table 2.1 shows results from this study.

		Circumferential stretch ratio				
		1.0	1.2	1.4	1.6	1.8
Long. stretch ratio	1.0	0.00	0.66	3.27	8.99	19.74
	1.2	3.46	2.87	5.16	10.34	20.79
	1.3	8.44	6.89	8.32	13.47	23.85
	1.4	16.06	13.68	14.24	18.97	29.20

Table 2.1 Data from [62] showing variation of 'degree of nonlinearity' with Circumferential and Longitudinal Stretch ratios. Zhou and Fung's stretch ratios relate the stretched dimension to the reference dimension of the tissue sample (measured once the material was loaded into the testing machine with a preload around 3% of maximum load).

A variety of authors have measured radial pulsation in various parts of the aorta of dogs and men [56]; results ranged from 1% to 6.8% deviation from mean aortic radius. This suggests that it is sensible to consider a range of circumferential stretch ratios from 1.0 to 1.2 as the likely range of normal aortic dilation.

Bergel, in 1961 [59], reported that, on excision, the thoracic and abdominal aortas of dogs shortened by around 30%. He did not relate an equivalent reduction in vessel radius.

The worst-case scenario is therefore a circumferential stretch of 1.2 along with a longitudinal stretch of 1.3. Under these conditions the maximum degree of non-linearity is 8.44%, i.e. the static arterial wall stiffness is more than 91% linear.

The anisotropy mentioned above is of little concern as regards modelling the aorta; since the vessel is securely attached to the spine, it is not free to lengthen or shorten; most movement must be dilatative. For this reason, we are primarily interested in the Young's modulus associated with dilation.

The vessel wall is known to have some viscoelastic properties, that is, it has been shown to exhibit 'creep' (increased extension under constant load) and 'relaxation'

(reduced tension under constant strain) [56]. These properties can also been seen as a change in effective Young's modulus with frequency.

Bergel considered this problem in a second 1961 paper. Bergel found that effective Young's modulus of the abdominal and thoracic aortas of dogs was between 10% and 20% greater for frequencies of 2Hz and above, than in the static case; from 2Hz to 20Hz, the effective elastic modulus was constant within experimental error. The transition from the 0Hz case to the 2Hz case was not examined, so it is unclear at what frequency the increase in stiffness occurs. However, it is clear that for the large proportion of the frequency range of interest (and over the frequencies contributing most of the power of the signal) the Young's modulus can be assumed to be constant.

If one (carefully) discards the extraneous complexity, the vessel wall may be considered to behave in a Hookean manner, thus its elastic properties may be fully determined by any two of five inter-related elastic constants; the Young's modulus, shear modulus, bulk modulus, generalised longitudinal modulus, and the Poisson ratio. It is common to choose the Young's modulus and Poisson ratio as the variables of interest in engineering problems.

Evaluating the Poisson ratio is fairly straightforward. For small strains (i.e. those not leading to vessel damage), the bulk modulus (resistance to volumetric compression) of the wall is several orders of magnitude greater than its Young's modulus [56] and the two are related by equation 2.1

$$B = \frac{E}{3(1-2\nu)} \qquad 2.1$$

Where, E is the Young's Modulus, B the bulk modulus, and ν the Poisson ratio. Under these conditions, it is straightforward to show that the Poisson ratio rises to asymptotically approach 0.5.

Even assuming Hookean elasticity, finding the Young's modulus is not straightforward.

Many authors use an elastic modulus (E_P) defined as change in pressure over change in external radius (equation 2.2). For an isotropic tube not changing length on inflation this was related to Young's modulus by Love as early as 1927 [63] by equation 2.3.

$$E_P = \frac{\Delta P}{\Delta R_o} \qquad 2.2$$

$$E = E_P \times \frac{2(1-\nu^2)R_i^2 R_o}{(R_o^2 - R_i^2)} \qquad 2.3$$

Where R_i is the internal radius of the tube and R_0 is the external radius.

Combining 2.2 and 2.3 and assuming that the wall thickness is small compared to the radius, one can find the thin-walled approximation for arterial stiffness as given in 2.4

$$\Delta R_0 = \frac{\Delta P R^3 (1-\nu^2)}{Eh} \qquad 2.4$$

Where h is the wall thickness of the tube in metres.

Figure 2.3 shows the variation of E_P in the abdominal aorta with age in human subjects reprinted from Berne and Levy [64], from work originally performed by Imura et al [65]. While a positive correlation is seen between age and vessel stiffness, the data are quite widely spread; even for those under 30, stiffness varies by a factor of four between subjects.

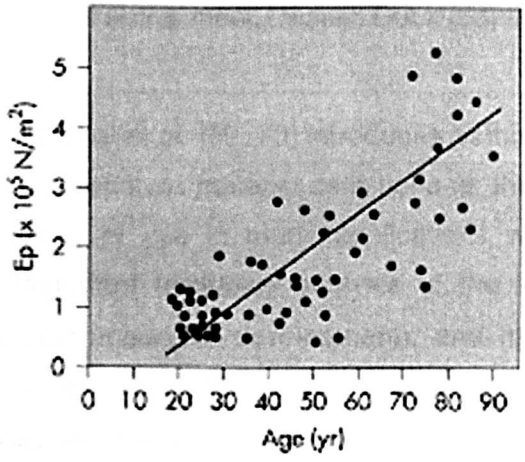

Figure 2.3. The effect of age on E_P. Reproduced from [64]

If one is to use E_P to calculate a representative Young's modulus for a vessel wall, difficulty also occurs in measuring the wall thickness of the artery; or more accurately in deciding where the adventitia stops and the surrounding tissue begins. It is necessary to know how much of the surrounding tissue has a significant effect on the movement of the intima and hence the calculated Young's modulus.

A large number of authors agree that under physiological pressures the ratio of wall thickness to lumen radius lies in the range 0.06 to 0.16 (equating to 0.18 to 0.48mm in the SMA) [56].

As will be shown in 2.2.5, the elastic properties of the artery and the wall thickness play an important role in determining the propagation speed of the pressure pulse along the blood vessel, which in turn is important in determining the pressure/flow relationship in the vessel. As pulse propagation velocity is arguably the most important flow feature associated with vessel wall elasticity, it is reasonable to use this as a basis for estimating wall stiffness. Under certain conditions – discussed later – the wave speed can be described by the modified Moens-Korteweg equation, 2.5

$$c_m = \sqrt{Eh/\rho d_0\left(1-\nu^2\right)} \qquad 2.5$$

Where ρ is the fluid density, and d_0, the internal diameter of the tube[1]. Taking a range of published values for wave velocity in the human abdominal aorta of 5-5.7 ms^{-1} [66, 67] and considering wall thicknesses in the range 0.18 to 0.48 mm, with blood density of 1000 kg m^{-3}, aortic diameter of 23mm and Poisson ration 0.5, we find that the range of wall stiffness which solves this equation is E = 0.89-3.1 MPa. This gives a good idea of sensible values for wall stiffness when modelling the abdominal aorta.

In terms of mass, the arterial wall is mostly water; Duck [68] lists its density as 1050-1075 kg m^{-3}.

More recent work by Holzapfel et al. [69, 70] introduces pathologically based models of the vessel wall including separate material definitions for the media and adventitia. Such models are definitely of use in many applications where subtle local and nonlinear effects are important (including analysis of the vessel wall around an atherosclerotic plaque and aneurysm development), and may be the appropriate choice for a full fluid-structure interaction (FSI – described in 2.4.3) analysis of the SMA and AA. However, for any preliminary work however, the advantages of a simple Hookean model, allowing direct comparison between computational fluid dynamics (CFD – described in 2.4) and Womersley's theoretical results, outweigh the increased biological accuracy of the Holzapfel models. For this reason the Hookean model will be used in the initial CFD analyses; more complex material properties can always be included later.

---

[1] While the subscript '$_0$' used to denote internal diameter of a tube is in direct contradiction of the previous definitions of R_i and R_o (equation 2.3), it is kept in it's original form so as to leave the equations in their published and recognised forms. Hopefully this will cause little confusion, as R_i and R_o have now served their purpose and will not be revisited.

2.2.3 – Modelling Blood

2.2.3.1 – Viscous Behaviour of Blood

As described in 1.2.1, blood is a suspension of cells in a liquid. Under certain conditions the cells affect the viscous properties of the blood causing an increase in apparent viscosity when compared to the plasma, which was found, by Merrill et al. [71], to behave as a Newtonian fluid with viscosity $1.2*10^{-3}$ Pa.s [72]. Two key determinants of the viscous behaviour of normal blood are vessel size and shear rate.

Merrill et al (1963) [73] showed that effective blood viscosity varies with shear rate; figure 2.4 is a reproduction of Merrill's results, showing this variation for a range of temperatures.

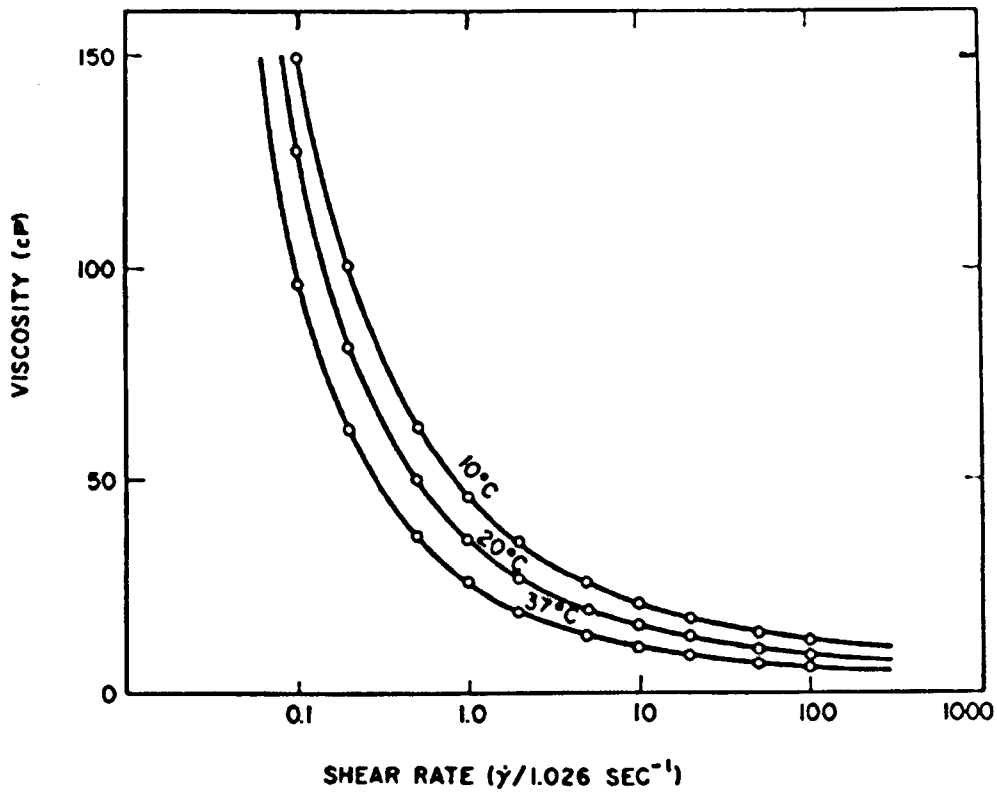

Figure 2.4. 'The variation of the viscosity of human blood with shear rate $\dot{\gamma}$ and temperature for a male donor, containing acid citrate dextrose, reconstituted from plasma and red cells to the original haematocrit of 44.8'. Reproduced from [73].

From this figure, it is clear that viscosity is close to constant for shear rates greater than $10s^{-1}$. Moore et al. measured the mean wall shear stress in the abdominal aorta at the level of the diaphragm to be 0.13±0.06 Pa; assuming blood viscosity of 0.003

Pa s; this equates to a wall shear rate of 43.3±20 s^{-1}, well into the near-linear range. The viscosity recorded at high shear rate is sometimes referred to as the asymptotic viscosity.

In vessels where the largest dimension of the erythrocyte (~8μm) is an appreciable percentage of the lumen diameter, asymptotic viscosity increases. This is due to interactions between erythrocytes and the vessel wall, and between fellow erythrocytes [56]. At ~6mm the lumen diameter of the SMA is about 750 times greater than erythrocyte diameter, as such these effects are negligible.

Unsurprisingly, the asymptotic (high shear rate) viscosity of whole blood varies with haematocrit; this is shown in figure 2.5, reproduced from [56], from data recorded by Whitmore [74]. From this figure we can infer that for a haematocrit of 40%, the asymptotic viscosity of whole blood is around 4.5 Pa s. The nonlinearity of the curve for haematocrit above 60 reflects the saturation of the blood with red cells; the behaviour changes from that of a Newtonian fluid (modified by the presence of a suspension of cells), to something more akin to the lubricated flow of a set of deformable particles.

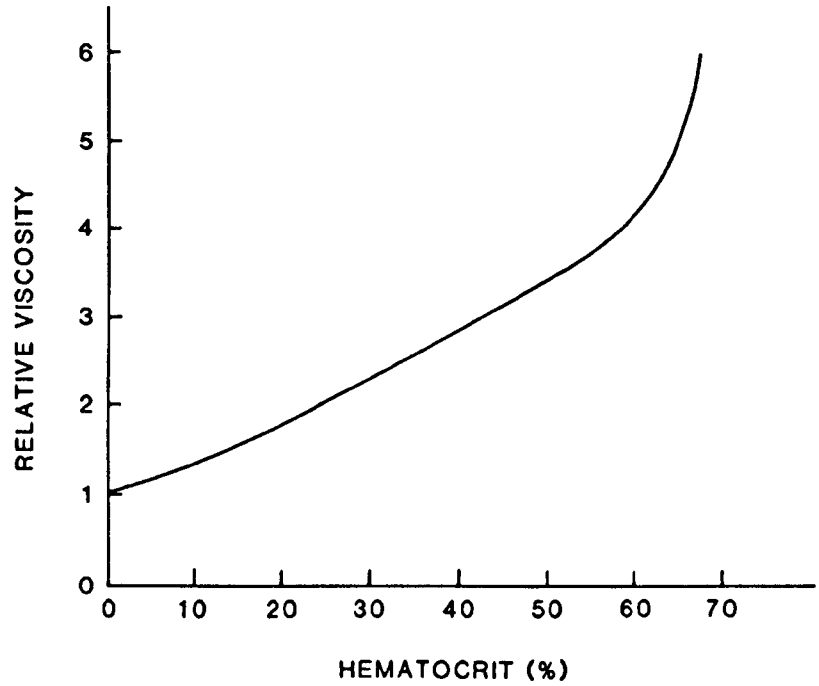

Figure 2.5. 'The variation of viscosity with haematocrit. The ordinate is the asymptotic viscosity relative to that of plasma = 1. The normal value for plasma viscosity is 1.6 cP' Reproduced from Nichols [56]

From the above results, we see that healthy blood flow in the arteries of interest can be described well by a Newtonian model with a viscosity of around 0.0045 Pa s.

2.2.3.2 – Blood Density

Apart from its viscous behaviour, the key fluid dynamic property of blood is its density. The specific gravity of red cells is 1.1 and the specific gravity of plasma is 1.03 [75]. For a haematocrit of 40%, this equates to a whole blood density of 1060 kg m^{-3}.

2.2.4 – The Navier-Stokes Equations

The Navier-Stokes equations, consisting of 3 momentum equations, are the equations of motion for a viscous Newtonian fluid. The Navier-Stokes equations for an incompressible fluid are given in equations 2.6 to 2.8 for a 3-dimensional Cartesian coordinates system [76]. Equation 2.9 is the continuity equation, which can be used to close the Navier-Stokes equations.

First define

$$\frac{D}{Dt} = \frac{\partial}{\partial t} + u\frac{\partial}{\partial x} + v\frac{\partial}{\partial y} + w\frac{\partial}{\partial z} \qquad \text{and} \qquad \nabla^2 = \frac{\partial^2}{\partial x^2} + \frac{\partial^2}{\partial y^2} + \frac{\partial^2}{\partial z^2}$$

the momentum equations are then given by

$$\rho\frac{Du}{Dt} = F_x - \frac{\partial P}{\partial x} + \mu\nabla^2 u \qquad 2.6$$

$$\rho\frac{Dv}{Dt} = F_y - \frac{\partial P}{\partial y} + \mu\nabla^2 v \qquad 2.7$$

$$\rho\frac{Dw}{Dt} = F_z - \frac{\partial P}{\partial z} + \mu\nabla^2 w \qquad 2.8$$

and the continuity equation is

$$\frac{\partial u}{\partial x} + \frac{\partial v}{\partial y} + \frac{\partial w}{\partial z} = 0 \qquad 2.9$$

Where:

u, v and w are fluid velocities in the x, y and z directions respectively

ρ is the fluid density (kg m^{-3})

μ is the fluid viscosity (Pa s)

F_i is the body force density in the i direction

P is fluid pressure (Pa)

The momentum equations govern the interaction of forces in the fluid; the forces due to pressure gradients, inertia, viscosity and body forces are balanced in each plane. The continuity equation ensures that, for any volume in the fluid domain, the flow out is equal to the flow in; no fluid is arbitrarily created or destroyed.

2.2.5 – The Womersley Equations

While blood pressure and blood flow are related by the Navier-Stokes equations, this level of abstraction gives little direct insight to the clinician or scientist. A more specialised treatment of pulsatile flow in tubes, showing how pressure and flow are related, may aid understanding, for it is this relationship that clinicians (often unknowingly) consider when drawing conclusions from blood pressure measurements.

Attempts were made to describe this relationship mathematically as early as 1914 [77]. In the 1950s, with McDonald and Womersley's interest in pulsatile pressure/flow relationships, great progress was made.

One key point was McDonald's realisation, published in his 1955 paper, that pressure gradient, not pressure, is the driving force behind fluid flow. Until this time, the fact was not understood that a pressure wave travelling along a compliant tube is preceded by the associated flow wave rather than followed by it. McDonald's observation was described quite reasonably, using J.B.S. Haldane's phrase, as a 'blinding glimpse of the obvious' [56].

Womersley's papers of 1955 and 1957 [78-80] explored the mathematics of pulsatile flow in compliant vessels. The key results of these papers are outlined below.

In his first paper on this subject [78], Womersley considered rigid walled tubes and derived expressions for the volume flow, Q and velocity, w (at a distance of y=r/R from the tube axis, where r is distance from vessel centre-line in metres), these expressions are equations 2.10 and 2.11 below. The key assumptions of the Womersley equations are as follows [56]:

- The flow is laminar.

- The length of the tube is long compared to the region being studied.
- The fluid is homogenous and Newtonian (having a viscosity which does not vary with the rate of shear or the velocity gradient).
- The flow is through a cylindrical tube with constant diameter.
- The flow may be expressed as a sum of harmonic components calculated from the individual harmonic terms of the pressure gradient.
- No 'slip' occurs at the walls.

$$Q = \frac{\pi R^2 A^*}{i\omega\rho}\left(1 - \frac{2\Im_1\left(\alpha i^{3/2}\right)}{\alpha i^{3/2}\Im_0\left(\alpha i^{3/2}\right)}\right)e^{i\omega t} \qquad 2.10$$

$$w = \frac{A^*}{i\omega\rho}\left(1 - \frac{\Im_0\left(\alpha y i^{3/2}\right)}{\Im_0\left(\alpha i^{3/2}\right)}\right)e^{i\omega t} \qquad 2.11$$

Where

α: the dimensionless Womersley number is given by equation 2.12.

$$\alpha = R\sqrt{\omega\rho/\mu} \qquad 2.12$$

Where R is the radius of tube, ω is the angular frequency.

$\Im_n$: An n^{th} order Bessel Function being a solution to the differential equation given in equation 2.13.

$$x^2\frac{d^2y}{dx^2} + x\frac{dy}{dx} + \left(x^2 - n^2\right)y = 0 \qquad 2.13$$

The known pressure gradient is described in terms of simple harmonic motion in equation 2.14.

$$\frac{\partial p}{\partial z} = A^* e^{i\omega t} \qquad 2.14$$

In a subsequent paper [80] considering flow in elastic walled tubes, Womersley showed that, while the time-varying velocity profiles remain the same as for the rigid

walled tube, the wave velocity along the tube becomes finite and is governed by the equations below. Additional assumptions for the treatment below are:

- A longitudinal movement constraint was imposed, such that any element of the tube wall can only move radially.
- The wall is thin, elastic and has homogenous material properties.

Using these assumptions, Womersley proposed an extension to the Moens-Korteweg equation, which can be used to calculate the wave speed for a non-viscous fluid in an unconstrained compliant tube (2.15) [81].

$$c_0 = \sqrt{Eh/\rho d_0} \qquad 2.15$$

Where c_0 is the wave speed; E, the Young's modulus of the tube material; h, the wall thickness; ρ, the wall density; and d_0, the internal diameter of the tube.

Womersley showed that for a viscous fluid, and taking into account the effect of the longitudinal constraint, a modified (complex) wave speed c is given by equation 2.16.

$$c = c_0 \sqrt{\frac{M'_{10}}{(1-\nu^2)}} \sec\left(\frac{\varepsilon'_{10}}{2}\right) \qquad 2.16$$

Where ν is the Poisson's ratio of the wall material – $c_0/(1-\nu^2)$ is often known as the modified Moens-Korteweg equation; M'_{10} and the phase of the unit length vector ε'_{10} are the magnitude and phase of the spatial pressure gradient respectively, these can be written as equation 2.17 below.

$$M'_{10}e^{\varepsilon'_{10}} = (1-F_{10}) = 1 - \frac{2\Im_1(\alpha i^{3/2})}{\alpha i^{3/2}\Im_0(\alpha i^{3/2})} \qquad 2.17$$

Substituting this back into equation 2.16 giving equation 2.18

$$c = c_0 \sqrt{\frac{(1-F_{10})}{(1-\nu^2)}} \qquad 2.18$$

The definition of a complex wavespeed describes two key effects. The first is that different harmonics travel at different speeds; this apparent wavespeed for each frequency is referred to as c_1 and is given by 2.19.

$$c_1 = \frac{1}{real(1/c)} \qquad 2.19$$

The second effect is that, for each harmonic, a damping factor, λ, reduces the amplitude of the pressure wave per wavelength travelled according 2.20

$$\lambda = 2\pi \tan\left(\varepsilon_{i0}''/2\right) \qquad 2.20$$

With this damping factor taken into account, the following relations are found

$$p = A^* e^{i\omega(t - z/c)} \qquad 2.21$$

$$\frac{\partial p}{\partial t} = A^* e^{i\omega(t - z/c)} \qquad 2.22$$

Assuming frequency superposition holds (although not strictly true, shown to be a reasonable assumption in a wide variety of cases [56]); Fourier analysis can be used to find an overall Womersley flow profile for any repeating waveform. This means that for a straight tube, the Womersley equations can be used to calculate wall shear stress varying with time for any repeating waveform.

To demonstrate the usefulness of the Womersley equations, 2.2.6 shows results that can be obtained for a straight tube of similar nature to the SMA.

2.2.6 – The Womersley Equations Applied to the SMA

A representative SMA flow waveform measured using phase contrast MRI (described in chapter 3) is shown in figure 2.6, this flow profile was applied to a Womersley model of an infinite length straight tube of 6mm diameter, containing an incompressible Newtonian fluid of density 1000 kg m^{-3} and viscosity 0.004 Pa.s.

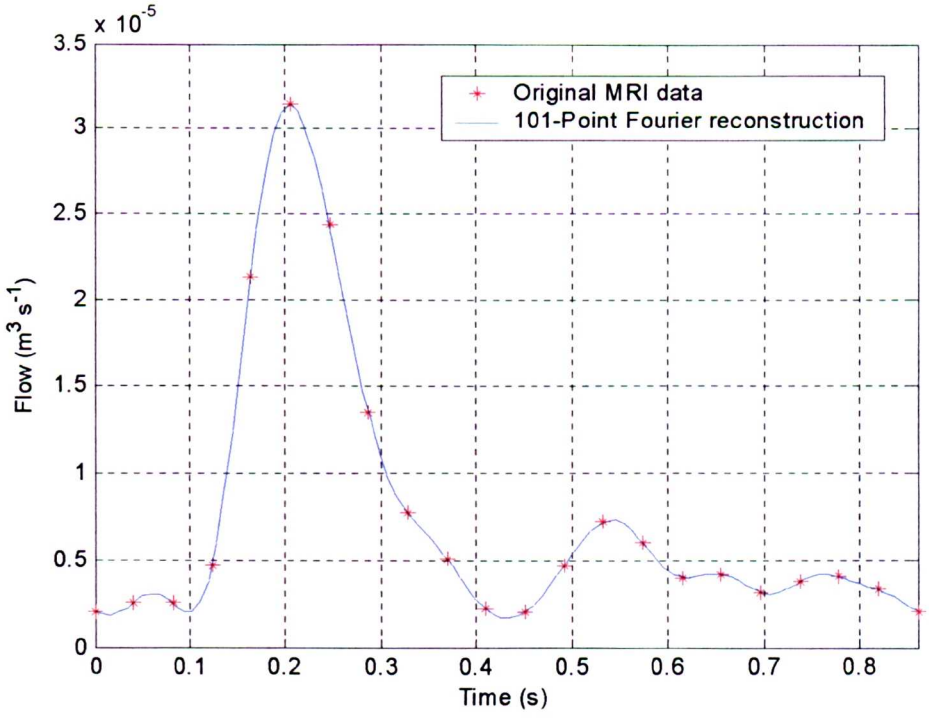

Figure 2.6. Representative SMA flow waveform, raw MRI data and 101-point Fourier reconstruction.

The input is repeating but not sinusoidal, so it contains a range of frequencies and hence a range of Womersley numbers; figures 2.7 and 2.8 show flow profiles varying through the cardiac cycle and across the tube for the fundamental (corresponding to a Womersley number of 4.1) and highest (corresponding to a Womersley number of 13.4) harmonics respectively. Combining the contributions from all frequencies present in the signal (as well a separately calculated Poiseuille flow component for the steady flow term) gives the time-varying flow profile for the whole waveform; this is shown in Figure 2.9.

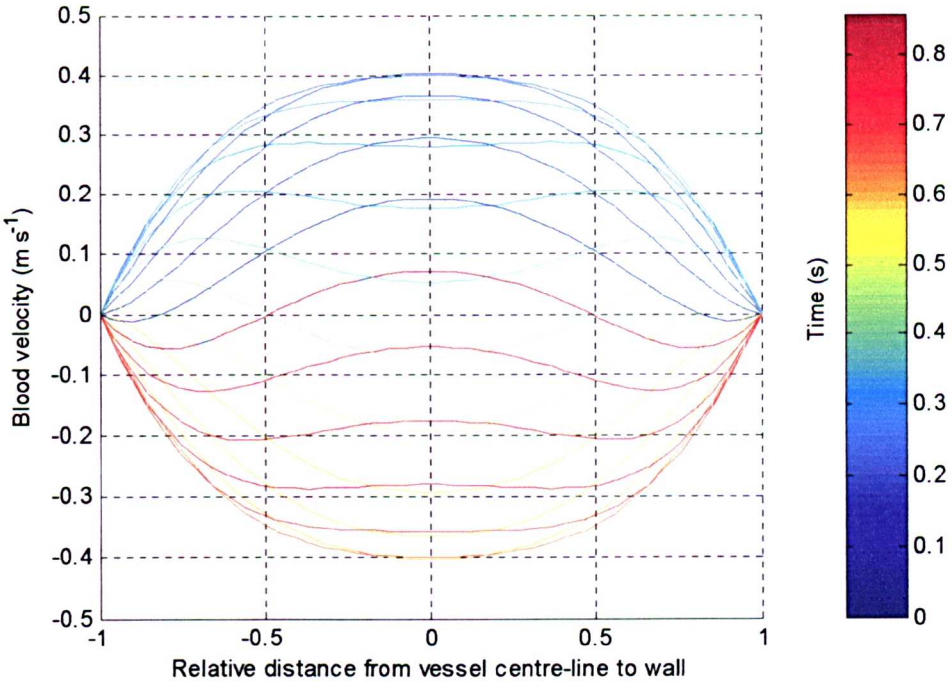

Figure 2.7 Time-varying flow profiles across the tube at α=4.1

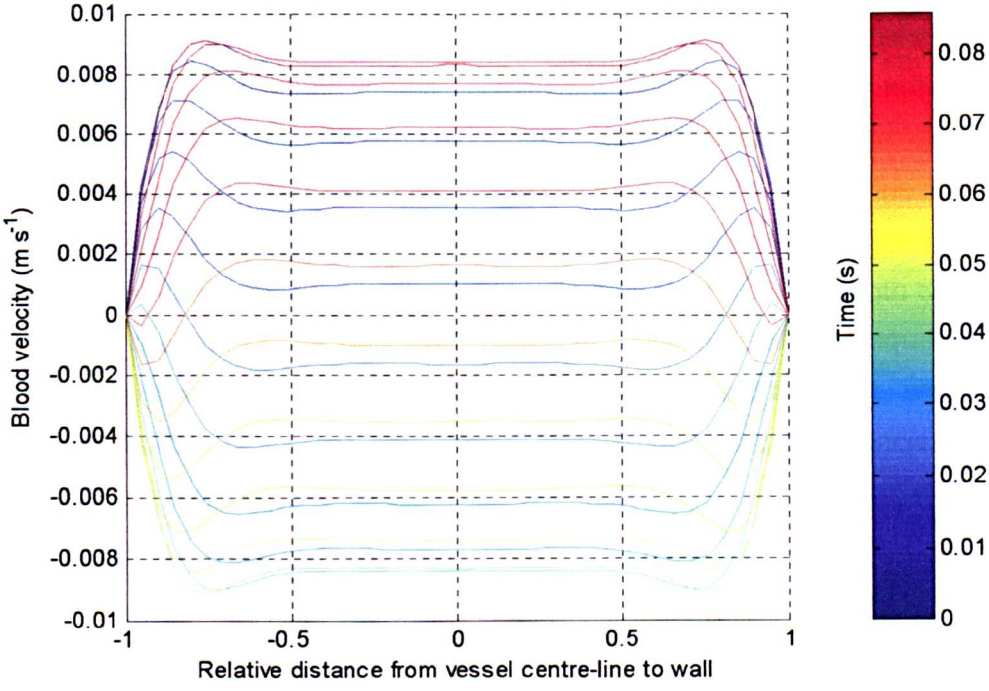

Figure 2.8 Time-varying flow profiles across the tube at α=13.9

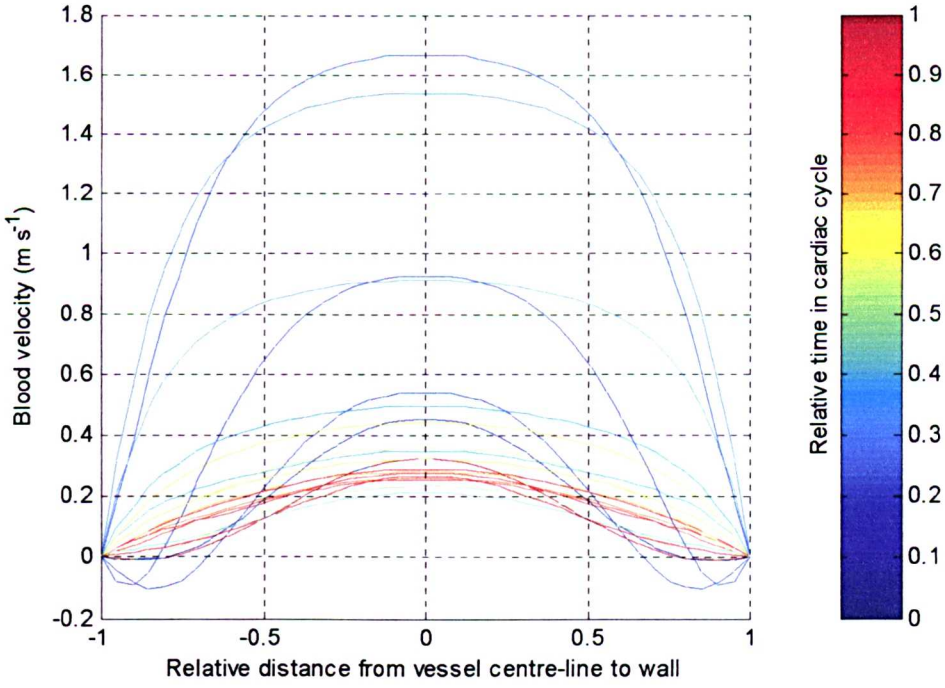

Figure 2.9 Time-varying flow profiles across the tube for representative abdominal aortic waveform.

Making the further assumptions that the vessel wall has a stiffness of 1MPa, Poisson's ratio of 0.499 and a thickness 0.1mm, gives enough information that the Womersley equations can be used to calculate the pressure waveform necessary to produce such a flow pattern in an infinite length tube – for this part of the analysis the steady flow component is disregarded as infinite pressure would be required to overcome the fluid inertia and produce steady flow in an infinite length tube. Figure 2.10 shows the necessary pressure waveform; note that in this frequency range, although the flow shows pulsatile characteristics with regard to profile, pressure and flow are close to in phase and have similar attenuations for all frequencies.

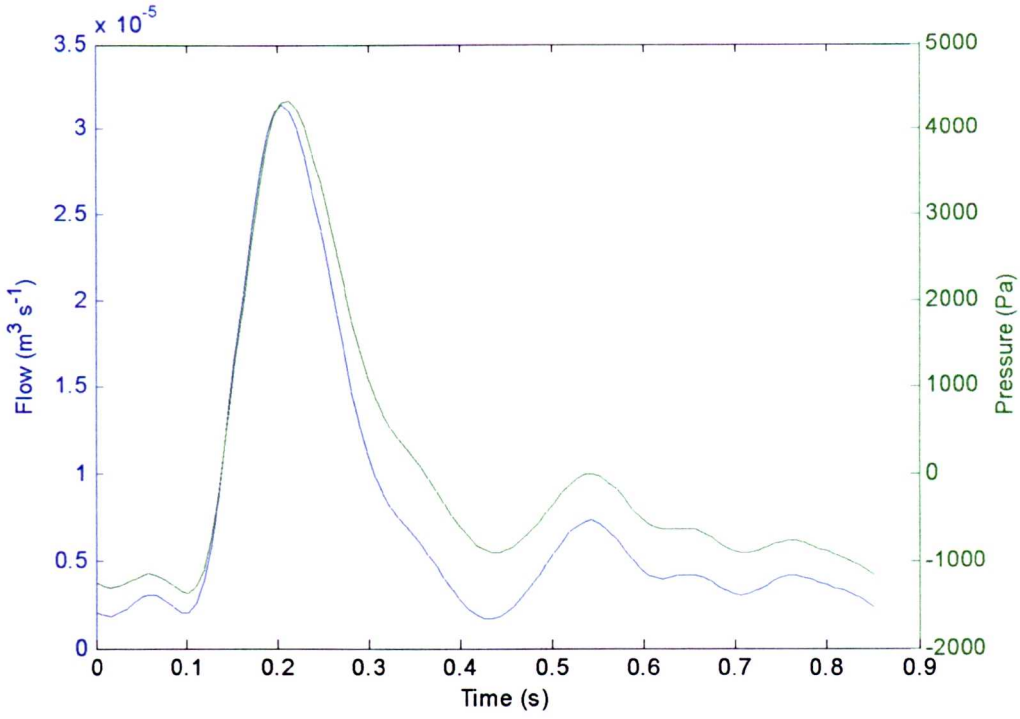

Figure 2.10. Fourier-interpolated pressure and flow waveforms for flow in the Womersley SMA Model.

Figure 2.11 shows the Moens-Korteweg, modified Moens-Korteweg and apparent wave-speed for all frequencies present in the waveform.

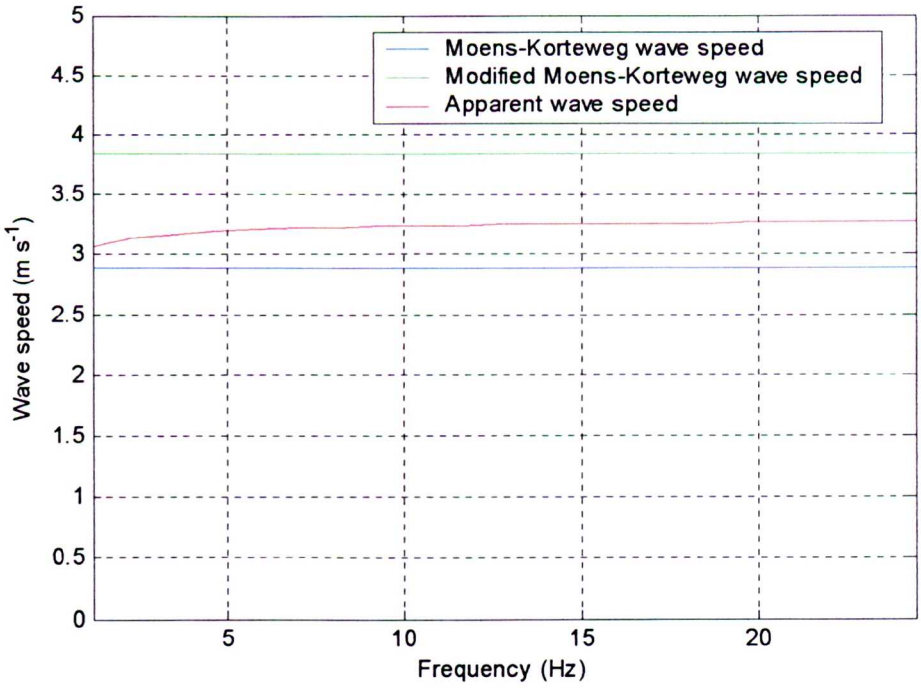

Figure 2.11. Modified Moens-Korteweg and apparent wave-speed for all frequencies present in the flow waveform.

The effect of the damping of the pressure wave can be seen if pressure at a single point in time is plotted as a function of distance along the tube; this is shown in figure 2.12 for the Fourier interpolated waveform. Note particularly the x-scale. The wavelength is substantially longer than the vessel length, so as the pressure wave passes along the vessel it will be seen as a general dilation rather than a travelling pulse.

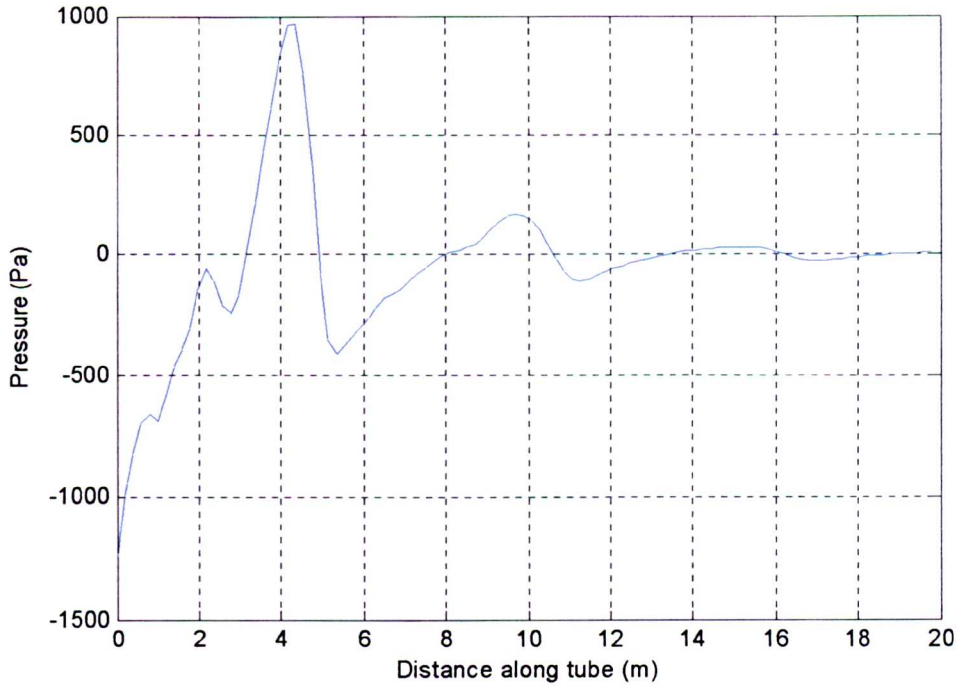

Figure 2.12. Pressure against distance along tube at one point in time for Womersley model of the SMA.

2.2.7 – Turbulence and Disturbed Flow

Probably the most important non-dimensional number in fluid dynamics is the Reynolds number (given in eq 2.23), this takes into account the effects of density, viscosity, fluid velocity and a characteristic length and combines them to give a measure of the stability of a flow.

$$\mathrm{Re} = \frac{\rho V D}{\mu} \qquad 2.23$$

Where

V is fluid velocity (in this case the average flow velocity across the tube)

D is the tube diameter (more generally, the characteristic length)

Small Reynolds numbers are associated with ordered, laminar flow, while higher numbers are associated with disordered, turbulent flow. Between these two states, lies a region of transition where flow may be disturbed but this disturbance will tend to die out. The Reynolds number at which the transition to turbulence takes place is dependent on the geometry being studied, for a straight tube, Re=2300 is often given as the point at which flow becomes turbulent. For a very smooth tube and very well ordered inlet flow, laminar flow can be preserved for Re ~40 000 [76].

When using the Reynolds number to characterise pulsatile flow, one has to decide what measure of fluid velocity to use. Reynolds number based on temporal peak spatial average velocity (peak Reynolds number) is often used.

Whilst the assumption of laminar flow in the SMA seems appropriate as the available data suggests a peak Reynolds number of around 900 [47], the Reynolds number governs the transition to turbulence in a steady, Newtonian flow in a straight rigid, tube. Clearly, it is not appropriate to assume that Reynolds number alone is a good indicator of when the transition to turbulence will take place in the cardiovascular system. Local anatomical feature can also play a major part; if the flow is obstructed by a stenotic heart valve or an atherosclerotic lesion for example, turbulence could be observed at Reynolds numbers as low as several hundred [56].

While the Reynolds number is key to determining the stability of steady, Newtonian flow in a straight pipe, in pulsatile flow the Womersley number (defined in 2.11) is also important for unsteady flow.

The Womersley number, like the Reynolds number, is dimensionless; it fully describes the level of pulsatility of a Newtonian flow regime in a straight tube. A low Womersley number indicates a relatively steady flow where, even though there may be flow reversal, the flow profile at any point in time is parabolic, as in Poiseuille flow and in figure 2.7. At higher Womersley numbers the effect of the pulsatility is felt and the flow profile is more plug-like [78] as seen in figure 2.8.

The Womersley number (for the fundamental frequency) in the human proximal aorta is around 22[56], giving the flow profile shown in figure 2.13. Clearly, the effect of pulsatility is important in both the abdominal aorta and SMA.

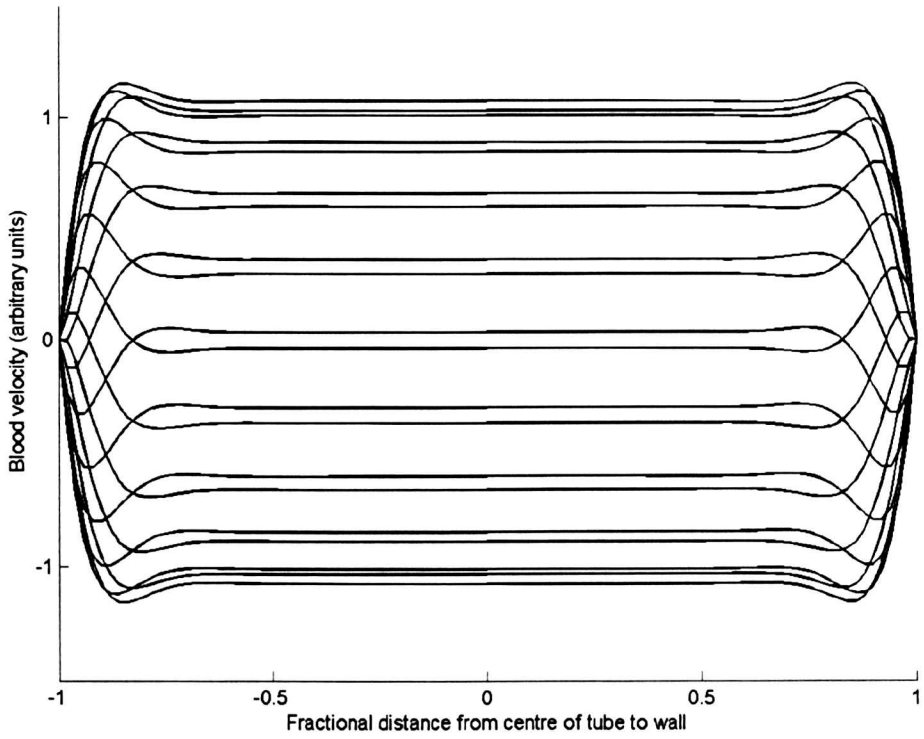

Figure 2.13. Flow profiles for α = 22.

Work done in 1972 by Nerem and Seed [82] showed that pulsatility has a clear effect on the transition to turbulence. The main outcome of this work is shown in Figure 2.14.

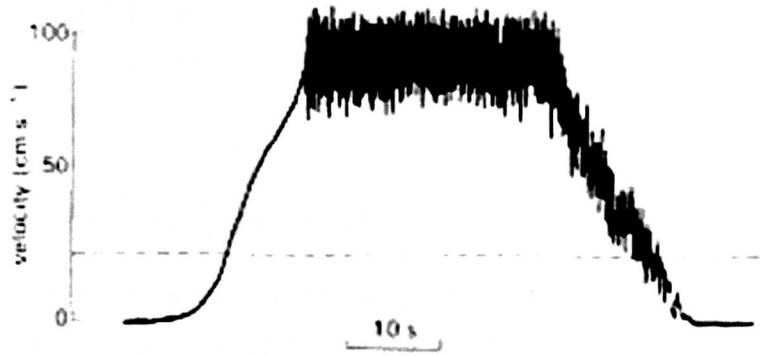

Figure 2.14. A turbulent flow velocity-versus-time record made with a hot-film probe in a pipe (dotted line represents Re = 2300)[82].

In the above study, fluid velocity was increased until turbulence set-in and then allowed to decrease until the flow returned to its laminar state. The flow was seen to remain laminar until a Reynolds number of 9500 was reached. The reason given for these results was firstly that in the accelerating phase, time was needed for turbulence to develop and hence would be expected to develop some time after the critical Reynolds number was reached, likewise time is needed to allow the disturbance to diminish once the Reynolds number has fallen below the critical level. Fung also mentions the inherent stability of accelerating flow and instability of decelerating flow when compared to steady flow, this is a function of the non-linear nature of the Navier-Stokes equations.

Pedley [83] reviewing Nerem et al.[84], suggested that in the thoracic aorta of dogs, flow with $Re_{PEAK} > 250\alpha$ indicated disturbed flow while below $Re_{PEAK} < 250\alpha$ would lead to undisturbed flow.

Stein et al. [85] carried out hot-film catheter anemometry on the abdominal aorta in two positions, (near the renal artery and above the aortic bifurcation) on seven live human subjects; they classified the flow as undisturbed at both locations in all subjects.

2.2.8 – Swirling Flow in the Aorta

The geometry of the aortic arch and the left ventricle's pumping action impart a vortical component on flow in the ascending aorta and aortic arch [86]. Studies in dogs have shown this swirl to extend into the thoracic aorta [87]. More recent MRI based work in young and elderly human subjects [88] characterized the vortical flow in the ascending aorta, aortic arch and descending aorta of 16 volunteers; in all but 3 no helical component was seen in the descending aorta.

2.3 – Simulation of Blood Flow – Lumped Parameter Models

Lumped parameter models are mathematical models where distributed effects, such as the resistance to flow in a tube (which is actually a sum of all the viscous losses encountered anywhere in the tube) are lumped together and regarded as a single loss. Such models can be written down in terms of ordinary differential equations; the values of flow and pressure being calculated as a function of time.

2.3.1 – Windkessel Models

The first reference to the term 'windkessel' with regard to the circulatory system comes from the German translation of Hales 1733 book 'Haemostatics'. Hales likened the smoothing of the pressure pulse as it moves into the smaller blood vessels to the action of the inverted air-filled dome on a contemporary fire engine in smoothing the hand-pumping action to give a near steady flow of water; in the German translation, this dome became a windkessel.

The term windkessel is now used to describe simple lumped parameter models of the circulation, comprising 2, 3 or 4 elements. Such windkessels are often considered in terms of their electrical analogue, with pressure and flow represented by voltage and current; in this context, resistances, capacitances and inductances represent fluid resistance, vessel compliance and inertial terms respectively.

The first windkessel (using the definition above) was Otto Frank's 2-element model first presented in a paper of 1899 [89]. This comprised a resistance and a capacitance in parallel. The resistance represented systemic resistance to flow (sited primarily in the arterioles), while the capacitance represented the dilation with pressure of the large, elastic vessels (primarily the aorta). As the first model of the systemic circulation, the 2-element windkessel gave insight into pressure-flow relationships, but its simple form meant that it could not model the system adequately for quantitative work. At high frequencies impedance drops to zero for the 2-element windkessel, for this reason it was found to give poor results with regard to modelling aortic pressure for a given aortic flow waveform [90].

To overcome the problems of the 2-element windkessel, Westerhof et al added a third element, a resistance in series with the parallel pair [91]; the resistance accounts for the effect of the local inertia and compliance of the proximal ascending aorta, and is associated with wave transmission effects, this component is referred to by Westerhof as the characteristic impedance. The characteristic impedance is, strictly-speaking, a complex impedance in its own right, but has been shown to be real for large arteries [92].

Westerhof's 3-element windkessel, sometimes referred to as the westkessel, is now the most widely used windkessel [93-95], its circuit diagram is shown in figure 2.15.

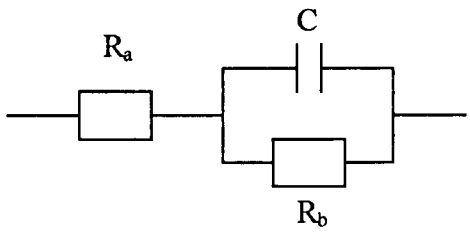

Figure 2.15. Circuit diagram for 3-element windkessel.

Where C is system compliance; R_P is peripheral resistance, and R_C the characteristic impedance.

With appropriate parameter selection, this model has been shown to reproduce pressure-flow relationships well in the large arteries [90].

Stergiopulos et al. [90] noted that the parameters necessary to obtain a good fit to experimental data differed markedly from those measured *in vivo.* In a separate paper, they contend that as R_C is associated with wave transmission effects, it should have no effect on steady flow. Their solution is to add an inductive (inertial) element in parallel with R_C accounting for the inertia of the whole arterial system [96]. The circuit diagram for such a windkessel is shown in figure 2.16

.

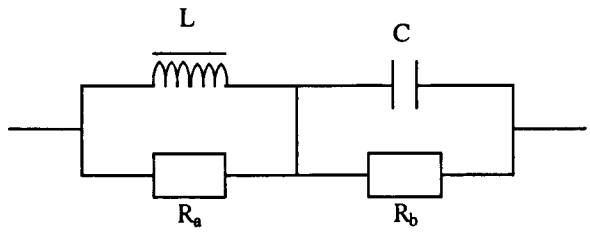

Figure 2.16. Stergiopulos 4-element windkessel.

Where L is the total fluid inertance for the system – the sum of all local fluid inertances. Fluid inertance L_f for a pipe section of length l; cross-section, A; containing a fluid of density, ρ is given by 2.24

$$L_f = \frac{\rho L}{A} \qquad 2.24$$

Stergiopulos showed that this 4-element construction gave better results than the 3-element model in terms of predicting the pressure flow relationship accurately using measured parameter values.

Other 4 element windkessels have also been suggested and used; two such models are shown in figures 2.17 and 2.18.

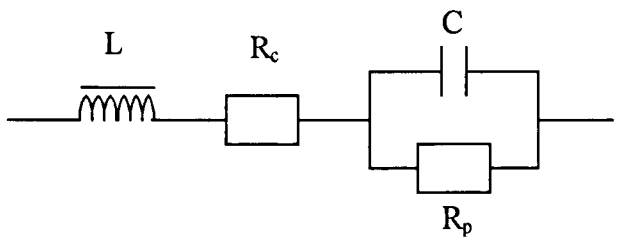

Figure 2.17. RL series 4-element windkessel.

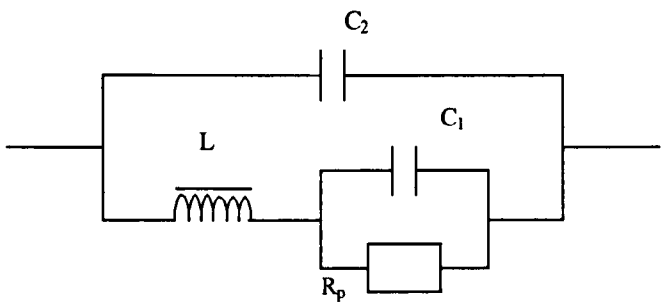

Figure 2.18. Goldwyn-Watt 4-element windkessel.

In the Goldwyn-Watt model shown in figure 2.18, C_2 is said to characterise the oscillatory nature of the pressure wave, but its exact physical meaning is unclear and the model suffers from similar problems to the westkessel – in that when fitting parameters to model data, it gives estimates of model parameters that differ substantially from measured values [97].

The frequency domain characteristics of windkessels are analysed in chapter 5.

2.3.2 – Structured Tree Models

An inherent problem with windkessel models is that they assume that pressure and flow are the same everywhere in the circulatory system at all points in time; meanwhile, the more complex windkessels attempt to take wave propagation effects into account. Clearly there is a paradox here.

Structured tree models attempt to keep most of the simplicity of the windkessel whilst modelling wave propagation effects more realistically. A structured tree is essentially a series of connected simple models (often windkessels), representing the large arteries of the body. Interrogating the model at any point will give information about blood pressure and flow-rate at this point, these values will vary throughout the model. Figure 2.19 shows the standard repeating unit for the Westerhof structured tree published in 1969 [98].

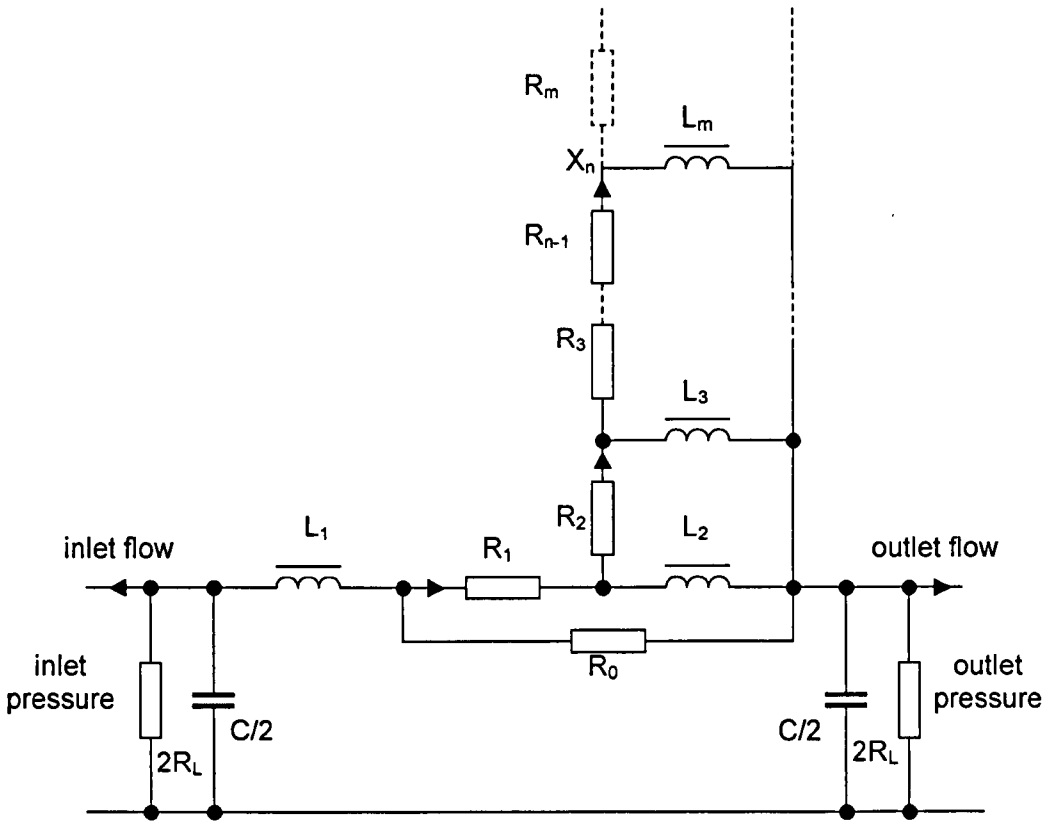

Figure 2.19. Westerhof's electrical representation of a segment of artery of length Δz.

Where (reproduced from [98])

$$R_n = R_n' \Delta z = \frac{8\pi\mu}{S^2} n \, \Delta z \qquad 2.25$$

$$L_n = L_n' \Delta z = \frac{\rho}{S} \frac{1}{2n-1} \Delta z \qquad 2.26$$

$$C = C' \Delta z = \frac{3\pi r^2 (a+1)^2}{E(2a+1)} \Delta z \qquad 2.27$$

$$R_0 = R_0' \Delta z \qquad 2.28$$

$$R_L = \frac{R_L'}{\Delta z} \qquad 2.29$$

R_n', L_n' and C' represent viscous and inertial properties of blood and the compliant properties of the arteries, respectively. (Primed quantities are used to indicate that they are given for unit length)

R_0 is a resistance for correction of anomalous viscosity, or to account for boundary layer of lower viscosity.

n = 1,2, up to m, being at least 3 and at most 5, depending upon the radius

R_L' = leakage per unit length through small branches.

Δz = length of arterial segment [varies from 0.02 to 0.075m in the model]

$S = \pi r^2$, r = radius, a = r/h

These segments can be connected together, simply by connecting the output of one segment to the input segment. If a bifurcation is required, two segments are connected to one outlet.

Westerhof collected data on section length, internal radius, wall thickness and wall stiffness for 120 segments representing all the major blood vessels of the systemic circulation (some split into multiple parts); from this he calculated the necessary values for the components in each segment. A resistance was placed at the termination of each branch.

Figure 2.20 shows a representation of Westerhof's structured tree. In this model, the SMA represents a terminal branch; a single pure resistance represents everything downstream of the proximal 5.9cm of the SMA.

Westerhof's model results correlated well with anatomical data and predict certain phenomena associated with wave reflection such as the dichrotic notch [99].

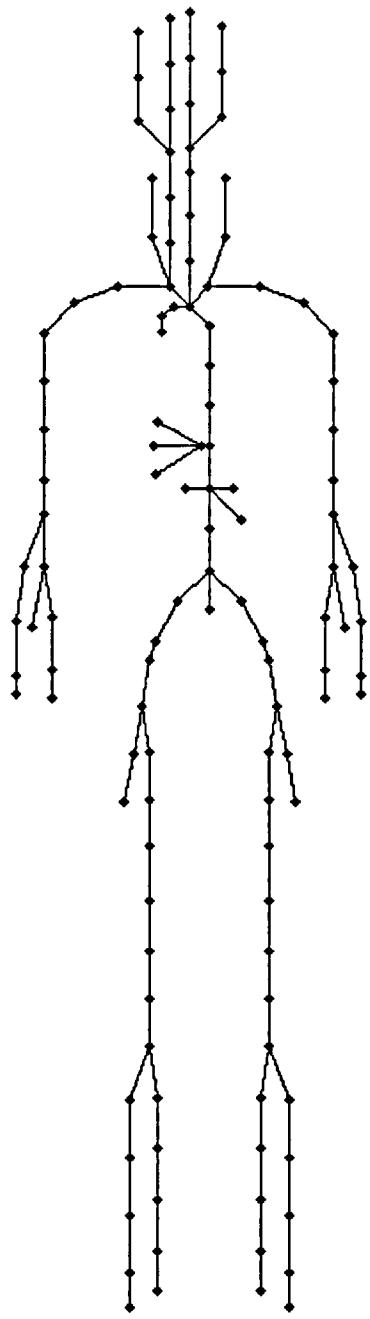

Figure 2.20. Representation of Westerhof structured tree model [99]. Each line represents an arterial segment, red point represents heart, blue segment represents SMA.

A similar model was designed by Avolio [100] in 1980. In this case, the model was based directly on the Womersley equations, rather than on windkessels; a characteristic impedance and propagation constant (which governs the exponential decay of a Pressure wave along a pipe at a point in time), based on material properties, were calculated, and transmission line theory used to connect them.

As with Westerhof's model each terminal branch was connected to a pure resistance.

A third, very simple approach formed from basic mathematical principles is that adopted by Zamir et al[101]. Zamir developed a fractal system for modelling arterial branching based on 'parametric Lindenmayer systems' or L-systems. According to the author, this approach allows the generation of 'branching tree structures that can incorporate the physiological laws of arterial branching'. The algorithm used in this paper is a true fractal in that if run continually it will keep generating patterns of branching of the same shape independent of scale; this leads to very straightforward programming, but does have some problems associated with it, which will be discussed later.

The approach used by Zamir is based upon a set of simple assumptions, these are:

- Each bifurcation is defined by the length and angles shown in figure 2.21.

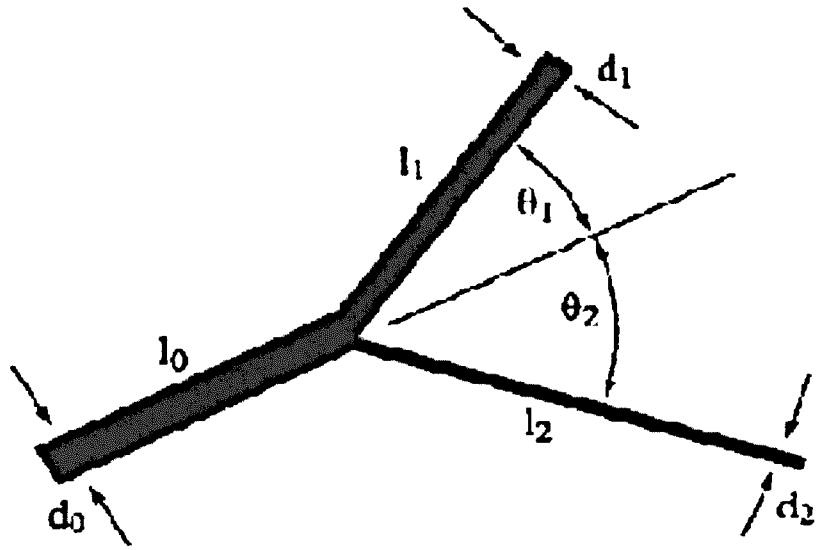

Figure 2.21. Reproduced from Zamir [101] 'The basic variables at an arterial bifurcation are the lengths and diameters of the three vessel segments involved, and the angles that the two branches make with the direction of the parent vessel. In this paper, the convention is used that subscript 1 always refers to the branch with the larger diameter, and in graphical constructions that branch is always placed at an angle in an anticlockwise direction from that of the parent vessel. The convention is purely arbitrary, but it has a bearing on the "slant" of nonsymmetrical trees constructed in this way.'

- The ratio of daughter to parent vessel diameter is given by

$$\lambda_1 = \frac{d_1}{d_0} = \frac{1}{\left(1+\alpha^k\right)^{1/k}} \qquad 2.30$$

and

$$\lambda_2 = \frac{d_2}{d_0} = \frac{\alpha}{\left(1+\alpha^k\right)^{1/k}} \qquad 2.31$$

Where α is given by d_2/d_1 and is called the bifurcation index or asymmetry ratio, and k is based on the power law, flow $\propto d^k$. Zamir suggests that $k \approx 3$ for much of the arterial tree, (particularly for anywhere where flow is steady), but may be closer to 2 in the larger arteries, this makes sense with regard to plug-like flow at high Womersley numbers.

- The length of each segment is calculated as a simple multiple of the segment diameter, average ratio of l/d = 10 is suggest and used for the following examples.
- For k = 3, the angles θ_1 and θ_2 are given by

$$\cos\theta_1 = \frac{\left(1+\alpha^3\right)^{4/3} + 1 - \alpha^4}{2\left(1+\alpha^3\right)^{2/3}} \qquad 2.32$$

And

$$\cos\theta_2 = \frac{\left(1+\alpha^3\right)^{4/3} + \alpha^4 - 1}{2\alpha^2\left(1+\alpha^3\right)^{2/3}} \qquad 2.33$$

These values minimise the total volume of the three vessel segments, and assuming k=3 minimise the pumping power required to drive flow through the bifurcation.

Figures 2.22, 2.23, and 2.24 show bifurcating trees based upon the above algorithm with varying values of alpha and k (for the diameter ratio part). Note that in figure 2.24, for a negative value of alpha, the tree is defined but not sensible.

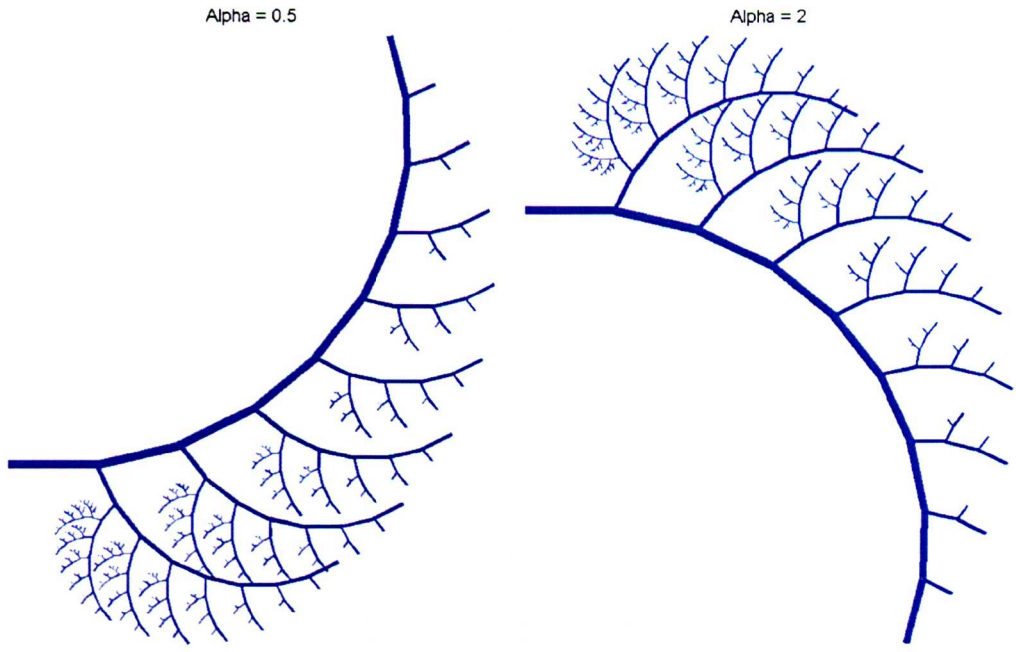

Figure 2.22. Examples of bifurcating trees for alpha = 2, and alpha = 0.5 (vertical reflection).

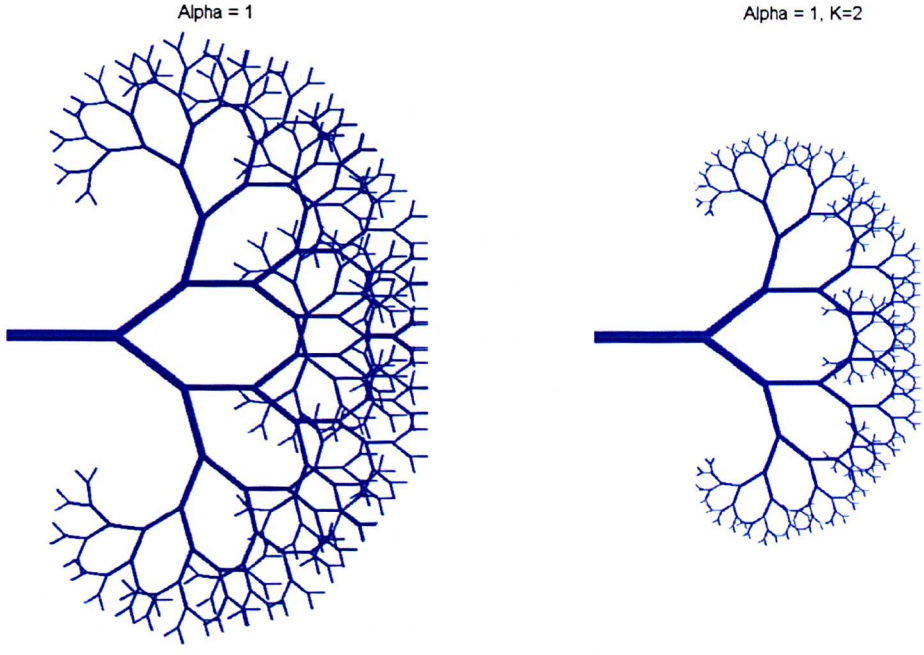

Figure 2.23. Symmetrical trees generated by alpha = 1, with k= 3 (left) and k = 2 (right), k = 2 only applied to the diameter ratio term.

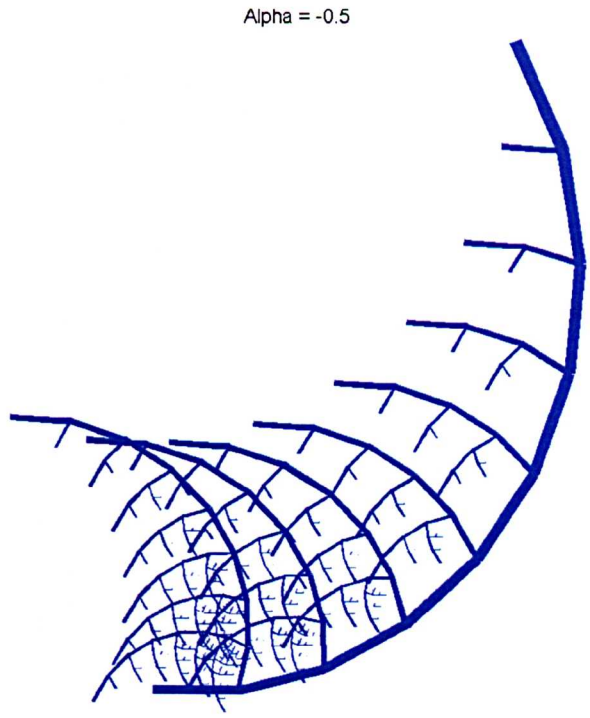

Figure 2.24. Bifurcating tree for alpha = -0.5.

Zamir's modelling technique does not predict flow, but may be used as a basis for the development of flow models using Westerhof's basic repeating unit.

While these models do not consider the subtle flow features that govern wall shear stress distributions, they may help in the design and validation of more complex models that can. The use of both structured trees and windkessels in conjunction with CFD models will be discussed in 2.4.5 and chapter 5

2.4 – Simulation of Blood Flow – Computational Fluid Dynamics (CFD)

2.4.1 – Basics of CFD Modelling

Computational fluid dynamics is a well-recognised and accepted branch of engineering practice used to calculate numerical solutions to fluid flow problems. A mesh is created, splitting the volume of interest into a large number of small, regular elements; when the Navier-Stokes equations are imposed on the mesh they take the form of a large set of non-linear equations. Solving these equations usually requires

the inversion of a large, sparse matrix. The computationally intensive nature of the task means that CFD modelling of the cardiovascular system has progressed substantially in recent years in parallel with computational power. A generation ago, the only models that could be routinely solved were those involving two-dimensional Newtonian, laminar flow in idealised geometries. Now, transient, full 3d analyses in realistic geometries can be run on the average desktop computer.

When the system has been solved it is possible to examine many aspects of the fluid flow in detail; of particular interest to this study is ability to examine patterns of wall shear stress.

Faithful representation of the geometry of the arteries is very important, as it is a key determinant of flow patterns and wall shear stress. Figure 2.25 shows an example mesh representing the geometry of the AA and SMA – in this figure the roots of other branches are also shown; these are included for anatomical context and will not be modelled

As only a small section of the complete cardiovascular system is being modelled, the conditions at the edges of the model must also be defined. These represent a model of the system outside the boundary and can vary greatly in their complexity, as will be seen.

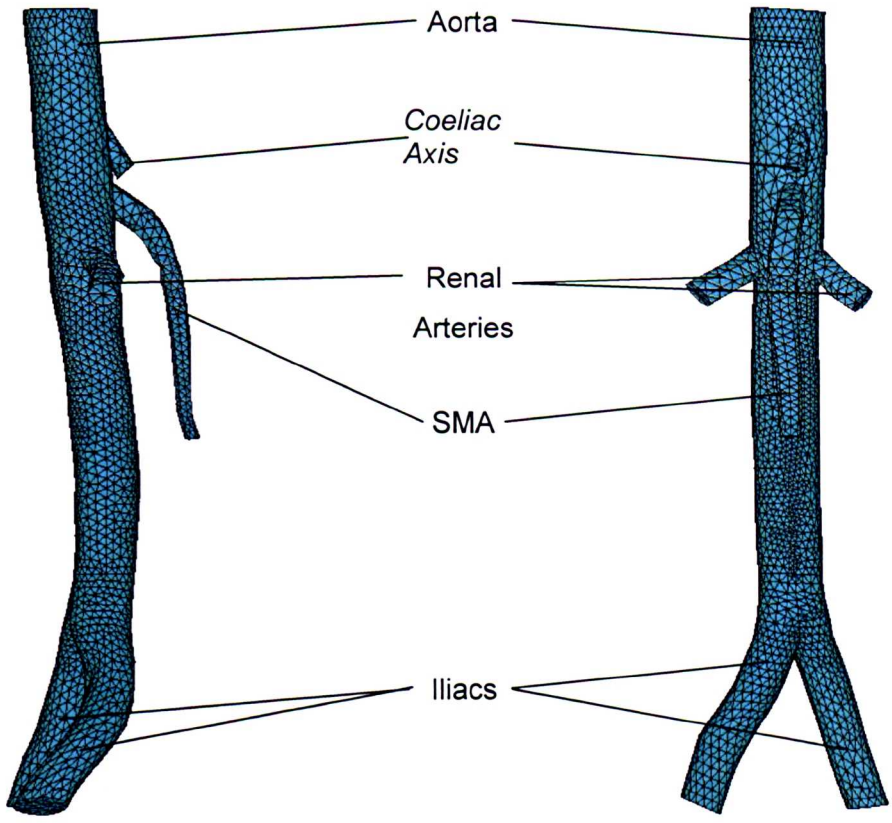

Figure 2.25. Representative geometry of the AA and SMA (with branches truncated).

2.4.1.1 – Inlet Boundary Conditions

Although flow in the arterial system is pulsatile, average flow over time is always from the heart to the periphery. For this reason it is sensible to refer to the proximal aortic cross-section of the model as the inlet. Either pressure or flow (with an appropriate profile) could be applied as a boundary condition to drive the model.

2.4.1.2 – Outlet Boundary Conditions

There are two outlets to the system as described. These are the downstream AA and the SMA; one role of the downstream boundary conditions is to direct an appropriate amount of flow along each of these branches. In the case of FSI analyses, impedance matching at the downstream boundaries is also important if pressure-wave reflections are to be avoided. This will be discussed further in 2.4.5.

2.4.1.3 – Wall Boundary Conditions

Boundary conditions at the wall are less problematic than at the openings. The standard treatment of 'no slip at the wall' – held to be universally true for liquids [56] – is appropriate for this problem. It is worth noting that should a turbulence model be introduced, further information is needed at the wall.

2.4.1.4 – Vessel Geometry (Static/Dynamic)

Due to the complexity of the governing equations, apparently subtle features of geometry can have significant effects in terms of fluid dynamics. Hence, an accurate map of 3d vessel geometry is needed; for the case of a vessel exhibiting significant gross motion, this map must be time-varying if all salient flow features are to be accurately modelled.

2.4.1.5 – CFD Theory 1 – Discretisation

In order to solve the Navier-Stokes and continuity equations for a given geometry and set of boundary conditions, the system must be discretised in space and time. Discretisation of the spatial domain is specified by the creation of the mesh, and discretisation of the temporal domain is specified by choosing a timestep size, and start and end times. A full run down of the theory for Ansys Flotran is provided in [102], this section highlights the key features of the approach used.

In order to work within this discretised domain, the equations must also be discretised in both space and time. Many approaches are available for these discretisations, for a straightforward and general review the reader is referred to Patankar [103]. The discretisation process can be considered as the derivation of the 'A' matrices in 2.34.

$$\left(\left[A_e^{transient}\right]+\left[A_e^{advection}\right]+\left[A_e^{diffusion}\right]\right)\left\{\phi_e\right\}=\left\{S_e^{\phi}\right\} \qquad 2.34$$

Where: φ represents vx, vy or vz; S represents the source term (dP/dx (or dP/dy or dP/dz) in the absence of gravity and distributed resistances); and $A^{transient}$, $A^{advection}$ and $A^{diffusion}$ represent the discretised versions of the transient, advection and diffusion terms in the Navier-stokes equations. The subscript 'e' states that these values must be defined for each element.

Flotran performs finite-element based discretisation for the transient and diffusion terms.

For the advection term, Flotran offers three approaches; the default 'monotone streamline upwind' approach, described in [104], was used throughout.

Throughout, the backward difference time integration method was used.

2.4.1.6 – CFD Theory 2 – Solution

Once the matrices have been generated using the approaches outlined above, the system of equations must be solved. Here a problem presents itself; as pressure is not mentioned in the continuity equation, it cannot be used directly to close the momentum equations. The SIMPLEF and SIMPLEN algorithms available are based on the SIMPLE (Semi-Implicit Method for Pressure-Linked Equations) algorithm developed by Patankar [103]. The basic SIMPLE algorithm (assuming a laminar, fluid-only problem) is outlined below:

1. Make p^* the initial guess at the pressure field.
2. Solve the momentum equations to obtain velocity estimates; u^*, v^* and w^*.
3. Solve a 'pressure equation', to give an updated guess, p.
4. Calculate a series of updated velocities x, y and z, from u*, v* and w* and a set of velocity-correction equations.
5. If convergence isn't achieved, treat the corrected pressure p, as a new p* and return to step 2.

The pressure and velocity correction equations are derived using the continuity and momentum equations, the exact details vary for each variation on the SIMPLE theme; for full details on SIMPLE, consult [103], for full details on SIMPLEF and SIMPLEN consult [102]. All analyses undertaken for this project used the Flotran default SIMPLEF algorithm.

Various approaches are available to solve the matrix equations

The default method for solving for u, v and w is an iterative approach called the tri-diagonal matrix algorithm (TDMA) and is described fully in [103]. TDMA breaks the problem down into a series of tri-diagonal sections with all other terms regarded as source terms and taking their values from the end of the previous iteration of the algorithm. This was used for the u, v and w throughout the project.

Flotran also offers a range of semi-direct methods, including the preconditioned conjugate residual (PCR) method, which is the default for the pressure equation. The PCR method iterates in an attempt to find an exact solution to the pressure equation, preconditioning substantially reduces the amount of memory required. Further information on the PCR method is given in [105].

2.4.2 – CFD Models of Blood Vessels

In the early and mid-nineties the majority of work involved idealised geometries, for example [106]. More recently much work has been carried out on geometries reconstructed from medical images [107-112], although more complex geometries with large numbers of outflow boundaries are often still idealised [32, 113]. The acquisition of image data and mesh construction based on such images are discussed in section 2.5 and 2.6 respectively.

Most cardiovascular CFD models deal with one of four cases; bifurcations, stenoses [114, 115] , effects of surgical interventions such as grafts [116, 117] and devices (such artificial heart valves). Of most interest to this project is the work on bifurcations [32, 106, 107, 113, 118-122].

CFD models of vessel bifurcations are usually created to analyse wall shear stresses and to consider atherosclerosis

In these models, standard practice is to impose a pressure or velocity profile at the upstream boundary and specify 0Pa at the output; this has been used freely until the introduction of FSI where large wave reflections can be observed (this is discussed below).

2.4.2.1 – CFD Models of the SMA

Few CFD analyses involving the SMA have been published; these are Lee and Chen [113], Taylor et al. [32], Kim et al. [123] and Buchanan et al. [124]. All studies, but the last, are based on idealised geometries; the first two are primarily concerned with the flow patterns around the iliac bifurcation in humans, while the third considers the effect of paired vessels (either the SMA and coeliac axis, or the renals) on WSS in the rabbit aorta.

The final study suggests that, in rabbits, although the SMA is spared the effects of atherosclerosis, this is not due to the flow patterns. This result could be due to the

rigid-walled, fluid-only nature of the analysis or the differences in anatomy between humans and rabbits.

2.4.3 – Fluid-Structure Interaction Models

Fluid-structure interaction (FSI) analyses model both the blood flow in the artery and the way this interacts with a structural model of the vessel wall. In some cases FSI is necessary to capture complex interactions between vessels and the blood flowing in them [125], this type of modelling has been shown to yield substantially different results to fluid-only CFD in some cardiovascular applications [126].

To implement an FSI analysis, one might couple together two separate modelling techniques, finite element structural analysis (FEA) for the vessel wall modelling and CFD for the blood flow. Two approaches are available for FSI modelling, strong coupling and weak coupling.

Strong coupling involves combining the structural and fluid problems at the solver level, and solving the systems together.

Weak coupling is the more commonly used approach for cardiovascular problems. In a weakly coupled analysis the fluid and solid models are regarded as separate entities and an iterative process used to solve each model and apply loads to the other until convergence is achieved. A weakly coupled FSI analysis can be either fluid-driven or structure-driven, for cardiovascular problems it is normal to use a fluid-driven approach as blood-flow is the key driving force behind vessel motion; such an approach is illustrated in figure 2.26.

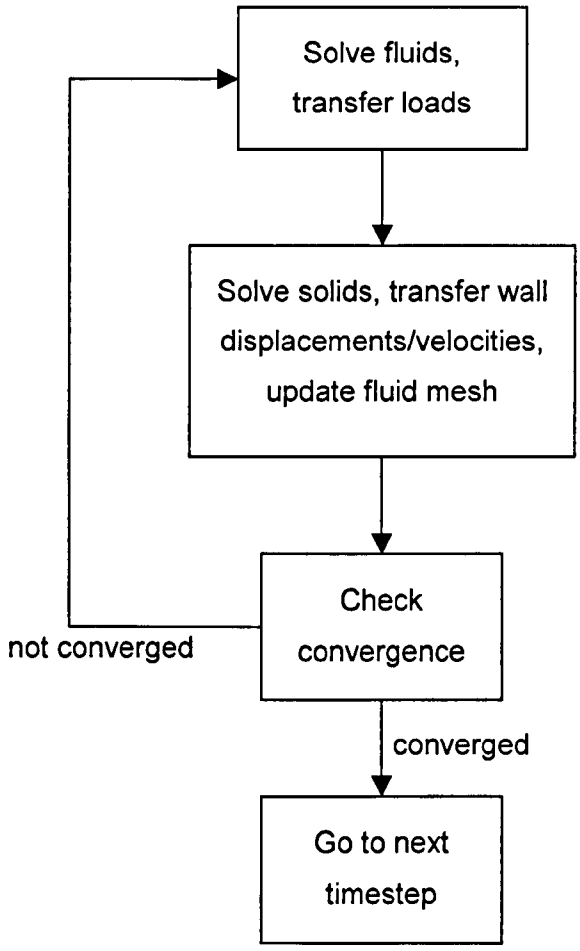

Figure 2.26. FSI iteration procedure.

Some researchers have used external coupling to 'graft' together commercially available CFD and Finite element analysis (FEA) codes [95, 127, 128]. While recent releases of some commercial codes (such as ANSYS and ADINA [129]) include a transient FSI capability.

Cardiovascular applications of FSI include; a cardiovascular assist device (the Korean artificial heart, [130]), the heart itself (a left ventricular filling model [131]), the carotid bifurcation [132], and several straight or stenosed tubes [95, 133-135]. The only published paper found on FSI in the abdominal aorta was [136] which deals with predicting aneurysm rupture in the abdominal aorta. A slightly more relevant piece of unpublished work by Van der Heide was found [137], this is however preliminary work and no results have yet been published. No FSI analyses of the SMA have been published.

The above vessel models only consider the dilation of the vessels, not any gross vessel motion. To include gross motion, a very complex solid model would be needed. In the case of the SMA and abdominal aorta, such a model would have to include large portions of the bowel, the liver, kidneys and spine; models of the vena cava and renal veins would also likely be necessary. The complexity of this type of model, both in terms of solution time and data-collection, has thus far precluded its use.

2.4.4 – Prescribed Wall-Movement Modelling

An alternative approach is to collect data on the moving geometry of the vessel and use this to prescribe the movement of the wall through the cardiac cycle. This removes the need for a complex solid model and will decrease computational burden significantly. This approach is not yet in widespread use in cardiovascular applications, but may provide the best solution for vessels with substantial gross motion.

Weydahl et al.[122] used such an approach to investigate the effect of changing curvature on an idealised model of a coronary artery bifurcation, they found that in this case WSS distributions were substantially different between the static and dynamic mesh models.

2.4.5 – Outlet Boundary Conditions

Considering a CFD model of a bifurcation, if the upstream boundary condition specifies a time-varying velocity profile across the inlet, then the down-stream boundary condition has to perform three functions; direct the correct flow along each vessel (at each timestep), enforce the correct pressure-flow relationship at the boundary and enforce the correct pressure variation through-out the model (absolute pressure is arbitrary in incompressible fluid dynamics). If the model is an FSI model, then boundary condition must also deal sensibly with pressure waves arriving at the boundary.

In the system being modelled, the behaviour downstream of the (essentially arbitrary) end-point for the computer model will be characterised by a continuum of partial wave reflections of different sizes and different time-delays, this results in complex behaviour at the boundary; approaches to modelling this will be described in chapter 5.

2.4.5.1 – FSI Boundary Conditions

If a constant pressure boundary condition is applied at the outlet of an FSI model of a fluid-filled elastic tube, any pressure wave reaching the outlet will be inverted and fully reflected. In order to stop this reflection occurring, a simple approach is available; add a long pipe to the downstream end of the 3d model. If the pipe is long enough, the wave will not reach the end before the simulation is completed and no reflection will be seen in the model. There are various ways of implementing this.

- Full 3d – Simply extend the mesh to include a large downstream pipe.
- 1d – Couple a one-dimensional model onto the downstream end of the 3d model.
- Impedance-matched lumped parameter – Couple a lumped parameter model onto the downstream end of the 3d model.

The first option is easy to implement but very computationally expensive. To run a 2 second analysis of a tube of the dimensions of the SMA, an outlet length of around 10m would be required to stop any reflected wave being visible in the section of interest.

The second option, as implemented by Formaggia et al. [138], couples the 3d model to a 1d model of a long pipe. This has the same effect as the first option but at greatly reduced computational expense.

A third option is to create an impedance-matched lumped boundary condition to stop any wave reflection at the end of the 3d domain; this is discussed in chapter 5.

The above options focus on wave reflection at the outlet of the 3d model, but do not account for the distributed wave-reflections downstream that play a significant role in determining flow parameters [56].

To model these reflections a more complete model of the downstream vasculature is needed. Some authors, including Olufsen et al [93], have designed structured trees similar in concept to those described in 2.3.2.

Pittaccio et al. [112] and Lagana et al [139] also show multi-scale models, although neither represents a structured tree

The situation in the SMA is further complicated by the inter-connectivity between the smaller arteries leading from the SMA meaning that the application of a mathematically elegant structured tree such as those described by Zamir [101] is not necessarily appropriate.

2.5 – *Imaging*

In order to perform a CFD simulation of the SMA, geometry on which to base the meshes of the fluid domain and the vessel wall is needed. In the past, many studies used idealised, cylinder-based geometries or casts taken from cadavers. More recently, *in vivo* measurements have been taken using x-ray computer tomography (CT), MRI or ultrasound (US). All three modalities can provide the information to build up a patient-specific model. Ideally, the following is required:

- High (sub-mm) spatial resolution.
- Sufficient temporal resolution (~0.1s) to capture any cardiac movement of the vessels.
- A high contrast, volume dataset showing the geometry of the AA and SMA.
- Slices showing blood flow along each vessel in appropriate places to validate model boundary conditions.

2.5.1 – Techniques Involving Ionising Radiation

The prime method of obtaining 3d data sets of useful resolution using ionising radiation is CT. This can produce images with resolution of the order of 0.1mm. However, the radiation dose given to a volunteer during a CT scan rules it out for a research project of this type.

2.5.2 – MRI for Geometry

MRI exploits the unpaired nuclear spin present in certain elements (almost exclusively hydrogen protons) and manipulates proton magnetisation to cause the emission of radio-frequency (RF) radiation; this is detected using RF coils and used to build an image based on the locations and environments of these nuclei. For a fuller description of the underlying physics of MRI, refer to Edelman et al [140].

MRI can provide 2d slices and 3d volumes in a fixed co-ordinate frame; sequences can generate varying information including liquid flow rates. One key problem with MRI is acquisition time; without contrast enhancement it may take of the order of minutes to collect enough information to clearly see the abdominal vasculature at a reasonable resolution. Over this time-scale, motion effects from both breathing and patient movement may markedly degrade image quality.

The use of a gadolinium chelate contrast medium intravenously injected can improve contrast dramatically and reduce scan times to the order of 15 seconds for a 3d volume dataset. A scan this short allows the subject to breath-hold, removing artefacts due to breathing and associated patient movement. The artefact due to pulsation is still present, and scans may show 'smearing' of some vessels, (a cylindrical vessel oscillating in one plane during the scan will appear elliptical in cross-section).

The safety of gadolinium-based magnetic resonance (MR) contrast agents is well documented [141] with the only recorded side effects being nausea (1-2% or subjects), hives (<1% of subjects), and the (extremely uncommon) potential for severe anaphylactoid reaction.

Crowe et al. [142] suggest an MR approach based on a turbo-spin echo sequence for measuring wall thickness and lumen diameter variation through the cardiac cycle (using 2mm slices).

2.5.3 – MRI for Flow

One key feature of MRI for this study is the ability to measure flow in deep-seated vessels in two dimensions, using a range of techniques. The large differences in signal strength between regions of flow and stationary regions allow good contrast between the lumen and the vessel wall. The information in this section is primarily based on [140]

2.5.3.1 – Time of Flight Imaging

Time of flight (TOF) imaging is a commonly used technique for analysis of flow and typically consists of a background tissue suppression followed by the generation of a bright flow signal. Only the slice of interest is affected by the presaturation (i.e. suppressed) and flow of blood into the slice will give a stronger signal (as the signal from the flow entering the slice will not have been suppressed). The signal intensity within the vessel will vary approximately linearly with blood velocity until wrap-around aliasing occurs for $V \geq th/TR$. Where V is though-plane blood velocity, 'th' the thickness of the phase-encoding slice and 'TR' is the pulse repetition time.

Note that as the flow velocity measured is that perpendicular to the slice, in order to accurately measure the velocity, the vessel must also be perpendicular to the slice.

Standard TOF images can be subject to signal loss in regions of disturbed flow (due to phase incoherence); Black blood TOF (where the signal from flowing blood is lost) can be used to identify the vessel wall in these instances, but, due to the reduction in signal from intra-voxel dephasing, is not useful for flow quantification.

2.5.3.2 – Phase Contrast Angiography

Phase contrast angiography (PCA, also called phase contrast magnetic resonance angiography or PCMRA) is an alternative flow quantification technique, based on the principle that "moving spins develop a phase shift with respect to stationary spins as they move in a pair of opposing magnetic field gradients"[140]. This phase shift is linearly related to the through-plane velocity and can be used to quantify blood flow rates. Adding cardiac gating to the system and acquiring data repeatedly at set points in the cardiac cycle allows us to record flow velocities in a thick slice at high temporal resolution (~30-40ms). As only ±180° of phase shift is possible before wrap-around, care must be taken to ensure that the maximum flow magnitude corresponds to a value of less than 180° to avoid aliasing. The blood velocity corresponding to this 180° phase shift can be chosen, and is called the velocity encoding (or V_{ENC}) parameter.

Good correlation has been shown between PCA and Doppler US images in the abdominal aorta [55].

2.5.4 – Ultrasound for Flow

Ultrasound is immediately appealing due to the availability of equipment and comparatively low cost. However, little work has yet been undertaken using a fixed co-ordinate system, those who have done such work found results not of good enough quality to use as a basis for 3d CFD [143].

IVUS (Intravascular Ultrasound) has been involved in several image-based CFD modelling studies [107]. However, the highly invasive nature of the procedure (involving catheterisation and x-ray angiography for guidance) precludes its use with healthy volunteers, as in this study.

Recently some authors have started estimating WSS directly from PC-MRI images [144-147]. This approach clearly has great potential but at present, the long scan times and arising concerns over spatial and temporal resolution preclude its useful application in areas of disturbed flow or complex flow, i.e. those in which the project

is interested. In addition, the effect of vessel motion on wall shear stress is not considered. Katz et als' technical note [148] outlining the significant effect of surface irregularity on wall shear stress should be taken into account when considering the validity of such measurements (and the design of CFD meshes).

2.5.5 – MRI for Imaging Plaques and Walls Directly

Ideally, a map of any atherosclerotic lesions in the SMA of each volunteer would be useful to support the evidence from the literature as to the sparing of the SMA. Such a map would also identify any areas of the SMA that may have a particularly low risk of atherosclerosis. Recently there has been some interest in MR imaging of atherosclerotic plaques and vessel walls [149, 150]. The deep-seated nature of the SMA would seem to preclude plaque characterization techniques using surface coils but it may be possible to image wall thickness in the SMA (at least in slices).

2.5.6 – Choice of Imaging Technique

Of the imaging techniques discussed, MRI was the obvious choice from a technical standpoint. The MR superintendent at Rotherham district general hospital was interested in the project and was able to devote his expertise to the project as well as finding a regular slot in the scanner's timetable for the project.

2.6 – Automatic Segmentation and Mesh Generation

With MRI selected as the imaging modality of choice, it was clear that a very large quantity of data would be collected during the project. Hand segmentation (extraction of the objects of interest from the images) of the data would be very time-consuming and any sort of manual mesh creation based on the images close to impossible. For these reasons, techniques for automatic segmentation and mesh generation were considered.

2.6.1 – Automated Segmentation

The simplest form of automated segmentation is 'intensity segmentation'; pixels with an intensity value greater than a threshold are deemed to be part of one group, whilst pixels of intensity less than the threshold are part of another group. This is simple,

computationally efficient and works well for high contrast images. However, this technique has no object specificity and hence often needs 'cleaning up' by hand once the initial segmentation has been performed.

Extensions to this algorithm are easily programmed, such as removing pixels not linked to a given pixel, or creating a set of gradient images based on the original and performing intensity segmentation on those.

Beyond these simple techniques, there is a wide range of methods used to extract vessel outlines from medical images. These techniques tend to be specific to the problem and imaging modality used. For a wide-ranging review of such techniques refer to Kirbas and Quek [151]. Each of their categories is briefly reviewed below. One category not covered in the above review, and of particular interest for this project, is segmentation by registration, this is covered in some detail in 4.3

2.6.1.1 – Image Registration

Registration is an image-processing technique whereby one image is made to look like another (these techniques can be applied to images of any dimension, although it is usual to consider examples in 2 or 3 dimensions). The moved image is usually referred to as the source, and the fixed image the target. The act of registration produces an image based on the source (the output image) which, by some definition and within some constraints (depending on the type of registration algorithm), is the closest possible match to the target; crucially, a mapping is also produced which states how the source image is altered to match the target.

The simplest form of image registration is rigid registration; in this, the output image is related to the source by a rotation and a translation. Clearly, rigid registration is limited in its usefulness in real-world problems.

Affine registration is a little more complicated than rigid registration; in affine registration, the output image is related by a series of rotations, translations, shears and dilations of the whole image. This offers substantially more freedom than rigid registration; parallelograms and rectangles can be registered onto squares and objects of the same shape but different size can be registered. Affine registration does not however offer the versatility that will be needed for segmentation by registration (and moving mesh generation by registration).

Non-rigid registration allows areas of local shear and dilation within the image; this allows much greater versatility than the simpler registration techniques.

2.6.1.2 – Segmentation by Registration

Segmentation by registration is a technique suitable for segmenting a series of similar images and has been used successfully on MRI scans of the human knee [152, 153]. The first image is segmented using some other technique, then the first image is registered to each other image requiring segmentation and the resulting mapping applied to the initial segmented image; this yields a full segmented data set. This technique will be considered further in 4.3

2.6.2 – Mesh Generation

Once the image has been pre-processed there are three options for meshing the volume of interest: structured, unstructured and adaptive meshing.

Unstructured meshing is the most widely used approach, and is simple to use; some basic parameters of the mesh are defined (element shape and element size range) and the software creates an unstructured mesh with elements of similar sizes. This procedure is quick and requires no expertise in mesh design. The downside is that the mesh is not tuned to be at its densest in the areas of greatest interest and hence resolution is lost in areas of importance or computational burden is increased.

Structured meshing is preferable where possible, giving reduced computational times and the ability to tune the mesh to perform best in the areas of most complex flow, it has been used successfully for an MRI dataset by Long et al. [110] using a series of smoothing operations on the MRI data.

The third option is that of adaptive meshing [154], in which a rough mesh is defined and local solution error is used to highlight areas where mesh refinement is needed, this procedure is iterated to give a mesh with highest resolution in the places where it is most needed. At this time, this approach has only been used for steady state analyses, although a mesh thus created could be used in transient analyses.

Little work has been carried out on realistic geometry FSI analyses, hence no literature would appear to be available suggesting the best way to generate the mesh for the vessel wall.

2.6 – Challenges of the project

The key challenges of the project are going to be as follows:

- Designing an approach to establish the geometry of the SMA in a pool of volunteers, this geometry may be dynamic or static depending on the initial results.
- Using this data to construct a good quality CFD mesh.
- Collecting data on inflow and outflow of the AA and SMA.
- Choosing, designing and implementing appropriate boundary conditions to impose the correct flows and movements on the CFD model.
- Interpreting results and drawing conclusions.

Chapter 3. MRI Studies of the Abdominal Vasculature

3.1 –Study Outline

An MRI-based imaging study was planned and undertaken. The aim was to map the geometry of the bifurcation of the SMA from the AA and obtain flow traces in both arteries to inform the design of boundary conditions.

The minimally invasive nature of the study meant that it was possible to use healthy volunteers. Ethical approval (Reference number RLREC:03/24L) for the study was sought and gained, including permission to use an intravenously injected contrast medium.

This chapter traces the development of the imaging protocol as the study progressed, and describes, illustrates and catalogues the image data that was collected. These data provide the basis of the quantitative morphological and haemodynamic characterisation that follow in subsequent chapters.

3.1.1 – Scanner Details

The scanner used for both studies was a Phillips Intera 1.5T clinical scanner with master gradients, operating on release 8 software, sited in Rotherham District General Hospital. The receiving coil for all scans was a Synergy body coil.

3.2 – Scans Undertaken for the Study

The original hypothesis being tested was that the unusual static geometry of the SMA produced haemodynamic characteristics, which spared the artery from the disease process. Therefore the initial aim was to map this static geometry as accurately as possible. From scans of the initial volunteers, it quickly became apparent that there was substantial gross movement of the SMA and characterisation of dynamic anatomy would be important; this led to a complete change of approach for imaging anatomy.

3.2.1 – Contrast Enhanced Scans

The original approach used contrast-enhanced magnetic resonance angiography to collect anatomical data. A gadolinium-chelate based contrast agent (which alters the magnetic properties of blood) was injected into the left median cubital vein, and a T1 weighted spoiled gradient echo sequence used to acquire data. This technique suppressed other signals and allowed high contrast between arteries and the surrounding tissue.

This sequence produced a volume image with voxel size 1.5*0.84*0.84mm (anterior-posterior, superior-inferior, left-right). Image size was 50*512*512, giving a field of view of 7.5*43*43cm. The image was a time average over the ~20 seconds that the sequence took to run. Figures 3.1 and 3.2 show annotated example coronal and sagittal maximum intensity projections (MIPs) through the contrast enhanced volume dataset.

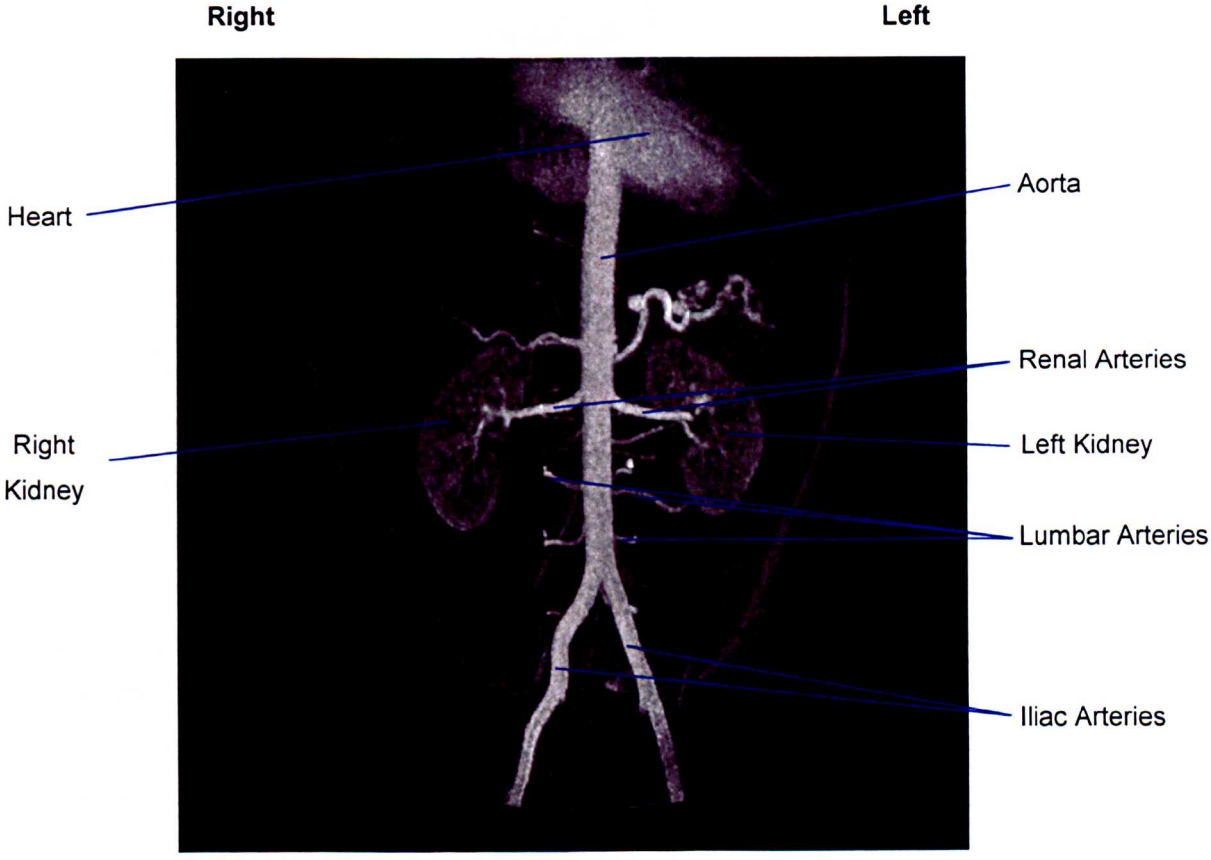

Figure 3.1. Annotated coronal MIP for contrast enhanced scan.

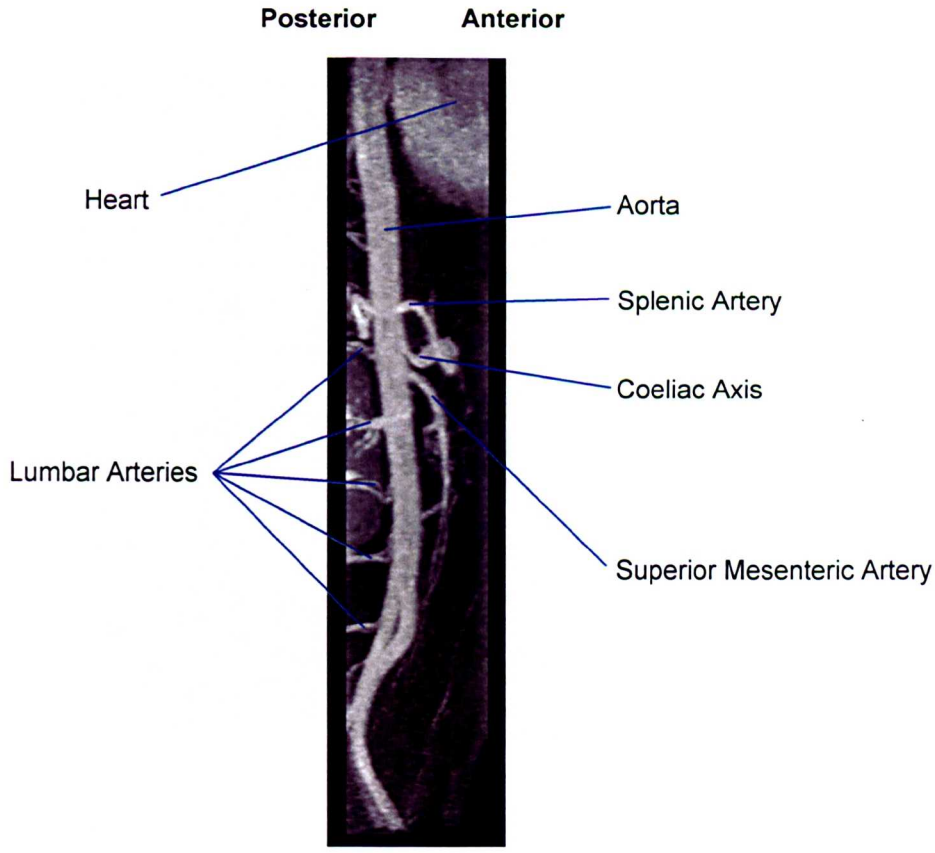

Figure 3.2. Annotated sagittal MIP for contrast enhanced scan.

3.2.2 – Dynamic Anatomy Scans

The dynamic anatomy scans were collected as series of parallel cine-slices approximately normal to the abdominal aorta, acquired under breath-hold. The sequence used was an ECG (Electrocardiograph)-gated balanced fast-field echo.

Each slice had a thickness of 8mm and pixel size of 0.977*0.977mm, in-plane image size was 256*256. Slices were overlapped by 50% in areas not close to the bifurcation, and by 75% around it; this gave effective slice thicknesses of 4mm and 2mm respectively, the aim being to obtain good resolution near the bifurcation whilst minimising scan time for the volunteer. The data would be post-processed later by interpolating between the wider-spaced slices to give a slice thickness of 2mm everywhere. Temporal resolution was 16 frames per cardiac cycle. The scan time was dependent on subject heart rate but was about 24 seconds per slice at 72 beats per minute (bpm). Around 30 slices were acquired in most subjects, giving a field of view of 25*25*~9cm*. An annotated example slice is shown in figure 3.3.

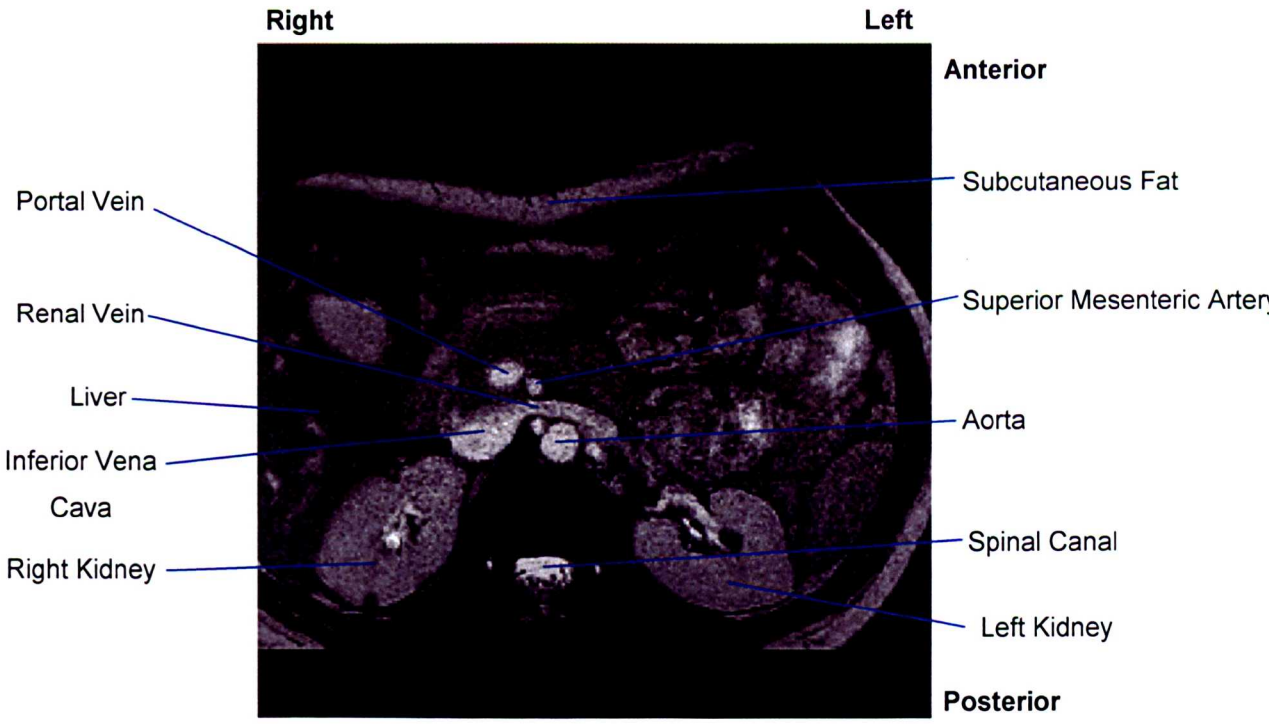

Figure 3.3. Example cine-slice image (note that this, and all transverse slices presented in this chapter, are shown as a feet to head view).

3.2.3 – Reference Anatomical Images

Reference breath-hold anatomical images were acquired using a non-gated, balanced turbo field echo sequence. Sixty slices aligned with the dynamic anatomy slices were contemporaneously acquired at 0.732*0.732mm pixel size and 8mm slice thickness, with 2mm between slice centre planes; in-plane image size was 384*384. An example image is shown in figure 3.4.

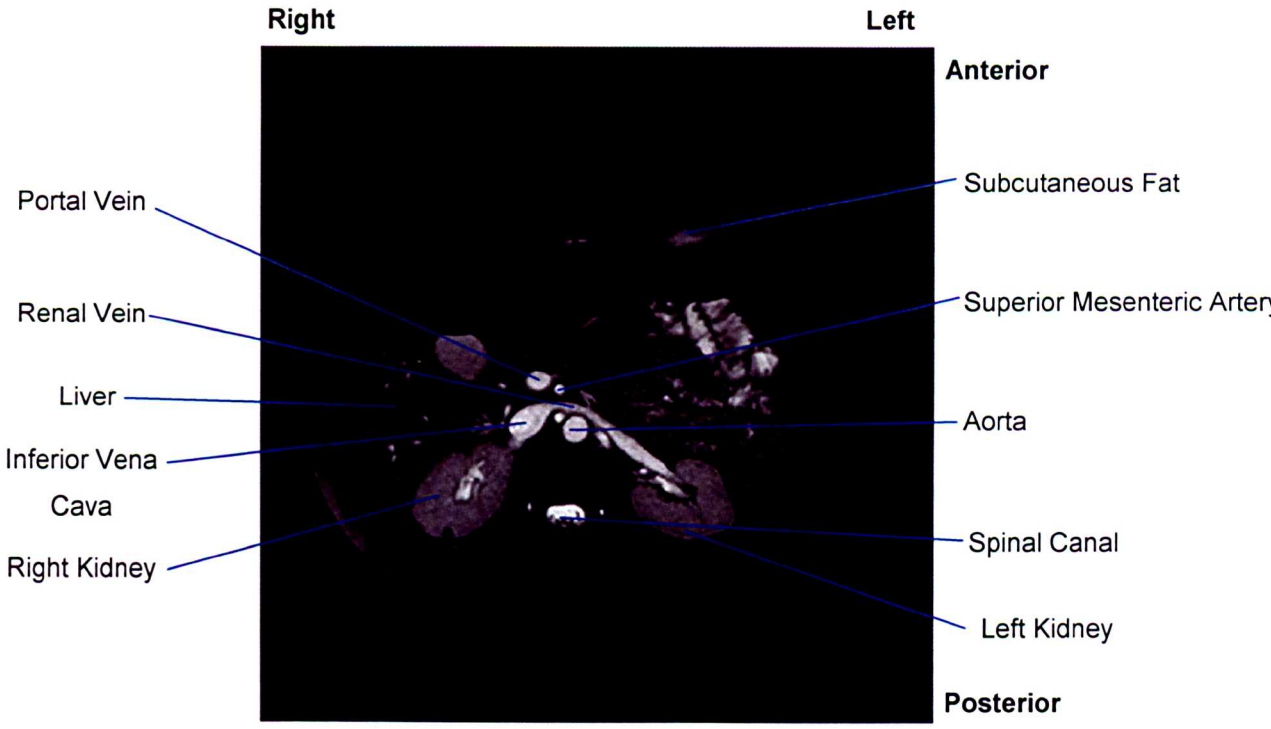

Figure 3.4. Example reference image.

3.2.4 – Phase Contrast

Flow quantification was performed using a 2d PCMRA sequence with retrospective gating and 2 signal averages; the V_{ENC} parameter was set to 150cm/s. The extra time associated with respiratory gating would have meant that the already long scan time (6 to 12 minutes, depending on subject heart-rate) would have been increased beyond what was acceptable for the study. The phase contrast sequence produces two images; a magnitude image and a phase image. A near-transverse slice was positioned below the point of the straightening of the SMA, and oriented such that flow in both the SMA and AA was close to directly through the plane.

Figures 3.5 and 3.6 show example magnitude and phase images from the first volunteer at end diastole and peak systole respectively.

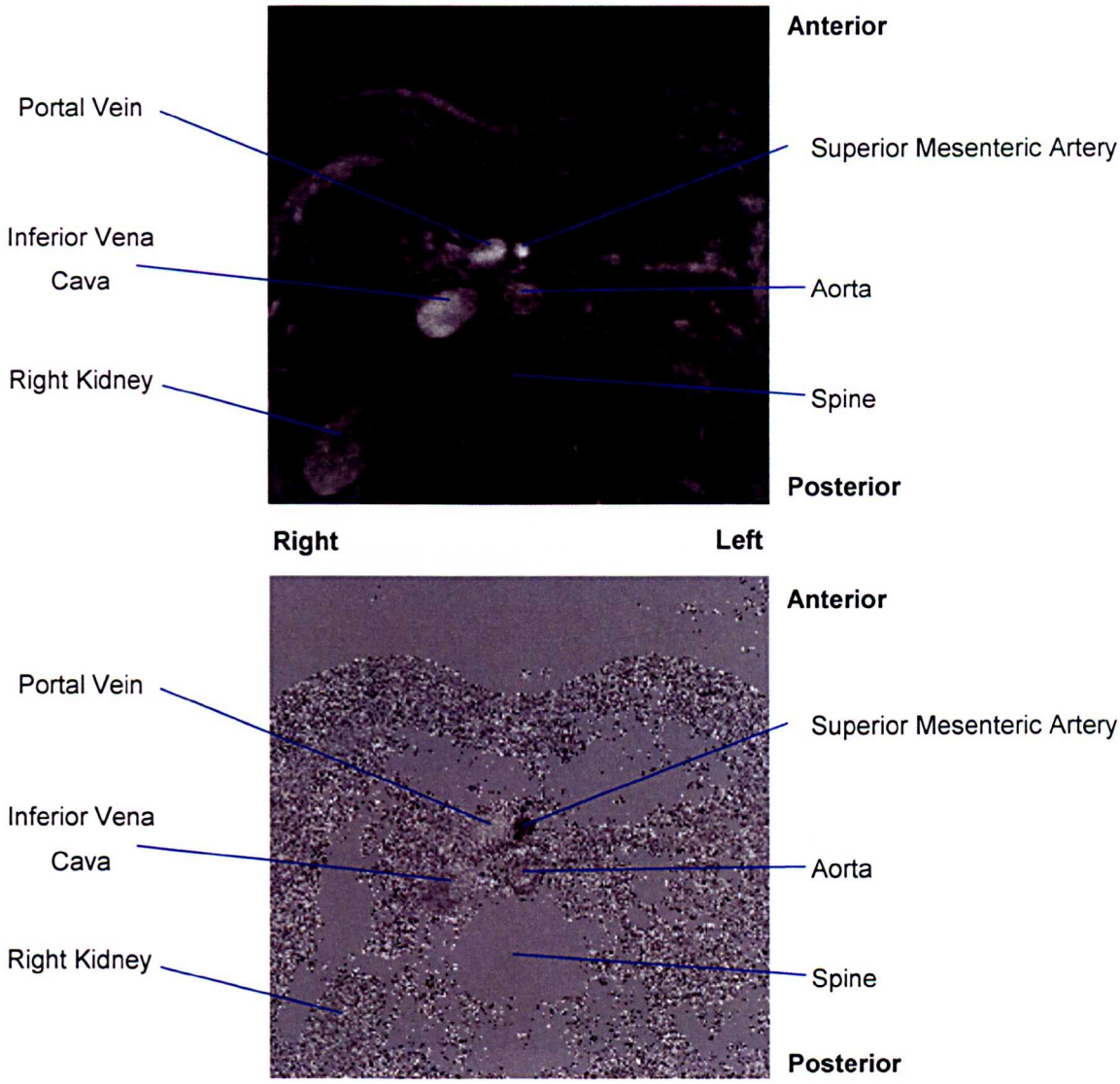

Figure 3.5. Magnitude (top) and phase (bottom) PCMRA images for first volunteer at end diastole.

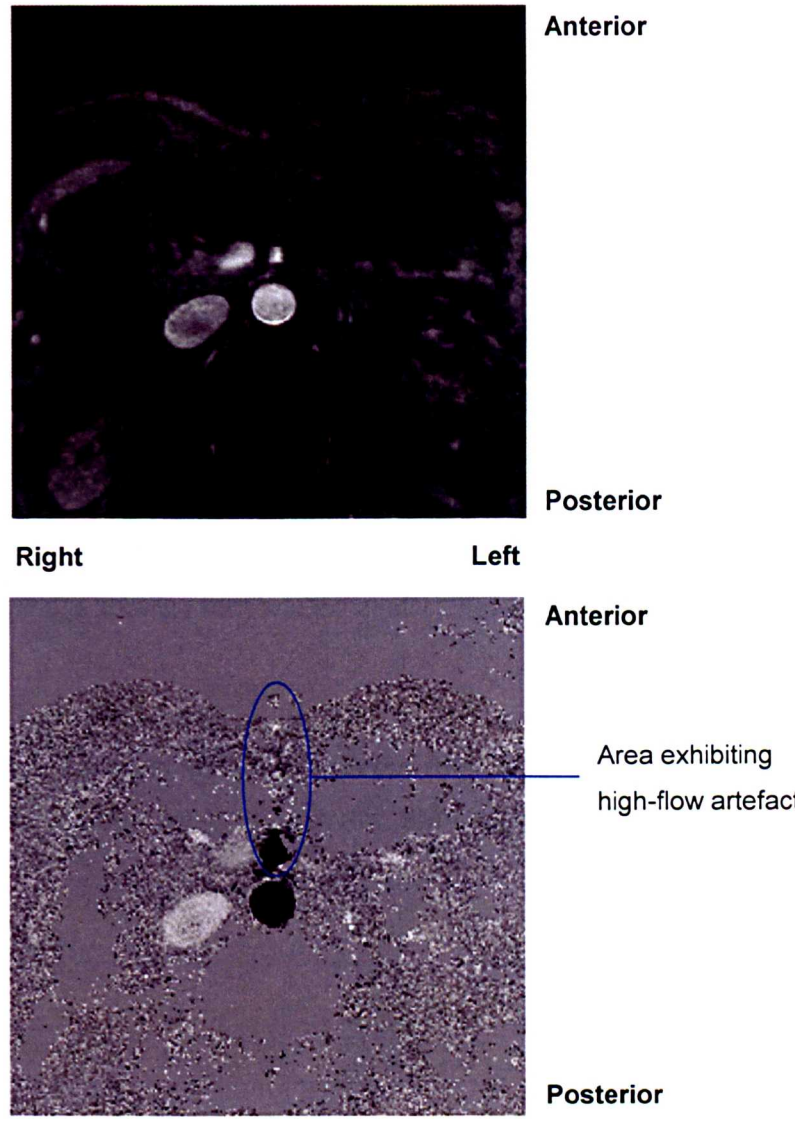

Figure 3.6. Magnitude (top) and phase (bottom) PCMRA images for first volunteer at peak systole.

Figure 3.6 shows an image artefact caused by the high flow rate in the AA, a band of disturbed signal is seen running up and down the image, in line with the AA, this was found to cause corrupt the flow signal from the SMA when it lay in this region. For this reason, the PCMRA approach was altered to cause the artefact to run left to right across the image. Figure 3.7 shows such a phase image, with artefact from the AA flow clearly visible, but now with no cross talk between the SMA and AA flow signals.

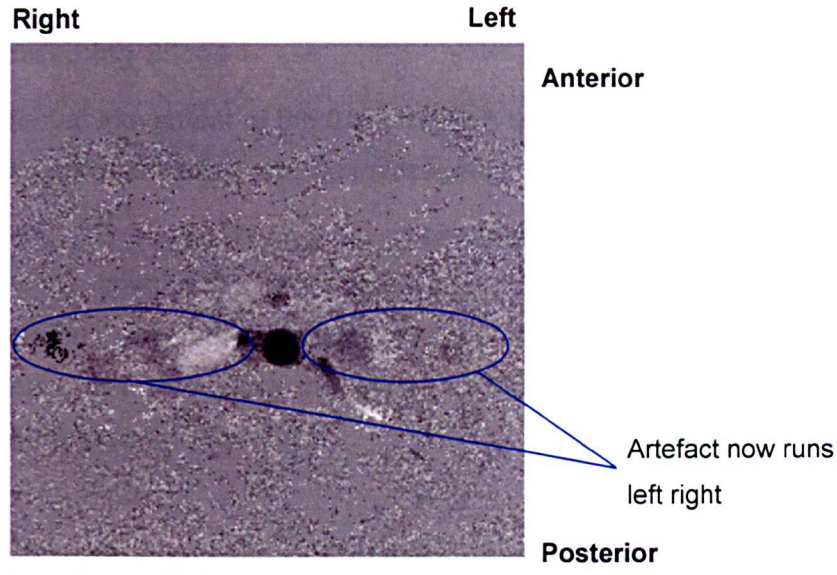

Figure 3.7. Phase image showing flow-induced artefact, now running left to right.

The phase images for each time-step can be used to create a graph of flow against time in the cardiac cycle for each vessel of interest (the technique is described in section 5.3), an example flow history for the AA and SMA is shown in figure 3.8.

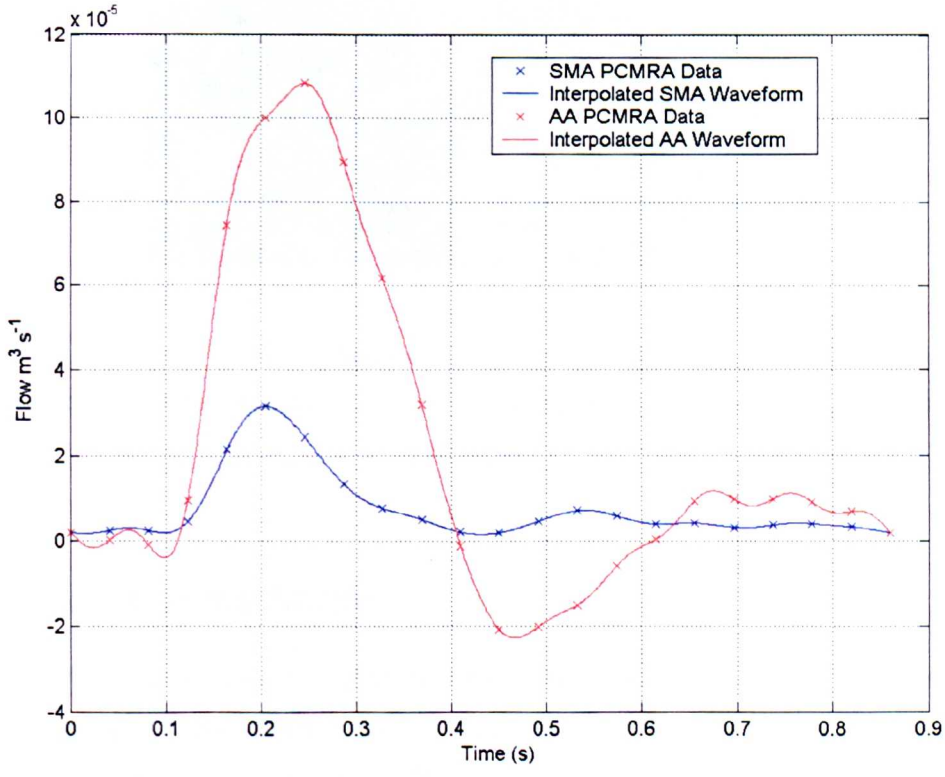

Figure 3.8. Example flow history for the AA and SMA based on PCMRA data.

3.2.5 – Sagittal Free-breathing Slices

Having observed substantial movement of the SMA through the cardiac cycle, it was decided that the respiratory cycle should also be investigated.

A balanced turbo field SENSE (sensitivity enconding) sequence was used to acquire 80 consecutive 0.5s duration images of a near-sagittal plane chosen to hold the aorta and SMA in plane as well as possible. In some cases the compound nature of the SMA curve made it impossible to capture the whole SMA throughout the cardiac cycle. An example image is shown in figure 3.9

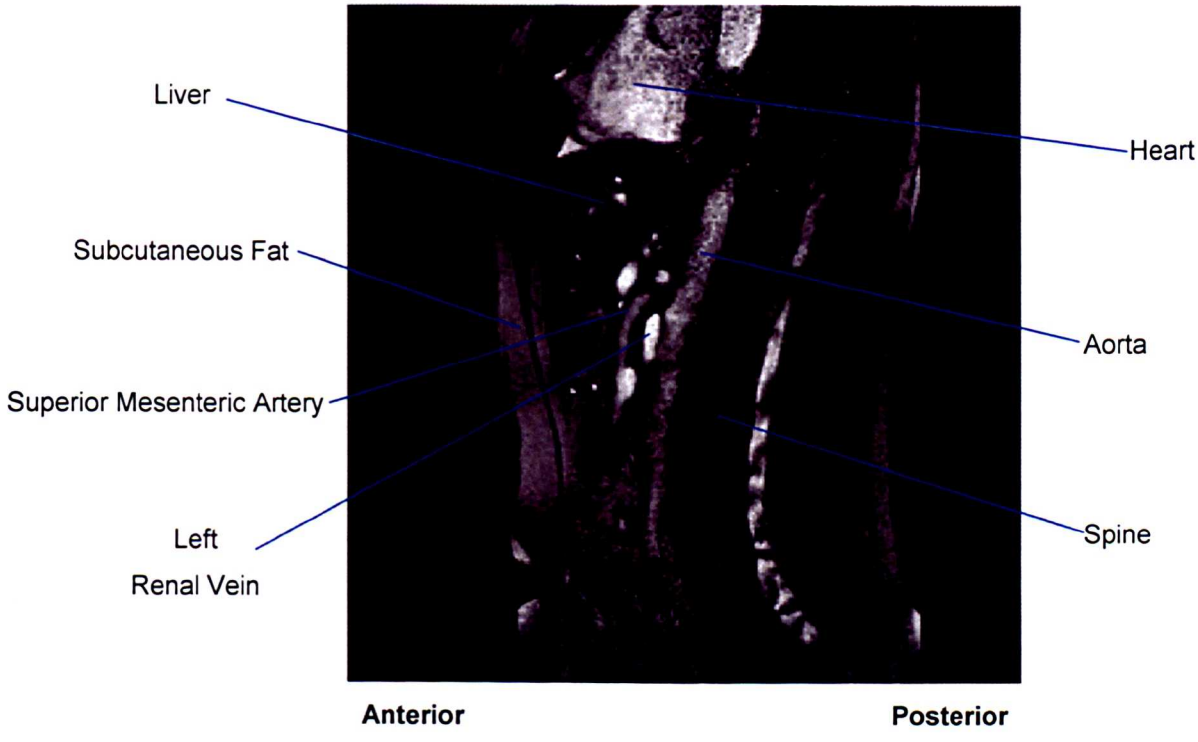

Figure 3.9. Example slice from a sequence showing the movement of the SMA through the respiratory cycle; artefact at top of picture is caused by lack of cardiac gating, SMA root is just out of plane.

3.3 – Details of the Study

Nineteen volunteers were recruited of which 18 (including 10 men) were scanned successfully. Volunteers were asked to fast from midnight and scanned between 9 and 11am, in order to minimise artefact due to gut motion, and to give a base-line value of SMA flow. One volunteer (GBFV17) failed to fast and was excluded from the study.

For the 18 volunteers scanned, the mean age was 35 years (range 23-63, standard deviation 12.3), mean weight was 70.8kg (range 51-97, standard deviation 11.9). The demographic data and scans undertaken in the study for each volunteer are shown in table 3.1.

One volunteer was scanned using both the contrast enhanced and the cine-slice techniques, and appears as GBFV1 and GBFV18.

Volunteer Identifier	Age	Sex	Weight (kg)	Anatomic Scans	Flow scans
GBFV1	24	M	90	contrast enhanced	phase contrast
GBFV2	31	M	74	contrast enhanced	phase contrast
GBFV3	23	M	80	contrast enhanced	phase contrast
GBFV4	23	F	61	cine-slices	none (interference)
GBFV5	41	M	80	cine-slices	phase contrast
GBFV6	28	M	64	cine-slices	phase contrast
GBFV7	39	F	69	cine-slices	phase contrast
GBFV8	26	M	78	cine-slices	phase contrast
GBFV9	47	M	76	-	phase contrast
GBFV10	24	M	65	cine-slices	phase contrast
GBFV11	26	F	66	-	phase contrast
GBFV12	26	F	58	cine-slices	phase contrast
GBFV13	45	F	64	cine-slices	phase contrast
GBFV14	63	F	51	cine-slices	phase contrast
GBFV15	23	M	76	cine-slices	phase contrast
GBFV16	47	M	97	cine-slices	phase contrast
GBFV17*	-	-	-	-	-
GBFV18**	24	M	92	cine-slices	phase contrast
GBFV19	50	F	68	cine-slices	phase contrast
GBFV20	46	F	56	cine-slices	phase contrast

Table 3.1 – Volunteer demographic and scans undertaken. * Volunteer GBFV17 did not fast and was excluded from the study. ** Vol GBFV18 was the repeat visit of volunteer GBFV1

3.3.1 – Progression of the Protocol

The phase contrast imaging technique was successful in all but one case. For volunteer GBFV4, radio-frequency interference from an unknown source made the acquisition of phase contrast images impossible.

The contrast-enhanced technique was used with 3 volunteers, but – as mentioned above – abandoned once it was realised that motion of the vessel occurred throughout the cardiac cycle, figure 3.10 shows a section of SMA from a contrast-enhanced image; the SMA is perpendicular to the plane, and the smearing is due to movement of the vessel.

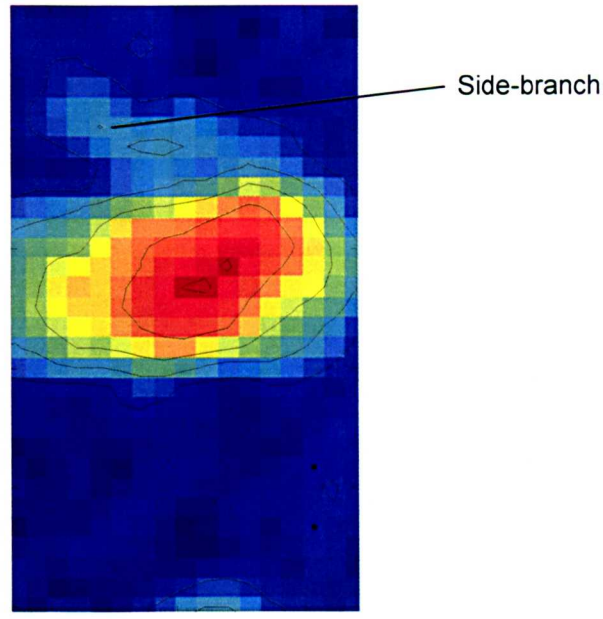

Figure 3.10. Example false colour PCMRA image of the SMA (with a small side-branch in the top of the image), the left to right smearing of signal from the SMA is due to motion. Contour lines show possible estimates of vessel outline.

Producing good quality data proved more difficult for the cine-scans. The main problem was volunteers moving both between, and particularly during, scans; figures 3.11 and 3.12 show images with these problems. In three cases (GBFV9, GBFV11 and GBFV15), the cine-slice acquisitions were aborted due to repeated volunteer movement.

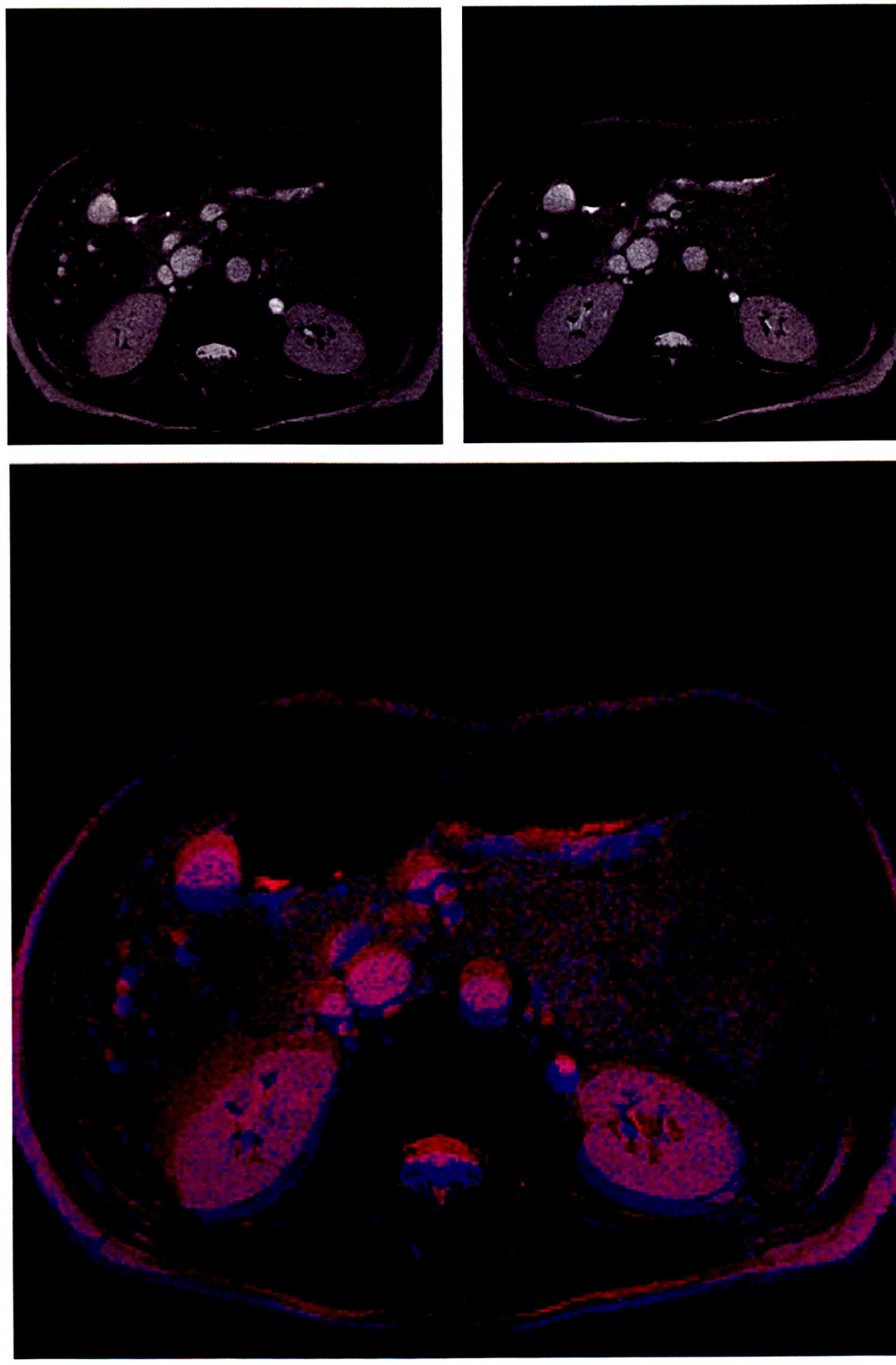

Figure 3.11. Pair of cine-scans with volunteer movement between slices. The top images show two separate scans which each appear fine, the bottom image shows the two scans overlaid with one represented by the red channel and the other by the blue, the lack of alignment between major structures is clear.

Figure 3.12. Cine-slice image with volunteer movement during scan.

For the first two sets of cine-slices (GBFV4 and GBFV5) the effective slice thickness used was 4mm throughout, this was found to lack the level of resolution required around the bifurcation; for this reason slice overlap was increased around the bifurcation to 75% giving the 2mm effective slice thickness.

As the scans proceeded and it became clear that volunteer movement between slices may have to be dealt with in the post-processing stage, it was decided to add a set of reference images matching the cine-slices in terms of orientation and placement but acquired contemporaneously to remove any motion artefact, these slices could then be used as a basis for any slice realignment.

Only 1 volunteer (GBFV12) moved little enough through the whole cine-slice collection phase that the cine-slices could be used directly without realignment.

Table 3.2 outlines the progression of the 3d imaging study and the outcomes described above.

Volunteer	Imaging type	Improvements	Outcome
GBFV1	Contrast	-	Good time averaged dataset
GBFV2	Contrast	-	Good time averaged dataset
GBFV3	Contrast	-	Good time averaged dataset
GBFV4	Cine slices	Move to cine-slices	Each slice ok, motion between slices, lack of resolution near bifurcation
GBFV5	Cine slices	-	Each slice ok, motion between slices, lack of resolution near bifurcation
GBFV6	Cine slices	Slices closer at bifurcation.	Each slice ok, motion between slices
GBFV7	Cine slices	-	Each slice ok, motion between slices
GBFV8	Cine slices	Reference set added	Each slice ok, motion between slices
GBFV9	No 3d images	-	-
GBFV10	Cine slices		Volunteer movement within some slices
GBFV11	No 3d images	-	-
GBFV12	Cine slices	-	Each slice okay; no detectable misalignment between slices.
GBFV13	Cine slices	-	Each slice ok, motion between slices
GBFV14	Cine slices	-	Each slice ok, motion between slices
GBFV15	Cine slices	-	Each slice ok, motion between slices
GBFV16	Cine slices	-	Each slice ok, motion between slices
GBFV17	No 3d images	-	-
GBFV18	Cine slices	-	Each slice ok, motion between slices
GBFV19	Cine slices	-	Each slice ok, motion between slices
GBFV20	Cine slices	-	Each slice ok, motion between slices

Table 3.2. Progression of 3d imaging studies

3.4 – Conclusions

This section of the project showed that MRI could be used to capture data on the anatomy and motion of the SMA. Two-dimensional cine-images were acquired showing the motion of the SMA with both the cardiac and respiratory cycles; this was extended to 3d for the cardiac cycle. Chapter 4 will consider the analysis of these data and the quantification of SMA motion in the volunteer group.

Chapter 4. Quantifying the Dynamic Anatomy of the SMA

4.1 – Introduction

Videos of slices of the moving aorta and SMA offer an insight into the nature and quantity of motion of the SMA, but to gain a full appreciation and be able to quantify this motion, as well as modelling flow in the moving geometry, 3d motion must be considered. This chapter sets out a technique for the extraction of this moving 3d geometry from a series of 2d cine-slices. The moving model created allows the separation of rigid body motion from dilation and maintains a form suitable for use in CFD modelling.

Section 4.2 considers the analysis of individual 2d cine-slices to obtain numerical data on SMA motion related to both the respiratory and cardiac cycles; subsequent sections deal, in some detail, with the derivation of a 3d model of the SMA geometry varying through the cardiac cycle.

4.2 – Motion of the SMA and AA – 2d Analysis

Whilst only a full 3d analysis of the vessel motion can fully characterise vessel motion, and is the only way to obtain the data for a moving wall CFD analysis, significant information can be obtained from measurement of 2d slices cine-slices; this method also allowed respiratory movement to be considered as well as cardiac motion.

The measurements recorded for the cardiac and respiratory slices are shown in figure 4.1. All measurements were obtained by hand, by a single investigator, using a Dicom viewing program to overlay angle callipers and rulers onto each image.

In some volunteers, data for angle a was impossible to collect due to difficulty in finding an imaging plane such that the SMA stayed in-plan throughout the respiratory cycle. Only volunteers for whom the whole set of measurements shown in figure 4.1 was available were included, this gave n=10 (5 males, age range 23-50, median age 42, weight range 56-97 kg, median weight 68.5 kg).

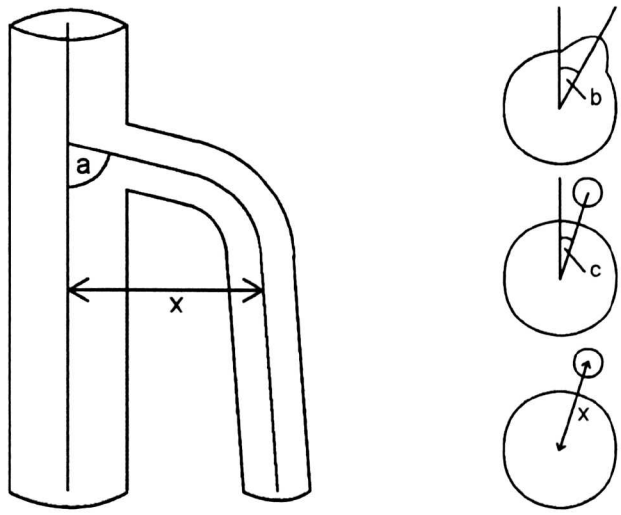

Figure 4.1. Diagrams showing measurements taken on SMA position for respiratory and cardiac motion, transverse slices are head-to-feet views. (Angle a: Initial SMA angle of origin measured from a cardiac average, at deep and shallow breath-hold, Angle b: Angle of SMA departure from a sagittal plane measured at peak systole and end diastole, Angle c: as angle b, but measured 24mm below branching from aorta, Distance x: distance between AA and SMA centre-lines measured on same plane as angle c.

4.2.1 – Respiratory Motion of the SMA

The primary respiratory motion of the SMA is seen as the abdominal contents move up and down with the motion of the diaphragm; this is most easily seen in an image obtained in a near-sagittal plane aligned with the SMA as shown in figure 4.2. Difficulty in capturing this motion occurs if the SMA curves substantially to the left or right close to its origin.

Figure 4.2. MRI Images showing the SMA whilst breathing in (left) and breathing out (right).

To quantify this motion, the angle of origin (angle a in figure 4.1) was measured at peak inhalation and peak exhalation. Results are presented in table 4.1.

Volunteer	Angle a (degrees)		*Change in Angle a (degrees)*
	Peak Inspiration	Peak Expiration	
GBFV7	44	68	*24*
GBFV8	68	92	*24*
GBFV9	46	57	*11*
GBFV10	54	71	*17*
GBFV12	87	107	*20*
GBFV13	90	110	*20*
GBFV15	23	29	*6*
GBFV16	65	70	*5*
GBFV19	80	114	*34*
GBFV20	74	100	*26*
Mean	**63.1**	**81.8**	***18.7***
Standard Deviation	**21.3**	**27.4**	***9.2***
Range	**23-90**	**29-114**	***5-34***

Table 4.1. Respiratory motion of the SMA

Clearly there was substantial respiratory motion of the SMA (with an average difference of 19° between inspiration and expiration), in the cohort studied. Note also that, contrary to received wisdom, in all but one of the subjects the SMA did not arise from the aorta at a sharply acute angle.

4.2.2 – Cardiac Motion of the SMA

Cardiac motion of the SMA arises from the expansion of the abdominal aorta as the systolic pressure wave passes along it. As the abdominal aorta sits directly anterior to the spine, the posterior aortic wall is constrained, thus the expansion pushes forwards displacing those structures anterior to the aorta. One structure affected in this way is the SMA, the displacement of the SMA can be measured as the change in

distance x (from figure 4.1) between end diastole and peak systole, results for this displacement are given in table 4.2.

A secondary effect of the aortic pulsation, present in some volunteers, is that the SMA is deflected sideways; this can be examined by considering the change in angles b and c, these results are given in table 4.3.

Volunteer	Distance x (mm)		*Change in Distance x (mm)*
	End Diastole	**Peak systole**	
GBFV7	23.4	24.4	*1*
GBFV8	28.3	30.3	*2*
GBFV9	39.1	41	*1.9*
GBFV10	15.6	16.6	*1*
GBFV12	13.7	14.6	*0.9*
GBFV13	21.5	22.5	*1*
GBFV15	23.4	25.4	*2*
GBFV16	27.3	30.3	*3*
GBFV19	20.5	21.5	*1*
GBFV20	17.6	19.5	*1.9*
Mean	**23.04**	**24.61**	***1.57***
Standard Deviation	**7.3**	**7.7**	***0.70***
Range	**13.7-39.1**	**14.6-41**	***0.9-3***

Table 4.2. Cardiac Motion of the SMA – displacement of SMA

Volunteer	Angle b (degrees)		*Change in angle b (degrees)*	Angle c (degrees)		*Change in angle c (degrees)*
	End Diastole	Peak Systole		End Diastole	Peak Systole	
GBFV7	-13	-12	*1*	-36	-34	*2*
GBFV8	-20	-18	*2*	-13	-12	*1*
GBFV9	0	0	*0*	-7	-8	*-1*
GBFV10	0	0	*0*	10	10	*0*
GBFV12	-11	-14	*-3*	-35	-36	*-1*
GBFV13	-3	-3	*0*	6	9	*3*
GBFV15	-19	-19	*0*	-3	-3	*0*
GBFV16	-4	-4	*0*	0	0	*0*
GBFV19	-16	-20	*-4*	0	0	*0*
GBFV20	-17	-16	*1*	-15	-21	*-6*
Mean	**-10.3**	**-10.6**	***-0.3***	**-9.3**	**-9.5**	***-0.2***
St. Dev.	**-7.9**	**-8.0**	***-0.16***	**15.8**	**16.3**	***-0.5***
Range	**-20 to 0**	**-20 to 0**	***-4 to 2***	**-36 to 10**	**-36 to 10**	***-6 to 3***

Table 4.3. Cardiac Motion of the SMA – angle change.

In all subjects, SMA movement due to the pulsation of the aorta was clearly visible, this ranged from 0.9mm (~1/3 of SMA radius) to 3mm (~1 SMA radius).

Angle change was less substantial and varied significantly from subject to subject, although some angle change is visible upon inspection of the videos, it did not exceed 6 degrees in the measurements taken.

These initial analyses give good quality quantitative data as to the motion of the SMA, however in order to fully capture the 3d motion of the SMA in a useful manner a more complex approach is necessary.

4.3 – Segmentation of the MRI Data

The first job in preparing the MRI data for model construction is segmentation, that is, drawing around the objects of interest in the MR images; segmenting by hand would prove to be very time-consuming, with around 30 slices and 16 timesteps for each

volunteer. To save on time and improve repeatability, a technique called 'segmentation by registration' was used. The process of segmentation by registration is described below.

4.3.1 – Initial Segmentation

Each slice for the first timestep was segmented by intensity and manually checked and tidied to remove any unwanted features, such as bifurcations into other vessels not to be modelled. This resulted in a smooth, segmented voxel image of the vessels of interest. The process is outlined for a single slice in figure 4.3.

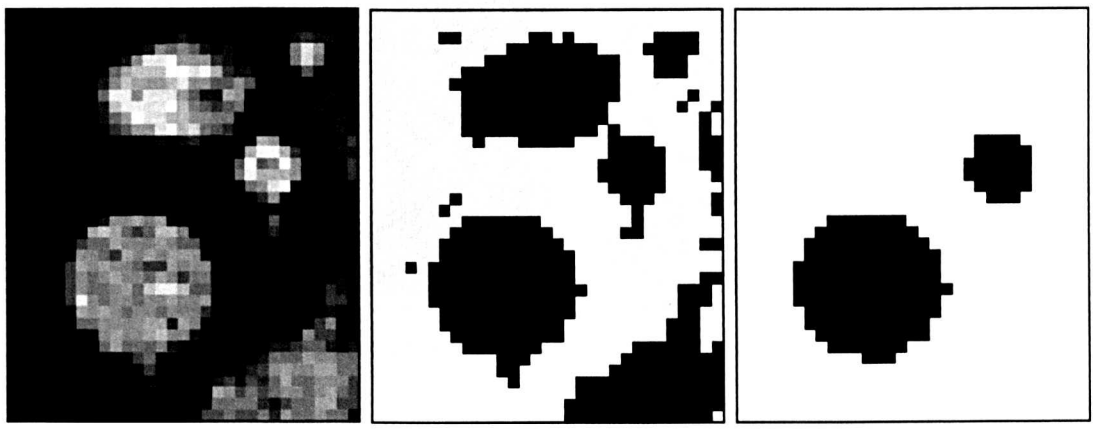

Figure 4.3. Original image (left), intensity segmented image (centre), and cleaned up version (right).

4.3.2 – Registration to Other Timesteps

The 3d intensity image for the first timestep was non-rigid registered onto that for each other time-step and the resulting mapping applied to the segmented image set for the first timestep. In this way, segmented image sets for each following timestep were generated; figure 4.4 shows this for a single slice.

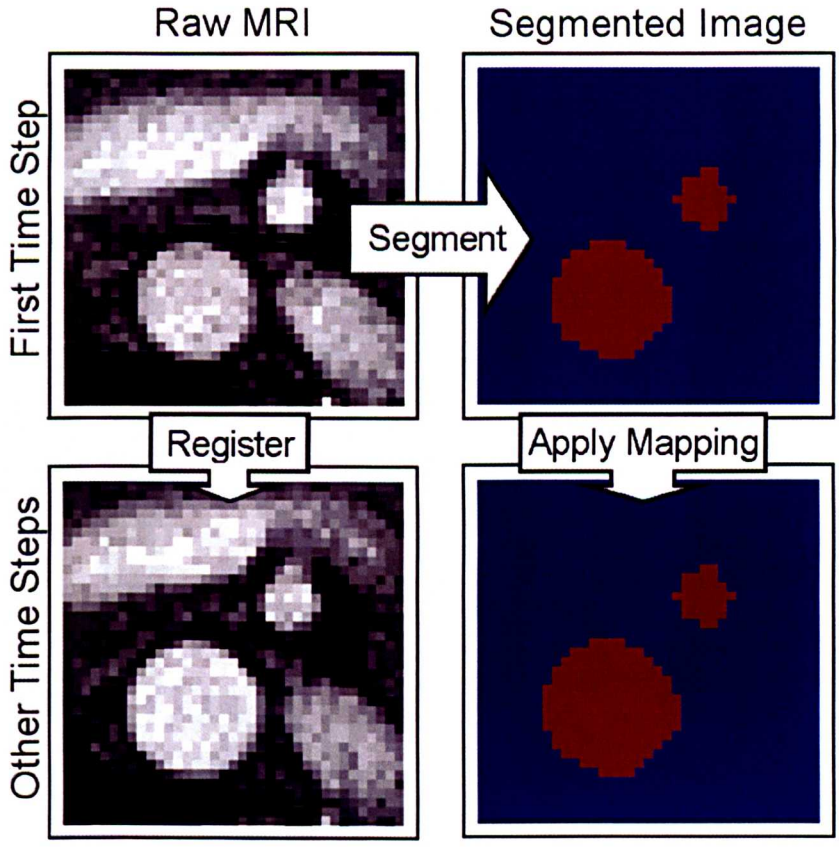

Figure 4.4. Example of segmentation by registration for a single slice.

4.3.3 – Interpolation by Registration

Until this point even spacing between slices had been assumed. However, as stated earlier, some slices were omitted during the MRI session to reduce scan time. To fill in the missing slices, the segmented image immediately above the missing slice was registered, using a single grid size non-rigid registration (a special case of the DCB algorithm described later), to the segmented image immediately below the missing slice. Half of the mapping was then applied to the first segmented image, leaving an intermediate slice being a linear interpolation between the slices either side of it.

In this way, a time-varying voxel data set was created with a voxel size of 0.98*0.98*2mm everywhere. Figure 4.5 shows the full, segmented data sets for timesteps 2, 7 and 12.

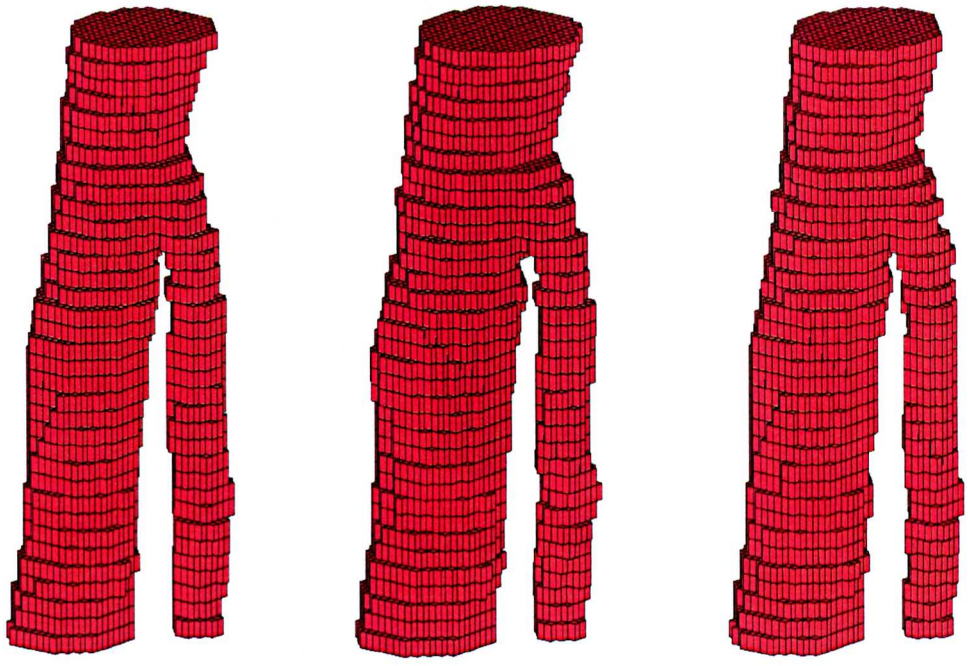

Figure 4.5. Segmented MRI data sets for timesteps 2(left), 7(middle) and 12(right).

4.4 – Mapping a Mesh onto the Segmented MRI

An idealised, unmapped tetrahedral volume mesh was created in Ansys and imported to Matlab. This mesh shared the same basic shape and size as the MRI data set and was created from a series of conical frusta, and partial tori; an example mesh is shown in figure 4.6. A volume image with voxel size matching that of the segmented MRI images was created from this mesh.

Figure 4.6. Example idealised mesh.

The segmented MRI voxel image for one time step was registered onto the idealised image and the reverse mapping applied to the idealised mesh to create a subject-specific mesh for the given timestep[2]. This mesh was then used as the basis for the registration to the other timesteps in the same manner.

The key aims of this procedure were to produce a mesh which quantifiably matched the segmented MRI data, but maintained element quality through the cardiac cycle. Mesh quality measurement is discussed in 4.5.2.

Two algorithms (both developed within the department) were available for the registration. The first, written by Professor Barber [153] (the DCB algorithm), takes two arguments, the starting and ending grid sizes, that set the largest and smallest regions of interest that the registration algorithm considers, these govern the trade-off between; smoothness, flexibility, and computational cost of the registration algorithm. The second, written by Dr Steven Wood (the SMW algorithm), takes a stiffness parameter that governs the cost of areas of high shear in the algorithm to perform the same trade-off.

---

[2] The counter-intuitive direction of registration at this stage is due to the fact that the mapping generated is not analytically invertible, and that the 'forward' mapping for the images (from the source image to the target image) becomes the 'reverse' mapping for the meshes (from the target mesh to the source mesh).

Registration performance was measured by the linear displacement of each point on each morphed mesh surface from a surface representing the edge of the appropriate segmented MRI volume data-set; this is discussed in 4.5.1.

4.5 – Quantification of Registration Performance – Differences Between Meshes and Images

4.5.1 – Techniques for Comparing Meshes and Images

An algorithm was written to find the distance of each of a series of points from the closest point on a surface mesh. This code could be used to directly compare one mesh to another. Alternatively, an image was converted to an equivalent mesh defined by a series of nodes at the exterior corners of surface voxels (with appropriate connectivity) and this mesh compared to another surface mesh.

The algorithm takes two arguments; the input mesh and the reference mesh, both defined as; a number of nodes in 3d space, and a set of triangular surface elements (themselves defined by three nodes each). For each node on the input mesh, the following is carried out:

- The nearest node on the reference mesh is found. The distance to this node is recorded as h_1.
- Elements associated with this node are found (the reference elements).
- For each edge of each element, normal distance from the input node to a line of infinite length including the edge of the element is found. It is then checked that the point on the line, to which the normal distance corresponded, was associated with a point on the edge of the triangle, if it did not the distance is discarded. The smallest of the non-discarded distances is then recorded as h_2.
- In a similar fashion to the lines, for each element the normal distance from the input node to an infinite plane including the element is found, and it is checked that the point on the infinite plane for which the normal passes through the input node is within the element, if this is the case, the distance is recorded as h_3.
- The minimum distance from the input node to any point on the reference mesh is then the minimum of h_1, h_2 and h_3.

This output of the algorithm is therefore a vector of distances forming the linear displacement spectrum (LDS) from one mesh to another; the mean of this spectrum is the average linear displacement (ALD). This forms an extension of the 2 dimensional definition of ALD given by Barber [155].

A convenient and informative method of displaying LDS data is to plot a surface model of an object, and to colour each face according to the mean LDS value of the adjoining surface nodes. Figure 4.7 uses this technique to show the distance between the surfaces of a sphere of volume 1 and concentric cube of volume 0.125.

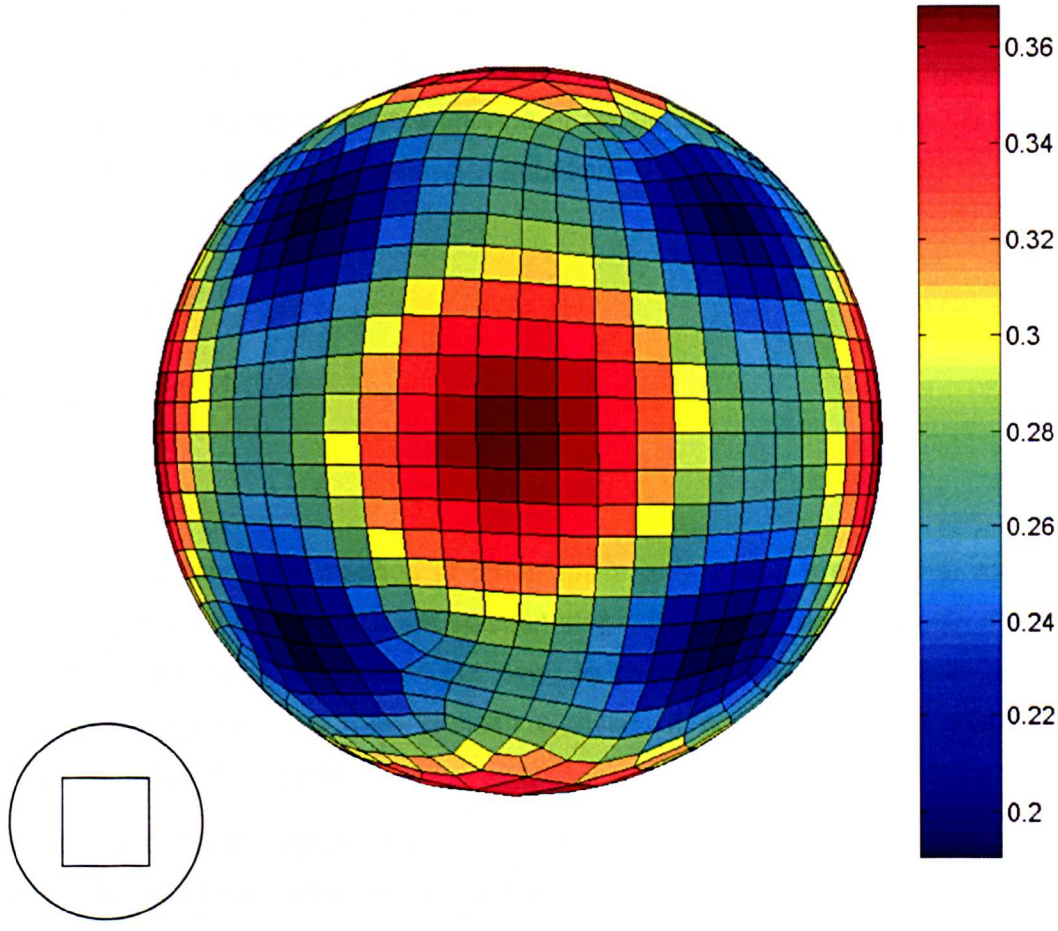

Figure 4.7. Distance map between sphere and cube (line drawing shows relative size and position of sphere and cube).

4.5.2 – Mesh Quality Measures

Mesh quality was measured in terms of number of degenerate elements and generalised aspect ratio of each element, defined in 4.1. Degenerate elements occur when any node on a tetrahedral element passes through the plane formed by the other three nodes; they cause the breakdown of the solution and must not occur anywhere in a mesh to be used for CFD.

$$Generalised\ Aspect\ Ratio = \frac{(l_{avg})^3 / V}{8.48} \qquad 4.1$$

Where l_{avg} is average length of the element edges, V is the element volume. For a regular tetrahedron, the numerator equates to the normalising factor of 8.48. By default, Ansys will remesh for GAR ≥ 10 for any element. Ansys also makes two other tests of mesh quality, volume change of an element (VOCH) and aspect ratio change of an element (ARCH) defined in equations 4.2 and 4.3 respectively.

$$VOCH = \exp\left|\frac{\log V(t_b)}{\log V(t_a)}\right| \qquad 4.2$$

$$ARCH = \exp\left|\frac{\log GAR(t_b)}{\log GAR(t_a)}\right| \qquad 4.3$$

These tests compare the meshes at timesteps a and b, and are used to monitor mesh changes through the transient solution stage; these two results should are not important for the initial registration but need to be considered when choosing the time-step for any transient moving-mesh analysis. If any element has VOCH or ARCH ≥ 3, Ansys will remesh.

The automatic Ansys re-meshing process is time-consuming and creates a new database for each re-meshed timestep; this greatly increases the difficulty of post-processing, hence re-meshing should be avoided if possible.

4.5.3 – Initial Registration Performance

The initial aim in using the registration software was to recreate the geometry for a single time-step as an intermediate goal, before moving onto recreating the full moving mesh.

Throughout this section the results for volunteer 12 are used as the primary example.

An initial analysis was tried using a simple idealised mesh; the volume dataset associated with this mesh is shown in figure 4.8 along with the segmented MRI dataset to be registered to it.

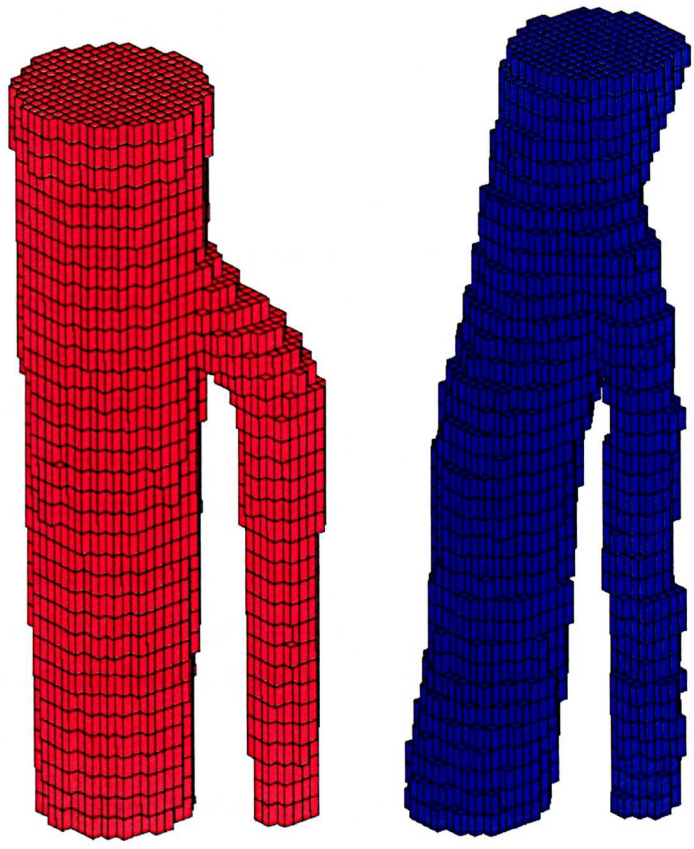

Figure 4.8. Segmented volume data sets based on initial idealised mesh (red) and segmented MRI (blue).

The results for the initial registrations were fairly poor. The DCB algorithm could not find a solution, regardless of input parameters. The SMW algorithm faired a little better and produced results, but element quality was poor (maximum GAR >10) for all stiffness parameters for which the 2d validation of the algorithm had been carried out (validation details in Appendix A, full details of initial registration runs in appendix B).

Only with a stiffness parameter of 10^7 did the algorithm perform acceptably in terms of GAR; for this analysis, the ALD appeared reasonable, being below the smallest voxel dimension (at 0.92mm), but the maximum linear displacement between the

resulting mesh and the target was more than one and a half times the largest pixel dimension (over 3mm), this was deemed unacceptable.

There were several options available to improve the results:

- Improve the match of the idealised mesh to the segmented MRI images. This has the advantage that the general approach is unchanged.
- Use an alternative timestep for the initial registration.
- Perform the initial registration to a lower degree of accuracy and then register this to all timesteps.
- Morph a surface mesh of triangles and then use these to create the tetrahedral volume mesh (meshes for further timesteps must still be morphed as a volume in the original manner, to allow interpolation between timesteps). This approach guarantees zero degenerate elements, however the surface triangles may still have large aspect ratios and may result in volume elements with poor aspect ratio, which may become degenerate under the comparatively small shears expected in the time-step to time-step morphing.

The chosen approach was discard the fourth option and retain the first three, as this would allow the full registration process to take place in Matlab without any intervention, rather than having to call Ansys during the registration process.

4.5.4 – Initial Registration Performance (Improved Idealised Model)

In 4.5.3, the main difference between the idealised mesh and the MRI geometry is that the mesh assumes that neither the SMA nor the aorta is inclined to the left or right. A new, more flexible geometry structure was created to allow this deviation. Images of meshes created using this structure are shown in figure 4.9.

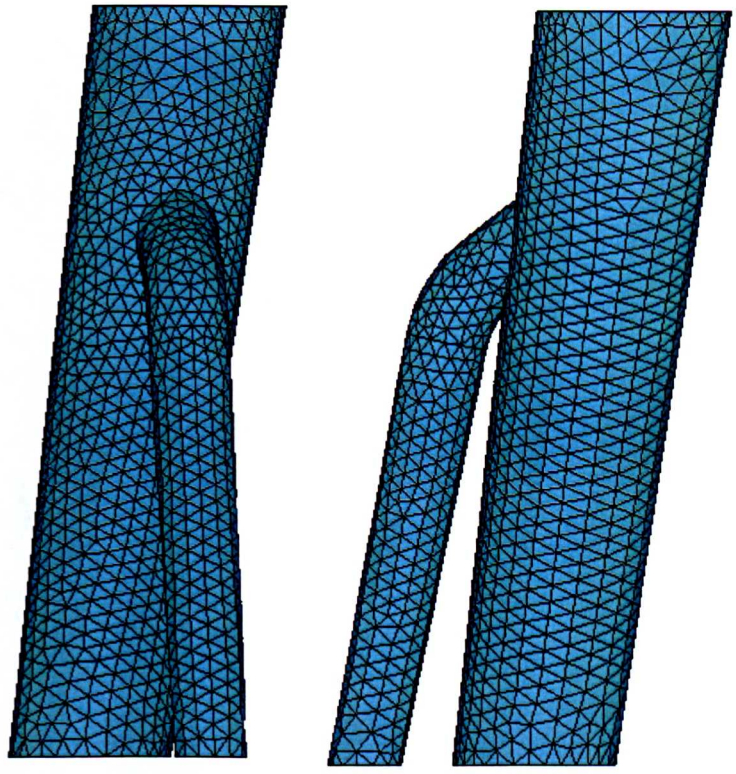

Figure 4.9. Updated idealised mesh.

It was found that the improved mesh structure both improved the results for the SMW algorithm and allowed the DCB algorithm to solve for a wide range of parameter values.

For the SMW algorithm, lambda values of 10^5 or greater now gave zero degenerate elements and acceptable values of GAR. At lambda = 10^5 the ALD was reduced to 0.4mm. This value of ALD was not improved substantially by further decreasing lambda (although this did cause element degeneracy). The best result obtained was that using the improved mesh with lambda = 10^4. The linear displacement map for this registration is shown in figure 4.10.

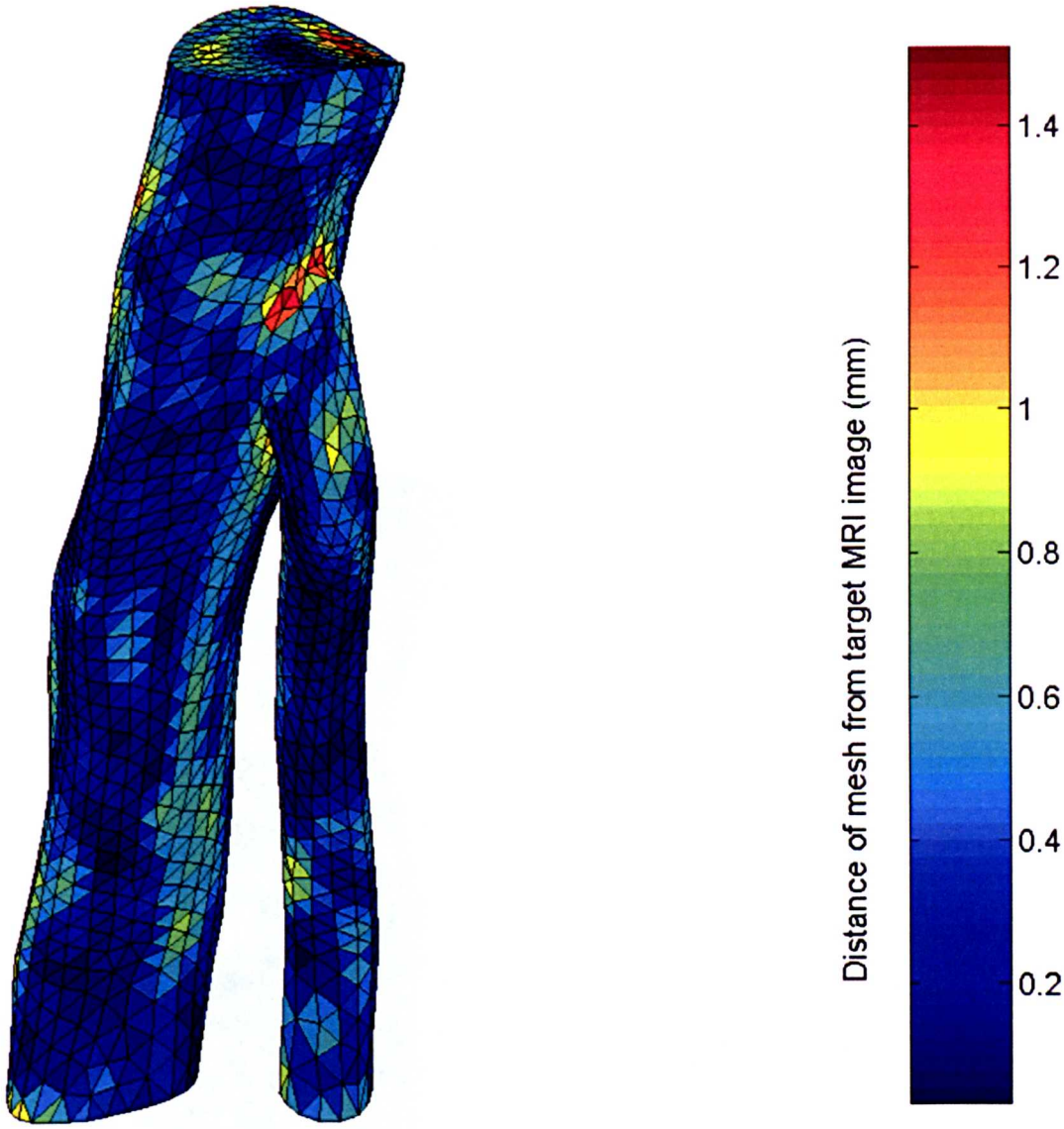

Figure 4.10. Linear displacement map for lambda = 10 000 (improved idealised mesh).

For the DCB algorithm, very good results were obtained with an end grid size of 8 or 16 (regardless of start grid size), in these cases ALD was always less than 0.5mm, no elements degenerated and maximum GAR was close to the value of 4.17 from the idealised mesh. Overall, the best results were obtained with start and end grid sizes of 32 and 8 respectively, maximum GAR was 5.1, ALD was 0.315mm; the resulting linear displacement map is shown in figure 4.11.

For end grid sizes of two and four, mesh quality started to degrade substantially without substantially improving the ALD (which actually increased for a grid size of two). At the higher end grid sizes, ALD increased beyond one voxel width and

showed notable mismatches between mesh and target image, but mesh quality remained almost unchanged from the idealised mesh. In contrast to figure 4.10 or 4.11, figure 4.12 shows the linear displacement map for a start grid size of 64 and an end grid size of 32.

Figures 4.13 to 4.15 show histograms of the linear displacement spectra for; the SMW algorithm with lambda = 10 000, the DCB algorithm with start grid size = 32 and end grid size 8, and the DCB algorithm with start grid size = 64 and end grid size 32.

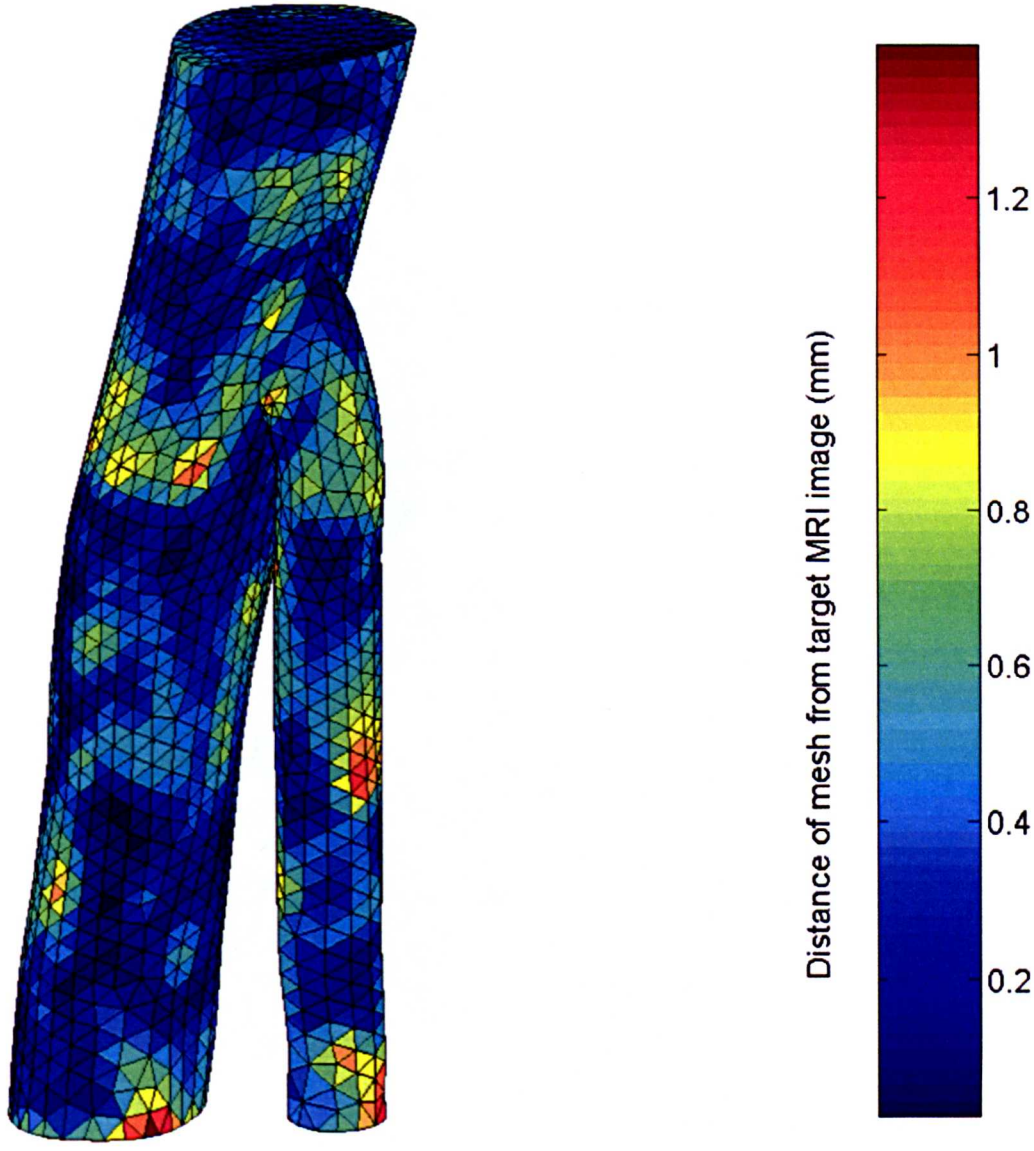

Figure 4.11. Linear displacement map for start grid size of 32 and end grid size of 8.

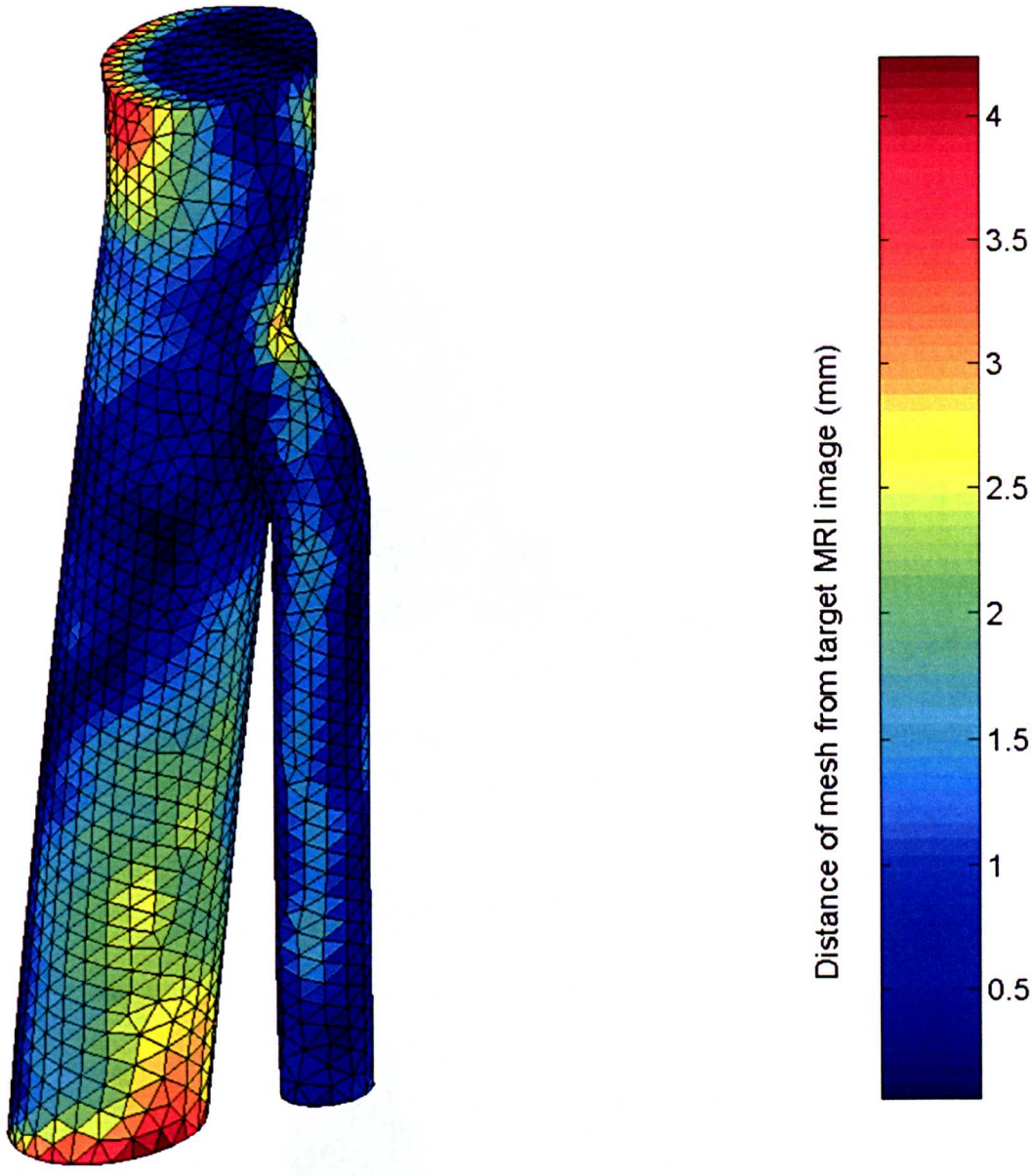

Figure 4.12. Linear displacement map for start grid size of 64 and end grid size of 32 (note the change in scale compared to figure 4.11).

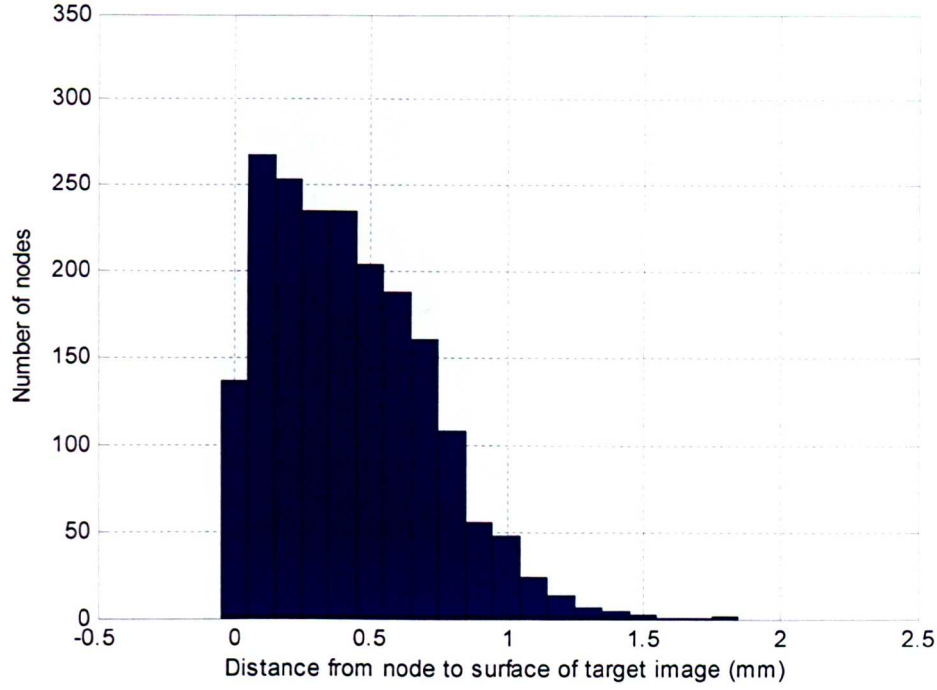

Figure 4.13. Linear displacement spectrum histogram for SMW algorithm with lambda = 10 000.

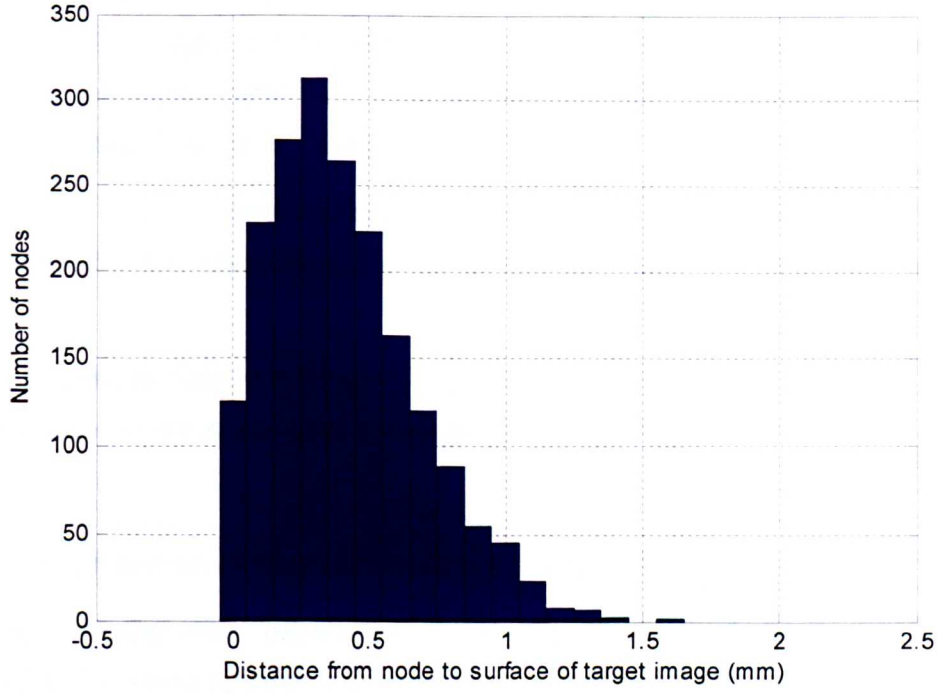

Figure 4.14. Linear displacement spectrum histogram for DCB algorithm with start grid size of 32 and end grid size of 8.

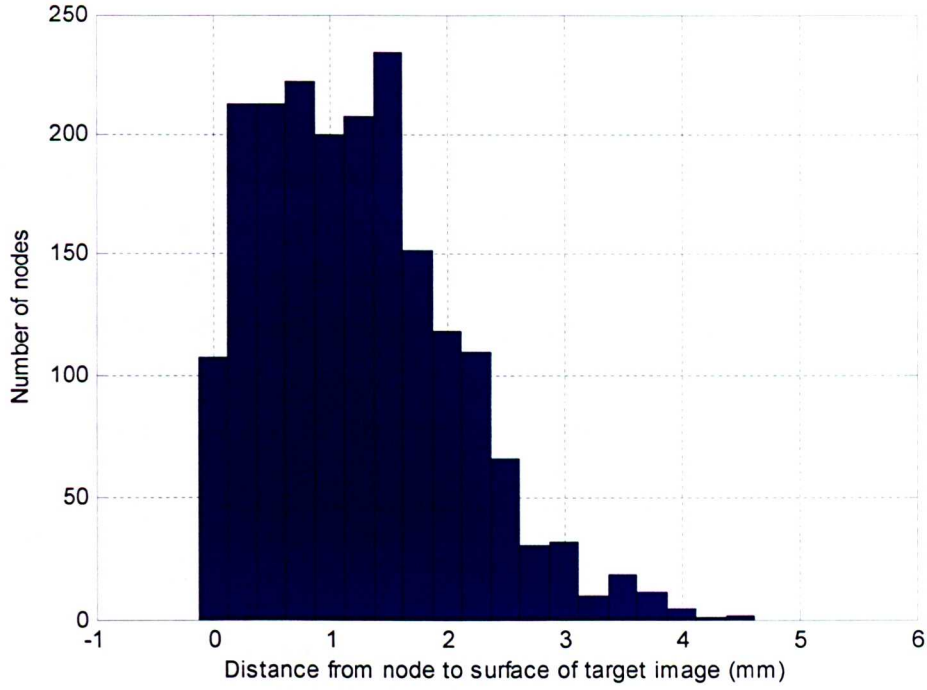

Figure 4.15. Linear displacement spectrum histogram for DCB algorithm with start grid size of 64 and end grid size of 32 (note that x-scale is different to figures 4.13 and 4.14).

From figures 4.10 and 4.11, it appears that while similar in terms of ALD and element quality, the DCB algorithm delivers a smoother, more plausible surface. This may be related to the slightly better ALD achieved with the DBC algorithm, or may be due to some internal difference in the algorithm's structure.

Figure 4.12 clearly shows the under-fitting caused by a large end grid size; patterns of increased linear displacement occur over larger regions than in figures 4.11 and 4.10.

One key point to note from figures 4.13 and 4.14 is that in both cases the maximum linear displacement is less than the largest voxel dimension.

4.5.4 – Registration Performance – Inter-Timestep Registrations

Moving from the initial registration to the inter-timestep phase it was found that extending the same approach quickly led to element degeneracy in time-steps other than the initial one.

A modified approach was adopted whereby the initial timestep was registered with a coarse end grid size and this 'semi-idealised' mesh used as the basis for further registrations. It was found that meshes from part way through the dilation of the aorta

worked best, for this reason the TS4 mesh was used as the initial timestep. As the DCB algorithm works with intensity images as well as binary images (as used until now), a Gaussian blur of width 2 pixels was applied to both source and target images before registration (at the algorithm author's suggestion), this further improved results. The best results were achieved with starting and end grid sizes of 32 and 8 respectively for the pre-registration, and 16 and 4 for the final registrations. The results for each timestep (in terms of ALD, maximum linear displacement and maximum GAR) are shown in table 4.4. A histogram of the linear displacement spectra at each timestep is shown in figure 4.16, linear displacement maps of the mesh at timesteps 2, 7 and 12 are shown in figure 4.17.

Timestep	Maximum GAR	ALD (mm)	Maximum LD (mm)
1	7.7	0.37	1.5
2	7.6	0.37	1.5
3	7.9	0.37	1.5
4	7.0	0.35	1.8
5	7.3	0.39	1.9
6	6.8	0.37	1.8
7	6.9	0.37	1.9
8	6.8	0.38	2.0
9	6.8	0.35	1.9
10	7.5	0.36	1.7
11	7.6	0.37	1.8
12	6.9	0.39	2.0
13	7.0	0.35	1.4
14	7.3	0.35	1.5
15	6.7	0.35	1.5
16	6.8	0.38	1.8

Table 4.4. Results for the inter-timestep registrations

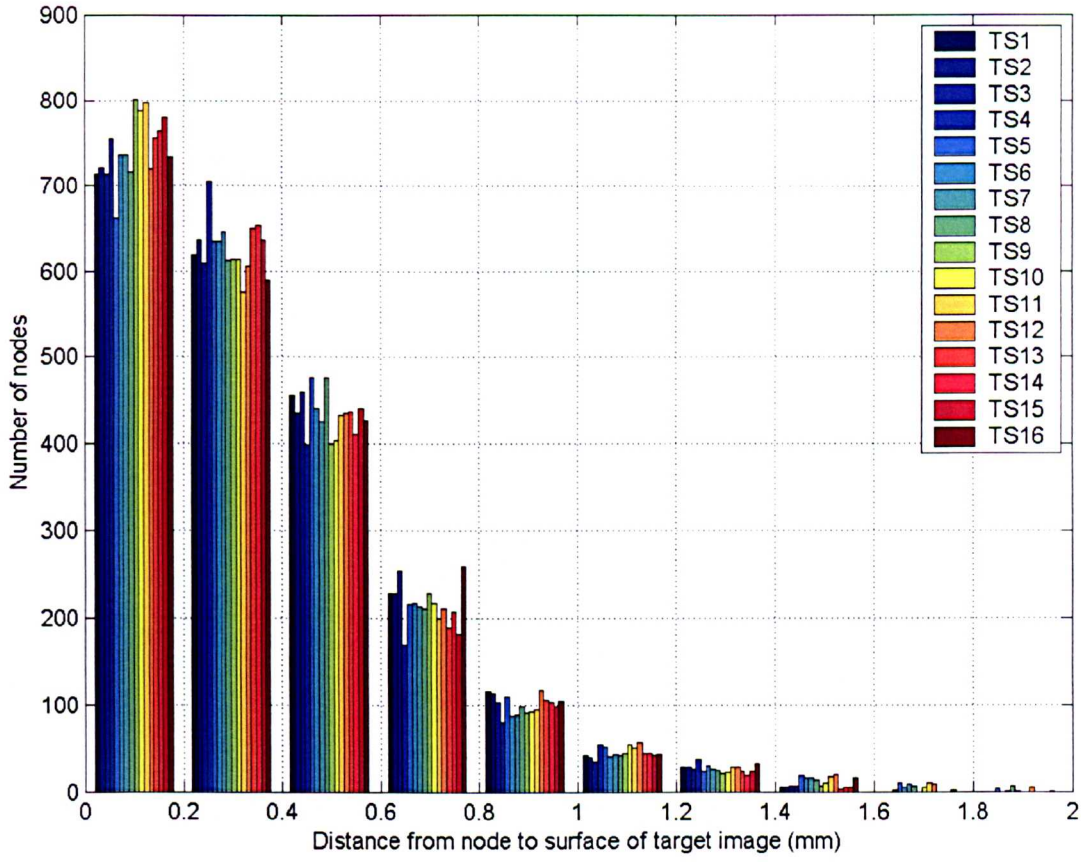

Figure 4.16. Histogram showing linear displacement spectra for mesh at each timestep (TS).

Once more, no node was further than the largest voxel dimension from the segmented MRI image and ALD was below half of the smallest pixel dimension for all timesteps, the largest GAR was 7.9 (comfortably below the Flotran remeshing limit).

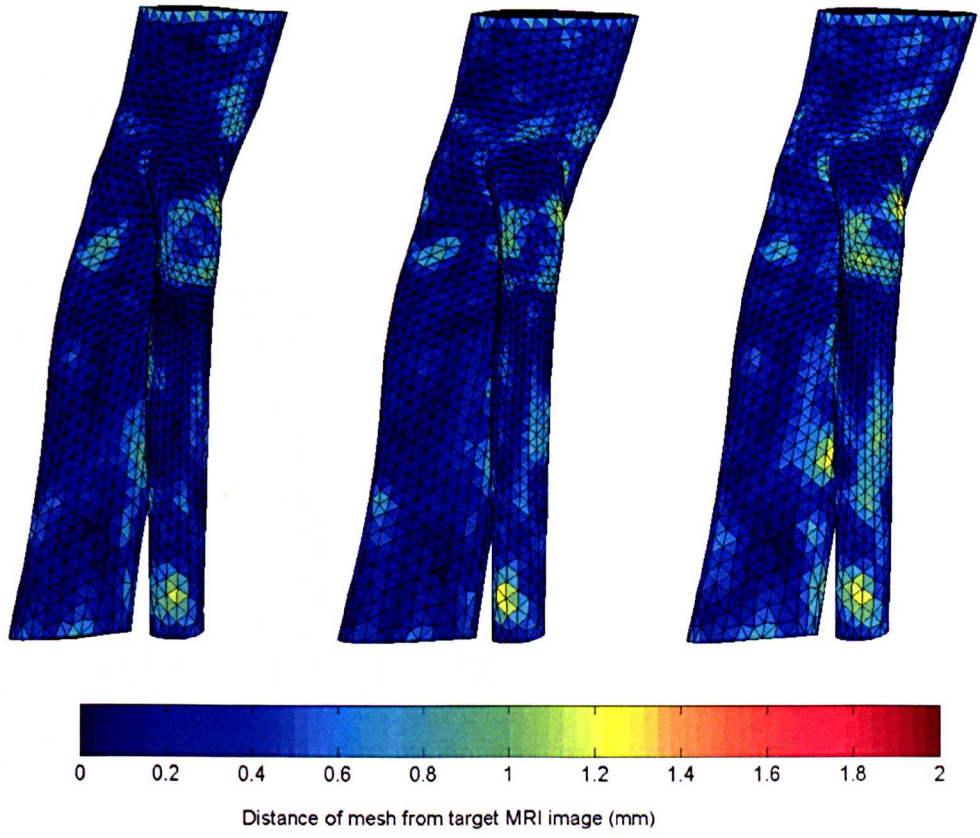

Figure 4.17. Linear displacement maps for mesh at timesteps 2, 7 and 12.

4.6 – Skeletonisation and Quantification of Vessel Motion

One by-product of using the above method of mesh generation is that an elegant method of vessel skeletonisation presents itself. As the centreline of each section of the geometric primitive mesh is well defined, a skeletonised representation of this mesh can be created as a series of nodes along the centreline of each vessel. The same mapping used for the full primitive mesh can be applied to the centre-line nodes to give the centre-line of the morphed mesh. A validation case for centre-line extraction by registration for simple shapes is included in appendix A.

An example morphed mesh and centre-line is shown in figure 4.18.

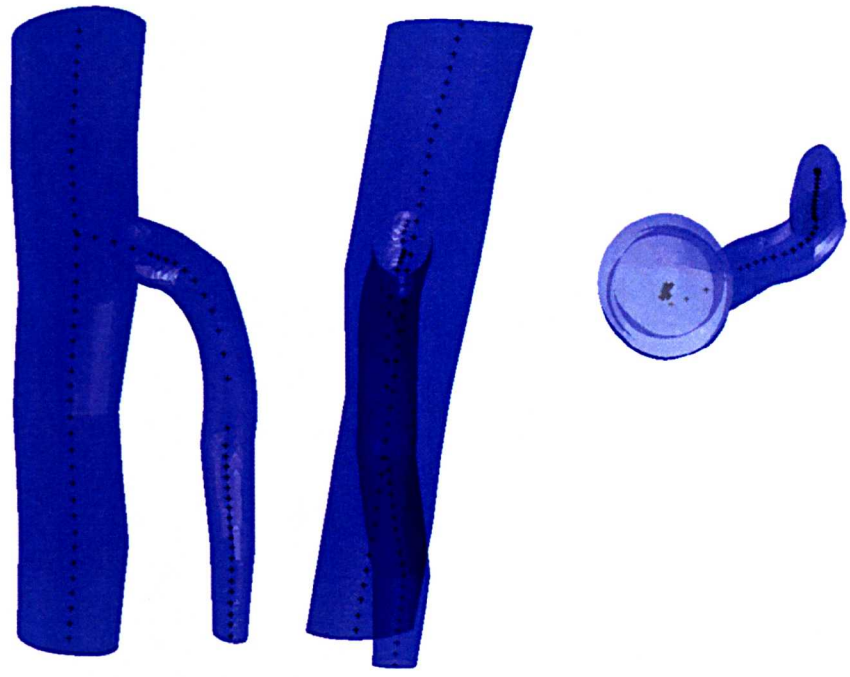

Figure 4.18. Example morphed mesh and centre-line.

4.6.1 – Quantifying Centreline Extraction Performance in a Complex Geometry

An algorithm was developed to quantify performance of the registration. At each centreline point, a plane was defined normal to the centreline direction (defined by the vector between the centreline points either side of the point of interest). The surface model was cut along this plane leaving a 2d set of points defining the outline of the model on this plane. The centre of gravity of the area defined by these points was then calculated and the distance between this point and the morphed centreline point calculated and normalised against the mean distance from the morphed centreline point to the boundary of the 2d area. The results can be seen in figures 4.19 to 4.21. For the example shown in the figures (excluding points near bifurcations) the mean normalised displacement was 0.081.

Figure 4.19. Morphed vessel centrelines for AA (left) and SMA (right) (yellow stars), alongside 2d centres of gravity (dark blue).

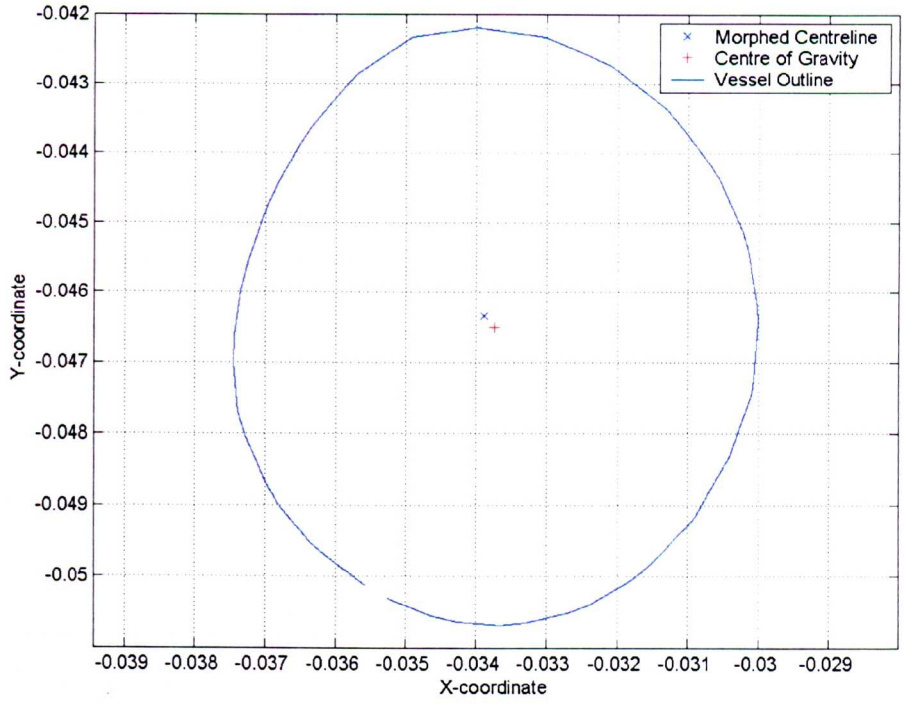

Figure 4.20. Vessel outline, centre-point and centre of gravity for distal SMA (normalised difference between centre-line estimates equals 0.05).

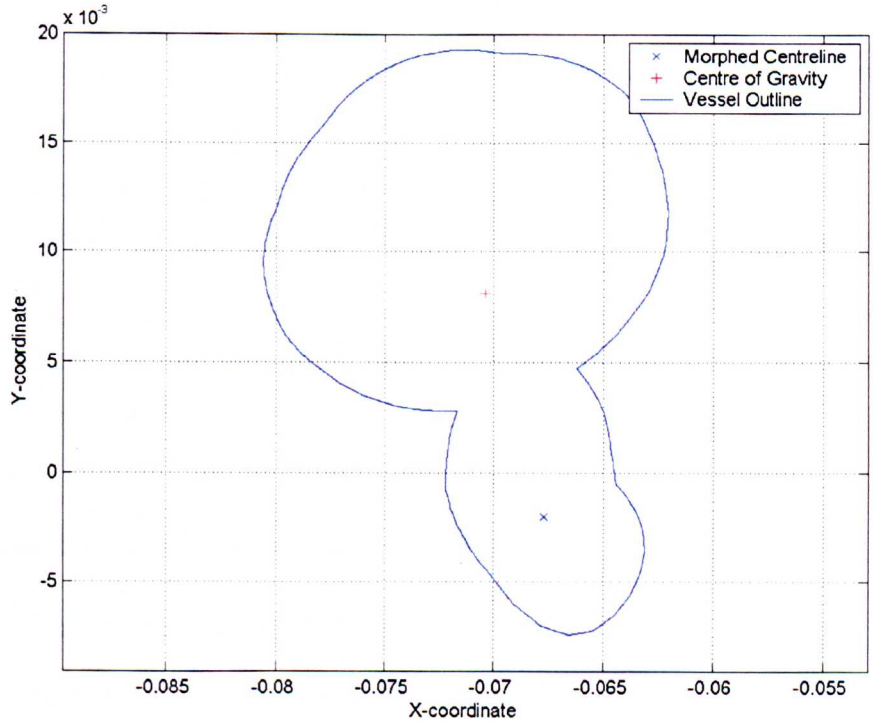

Figure 4.21. Vessel outline, centre-point and centre of gravity for SMA close to its origin (normalised difference between centre-line estimates equals 1.11).

The above figures show that the method of centreline extraction by registration works well in the AA and SMA, particularly around the bifurcation, where other techniques often fall down.

4.6.2 – Separating Gross Vessel Motion from Dilation

Once a moving centre-line model was available (described as a series of discrete points), it was possible to separate the gross vessel motion of any point in the model from the dilation.

To do this for a given node, the following procedure was undertaken:

- The closest centre-line point to the node was found.
- The gradient of distance to the node was found as one moves a small distance each way along the centreline.
- The next centre-line point in the direction that initially decreased distance to the node was chosen. If neither direction decreased the distance, this implied that the centre-line must be convex from the node's perspective, and the centre-line point already selected was the closest point to the node anywhere on the centre-line.
- The centre-line was assumed to run straight between the two chosen centre-line points.
- The closest point on this section of centreline was found and its motion calculated by linearly interpolating between the motions of the points on either side.
- This motion was subtracted from the motion of the node to give the dilatative component of node motion.

4.6.3 – Motion of the SMA and AA – 3d Results

4.6.3.1 – Gross Motion of the SMA and AA

First let us consider the gross – or centre-line – motion of the SMA. Figure 4.22 shows the trajectory of each centre-line point through the cardiac cycle, for context and scale, the original position of the SMA and AA is overlaid.

Figure 4.22. Outlines of TS1 mesh with centreline point trajectories (black dots indicate TS1 centreline position), shown from the front (left) and from the right (right).

Figure 4.22 clearly shows the significant movement of the SMA as the aorta expands, it is immediately clear that the centre-line movement of the SMA is approximately equal to its radius. The anterior motion of the AA due to its dilation and the constraint of the posterior aspect by the spine is also clear. The apparent lack of motion in the image on the left shows that the majority of the SMA's motion is in the anterior/posterior plane for this subject.

Figure 4.23 shows the outline of the initial mesh along with five centreline node positions of interest. Figures 4.24 and 4.25 show the x, y, and z components of motion of the SMA and AA centre-line nodes (chosen in figure 4.23) respectively.

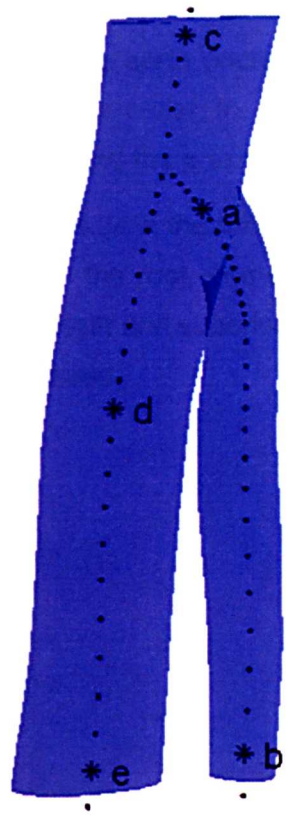

Figure 4.23. Centre-line points (points chosen for further analysis highlighted with stars).

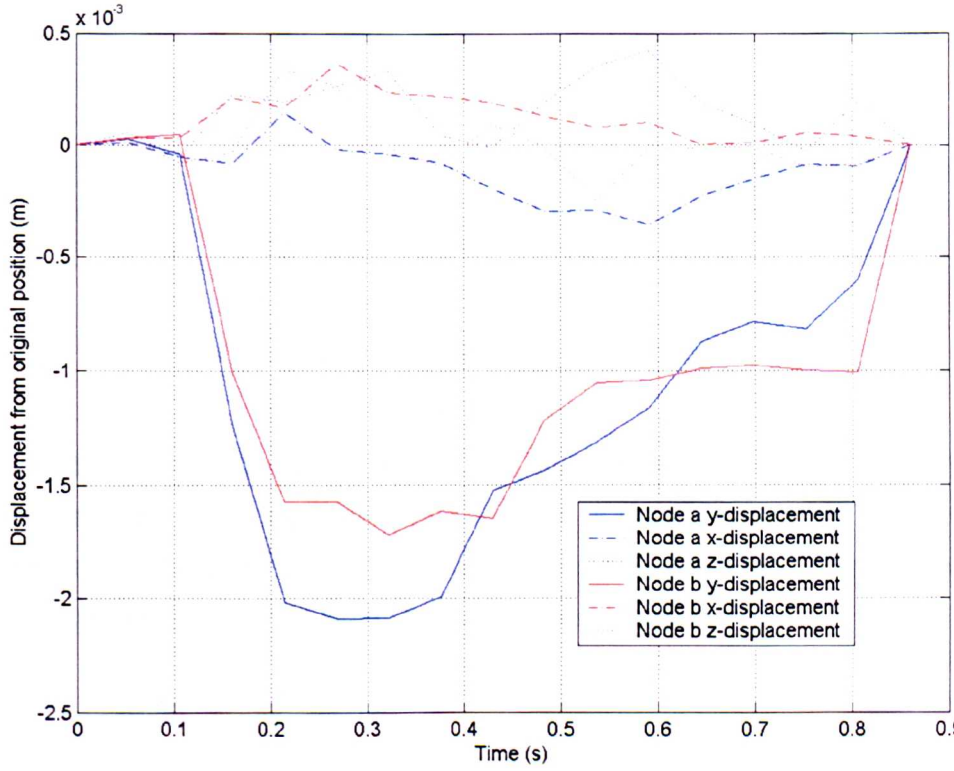

Figure 4.24. Motion of a SMA centreline points 'a' and 'b'.

Recall from chapter 3 that the imaging volume is aligned with the abdominal aorta such that the z-axis runs parallel to the aorta (increasing z in the cranial direction), the y-axis then runs close to from anterior to posterior (although with a slant associated with the angle of the AA), and the x-axis runs left to right.

Thus, the main motion seen in figure 4.24 is the anterior-posterior motion of the SMA, this is of the order of 2mm close to the root, decreasing slightly to around 1.7mm closer to the end of the vessel. Left-right and superior inferior motions of the SMA are less than 0.5mm at the points measured.

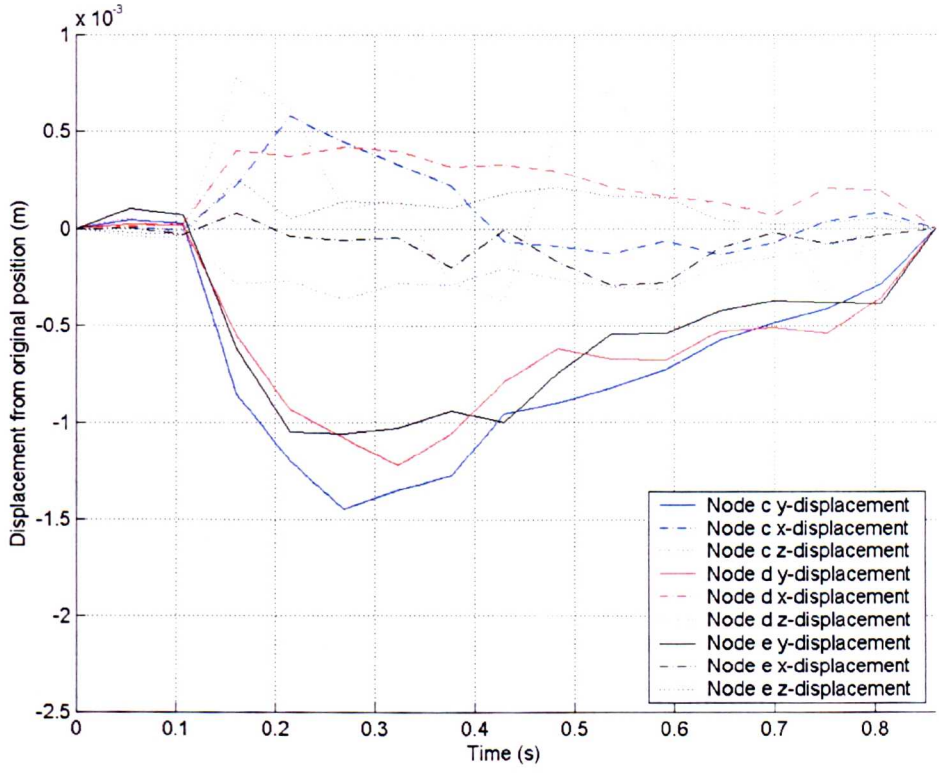

Figure 4.25. Motion of AA centreline points 'c' and 'd' and 'e'.

Figure 4.25 shows similar results to 4.24, the anisotropic expansion of the AA caused by the solid structure of the spine posterior to it, is clearly visible, as the centre-line moves anteriorly by up to 1.4mm with the systolic pressure pulse. Motion in the other planes is greater than for the SMA, but barely exceeds 0.5mm.

4.6.3.2 – Dilation of the SMA and AA

Using the technique outlined in 4.6.2, the gross motion of the vessels was removed to leave the dilatory component, this was analysed for a series of nodes as shown in figure 4.26.

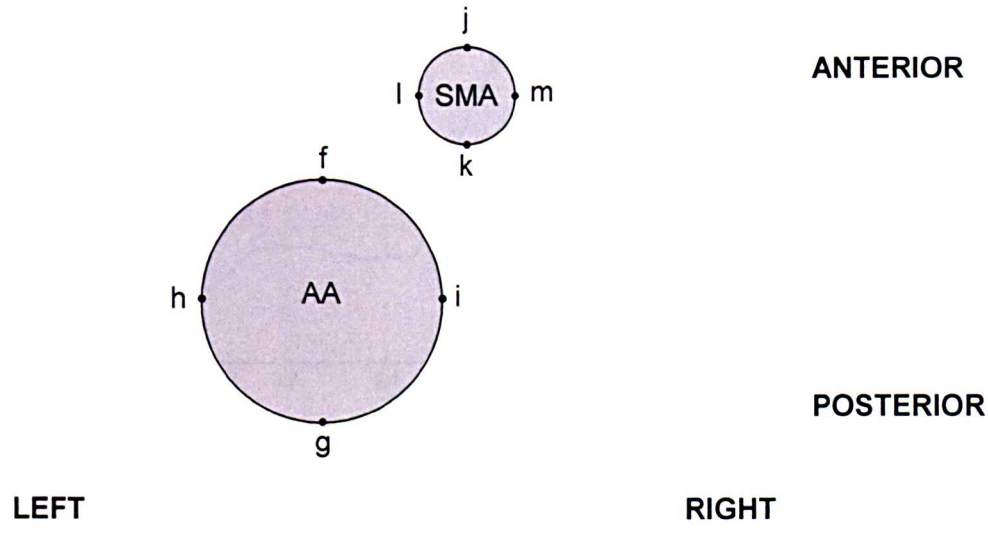

Figure 4.26. Diagram showing nodes of interest for analysis of dilation (all nodes selected close to, but not on, the outlet region of the model).

Figures 4.27 to 4.30 show the y-component of motion for nodes f, g, h and i respectively both with the full-motion and the dilation-only motion.

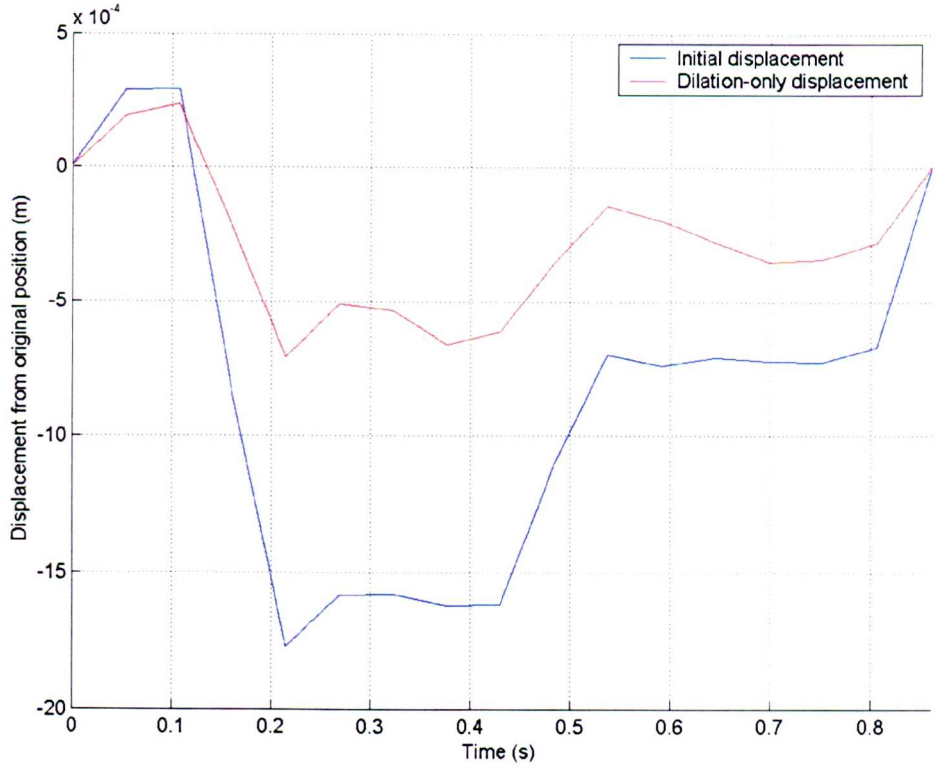

Figure 4.27. Y-component of motion of AA node f (full motion and dilation-only).

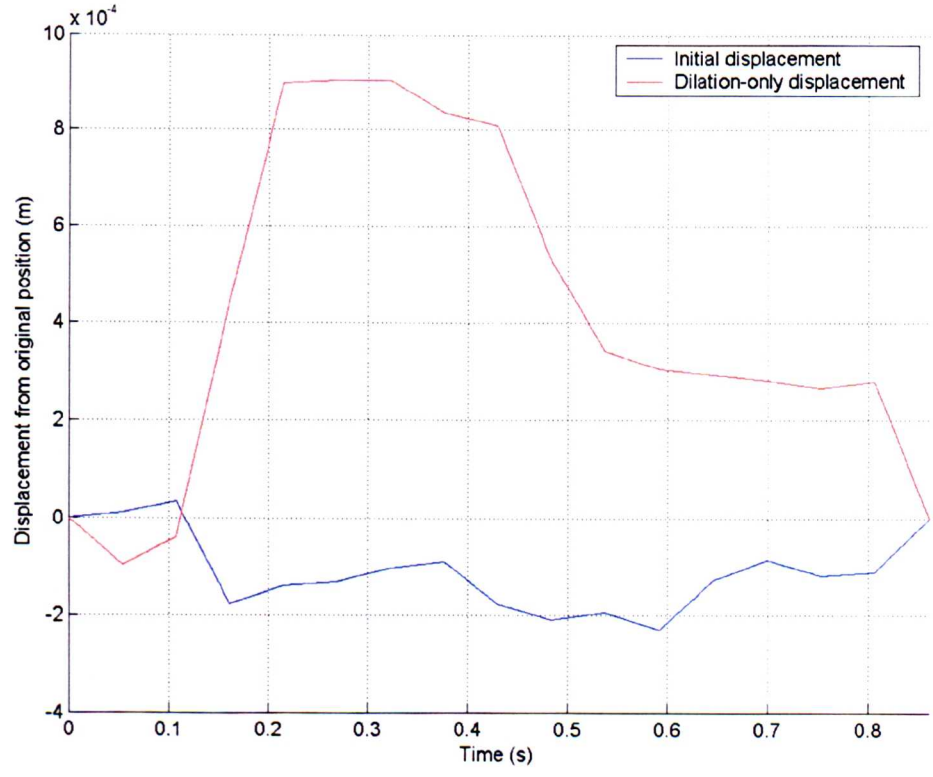

Figure 4.28. Y-component of motion of AA node g (full motion and dilation-only).

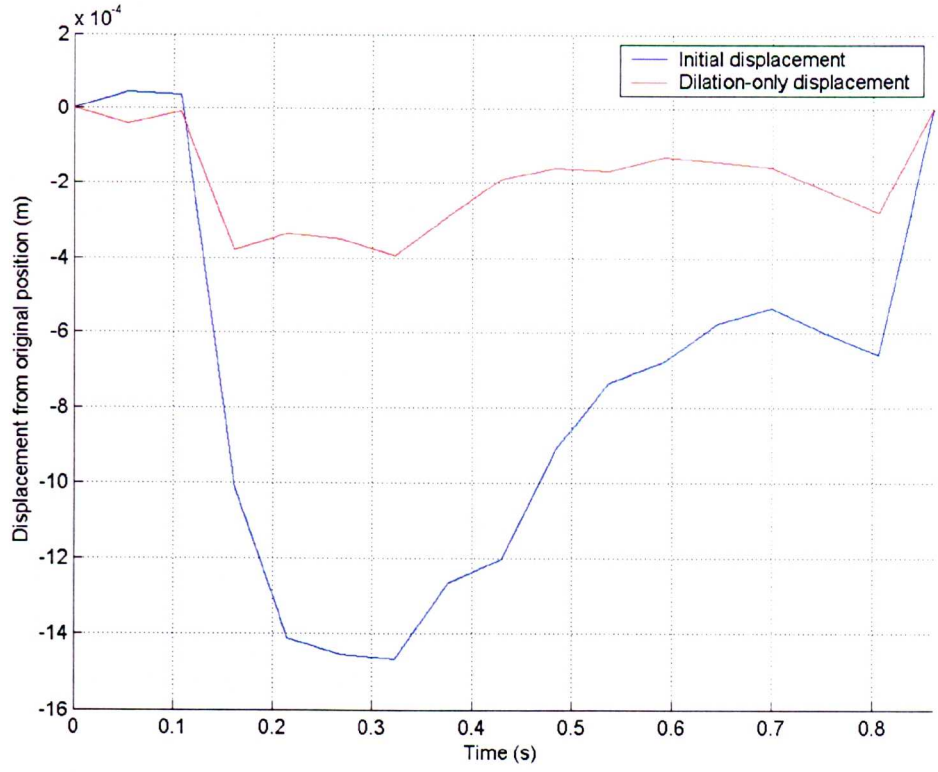

Figure 4.29. Y-component of motion of AA node h (full motion and dilation-only).

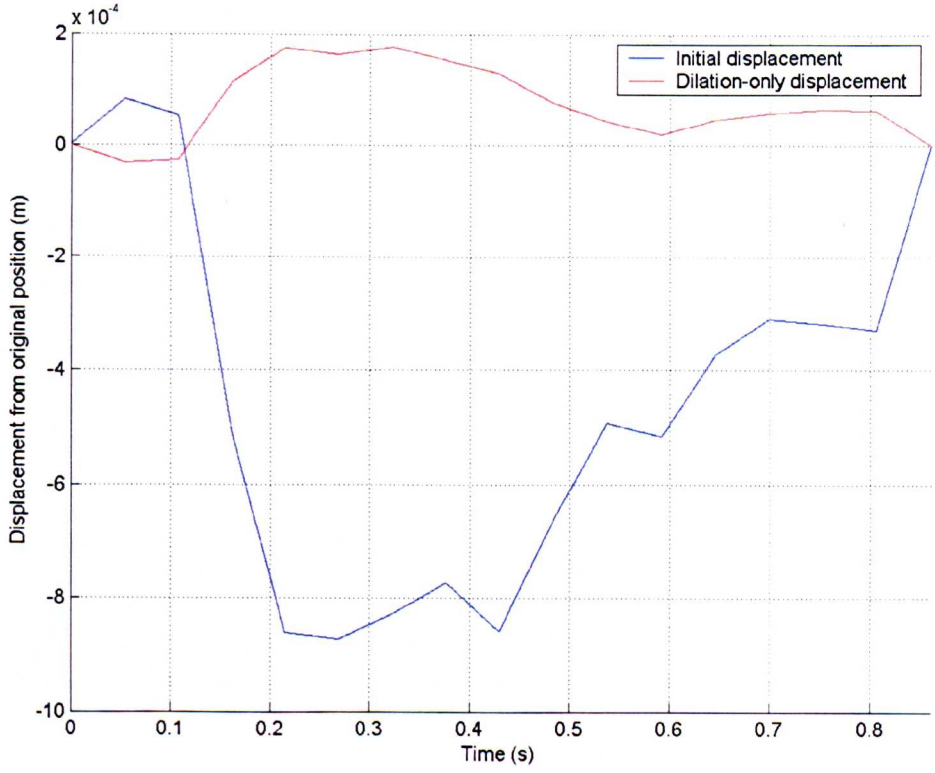

Figure 4.30. Y-component of motion of AA node i (full motion and dilation-only).

Figure 4.27 shows that much of the motion of the anterior wall of the aorta is due to the aorta's bracing against the spine, as would be expected in this situation roughly half of the anterior wall's motion is due to expansion from behind the centre-line and half from in front.

The dilation-only trace in figure 4.28 shows what one would expect to see were the aorta suspended in space, with the posterior wall moving a similar amount to the anterior wall.

Figures 4.29 and 4.30 show that the forward movement of sidewalls of the vessel is removed in the dilation-only case. The positive peak remaining in figure 4.30 and negative peak remaining in figure 4.29 suggest that the y-axis is not perfectly aligned with the centre-line motion of the AA. Figure 4.31 below shows the x-axis (right to left) motion of the node on the left hand wall of the AA; this motion was barely affected by the removal of the centre-line motion. Graphs of z-axis motion are not shown, as this was small and unaffected by removing the gross motion component.

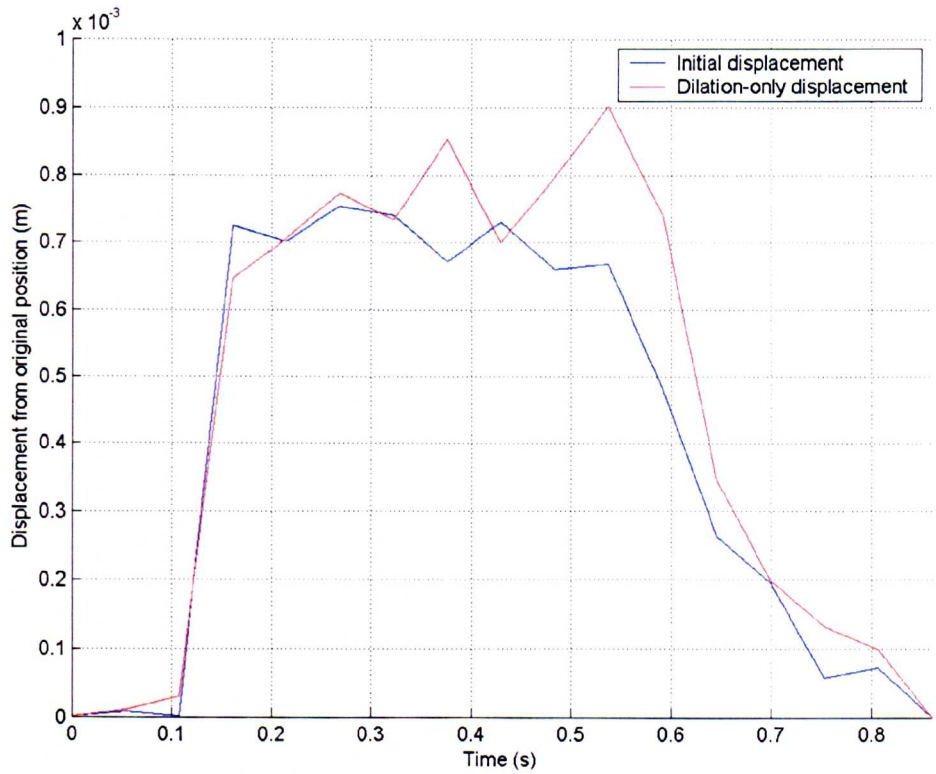

Figure 4.31. X-component of motion of AA node h (full motion and dilation-only).

Averaged over the four points of interest, peak increase in radius during systole was 0.83mm or 11.8% for this subject.

The same approach was applied to the nodes j and k on the SMA, the results are shown in figures 4.32 and 4.33.

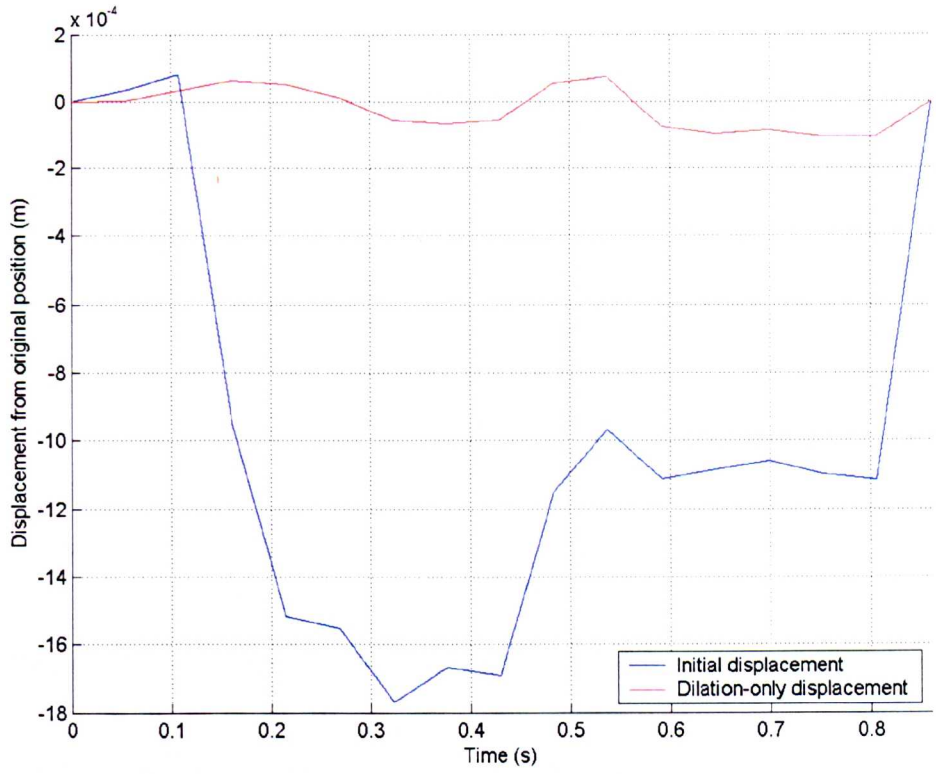

Figure 4.32. Y-component of motion of SMA node j (full motion and dilation-only).

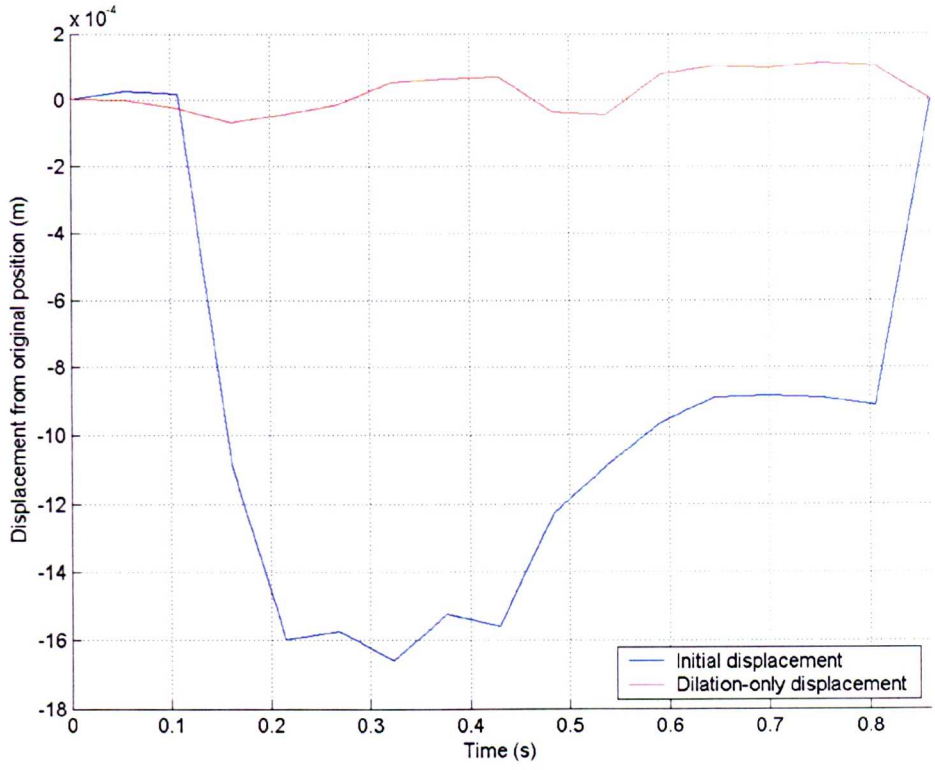

Figure 4.33. Y-component of motion of SMA node k (full motion and dilation-only).

In both cases above, the rigid motion caused by the AA's expansion swamped the dilation component of the displacement. No clear peak was seen in displacement at peak systole; assuming that the percentage expansion of the SMA was the same 11.8% as the AA, this would lead to the each wall moving about 0.3mm, considering the resolution of the MRI at 1mm, and the ALD of the mesh itself from the MRI, at 0.4mm, it is unsurprising that this subtle feature is lost. This result did not change when nodes l and m (on the sides of the SMA) were considered.

4.7 – Conclusions

Movement of the SMA with both the cardiac and respiratory cycles was observed and quantified in a group of 10 normal volunteers.

The cardiac SMA motion was captured in full 3d for one volunteer. The method used allows the quantification of model fit to the MRI data, is suitable as a basis for 3d moving-wall CFD analyses, and allows the separation of gross vessel motion from dilation.

In both studies, it was seen that the motion of the SMA is largely driven by the expansion of the aorta and its posterior physical constraint of the spine. In some subjects (in whom the SMA did not arise directly anterior to the AA) the angle of the SMA changed slightly through the cardiac cycle.

The successful separation of gross vessel motion and dilation is a significant development, and may in the future allow the development of models where gross motion is specified and FSI allowed to control the dilation component.

Chapter 5. Implementation of Boundary Conditions

5.1 – Introduction

The appropriate choice and implementation of boundary conditions is crucial for the success and validity of any CFD model. In the case of a bifurcation it is important to ensure that flow splitting is carried out correctly, while for any model attempting to capture wave propagation, correct impedance at each boundary is crucial. This chapter considers these issues and outlines a computationally efficient approach for the application of appropriate boundary conditions.

5.2 – Options for Boundary Condition Set-up

From our MRI studies, PCMRA flow profiles were available for the SMA and AA downstream of the bifurcation. These could either be used separately, or combined to give a flow profile for the AA inlet.

Two options presented themselves for consideration:

- Apply the appropriate flow profile at each outlet, and apply a pressure profile (from elsewhere) at the inlet to govern pressure throughout the model.
- Apply a flow-profile at the inlet and allow lumped-parameter downstream models coupled to the CFD model to govern the flow splitting between the branches and the pressure distribution in the model.

Both approaches have benefits and limitations.

The first approach is straightforward to implement but relies on the use of a pressure profile from elsewhere as well as requiring a set of PCMRA data for each outlet. If it were to be used in a clinical context, the extra time and cost associated with obtaining multiple sets of PCMRA data (about 10 minutes scanner time), may become important, especially if several outlet boundaries lying on different planes are present.

The second approach requires the derivation of appropriate downstream models, which must be good quality, and (to an extent) subject-specific, to give good results in terms of flow-splitting and pressure distributions. However, the approach is easily

extensible to multiple down-stream branches, requires only one set of flow data and obviates the need to obtain a pressure waveform from elsewhere (assuming that the model assumes zero pressure or constant pressure at some point).

5.3 – Applying a Flow Boundary Condition

Although PCMRA provides velocity point values at each pixel, directly applying such measurements as the boundary conditions does not make any attempt to deal with the random noise in the velocity signals or sensibly interpolate between the 21 PCMRA timesteps. Figure 5.1 shows surfaces representing the inlet flow at each PCMRA timestep for volunteer GBFV12, the random noise element in the signal makes direct interpolation from these results likely to cause very unreliable CFD results further down the line, some attempt must be made to smooth the data.

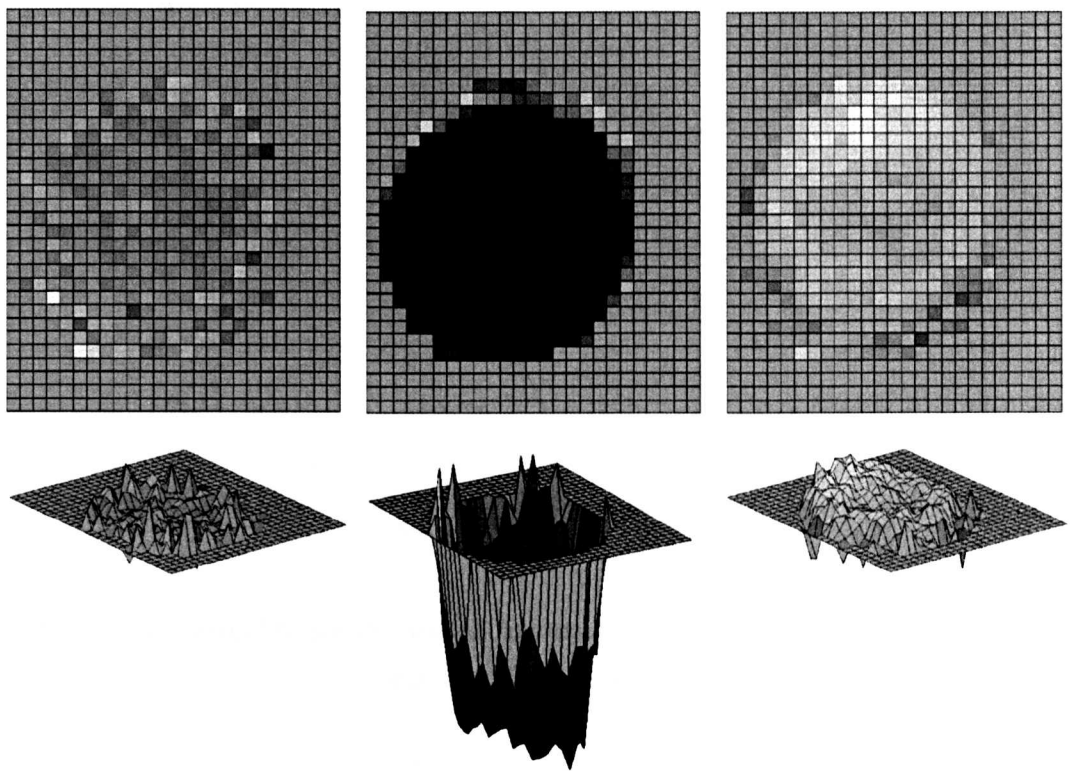

Figure 5.1. PCMRA velocity maps for the abdominal aorta at timesteps 1 (left), 7 (middle), and 14 (right).

Assuming that the profiles associated with spatially developed flow in a straight tube are appropriate, knowledge of Womersley flow profiles can be used to provide an improved estimate of velocity at each inlet point. Whilst this approach is not ideal in

that any asymmetry of the flow in the aorta is not modelled, it does allow the production of a spatially and temporally smooth waveform crucial for successful CFD analyses.

Each vessel was segmented from the PCMRA image and velocity values for each pixel summed and multiplied by pixel area to give a 21-point waveform for the time-varying flow in each vessel. As discussed in 2.2, the resulting waveform contains all the important frequencies of the cardiac waveform and can be interpolated using Fourier interpolation to give 1000 points through the cardiac cycle. The interpolated waveforms and the PCMRA data-points for one volunteer are shown if figure 5.2.

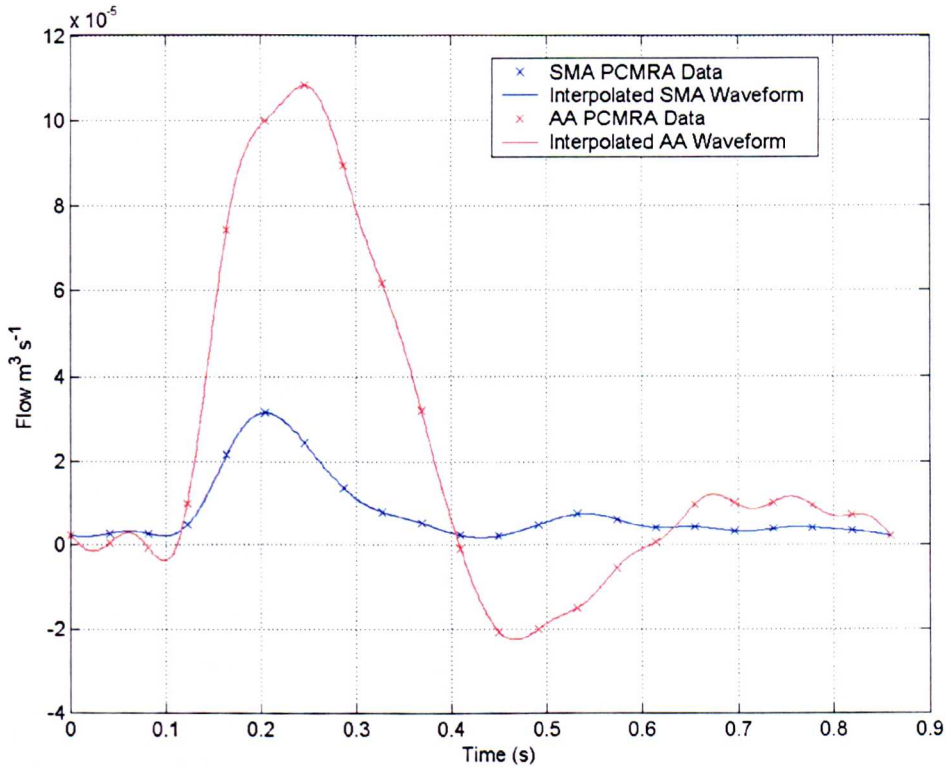

Figure 5.2. 1000-Point Fourier-interpolated flow waveform and original PC-MRI data points for the AA and SMA in GBFV12.

As the CFD mesh being has been morphed to match the segmented MRI data, the inlet is no longer a perfect circle and does not necessarily sit perfectly on a plane. For these reasons the Womersley equations cannot be used directly to find flow at each node, instead an estimate is made; the approach used is outlined below:

1. Inlet direction is found by taking the vector from the centre-line point on the inlet to the next point.

2. Approximate inlet radius for the first timestep is found, by finding the largest distance from the centre-line inlet node to any other inlet node.
3. This radius is used to calculate velocity variation with radial position over time according to the Womersley equations for the flow waveform input.
4. For each node its radial position (calculated by – distance from centre node to node *n* divided by approximate inlet radius) is used to find the appropriate fluid speed at that node.
5. Wall nodes are selected and the boundary condition (which should already have a small or zero magnitude) overwritten with zero for all time, to enforce the no-slip boundary condition.
6. The inlet direction vector is used to split the fluid velocity into appropriate u, v and w vectors.
7. As a final check, the applied flow is calculated by summing the flow through each element, small errors can be corrected by applying a scaling factor to all velocities.
8. In the case of a moving mesh analysis, all inputs are scaled with inlet area at that timestep, so that total inflow remains correct when the inlet expands or contracts.
9. The data is recorded as a set of Ansys tables to allow easy application of the boundary conditions.

The faithful recreation of the flow profile relies upon the inlet boundary being close to circular and planar. This was found to be a reasonable assumption for the morphed meshes developed in chapter 4; figure 5.3 shows the original flow input and the flow input reconstructed from the node-by-node velocities.

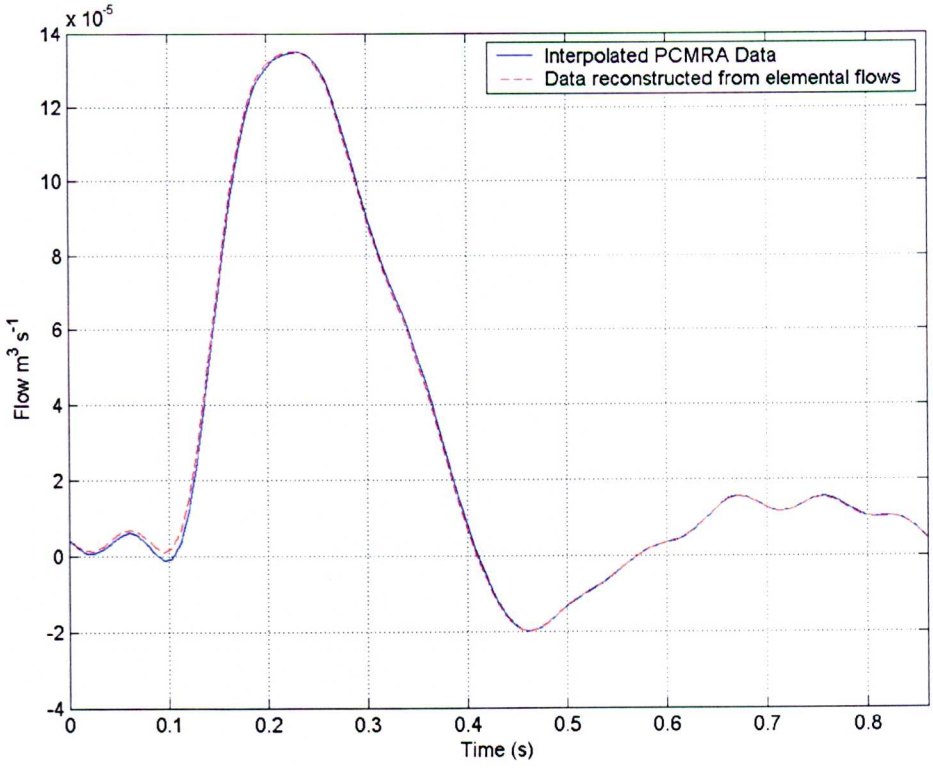

Figure 5.3. Original (Fourier-interpolated) and reconstructed inlet flow waveforms.

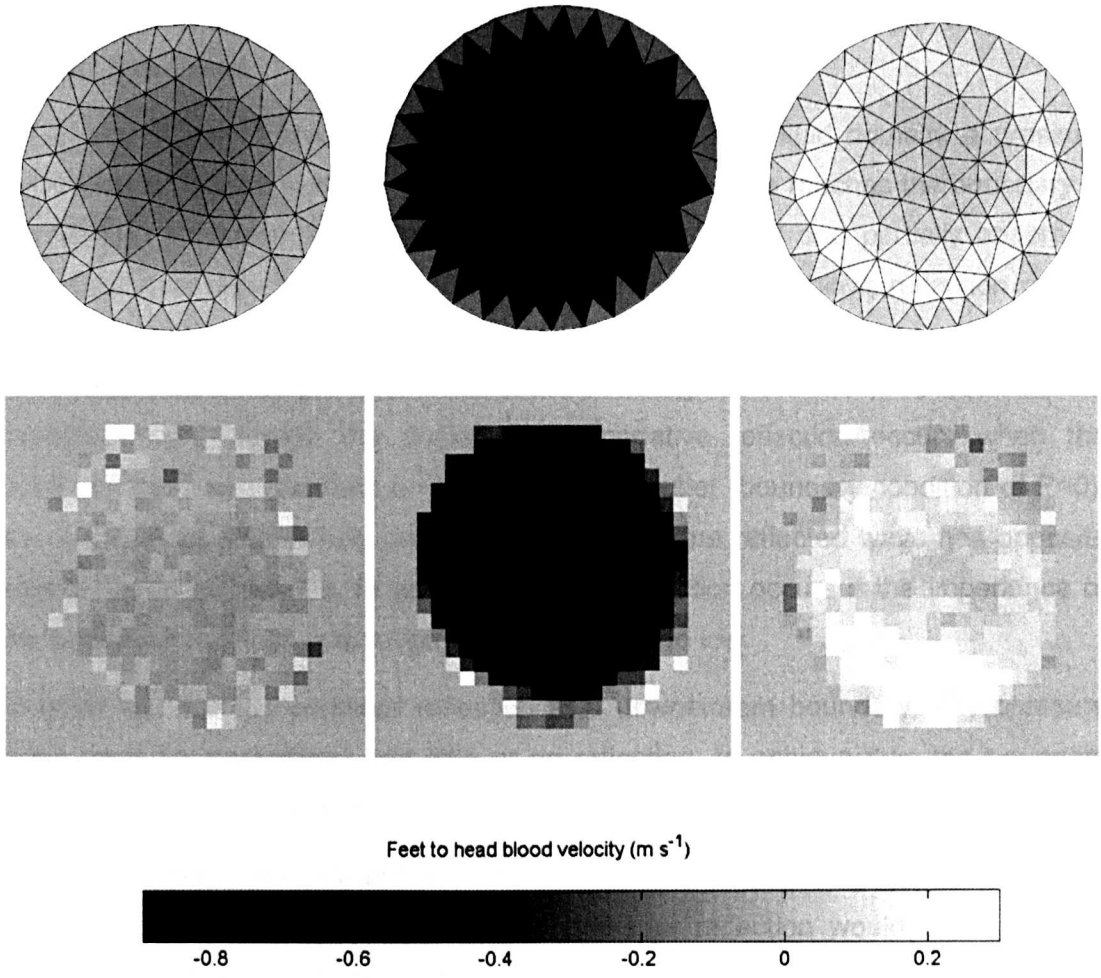

Figure 5.4. PCMRA data (above) and applied elemental velocities (below) for AA outlet, at PCMRA timesteps 1(left), 7(middle), and 14(right).

5.4 – Outlet Boundary Conditions 1 – Impedance-Matching

This section of the project was undertaken before the MRI study of the SMA had begun; at this stage, the working assumption was that the primary motion of the SMA was dilation. For this reason, FSI modelling was considered the likely choice, and avoidance of spurious reflection of the pressure wave at the (arbitrary) boundary of the 3d and 1d domains was a key concern. As the project moved on, the FSI was abandoned; however, understanding of wave propagation and reflection is crucial to the understanding of boundary condition design and implementation. Note that although wave-reflections do occur in the cardiovascular system, these are a distributed range of reflections; before modelling this downstream complexity it is

important to show that it is possible to transmit the entire pressure wave to the downstream model.

When any transient pressure is applied at one end of a fluid domain, a pressure wave travels through that domain, when this pressure wave reaches the boundary of the domain it is reflected, absorbed, or partially reflected and partially absorbed. Reflection can take two forms, positive or negative; total positive reflection occurs when no flow is allowed to pass through the boundary (boundary condition of u = v = w = 0) and results in a pressure wave of the same sign as the incident pressure wave travelling back through the domain, total negative reflection occurs when the pressure wave has no effect on pressure at the outlet (boundary condition of P=0), the wave is once more fully reflected but this time the reflected wave has opposite sign to the incident wave. In general, positive reflection occurs if the impedance of the boundary condition is too high, negative if it is too low.

In order to minimise pressure reflection at a downstream boundary, any pressure wave must be transmitted with little or no reflection; to achieve this, the boundary condition must be impedance-matched to the 3d model section.

It is intuitive that if the tube at the outlet were extended into infinity with no change in material properties or geometry then no pressure reflection would occur; such a condition is described by the Womersley equations, therefore, coupling these to the model outlet should result in an impedance-matched boundary condition.

5.4.1 – Impedance of the Womersley equations

One way of considering the Womersley equations is as three pairs of impedances relating pressure, pressure gradient and flow. These relationships are given in 5.1, 5.2 and 5.3

$$Z_L = \left(\frac{dP/dz}{Q} \right) = \frac{j\mu\alpha^2 e^{-j\varepsilon_{10}^{'}}}{\pi R^4 M_{10}^{'}} \qquad 5.1$$

$$Z_P = \frac{P}{dP/dz} = \frac{c}{j\omega} \qquad 5.2$$

$$Z_0 = \frac{P}{Q} = Z_L \cdot Z_P = \frac{\mu\alpha^2 e^{-j\varepsilon_{10}^{'}} c}{\pi R^4 M_{10}^{'} \omega} \qquad 5.3$$

Where all symbols represent values as laid out in chapter 2.

While non-linear (due to the complex wave-speed), these impedances can all be represented by a one to one relationship in the frequency domain; i.e. a sine wave input gives a sine wave output of different phase and magnitude. This phase shift and attenuation vary with frequency alone, hence gain and phase can be plotted as functions of frequency. If frequency is plotted on a log scale, gain in decibels and phase in degrees then the resulting pair of plots is called a Bode diagram. Figures 5.5 to 5.7 show the gain and phase response of the $1/Z_L$, Z_P and Z_0 respectively for a representative geometry; in each case altering the vessel properties will alter the position of the graphs along the x-axis (and the y-axis for magnitude), but the general shapes and hi/low frequency phase asymptotes will be unchanged.

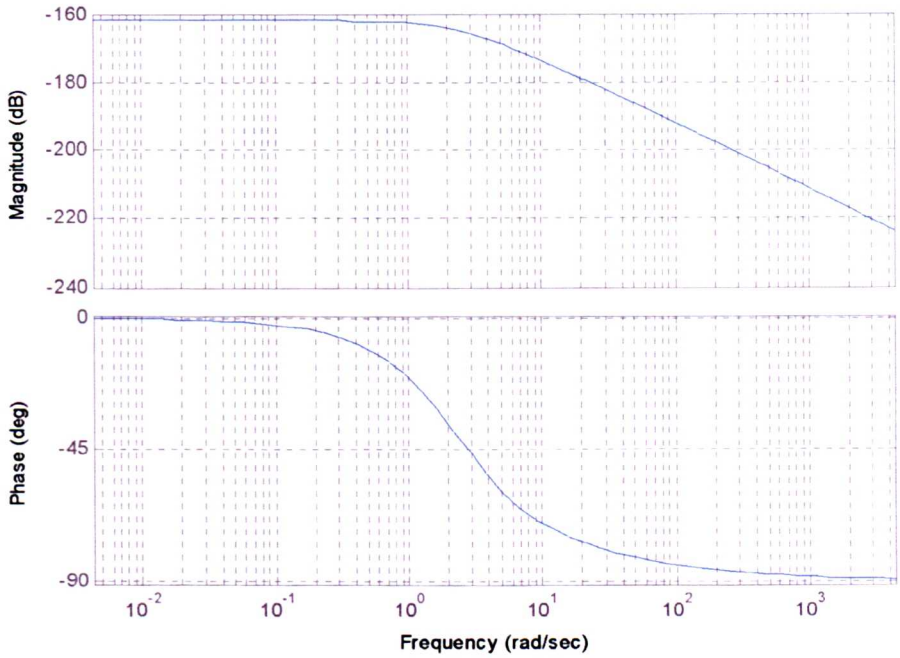

Figure 5.5. Bode plot for $1/Z_L$ (Q/(dP/dz)).

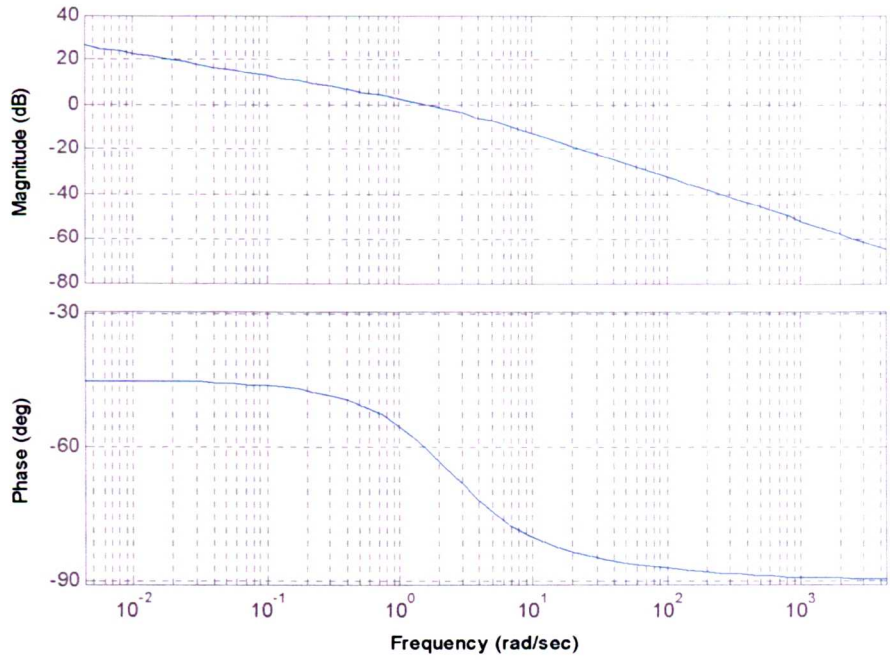

Figure 5.6. Bode plot for $Z_P(P/(dP/dz))$.

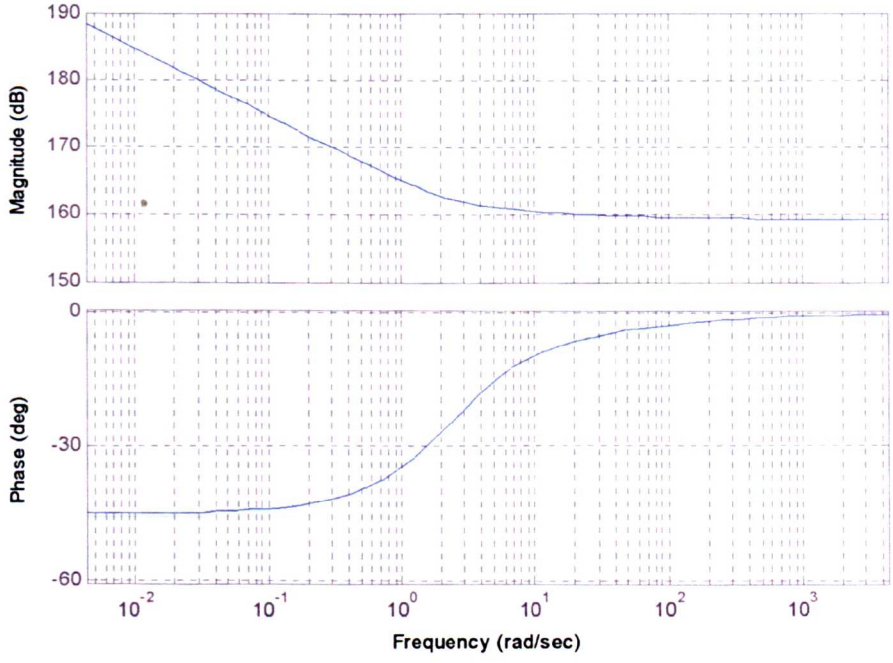

Figure 5.7. Bode plot for Z_0 (P/Q).

Z_0 is the most important of the relationships for our purposes, as it relates the two quantities we can most easily deal with in boundary condition implementation; pressure and flow.

An interesting feature of figure 5.5 is the 45° lag at low frequency (associated with complex wave speed), a feature not seen in any linear system (linear systems always asymptote to a multiple of 90° of lag). This reason alone is enough to mean that a linear model cannot faithfully represent the Womersley equations over the entire frequency range.

For any given frequency of input, we have a known relationship between pressure and flow, with pressure lagging behind flow. There are two options for the using this information as a boundary condition; find volume flow through the boundary and use this along with our knowledge of Z_0 to calculate pressure at the boundary, or work the other way round using pressure and $1/Z_0$ to calculate flow through the boundary.

The former approach has clear benefits; pressure lags flow so any downstream model will be deterministic, pressure can be simply applied as a given value everywhere across the boundary (in contrast to flow having to be applied as a spatially varying velocity profile). Building the model this way round also means that model can be easily understood using the electrical analogies of resistance and impedance.

5.4.2 – Lumped Parameter Models for the Womersley Equations

Due to the presence of Bessel functions in the equations and the fact that they are defined in frequency space, the Womersley equations are not appropriate to be directly applied as a boundary condition in a CFD package where only simple calculations can be performed easily. A simple system, which captures the key properties of the Womersley equations over a frequency range of interest, is necessary. For easy implementation, this system should be defined in discrete time.

Three frequencies were chosen representing the widest range of frequencies one might wish to model. The low frequency of 0.1 rad s^{-1} corresponds to about 1 cycle per minute and represents the lower end of respiratory frequencies (which may be included in future work). The middle frequency of 7.54 rad s^{-1} corresponds to 72bpm, the standard value for human resting heart rate. The high frequency of 100 rad s^{-1} lies just above the tenth harmonic in the abdominal aortic flow spectrum, which as discussed in 2.2.1 is the highest frequency needed to accurately reproduce the flow waveform. Figure 5.8 shows the bode diagram for an aorta of typical properties, overlaid with respiratory and cardiac frequency ranges and the three chosen frequencies of interest. Key parameters relating to the system are shown in table 5.1.

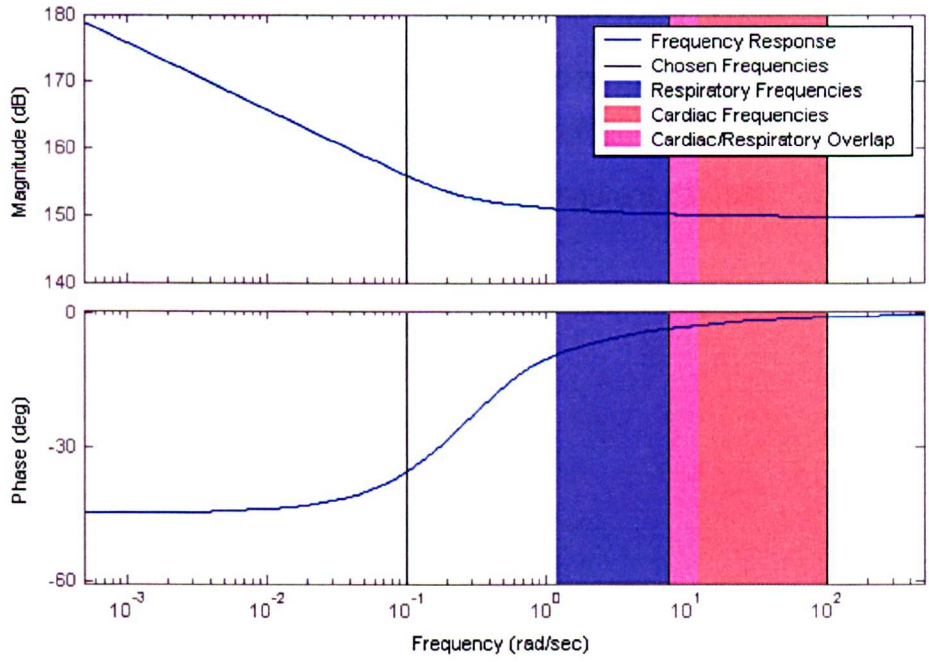

Figure 5.8. Bode diagram showing respiratory and cardiac frequencies, and frequencies chosen for this chapter.

Frequency (rad s^{-1})	**Phase lag**	**Gain ($m^3s^{-1}Pa^{-1}$)**	**Alpha**	**Wave speed (m/s)**	**Wave length/ tube length**	**Attenuation per tube length**
0.1	35.7°	6.92e7	1.42	5.18	1628	0.277%
7.54	3.47°	3.58e7	12.4	8.14	33.9	1.11%
100	0.915°	3.44e7	45.0	8.47	2.66	3.70%

Table 5.1. Frequencies of interest and associated parameters.

5.4.2.1 – Types of Windkessel Model

In this chapter, the performance of several Windkessel models will be compared at the different frequencies. In this context, Windkessel is taken to mean a low order lumped parameter system relating pressure and flow at the outlet boundary. Consider a series of electrical circuits as follows:

- A pure resistance
- An RC series circuit (figure 5.9)

- An RC parallel circuit (figure 5.10).
- A 'standard' three element Windkessel (figure 5.11) [91].
- A Piene four element Windkessel, claimed by the authors to model accurately the resistance of the pulmonary circulation (figure 5.12) [156].
- A Stergiopulos four element Windkessel (figure 5.13) [96].

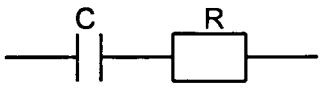

Figure 5.9. RC series circuit diagram.

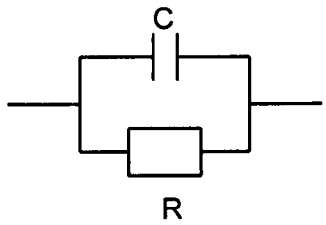

Figure 5.10. RC parallel circuit diagram.

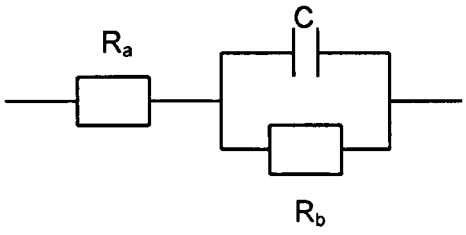

Figure 5.11. 3-element Windkessel circuit diagram.

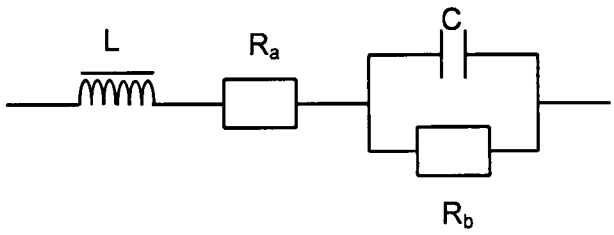

Figure 5.12. 4-element Piene Windkessel circuit diagram.

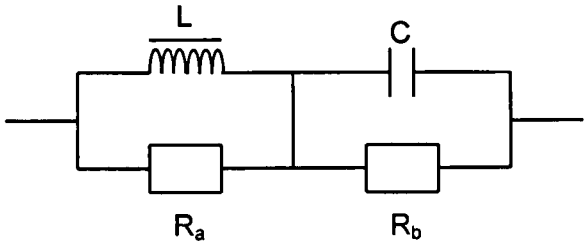

Figure 5.13. Circuit diagram for 4-element Stergiopulos Windkessel.

Each of these circuits can be considered as a Windkessel with pressure analogous to voltage and flow analogous to current. As discussed in 5.4.1, flow is the input to the boundary condition and pressure the output fed back to the CFD model.

The transfer functions for the circuits (variation of impedance with complex frequency) are as follows:

Pure resistance – $\frac{V_{(s)}}{I_{(s)}} = R$ 5.4

RC series – $\frac{V_{(s)}}{I_{(s)}} = \frac{Rs + 1/C}{s}$ 5.5

RC parallel – $\frac{V_{(s)}}{I_{(s)}} = \frac{R}{CRs+1}$ 5.6

3-element Windkessel – $\frac{V_{(s)}}{I_{(s)}} = \frac{R_a R_b Cs + R_a + R_b}{CR_b s + 1}$ 5.7

Piene 4-element Windkessel – $\frac{V_{(s)}}{I_{(s)}} = \frac{CLR_b s^2 + (CR_a R_b + L)s + (R_a + R_b)}{CR_b s + 1}$ 5.8

Stergiopulos 4-element Windkessel – $\frac{V_{(s)}}{I_{(s)}} = \frac{(1 + R_a C)s + \left(\frac{R_a}{R_b} + \frac{R_a}{L}\right)}{Cs^2 + \left(\frac{R_a C}{L} + \frac{1}{R_b}\right)s + \frac{R_a}{LR_b}}$ 5.9

The component values in each of the Windkessels can be changed to alter the shape of the bode diagram. Figure 5.14 shows example bode diagrams for the six Windkessels above; in this figure the key point is not the exact values on the frequency and magnitude axes (these can be tuned by parameter selection), but the general shapes of the frequency responses.

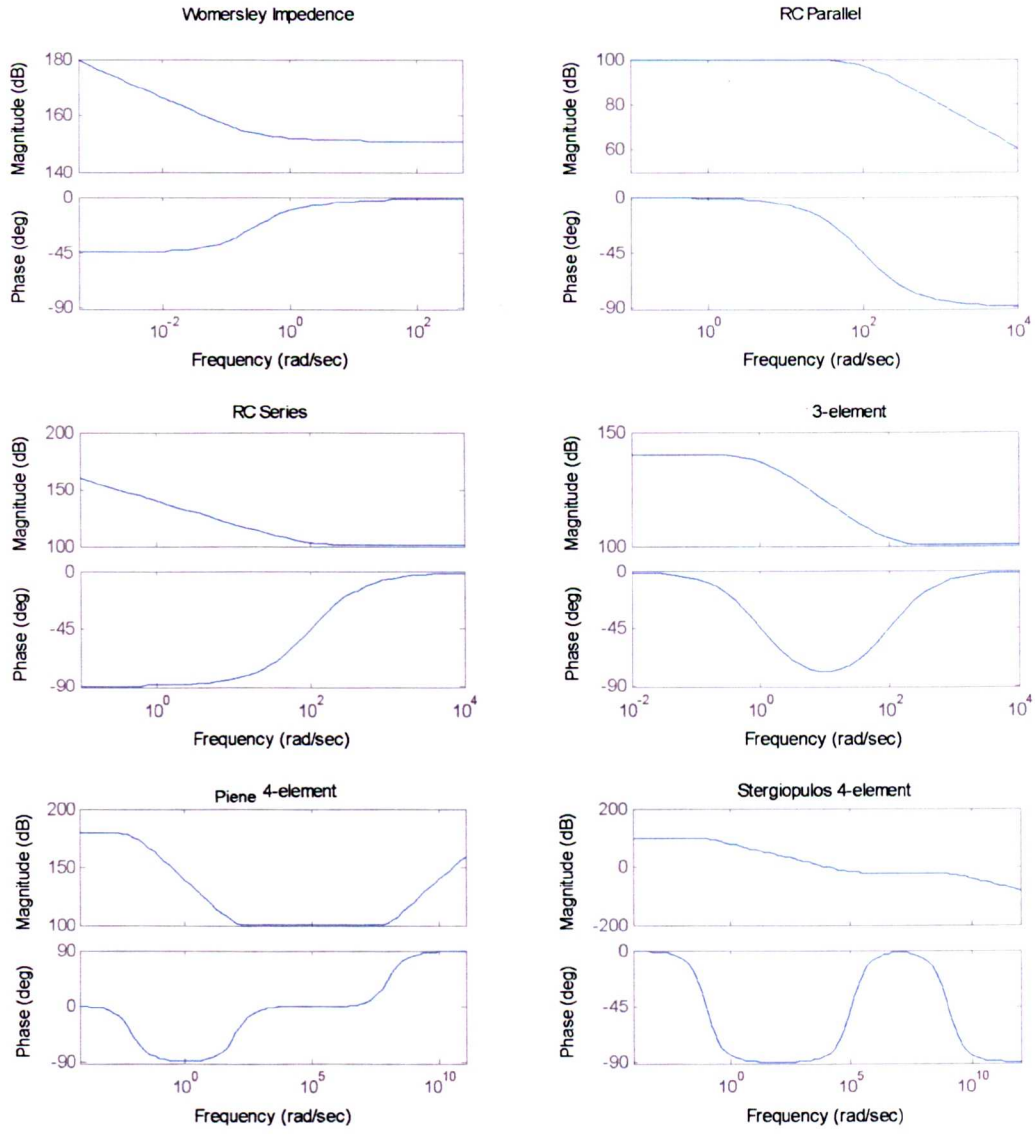

Figure 5.14. Bode diagrams of windkessels.

From Figure 5.14, one can immediately discard the RC parallel and Piene 4 element Windkessels. The RC parallel circuit does not have a phase response even qualitatively similar to that of the Womersley equations, gain is constant at low frequencies, rather than high, and the phase response is also inverted in terms of frequency. The Piene 4 element model exhibits phase lead (pressure leads flow) and increasing resistance at high frequency; phase lead is non-deterministic, hence the model cannot be realised in digital form; similarly to the RC Parallel, it is also not representative of the response of the Womersley equations, for completeness the RC parallel circuit will be included for the following work, the Piene 4 element will however be discarded.

An alternative representation of the above models is the state-space representation; the general form of such a model for a single input, single output (SISO) system is shown in 5.10

$$\dot{x}(t) = Ax(t) + Bu(t)$$
$$y(t) = Cx(t) + Du(t) \qquad 5.10$$

Where, for a system with n states; x(t) is a vector of 'state' values varying in time, $\dot{x}(t)$ is the time derivative of x, u(t) is the input, and y(t) is the output. A is the (n by n) state matrix, B the (n by 1) input vector, C the (1 by n) output vector, and D the scalar direct transmission coefficient. The number of states, n, will be determined by the number of energy storing elements in a system; in the case of a simple electrical circuit, such as a Windkessel model, this is combined number of capacitors and inductors, the vector of values of the state variables at any point in time completely describes the state of the system. Choosing the states as voltage across each capacitor and current through each inductor allows us to complete table 5.2 containing A, B, C and D matrices for each windkessel. Representing the models in this form aids the move towards the discrete domain.

Model	A	B	C	D
Pure R	0	0	0	R
Series RC	0	1/C	1	R
Parallel RC	-1/CR	1/C	1	0
3-element Windkessel	$-1/CR_b$	1/C	1	R_a
Stergiopulos 4-element windkessel	$\begin{bmatrix} -1/R_bC & 0 \\ 0 & -R_a/L \end{bmatrix}$	$\begin{bmatrix} 1/C \\ R_a/L \end{bmatrix}$	$\begin{bmatrix} 1 & -R_a \end{bmatrix}$	R_a

Table 5.2. Table of state-space models of various Windkessels.

5.4.2.2 – Digital Implementation of Frequency-domain Boundary Conditions

The transfer functions and state-space models shown above are all described in continuous time (in the Laplace domain), but they are to be applied to a CFD code solving at discrete time-steps. For this reason, the models must be transformed into a suitable form to be used in discrete time; an appropriate form is the discrete state-space form. A range of approximations are available to perform this transformation; the two most common are assuming zero order hold (ZOH) between discrete time-steps (the input to the model is assumed to remain constant through the time-step), and assuming first order hold (FOH) between discrete time-steps (the input to the model is assumed to change linearly, based on the gradient calculated at the start of the time-step, through the time-step).

Any state space model can be written in the discrete domain as shown in 5.11 [157].

$$\begin{aligned} x(k+1) &= Fx(k) + Gu(k) \\ y(k) &= Hx(k) + Ju(k) \end{aligned} \qquad 5.11$$

Where F, G, H and J are analogous to A, B, C and D respectively, k is the timestep number. The state at each timestep is a function of state and inputs at the previous timestep; output at each timestep is a function of state and input at that timestep. Note that, once the matrices are found, the output and next state are simple to calculate weighted sums of the present input and state. The relationships between A, B, C and D, and F, G, H and J are determined by the assumption made in the discretisation, i.e. ZOH or FOH [158].

For the ZOH case, the definitions of F, G, H and K are given in 5.12 to 5.15; T represents the discretisation timestep that is set equal to CFD timestep.

$$F = \exp(AT) \qquad 5.12$$

$$G = \left(\frac{\exp(AT)-1}{A}\right)B \qquad 5.13$$

$$H = C \qquad 5.14$$

$$J = D \qquad 5.15$$

For the FOH case, the definitions of F, G, H and K are given in 5.16 to 5.19.

$$F = \exp(AT) \qquad 5.16$$

$$G = \frac{1}{T}\left(\frac{\exp(AT)-1}{A}\right)^2 B \qquad 5.17$$

$$H = C \tag{5.18}$$

$$J = D + C\frac{A^{-2}}{T}(\exp(AT) - 1 - AT)B \tag{5.19}$$

Note that the first order hold assumption means that J is non-zero even for D=0, this means that $P(t_n)$ is a function of $Q(t_n)$ (among other things) and therefore the boundary condition must be iterated at each timestep.

In contrast, adopting a zero-order hold technique means that J is non-zero only for non-zero D.

Figures 5.15 and 5.16 show the same Kerner 3-element windkessel discretised using FOH and ZOH techniques at high and low sampling rates respectively.

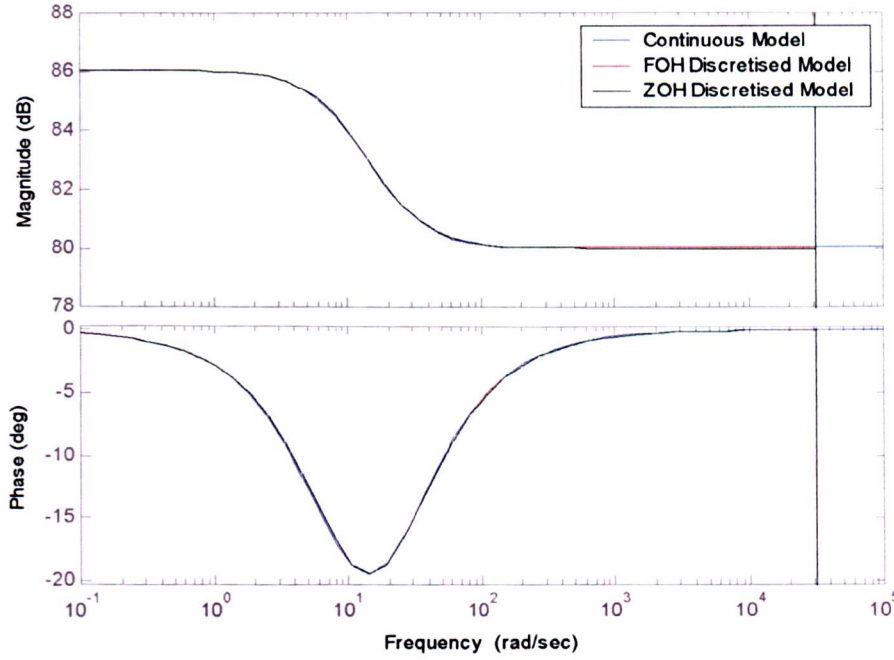

Figure 5.15. Bode diagram of analogue Windkessel model and FOH and ZOH digital implementations, T=0.0001s (vertical black line shows sampling frequency).

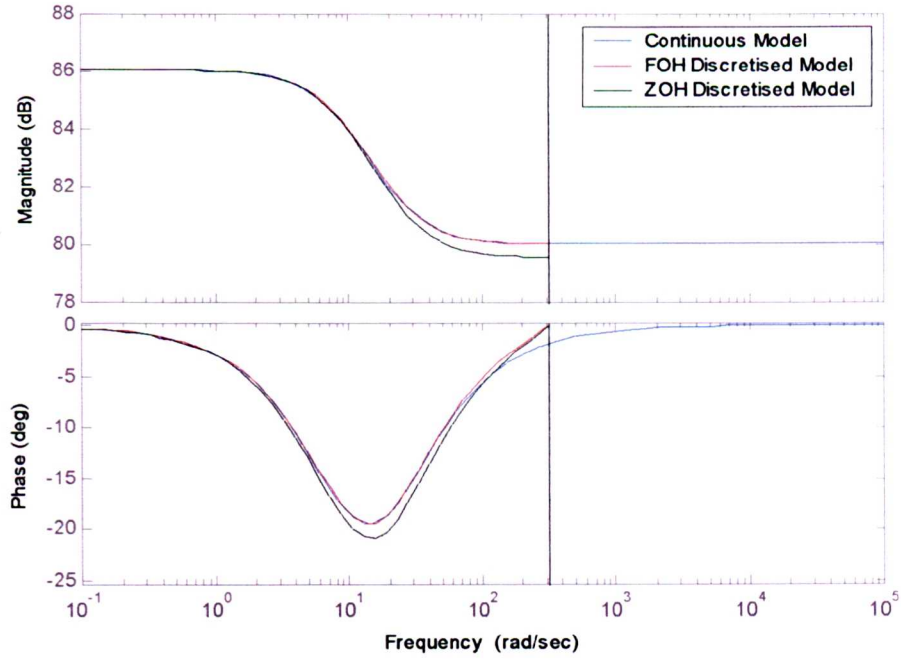

Figure 5.16. Bode diagram of analogue Windkessel model and FOH and ZOH digital implementations, T = 0.01s (vertical black line shows sampling frequency).

From the above, it is clear that if the sampling period is suitably small there is no significant difference between the ZOH and FOH implementations. ZOH is simpler and does not lead to the problems with J becoming non-zero that occur with FOH; for these reasons ZOH is to be used for discretisation throughout this section.

The ZOH-discretised state-space matrices for the five windkessels are given in table 5.3.

MISSING PAGE/PAGES HAVE NO CONTENT

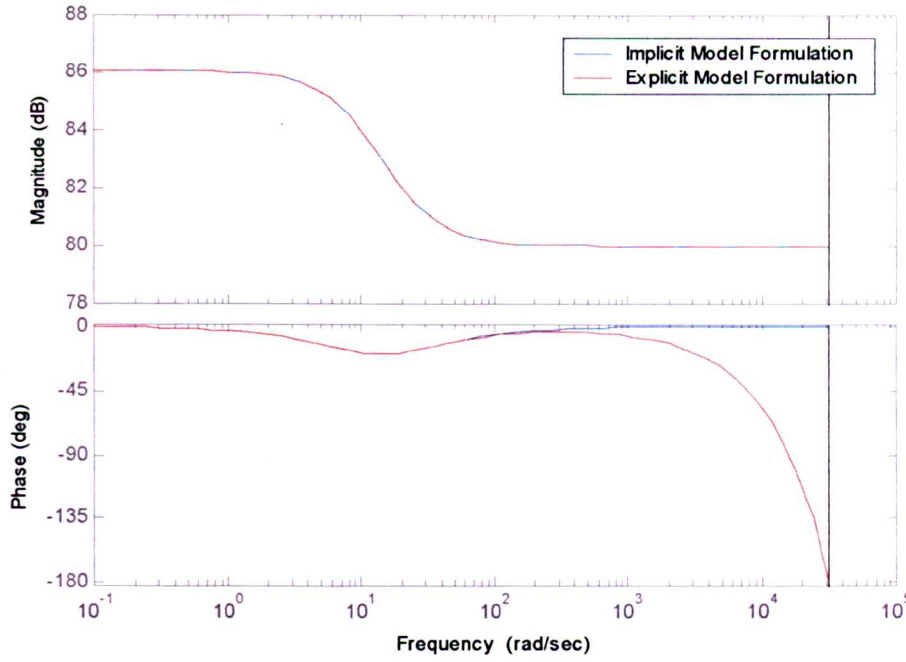

Figure 5.17. Bode diagram of implicit and explicit digital implementations, T= 0.0001s (vertical black line shows sampling frequency).

The implicit and explicit formulations give the same results for magnitude for all frequencies, and for phase for low frequencies; at high frequencies the delay inherent in the explicit formulation causes phase error in the explicit formulation. In this case, as in the choice between ZOH and FOH discretisation, there is a trade-off between extra computational time needed at each timestep for an iterating boundary condition, and increased number of timesteps necessary in the non-iterating case. In CFD analyses, small timesteps are often needed for convergence; if this time-step is small enough that non-iterating boundary conditions perform well, the benefit of an iterating boundary condition disappears. The relative performance of explicit and implicit implementation of boundary conditions will be one of the results considered in the following sections.

5.4.3 – Matching impedance at a single frequency

For these analyses, a 0.2 metre length of tube, 9mm in radius filled with a fluid of density 1000 Kg/m^3 and viscosity 0.004 Pa.s was modelled. For the FSI, a wall-thickness of 1mm, wall density of 1200 Kg/m^3, wall stiffness of 1MPa, and wall Poisson's ratio of 0.4999 were used; this gave effective wave-speeds of 5.18m/s, 8.14m/s and 8.47m/s for 0.1Rad s^{-1}, 7.54 Rad s^{-1} and 100 Rad s^{-1} respectively. The

aim of this section is to produce and compare impedance-matched boundary conditions of varying complexity at the three different frequencies of interest. In each case, the tube was modelled as a 2d axisymmetric model with 20 elements radially (weighted to be five times larger at the tube centre than at the wall) and 200 equal length elements axially.

Before CFD work began for this section, it was checked that, given inlet and outlet pressure boundary conditions and no information about flow profile, Flotran would reproduce the correct Womersley flow profiles at the Womersley numbers, flow rate and mesh density of interest. This test was successful; for a sinusoidal pressure gradient (matching what would be expected in an infinite-length elastic tube of the chosen properties), profiles at each node matched the Womersley profile to within 5% (Womersley number 1.42, 12.4 or 45; 20 nodes across radius). Figure 5.18 shows an example plot of Womersley and Flotran flow-profiles varying with a sinusoidal pressure gradient. As the two surfaces are very similar in shape, figure 5.19 shows the percentage difference between the two flow profiles, normalised against maximum velocity anywhere in either profile, in this case the maximum value anywhere is the domain was 1.6%.

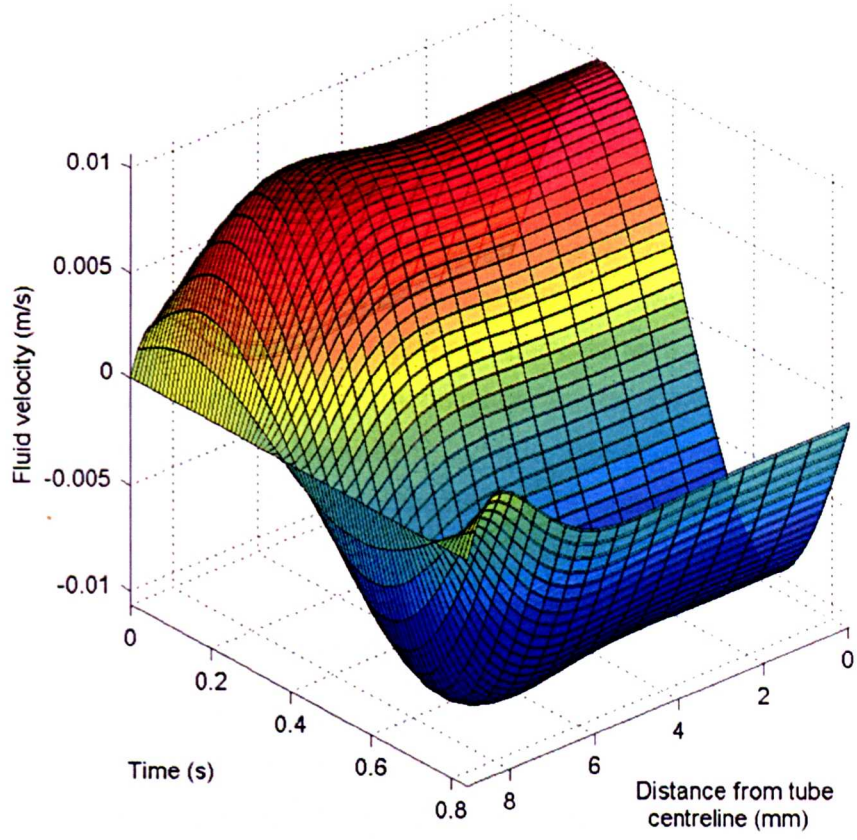

Figure 5.18. Womersley and developed Flotran CFD profiles at 7.54 rad s^{-1} (pressure gradient is 14.8 Pa over 0.2m, equivalent to 10mm Hg pressure in an infinite elastic tube of properties similar to the abdominal aorta).

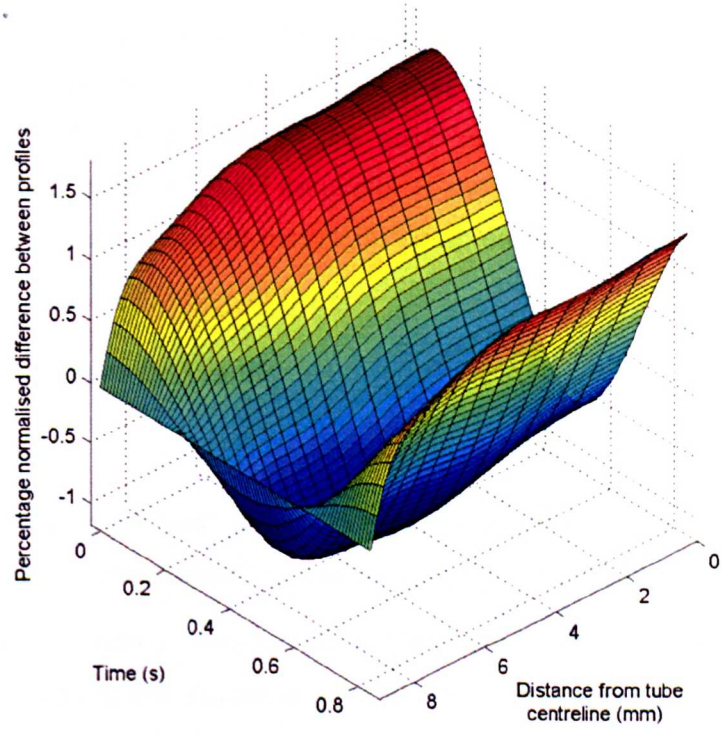

Figure 5.19. Percentage normalised difference between the Womersley and Flotran profiles.

5.4.3.1 - Compressibility as an analogue for FSI

One limitation of FSI analyses is the large computational expense. In the development stage, using compressibility as an analogue for FSI can reduce this. According to Womersley, for a given geometry, wave speed varies with frequency, but at each frequency wave speed is constant. Single wavespeed problems can be approximated using compressible fluid-only analyses with fluid density given as a function of pressure, through a bulk modulus parameter, $\beta_P = dP/d\rho$. The wavespeed due to this compressibility is given by $C_{comp}=\sqrt{\beta_P}$. The compressible wavespeed can thus be set equal to the wavespeed expected for the compliant tube.

5.4.3.2 – Compressibility to aid stability of FSI

Convergence of weakly coupled FSI models can be very difficult to achieve, especially in the case of pressure wave propagation where the wavelength is similar to, or smaller than, the domain length. Fluid compressibility can be used to increase the numerical stability of such FSI analyses.

If the fluid is treated as incompressible, the wavespeed in the domain is infinite and the pressure gradient across the domain in the first iteration will be constant. This will imply a conical shape of the vessel at the first solid solve. This is a good approximation when the length of the domain is a small proportion of the wavelength, but poor if the converse is true. In the latter case the introduction of a compressibility term, which is sufficient to prevent the solid 'overshoot' but not so great that it influences the final solution, might be useful. It should be noted that in practice there will always be some uncontrolled numerical 'compressibility ' in the solution

5.4.4 – Single Frequency Results

5.4.4.1 – Fluid-only

For each frequency of interest, simulations were undertaken for a variety of boundary conditions using the compressibility analogue for FSI described above.

The most basic boundary condition available is a simple, zero pressure, boundary condition. Considering the Womersley equations, this is clearly inappropriate; if an inlet pressure sinusoid of 10mm Hg is applied, the pressure will all be lost over the

length of the tube, thus the pressure gradient will be much higher than that of the Womersley equations which are being modelled. Traditionally, the approach would be to alter the magnitude of the inlet sinusoid to yield the appropriate pressure gradient and add the (arbitrary) steady pressure back in at the post-processing stage. This approach is limited in a number of ways:

- One must be able to calculate the appropriate pressure gradient from the pressure inlet; this is reasonably straightforward for a straight tube coupled to the Womersley equations, but in other cases can become very difficult.
- For FSI analyses, the steady pressure term is important for the structural part of the analysis.

For these reasons it was deemed important to keep the inlet pressure waveform in it's full form, and rely on the downstream model to impose the correct pressure gradient.

Analyses were first carried out using pure resistance boundary conditions. In each case, the resistance was selected to match the magnitude of the frequency response at the inlet frequency. Due to the pure nature of the resistance, pressure and flow were always in phase at the outlet (sampling rate issues aside).

For the implicit formulations, convergence of outlet flow was checked using the algorithm outlined below.

```
norm_fact = max(1e-15,abs(inflow_new),abs(outflow_new))

flow_change = abs((outflow_old - outflow_new)/norm_fact)

outflow = (outflow_new*bc_urf)+(outflow_old*(1-bc_urf))

converged = 0
*if,bc_conv_crit,gt,flow_change,then
            bc_conv_flag = 1
*endif
```

Where the relaxation factor (`bc_urf`) was 0.3 and the convergence criterion (`bc_conv_crit`) was 1e-2, the algorithm was allowed to run for a maximum of 100 iterations before a flag was sent to indicate non-convergence of the boundary condition. The minimum value of 10^{-15} for the normalisation factor was to prevent instability at zero inlet and outlet flow

Figure 5.20 shows the frequency response of the pure resistance boundary conditions chosen alongside the frequency response of the tube modelled by Womersley.

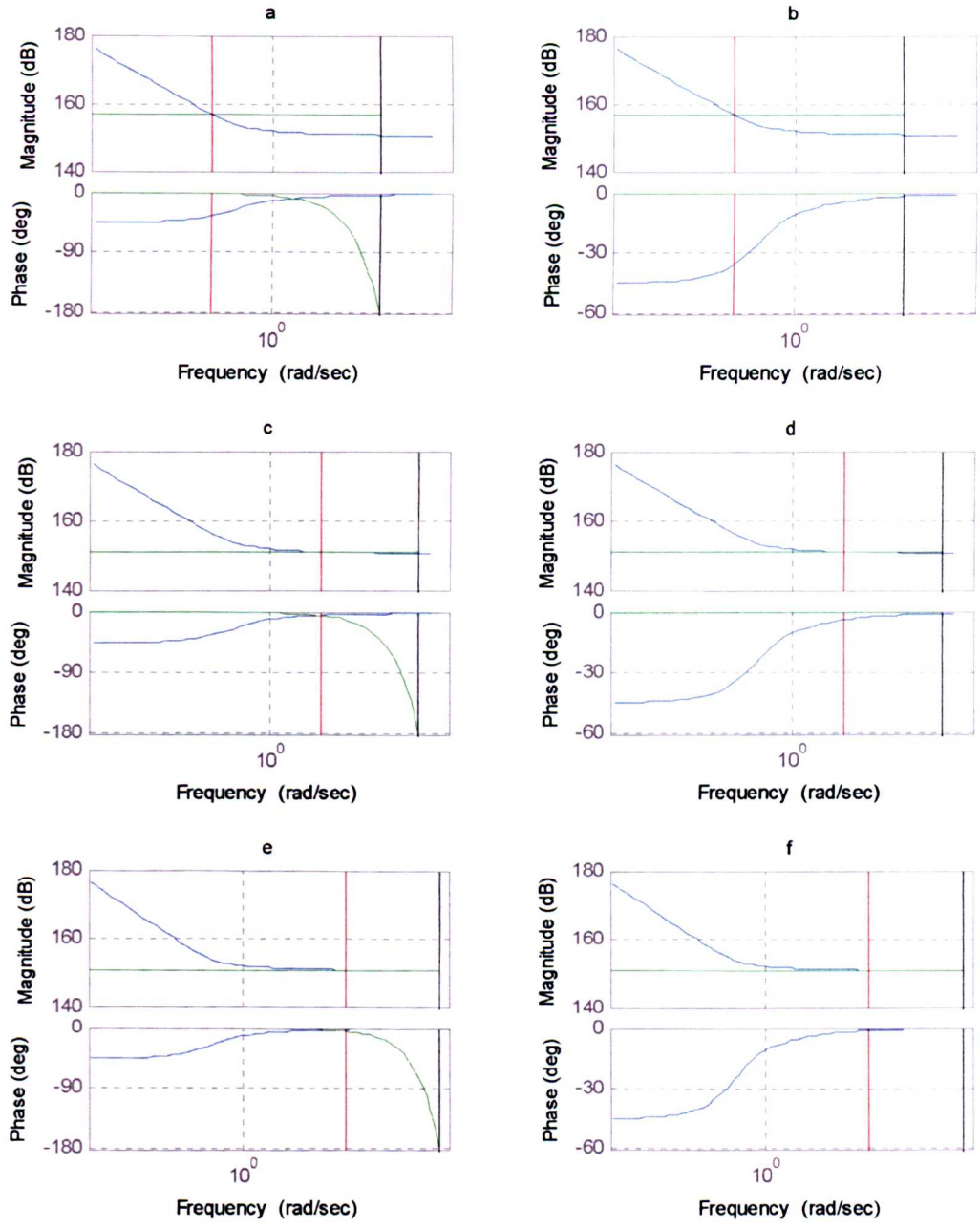

Figure 5.20. Frequency response of Womersley equations (blue) and pure resistance boundary conditions (green); (a) Low frequency explicit (timestep = 0.1s), (b) Low frequency implicit (timestep = 0.1s), (c) Medium frequency explicit (timestep = 0.02s), (d) Medium frequency implicit (timestep = 0.02s), (e) High frequency explicit (timestep = 0.001s), (f) High frequency implicit (timestep = 0.001s). Red line is frequency of pressure wave, black line is time-step frequency.

Each analysis was compared to the Womersley solution for that flow and the boundary condition's performance characterized by a number of indices:

- Attenuation Index (AI) – Peak outlet pressure predicted by Womersley divided by peak CFD outlet pressure.
- Wavespeed Index (WI) – Womersley predicted wavespeed divided by CFD wavespeed.
- Phase Error Index – Womersley predicted phase lag (of pressure after flow) at outlet minus outlet phase lag in CFD model.

All analyses were run until outlet flow history agreement to within 5% between two consecutive cycles was obtained, this took between 2 and 5 cycles. Timestep was initially 50ms for the low frequency analyses, 10ms for the medium frequency, and 0.5ms for the high frequency; in some cases these values were changed to aid stability. Results are shown in table 5.4, error values shown are those in measuring peak times (used to calculate wavespeed and phase) due to discrete timesteps.

Frequency	Implementation	AI	WI	Phase error (°)
Low	Explicit	Convergence not achieved		
Low	Implicit	1.00	1.28±1.28	35.4±0.3
Medium	Explicit	1.01	0.819±0.407	3.47±4.32
Medium	Implicit	1.02	1.22±0.407	-0.89±4.32
High	Explicit	1.01	1.02±0.021	-1.95±2.865
High	Implicit	0.99	1.02±0.021	-1.95±2.865

Table 5.4. Results for pure resistance boundary conditions – fluid only analyses.

Table 5.4 shows that the pure resistance boundary conditions worked well for the medium and high frequency inputs. Error bars in both wavespeed index and phase error are due to both calculations using the peak of the sinusoid as the basis for phase measurement; for simplicity, it is assumed that the true peak could lie at any point within one time-step either side of the observed peak.

In each case, the wave speed and phase were correct within the error bounds, note that in both cases the error bars for phase lag are larger than the phase lag itself, so

the effect of the pure resistance holding pressure and flow in phase at the outlet is not seen. The attenuation was always within 2% of that predicted by Womersley.

For the low frequency, propagation of the pressure wave through the 0.2m computational domain took only 39ms; in contrast to this, the period of the sinusoidal input was 63 seconds. These widely varying timescales made accurate modelling difficult and computationally expensive. To resolve the pressure pulse's travel along the tube at, for example, five points, while modelling a whole repetition of the input sinusoid would take around 8000 timesteps. In order to keep modelling time reasonable (especially considering the desire to extend the analysis to the FSI case), the timestep for the implicit analysis was set to 50ms, this lead to a very wide error bar for wavespeed index, but allowed the attenuation index and phase error to be checked. As with the medium and high frequency analyses, attenuation index was close to one showing a good match with the Womersley equations.

In the low frequency implicit analysis, once more pressure and flow were held in phase at the outlet, this time the Womersley predicted phase was much greater than the error bar width, so a substantial phase error was seen.

For the low frequency explicit analysis the system became unstable with oscillation in the boundary condition making the CFD solver unable to converge after 0.2s (simulation time); shorter timesteps of 25ms and 10ms (resulting in 6300 timesteps per cycle) were tried but also diverged (at 0.175s and 0.13s solution time respectively). Further analyses with even shorter timesteps were decided against, the time cost associated with decreasing the time step so drastically would outweigh any advantage over the implicit method gained by only having to run each timestep once.

To improve on these results, three-element windkessel models were designed to match gain and phase for each frequency of interest. The three-element model was chosen as it is a fairly simple and widely used model, there was no difficulty associated with choosing parameters to match gain and phase at a given frequency, and the model behaved sensibly over the whole frequency range (ensuring that start-up transients would be dealt with sensibly), results are shown in table 5.5.

Frequency	Implementation	AI	WI	Phase error (°)
Low	Explicit	Convergence not achieved		
Low	Implicit	1.00	1.30±1.30	0±0.3
Medium	Explicit	1.00	0.977±0.081	-0.849±0.864
Medium	Implicit	1.00	1.22±0.407	-0.849±4.32
High	Explicit	1.00	1.01±0.011	2.42±1.432
High	Implicit	0.99	1.02±0.021	-1.95±2.865

Table 5.5. Results for 3-element windkessel boundary conditions – fluid-only analyses.

Once more the explicit implementation failed to converge at low frequency. As with the pure resistance model, smaller timesteps did not aid convergence. The three-element Windkessel performed well for the low frequency implicit analysis though, perfectly matching the Womersley phase lag at the outlet.

Both explicit and implicit formulations worked well for the medium and high frequency analyses, although a five-fold reduction in timestep (to 20ms) was needed to ensure stability of the medium frequency explicit boundary condition.

5.4.4.2 – FSI

The compressible analyses were repeated using the internal weak FSI coupling in Ansys; results are shown in tables 5.6 and 5.7.

Frequency	Implementation	AI	WI	Phase error (°)
Low	Explicit	Convergence not achieved		
Low	Implicit	Not run – time considerations		
Medium	Explicit	1.02	1.018±0.204	5.63±2.16
Medium	Implicit	1.02	1.05±0.204	-3.01±2.16
High	Explicit	1.03	1*	-0.518±1.432
High	Implicit	Not run – time considerations		

Table 5.6. Results for pure resistance boundary conditions – FSI analyses.
* – calculated indirectly, see below.

Frequency	Implementation	AI	WI	Phase error (°)
Low	Explicit	Convergence not achieved		
Low	Implicit	Not run – time considerations		
Medium	Explicit	1.01	0.814±0.204	3.47±2.16
Medium	Implicit	1.02	1.05±0.204	-3.01±2.16
High	Explicit	1.01	1*	1.95±1.432
High	Implicit	Not run – time considerations		

Table 5.7. Results for 3-element windkessel boundary conditions – FSI analyses.
* – calculated indirectly, see below.

The increased computation time for an implicit analysis was greatly exaggerated for FSI models implemented in Ansys 8.1, this was because the software did not support restarts from previous time-steps for FSI, while it did for fluid-only analyses. For this reason, back-up copies of the data-base and results file had to be made before each solve, and loaded back into memory if the boundary condition was not converged.

As before, it was impossible to achieve convergence for the explicit implementation of the low frequency case. Initial low frequency implicit runs suggested that a time-step of as little as 25ms would be necessary to allow convergence of the FSI and the boundary condition; this combined with the file management difficulties described above meant that (based on linear interpolation from the time taken to run the first

few timesteps) the estimated time taken to run the low frequency implicit analysis was 494 days, for this reason, this analysis was abandoned.

For the medium frequency case, all four boundary conditions worked well in terms of attenuation index and wavespeed index. For the pure resistances, the phase errors were as expected with phase itself within error bar limits of zero lag. For the Windkessel models, where the phase should match Womersley phase the results were marginally in error, having one timestep too little lag in the explicit case, and one timestep too much in the implicit case.

For the high frequency case, where the wavelength was close to the tube length, stability of the FSI algorithm was very hard to achieve. For this reason, compressibility was introduced; this slowed the wavespeed, but also allowed convergence to be reached.

For analyses with compressibility as well as FSI, the Womersley equations could not be used directly to choose suitable boundary condition parameters; instead, an analysis was run with a 0Pa outlet boundary condition to find the combined wavespeed, and the boundary condition calculated from the Womersley equations with the wall stiffness altered to yield the appropriate wavespeed.

For these analyses, the attenuation index and phase error were calculated based on the attenuation and outlet phase lag for the Womersley equations for the equivalent incompressible case. The wavespeed index was 1 by definition, as the Ansys wavespeed was used to calculate the wall stiffness to base the boundary condition on.

For the high-frequency case, the repeated restarts, described previously, would have meant an estimated run time of 68 days for the implicit analysis – based on the run-time of the explicit high-frequency analysis and an average of five timesteps per cycle (the mean number of iterations necessary for the convergence of the medium-frequency pure resistance analysis) – for this reason implicit FSI analysis of the high frequency model was abandoned.

5.4.5 – Matching impedance over a range of frequencies

The analyses in 5.4.4 only considered single frequencies, whereas most realistic problems involve multiple frequencies. Two inputs with multiple frequency components were chosen to replicate certain characteristics of the pulse propagation and impedance matching; the first input is a high frequency cosinusoidal pressure

pulse followed by a period of zero pressure, the second is the flow waveform in the abdominal aorta presented in 2.2.1. By matching the frequency response of the boundary condition to that of the Womersley equations over the frequency range of the waveform, a reflection-free boundary condition is designed. Once more, the aim is to create a reflection-free boundary condition at the reasonable computational cost.

It has been shown in 5.4.4 that, for single frequencies, explicit boundary conditions can offer good results at lower computational cost than implicit boundary conditions; hence, they are the first choice for consideration in this section.

5.4.6 – High Speed Pulse

The high frequency pulse consisted of a cosinusoidal pulse peaking at 1333.2Pa (10mm Hg) lasting 6ms, followed by 44ms at 0Pa; the waveform is shown in figure 5.21. The sampling interval for the signal was 0.25ms, so as to not loose information from the signal, 0.25ms was the longest timestep considered.

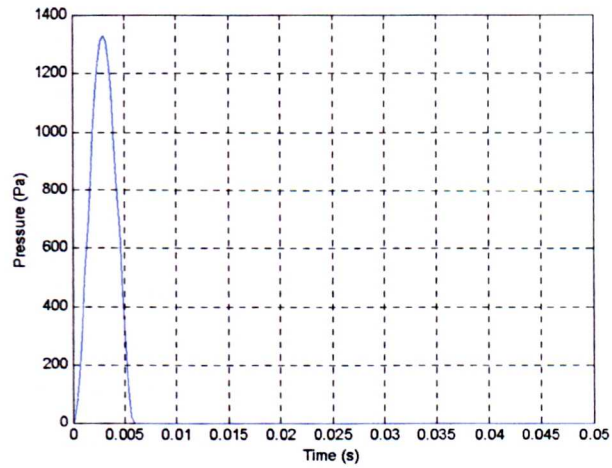

Figure 5.21. High frequency pressure pulse waveform.

For this waveform, a complete wave is contained within the tube; hence, wave propagation and reflection could be easily observed and studied.

A discrete Fourier transform was taken of this time series; it was found that to faithfully recreate the waveform the full frequency spectrum was needed, this is largely due to the long period of steady pressure. The frequency range of the signal is therefore 20Hz - 4kHz.

For the tube being studied, the Womersley effective wavespeed varied from 8.49ms^{-1} at 20Hz to 8.60 ms^{-1} at 4kHz. As only a single wave speed can be modelled using compressibility as an analogue for an elastic wall, the wavespeed chosen was 8.56ms^{-1}; this is the wave speed at 166.7Hz (the frequency of the cosinusoidal pulse).

As with the wavespeed, Z_0 varied slightly over the frequency range of interest. At 20Hz, the impedance was 3.43*10^7 Pa/(m^{3}s^{-1}) with a phase lag of 0.81 degrees; this became 3.39*10^7 with 0.057 degrees of lag at 4kHz. Once more, the value at 166.7Hz (3.40*10^7 with 0.28 degrees of lag) was used as the basis of the analyses.

5.4.6.1 – Fluid-only Results

The initial analysis was performed with a 0 Pa outlet boundary condition. Figure 5.22 shows the pressure distribution within the tube after 0.01 seconds; clearly the pressure wave is wholly contained within the tube.

Figure 5.23 shows the pressure varying with time for a point on the centre-line halfway (10cm) along the tube. As would be expected, the wave was reflected and inverted; secondary reflections can also be observed in the form of third and fourth pressure peaks passing the point. The diminution of the reflected wave was due to attenuation in the 20cm of travel to and from the boundary; the peak primary wave magnitude passing the mid-point was 1250Pa, the reflected wave magnitude was 1049Pa. The percentage reflection of other boundary conditions was, therefore, calculated by dividing the reflected wave amplitude by 1049 and multiplying by 100; positive values represent non-inverted reflection (impedance too high) while negative values represent inverted reflection. Positive to negative peak time was recorded as 0.024±0.00025 seconds giving an effective wavespeed of 8.33±0.09m/s (within 3% of the predicted compressible wavespeed).

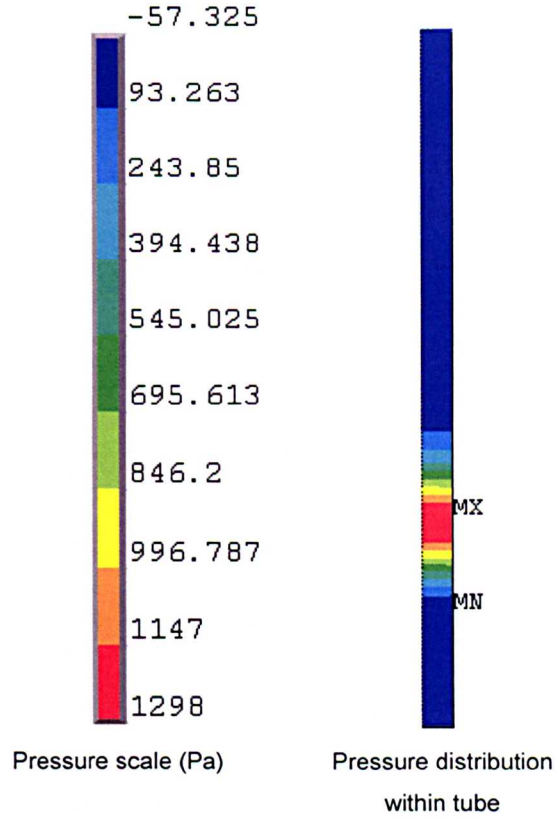

Figure 5.22. Pressure distribution within the tube after 0.01 seconds.

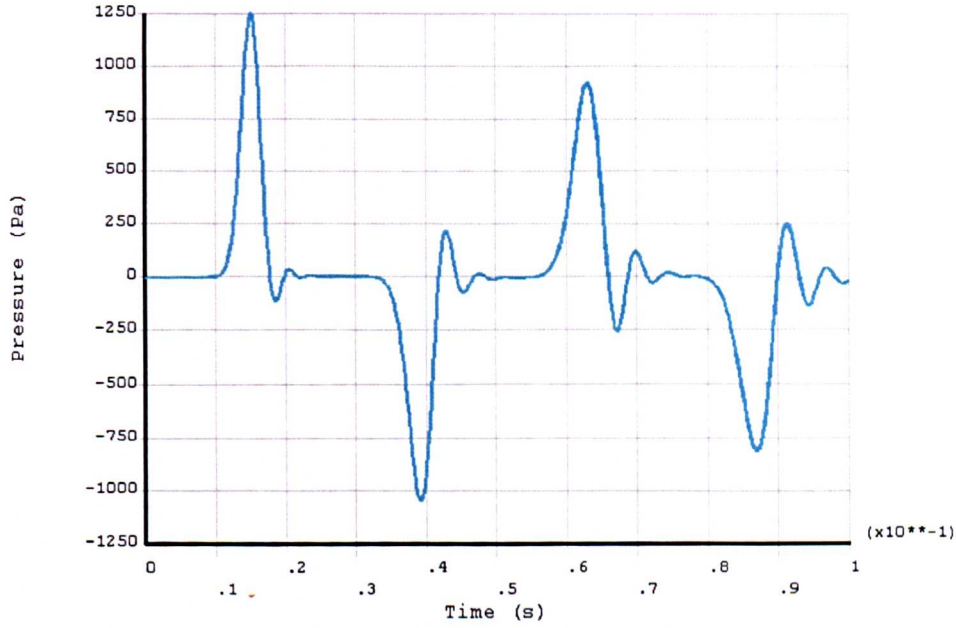

Figure 5.23. Time-history of pressure at a node on the centre-line 0.1 m from the outlet for a model with 0 Pa outlet boundary condition.

Figures 5.24 and 5.25 show the equivalent of figure 5.23 for the explicit implementation of the pure resistance boundary.

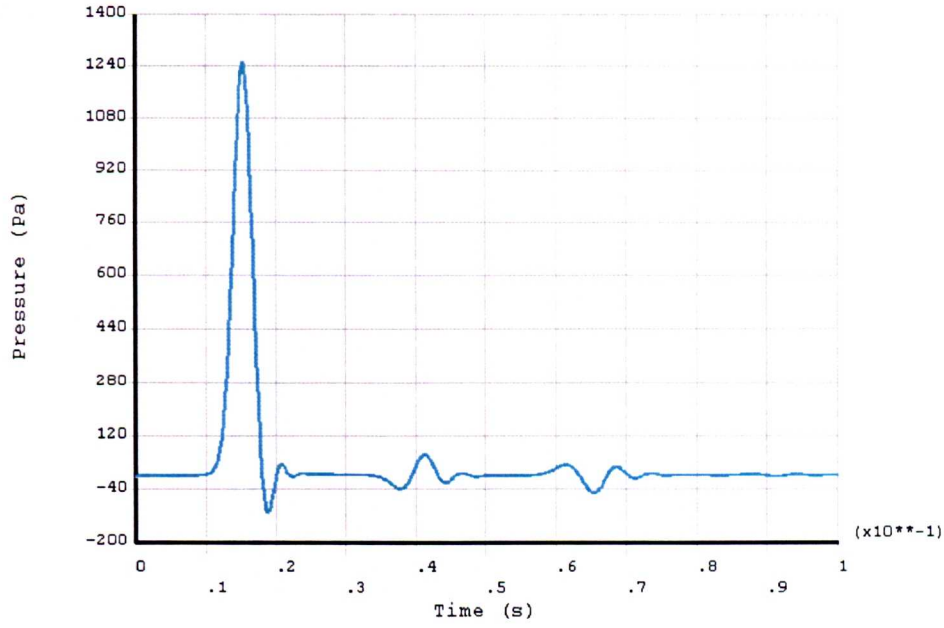

Figure 5.24. Time-history of pressure at a node on the centre-line 0.1 m from the outlet for a model with an explicit pure resistance outlet boundary condition.

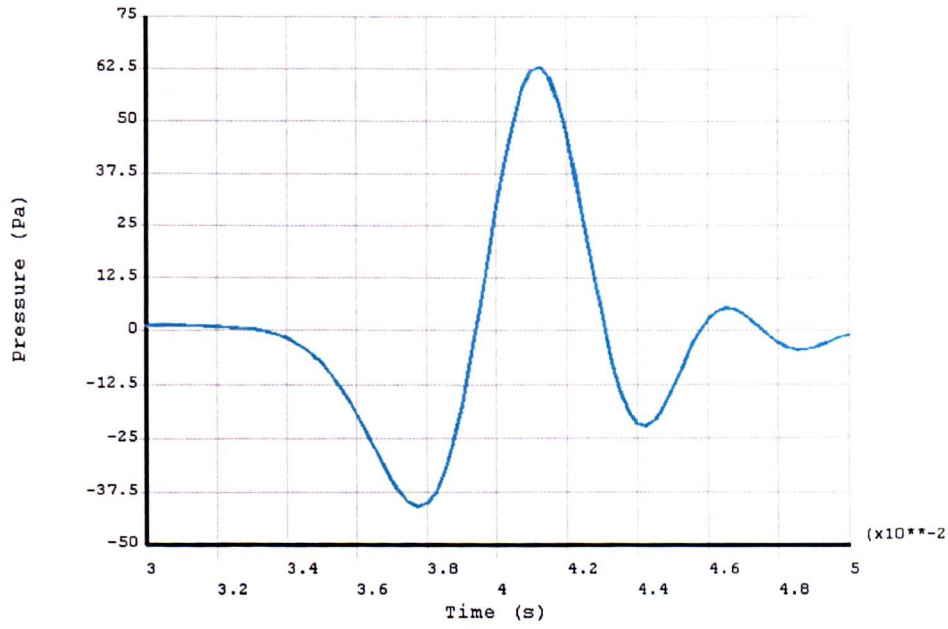

Figure 5.25. Detail for figure 5.24 showing reflected wave.

For the explicit pure resistance, the initial peak size was the same (to within 0.1%) as

in the 0Pa example. The wave was only 6% reflected with a peak reflected pressure of 63 Pa.

The results were improved further with the implicit implementation of the pure resistance, as shown in figures 5.26 and 5.27. The peak reflected magnitude was -4 Pa, giving a reflection percentage of -0.38%.

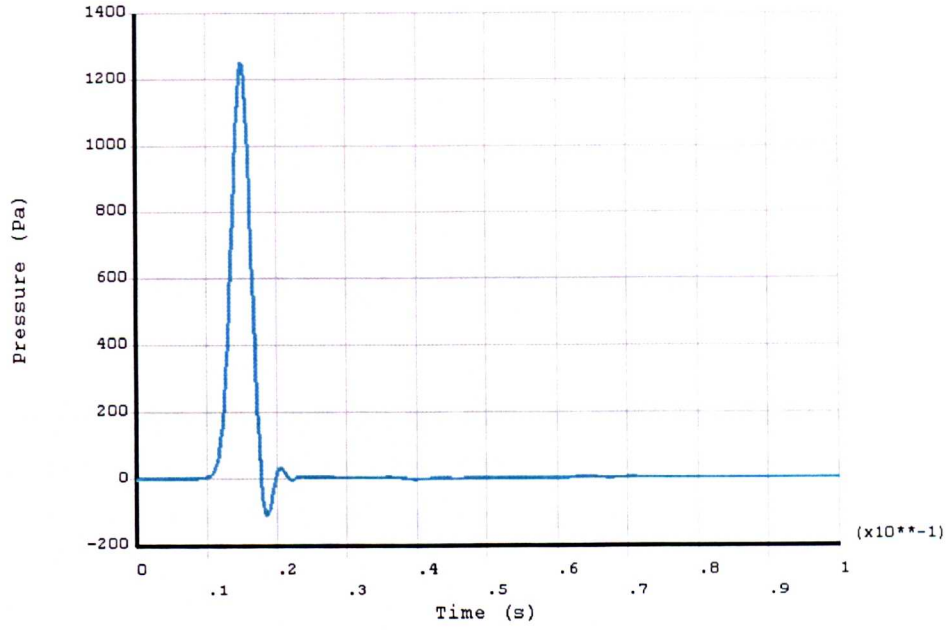

Figure 5.26. Time-history of pressure at a node on the centre-line 0.1 m from the outlet for a model with an implicit pure resistance outlet boundary condition.

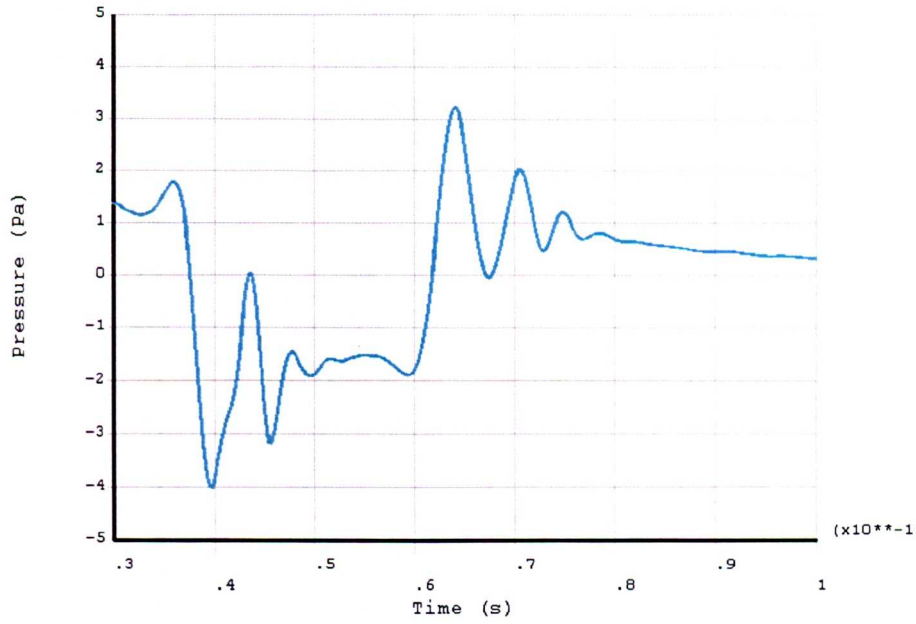

Figure 5.27. Detail for figure 5.26 showing reflected waves.

Due to the small (less than 1°) lag between pressure and flow, and the good performance of the pure resistance boundary conditions further analysis including Windkessel models was decided to be of little interest.

5.4.6.2 – FSI Results

As was the case in 5.4.4.2, convergence was difficult to achieve for the high frequency FSI model. In this case, compressibility was introduced to aid stability, as discussed in 5.4.3.2. The approach taken was to find the smallest degree of compressibility that would allow the model to converge, and calculate the wavespeed along the tube with a static 0 Pa boundary condition. This wavespeed was then used as a basis for the design of the outlet boundary conditions.

The bulk modulus parameter used was 256, yielding a compressible wavespeed of 16 ms^{-1}. Acting in conjunction with the elastic wall wavespeed (8.56 ms^{-1} at 166.7 Hz), this gave an overall wavespeed of 6.58 ms^{-1}, measured in an analysis of a tube with 0Pa outlet condition.

The weakly coupled FSI implementation led to significant numerical diffusion of the pressure wave, causing attenuation of the pressure wave not predicted by the Womersley equations, this can be appreciated by once more considering a plot of vessel centre-line pressure half-way along the domain (figure 5.28). As with the fluid-

only analyses, the percentage reflection of a boundary condition is calculated as the reflected peak size 0.1m from the outlet when using the boundary condition, divided by the reflected peak size with a 0Pa outlet boundary condition, (-549Pa).

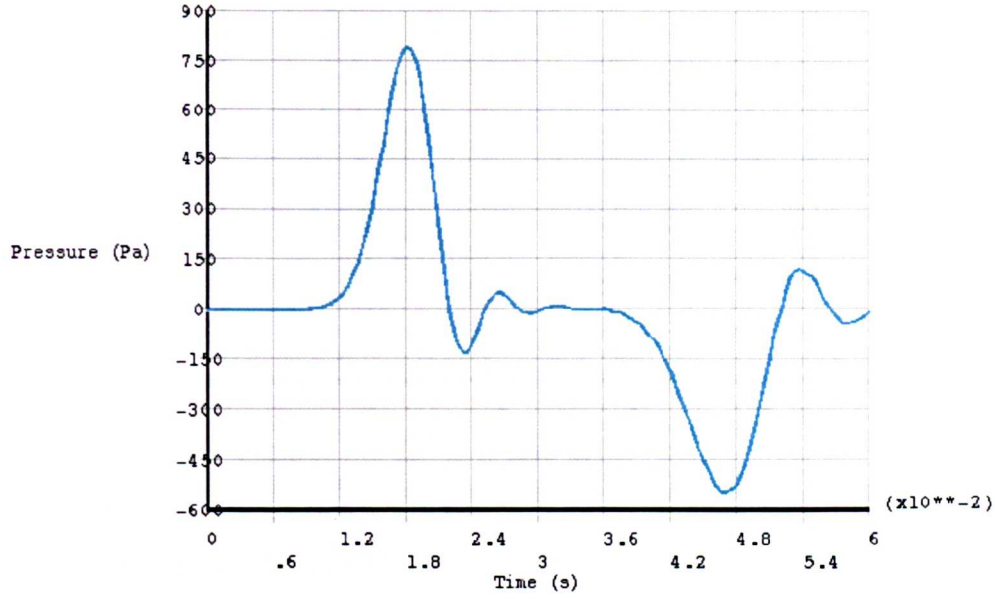

Figure 5.28. Time-history of pressure at a node on the centre-line 0.1 m from the outlet for a model with 0 Pa outlet boundary condition, implemented as a full FSI analysis.

Figures 5.29 and 5.30 show the results for an explicit pure resistance boundary condition. Peak reflected wave magnitude was –30Pa seen at 0.045s. This relates to a percentage reflection of 5.5%, very similar to the performance of the explicit pure resistance for the fluid-only case.

As anticipated from the fluid-only case, an explicit Windkessel model produced very similar results, with a peak reflection of 4.9% occurring at 0.045 seconds.

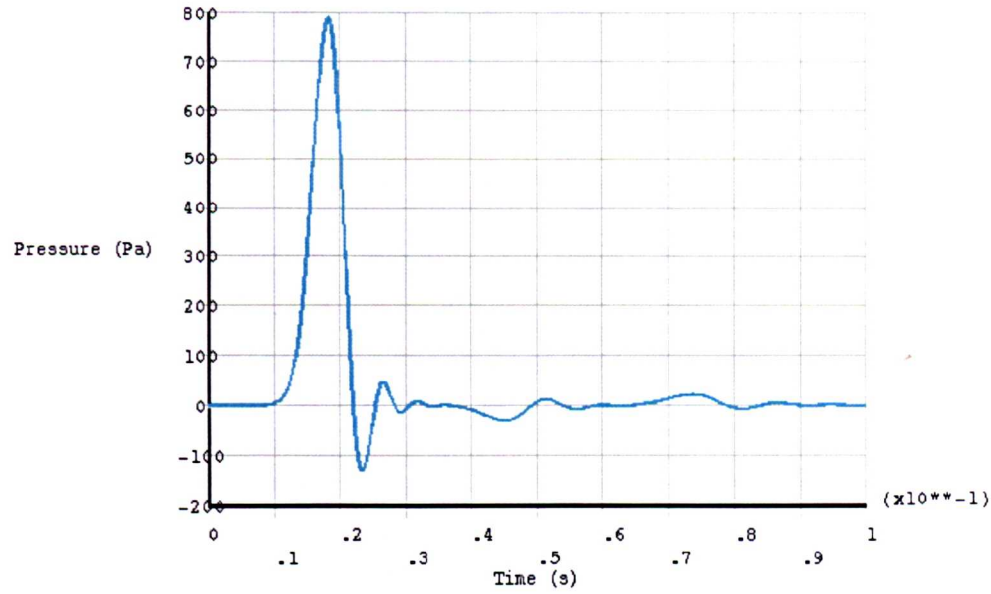

Figure 5.29. Time-history of pressure at a node on the centre-line 0.1 m from the outlet for a model with explicit pure resistance outlet boundary condition, implemented as a full FSI analysis.

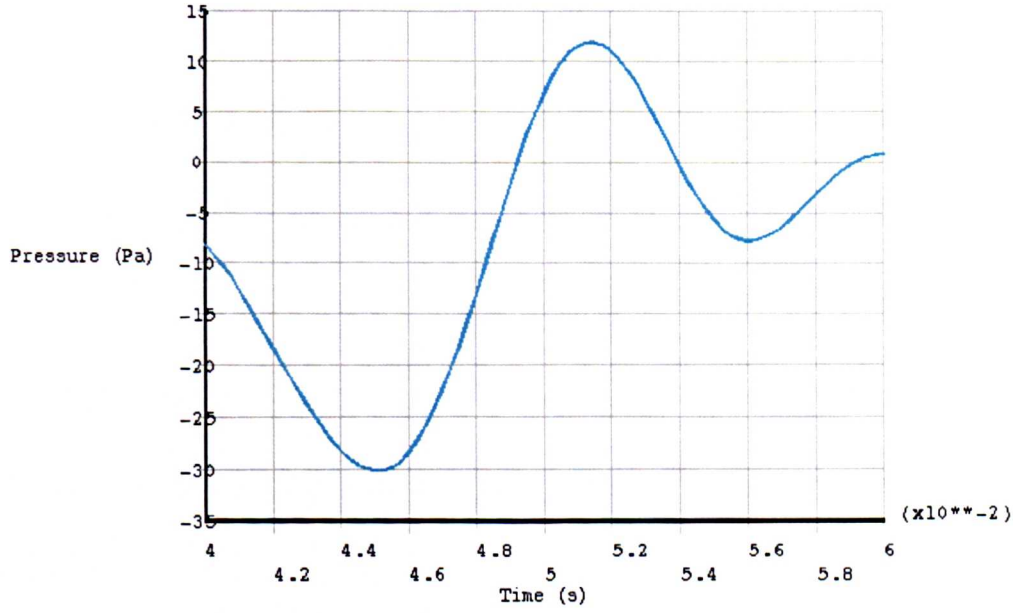

Figure 5.30. Detail from figure 5.29.

Figures 5.31 and 5.32 show equivalent results for an implicit pure resistance analysis.

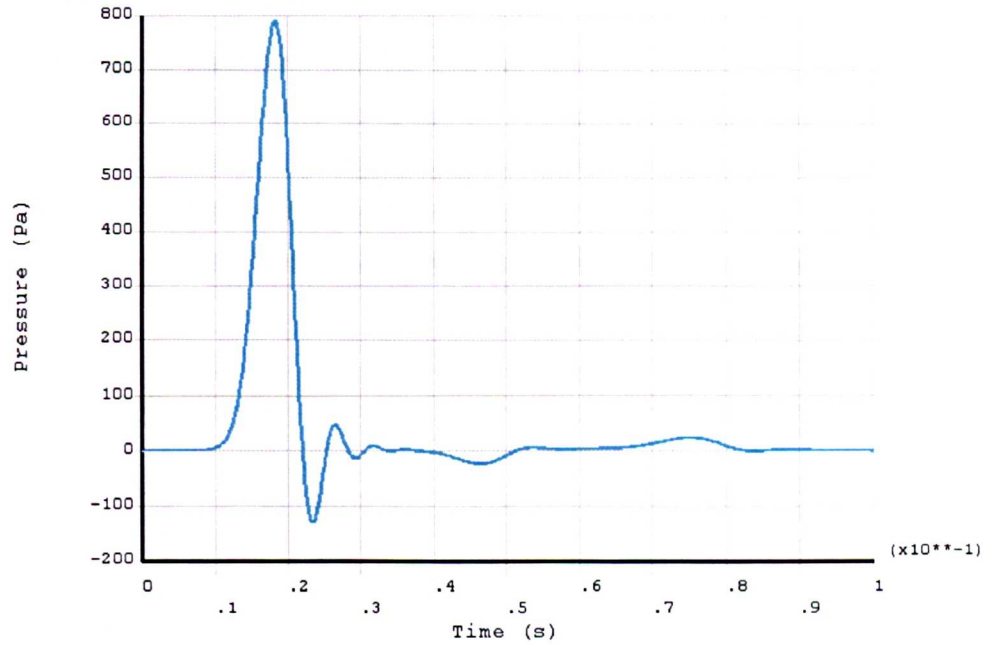

Figure 5.31. Time-history of pressure at a node on the centre-line 0.1 m from the outlet for a model with implicit pure resistance outlet boundary condition, implemented as a full FSI analysis.

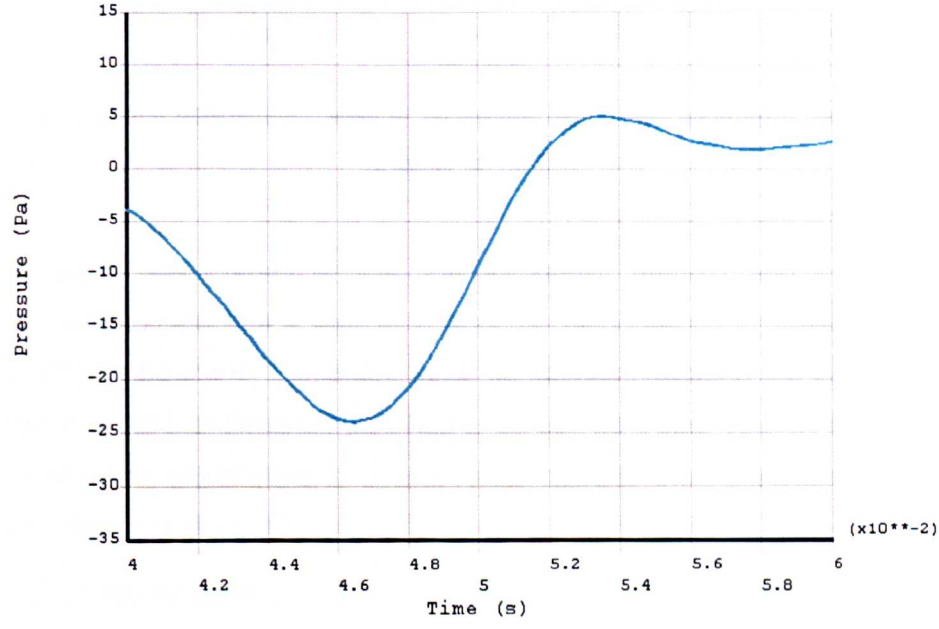

Figure 5.32. Detail from figure 5.31 (negative peak is –24Pa).

For the implicit implementation the peak reflection was 24Pa, giving a percentage reflection of 4.4%. Once more very similar results were seen for the Windkessel model, with a percentage reflection of 4.0%.

5.4.7 – Physiological Waveform

The physiological waveform used in this section was taken from Vieli et al [55], MR and Doppler US were used to measure blood flow in the abdominal aorta and compared, with good results. Figure 5.33 is a reprint of figure 2.1 (originally from Vieli et al. [55]). For this chapter only the ultrasound trace was used. As shown in 2.2.1, this flow trace could be well represented using only ten frequencies.

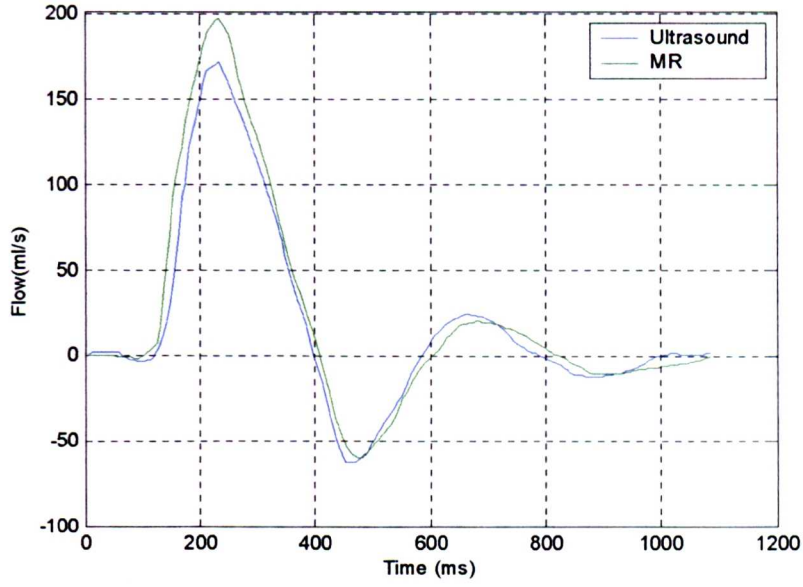

Figure 5.33. MRI and ultrasound traces of abdominal aortic flow waveform (Reproduced from Vieli et al. [55]).

The flow trace was converted into the frequency domain and the Womersley equations used to calculate a velocity history for each inlet node; these were applied as the upstream boundary condition. Initial conditions matching the initial velocity to inlet velocity at the first timestep also had to be set, as a zero velocity initial condition lead to a situation where (due to flow reversal close to the wall) the main flow path was in and back out through the inlet.

The fundamental frequency of the pulse waveform was 0.92 Hz and the maximum frequency of the reconstructed waveform used was 9.2 Hz. The frequency containing the greatest power was 1.84 Hz; this was used to calculate the compressible wavespeed of 8.23 ms^{-1} for the fluid-only analyses, and to calculate the value for the pure resistance boundary conditions.

In this case, as velocities had already been specified, it was the job of the boundary condition to impose the correct pressures at the inlet and outlet; these could be extracted and compared to those predicted by the Womersley equations.

5.4.7.1 – Fluid-only Results

For this problem, explicit analyses proved unstable, resulting in oscillatory pressure distributions within the vessel; even with small timesteps (down to 0.2ms – equating to over 5000 timesteps per cardiac cycle) the problem was not resolved. Figure 5.34 shows an outlet pressure history for a timestep of 0.2ms. Similar results were obtained using a Windkessel boundary condition.

Due to their simple structure, the boundary conditions themselves are inherently stable, hence the instability must result from the coupling of the boundary condition to the non-linear CFD model, beyond this, little can be said without resorting to a very detailed analysis of the two systems.

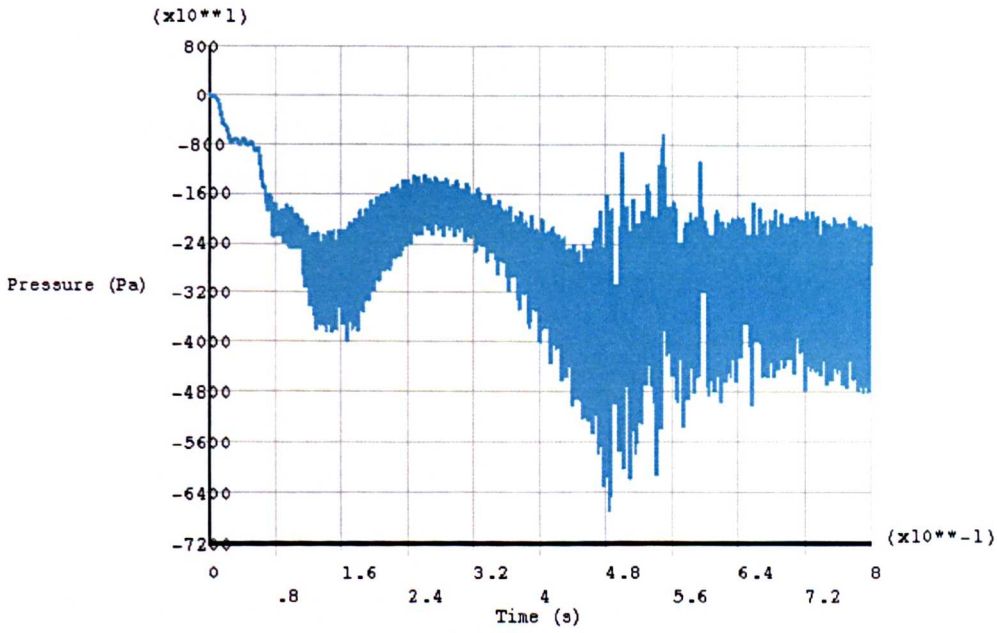

Figure 5.34. Outlet pressure history for explicit implementation of a pure resistance boundary condition.

Results were much more plausible when an implicit formulation was used for the boundary conditions, even with longer timesteps. Pressure wave velocity matched that expected, to within timestep accuracy. Figures 5.35 and 5.36 show inlet and

outlet pressure waveforms for an implicit pure resistance boundary condition analysis in Ansys, compared to the results predicted by the Womersley equations. An implicit formulation of an appropriate Windkessel model yielded very similar results.

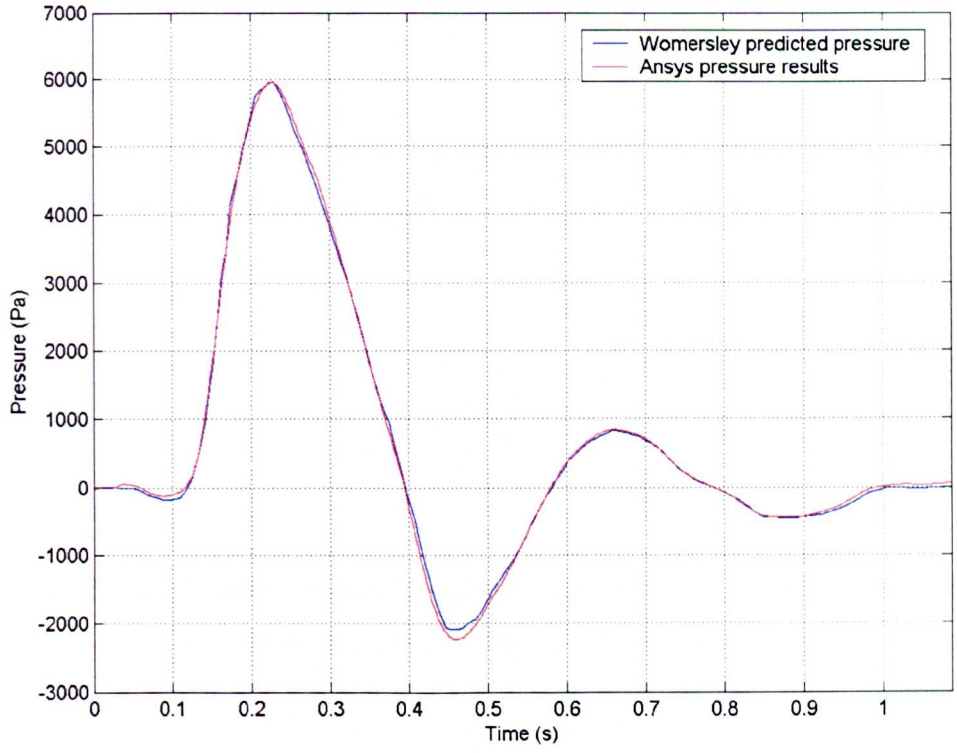

Figure 5.35. Inlet pressure history for implicit implementation of a pure resistance boundary condition compared to Womersley predicted values.

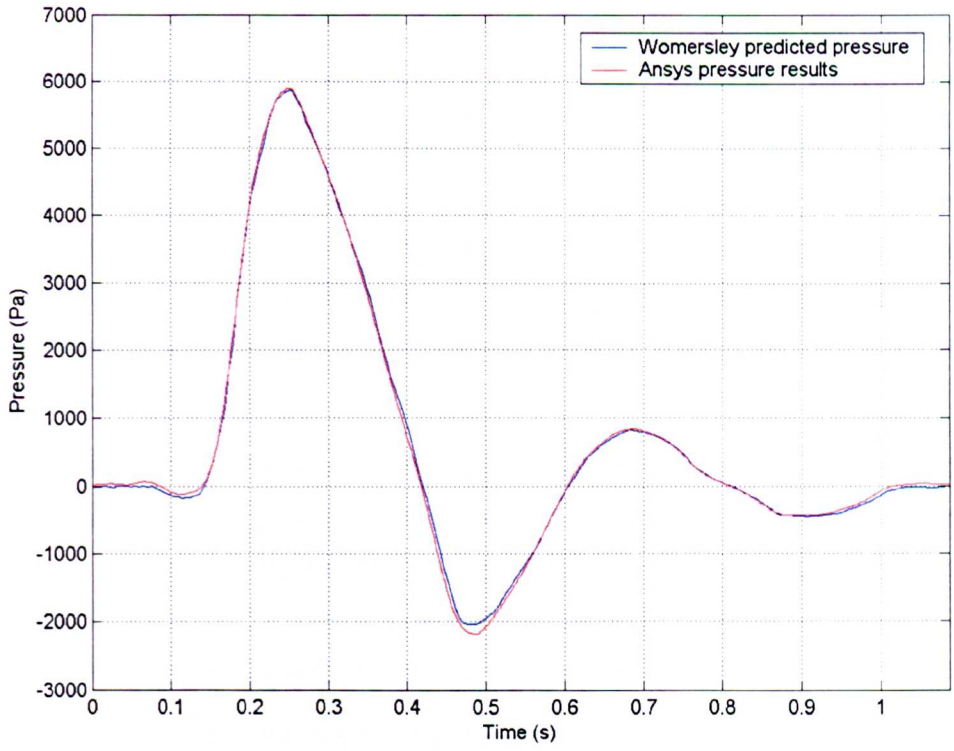

Figure 5.36. Outlet pressure history for implicit implementation of a pure resistance boundary condition compared to Womersley predicted values.

At the inlet, the mean percentage difference between the Womersley and CFD results (normalised against peak pressure) was 0.084%, maximum percentage difference was 2.9%. At the outlet, mean percentage difference was 0.012%, maximum percentage difference was 2.8%

5.4.7.2 – FSI Results

An attempt was made to recreate the analysis in 5.4.7.1 for an FSI analysis. As with the fluid-only analyses, convergence of the boundary condition was not achieved in the explicit case. Unfortunately, adopting the implicit approach did not allow convergence to be achieved. Various approaches, including altering mesh density, timesteps, and relaxation parameters and convergence criteria for the fluid solve, the FSI, and the boundary condition, were tried to no avail; in each case the fluid solve broke down by the first or second time-step and after several iterations of the FSI loop.

5.4.8 – Summary and Conclusions

In this section, simple boundary conditions based on the Womersley equations were applied in an attempt to match impedance to a simple model of a section of artery.

Both FSI and fluid-only (with compressibility used to model wave-propagation effects) models were implemented with implicit and explicit formulations of pure resistance and 3-element Windkessel boundary conditions. Where convergence of the CFD or FSI model itself could be achieved, the boundary conditions were seen to perform well with either a pressure history, or node-by-node velocity history imposed as the inlet boundary condition.

It was shown that, in the case of the abdominal aorta, individual cardiac frequencies could be successfully absorbed using pure resistance or three-element windkessel boundary conditions. Further, it was shown that with an appropriate choice of timestep, these could be implemented either implicitly or explicitly – in some cases, however there was a substantial time-penalty associated with the implicit formulation.

For a lower frequency (with the associated lower Womersley parameter), convergence was not achieved using the explicit formulation either for the FSI or fluid-only models; this was likely due to the conflicting requirements of a very small timestep to resolve the wave propagation speed and the need to be able to solve for a number of full cycles in a reasonable time. For these low-frequency analyses, an implicit pure resistance boundary condition failed to reproduce the necessary phase lag between pressure and flow at the outlet, as expected. The implicit 3-element Windkessel, however, performed well.

The analysis of a high-frequency pulse showed even more clearly the absorbing ability of the pure resistance and three element Windkessel boundary conditions; at this high frequency both performed well in explicit and implicit formulations.

For a physiologically derived waveform, the implicit approach worked well for a slightly different class of problem (inlet velocities defined rather than inlet pressures), but as with the low frequency analysis, convergence was not achieved for the explicit case. As described above, for this waveform, convergence was not achieved for either boundary condition implementation technique with the FSI model

Based on these results, it is concluded that, in designing reflection-free boundary conditions for computational models of blood vessels, explicit pure resistance or 3-element windkessels should be considered as a first option, due to their similar

performance and reduced computational cost when compared to their implicit counterparts.

For systems where lower Womersley numbers are of importance – including perhaps, inter-beat variation, respiratory-driven vessel motion, or pulsatile flow in much smaller vessels – pressure and flow may become significantly out of phase and the 3-element Windkessel becomes the simplest appropriate model. If this is combined with a situation where the time-scales of wave-propagation and input frequency are wildly different, the implicit approach is likely to become necessary.

Due to difficulties in obtaining convergence of the model itself (even for the first few timesteps), it is impossible to give any indication as to the appropriate form of boundary condition for an FSI analysis with velocity inlet boundary condition, beyond saying that the implicit approach which worked using a compressible fluid-only model, is likely to be successful.

Fluid-only and FSI models of a high-speed pressure pulse, showed that this approach is also applicable to situations where the wave length is significantly smaller than domain length, and illustrated very graphically the success of the boundary conditions, the implicit formulation was seen to perform a little better than the explicit version.

5.5 – Outlet Boundary Conditions 2 – Westerhof Boundary Conditions

The purpose of the boundary condition now moves from minimising reflection at the boundary to representing the downstream vasculature in order to ensure appropriate pressure distribution and time-varying flow patterns at the outlets.

The Westerhof structured tree was introduced in 2.3.2 and the discretisation of lumped parameter models covered in some detail in 5.4.2; combining these two, a Westerhof boundary condition can be developed, coupling a Westerhof model to each downstream boundary of the CFD domain.

From an implementation point of view, the D (continuous-time direct transfer) matrix is zero for all Westerhof structured tree models. Using the zero-order-hold discretisation method described earlier ensures that the J (discrete-time direct transfer) matrix is also zero. Thus, the boundary condition is explicit by its very nature and there is no need to iterate.

Even fairly large state-space models are simple to implement as boundary conditions; recalling equations 5.11 shows us that we merely have to perform four matrix multiplications (which further reduce to one matrix-vector product, and 2 vector-scalar products for our SISO systems with J=0).

$$x(k+1) = Fx(k) + Gu(k)$$
$$y(k) = Hx(k) + Ju(k) \qquad 5.11$$

As long as the software package being used has even the simplest of programming languages available, these equations can be programmed straightforwardly. In Ansys 8.1 (as used throughout this project), the matrix operations are available as functions and the problem reduces to one line of code for each equation.

5.5.1 – Westerhof Boundary Condition for the Abdominal Aorta

Below the abdominal aortic outlet, the standard Westerhof tree has a fairly complex model of the vasculature of the lower abdomen and legs with 49 downstream compartments and a minimum of three before a terminal resistance is met (in the inferior mesenteric artery).

This model can be shown to give a plausible pressure waveform with physiologically appropriate magnitude, when driven directly by a PCMRA derived flow waveform, as shown in figures 5.37 and 5.38.

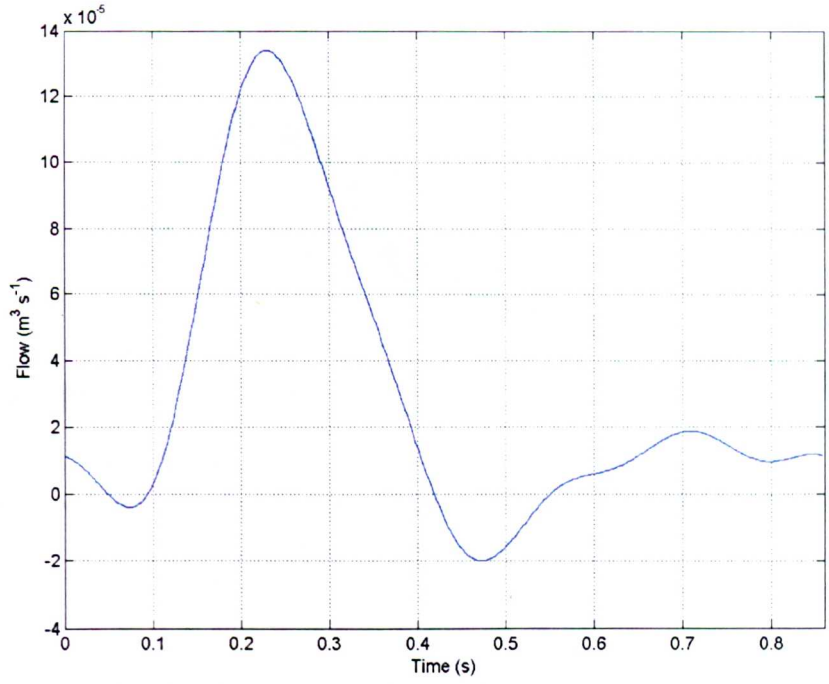

Figure 5.37. Flow waveform for Westerhof abdominal aortic boundary condition (Fourier interpolated PCMRA data).

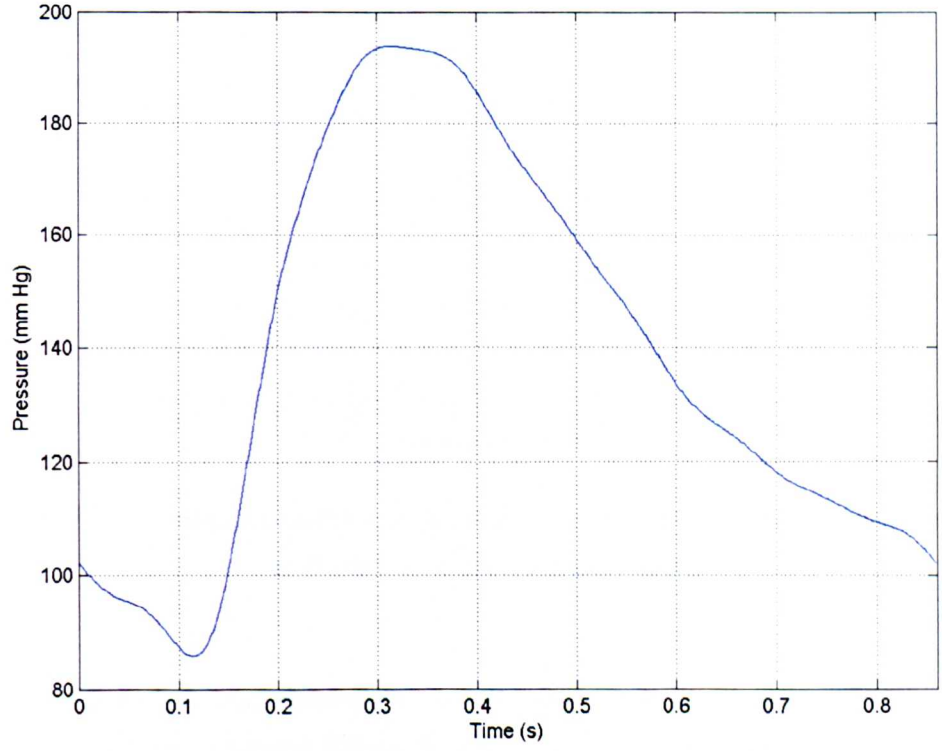

Figure 5.38. Pressure waveform for Westerhof abdominal aortic boundary condition driven directly from PCMRA data.

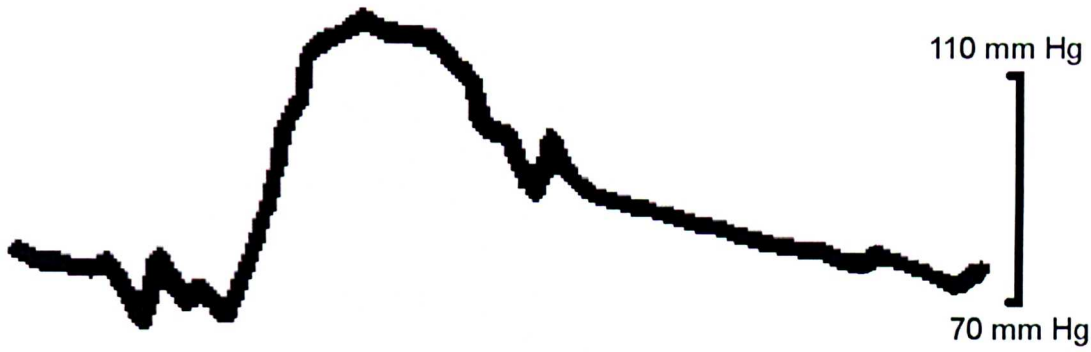

Figure 5.39. Abdominal aortic pressure waveform obtained using electromagnetic catheter transducer, reproduced from [56].

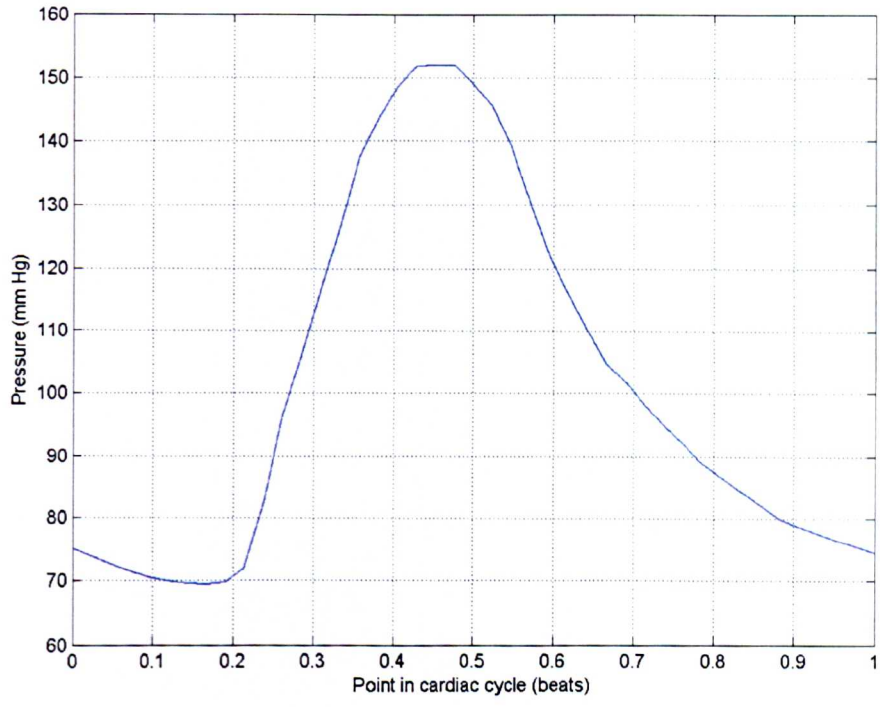

Figure 5.40. Iliac pressure waveform obtained using intra-arterial pressure catheter, acquired at Rotherham district general hospital.

When compared to published data for the abdominal aorta (figure 5.39), and that acquired in a clinical setting (figure 5.40) for the iliac, it is seen that the Westerhof model results are qualitatively similar, but quantitatively speaking, at 194/87 both systolic and diastolic blood pressure are overestimated (abdominal aortic blood pressure is usually within 10% of pressure measured at the brachial artery using a

sphygmomanometer [159]). This is likely due to a difference in size between our volunteer, from whom the flow data comes, and Westerhof's volunteer on whom the model is based. Thankfully, this type of error can be straightforwardly corrected, the linearity of the model allows a scaling factor to be brought into the calculations, this will be discussed further in section 5.5.2.

Whilst the Westerhof model is substantially more complex than the pure resistance or windkessel models used in 5.4, computation time is negligible compared to that for the CFD analysis itself.

While the above shows that the standard Westerhof model of the vasculature distal to the abdominal aorta can (with the addition of a scaling factor) reproduce the results found *in vivo*, the key to the success of the boundary condition is, how it works in the conjunction with a similar model attached at the SMA downstream boundary.

5.5.2 – Westerhof Boundary Condition for the Superior Mesenteric Artery

The standard Westerhof tree represents the SMA as a single pure resistance; this approach does not give an appropriate relationship between pressure and flow at the SMA outlet. However, knowledge of the anatomy and flow characteristics of the SMA, along with Westerhof's basic modelling unit and some assumptions about tree structure, can be used to generate a more appropriate model for the downstream SMA boundary condition.

When used in conjunction with the Westerhof abdominal aorta down model, the SMA-down model should match SMA flow in terms of mean flow, peak flow, and general wave shape; one key aspect is that the flow reversal (or lack thereof) should match that seen in the PCMRA data. The PCMRA data along with a Fourier-interpolated waveform is shown in figure 5.41.

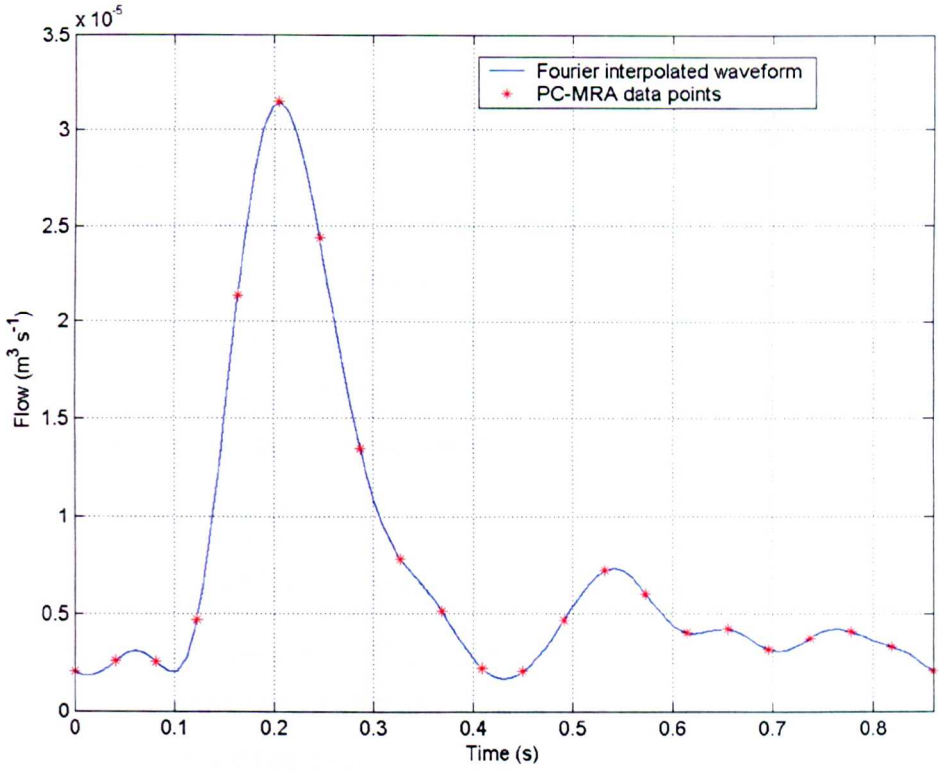

Figure 5.41. PCMRA data for the SMA with Fourier interpolated waveform.

The set-up used to design the SMA boundary condition has four parts:

- The abdominal aortic flow inlet boundary condition.
- A simple Westerhof-style model of the 3D computational domain.
- The AA-down model described in 5.5.1.
- The SMA-down model, of, as yet undecided structure.

Once a model has been developed which performs appropriate flow splitting, the resulting pressure distributions can be checked and the same scaling factor applied to both outlet models to yield an appropriate pressure waveform.

The basic structure of the SMA model was based on a fractal model of blood vessel architecture presented by Zamir et al. [101] and discussed in 2.3.2. This has been shown to be a simple, but effective way to represent the pattern of blood vessels in two dimensions – a reasonable assumption for the SMA's branches as the mesentery, through which the vessels run, is a large and multiply-folded two-dimensional sheet.

Various model parameters were tested in an attempt to match the flow in the SMA, The best results were obtained with:

- An asymmetry ratio of 0.95 – a little asymmetry stops the reflections from all branches being in phase.
- A bifurcation exponent of 2.7 – this in the range of values quoted based on autopsy studies and consideration of fluid dynamic principles. [160].
- Wall stiffness of 3 MPa for the first 2 generations, 6 MPa for the 3rd generation, and 12 MPa thereafter, this follows Westerhof's pattern of increasing stiffness in smaller vessels.
- Initial SMA radius of 3mm.
- Initial SMA branch length of 4cm.
- Leakage resistance of 720 kΩ on each terminal branch (measured in Ohms to match Westerhof's convention) – value was chosen to yield appropriate total flow over the cardiac cycle.

Figure 5.42 shows the structure of the SMA-down model; note that although the branches of the model apparently overlap in space, the Westerhof element does not make use of branching angle, and branches are regarded as non-anastomosing. Figure 5.43 shows the model predicted SMA-flow compared to the PCMRA flow readings, with the SMA-down and AA-down models running simultaneously and inlet flow driven by the combined SMA and AA PCMRA waveforms.

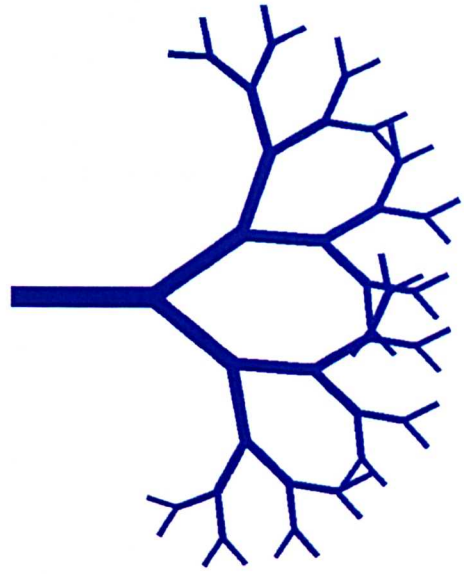

Figure 5.42. Structure of SMA-down model.

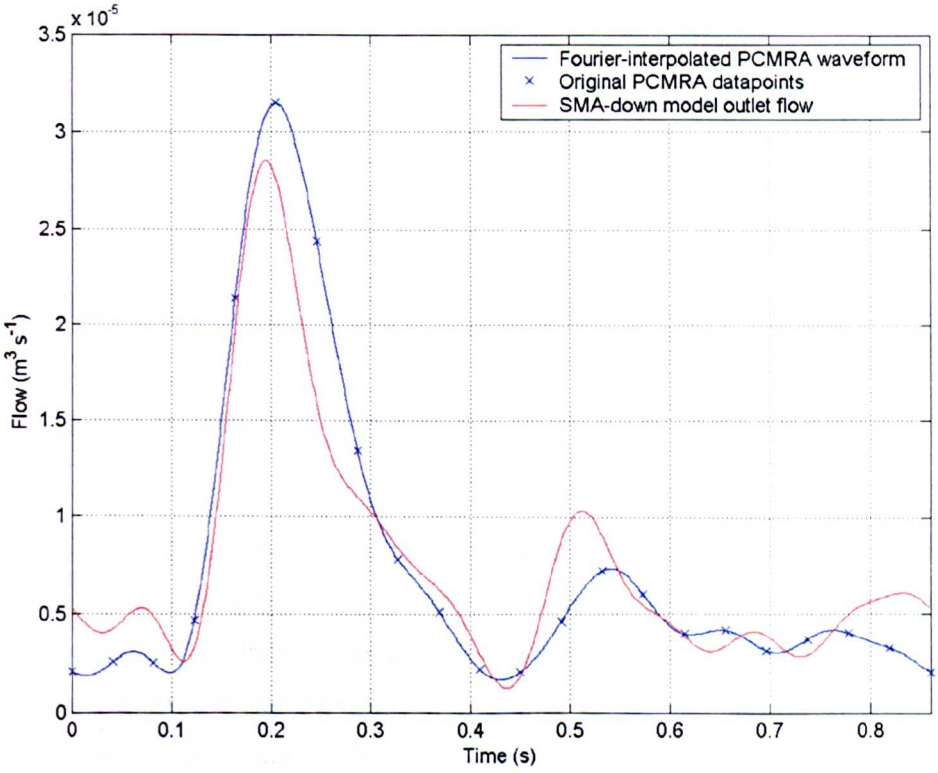

Figure 5.43. Original PCMRA flow data and SMA-down model predicted flow.

From figure 5.43, the SMA-down model recreates the SMA flow pulse very well considering that the exact nature of the vascular tree of the SMA has been approximated by a simple fractal model. All key flow features are present; a primary peak at around 0.2s (with magnitude correct to within 10%), a point of minimum flow

just after 0.4s followed by a secondary peak, and no overall flow reversal at any point in the cardiac cycle. Mean SMA flow per cycle matched to within 0.1%.

Figure 5.44 completes the picture in terms of flow, by repeating figure 5.42, but for the AA downstream of the SMA bifurcation.

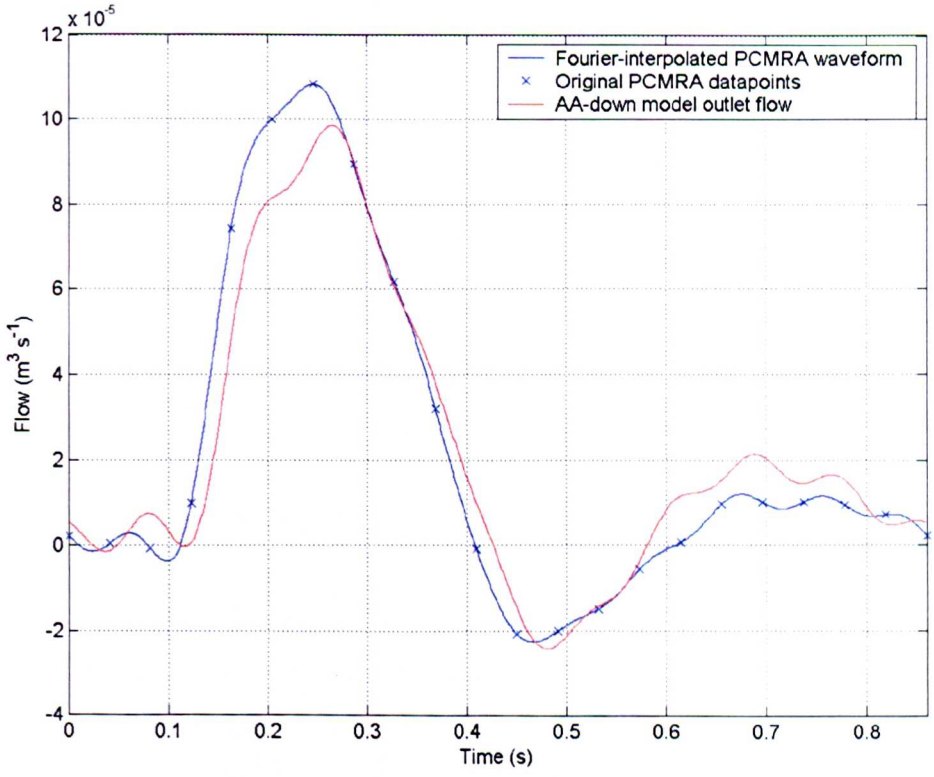

Figure 5.44. Original PCMRA flow data and AA-down model predicted flow.

While the flow profiles look promising, the pressure wave magnitude must still be dealt with. Figure 5.45 shows the pressure waveform at the SMA/AA bifurcation with both downstream models in place; the pressure waveform relates to a blood pressure of 151 over 108, this is well into the hypertensive range, multiplying by a factor of 0.7 gives 106 over 76, this data is also displayed in figure 5.45.

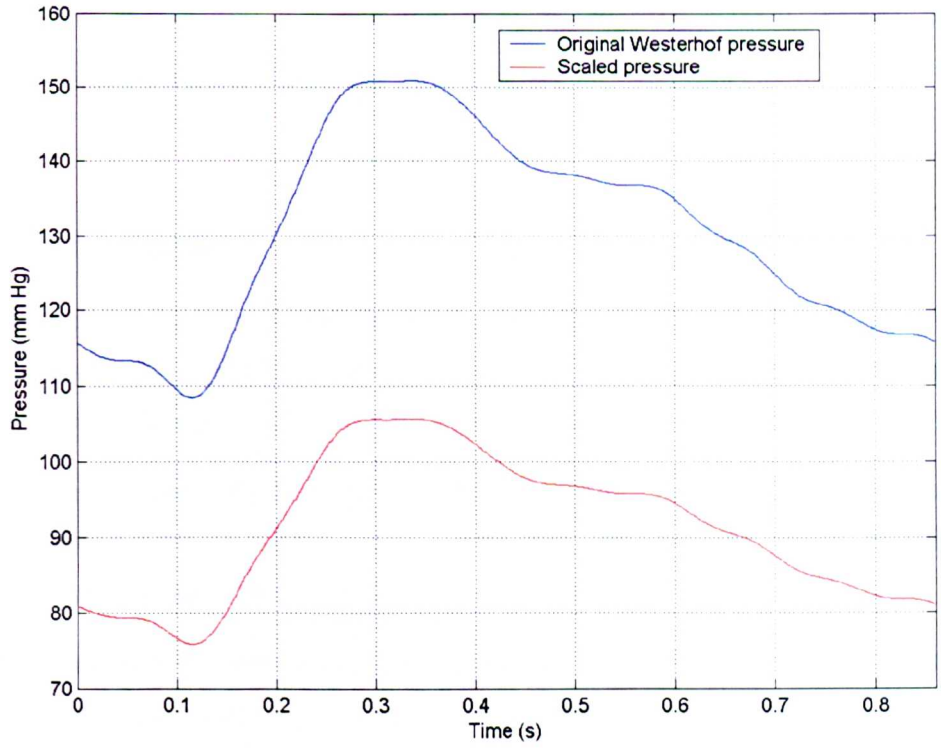

Figure 5.45. Original Westerhof model pressure data (blue) and more physiologically appropriate scaled version (red), both taken at AA/SMA bifurcation.

With the scaling factor applied, the pressure waveform looks qualitatively plausible and matches physiological values in terms of systolic and diastolic pressures.

5.5.3 – Conclusions

In this section, a pair of more complex models was developed to represent the vasculature fluid impedance of the vessels downstream of the SMA and AA geometries modelled in chapter 4. Together, these models give quantifiably appropriate flow splitting and impose an appropriate pressure at the boundaries. In the following chapter, these models will be used as downstream boundary conditions in the modelling of blood flow through the AA and SMA.

Chapter 6. The Effect of Wall Motion on Wall Shear Stress Distributions in the SMA

6.1 – Introduction

In this chapter, the somewhat disparate subjects of chapters 4 and 5 are brought together to model blood flow in the SMA and AA in one volunteer. Flow patterns and wall shear stresses are calculated in the static and moving geometries.

First, solution dependence on mesh density, timestep, and number of cardiac cycles were assessed for a static mesh. After this, the moving mesh analysis was implemented and wall shear results compared with those for the static mesh.

In both cases, the more traditional boundary condition approach was used, i.e. velocities were specified at the proximal AA opening and either the distal AA opening or the SMA, a pressure waveform (created using the Westerhof model) was imposed at third boundary[4]. The reason for this was one of time-saving. It was found that the Westerhof-style boundary conditions did work well for the 3d models; however, short-timesteps (around 0.5ms) were needed to maintain stability of the whole coupled system. In section 6.2.2 it will be shown that this is 10 times shorter than the timestep needed for adequate representation of the fluid model. This made the computational cost of using such an approach unjustifiable for a non-FSI model, where pressure magnitude is unimportant (only relative pressure are required) and more traditional boundary conditions can suffice.

6.2 – Static Mesh Run Details

For the static geometry, mesh density and timestep dependence were assessed using meshes based on the vessel geometry at MRI timestep 4. This timestep was chosen as it represented a mid-point point with respect to vessel position and volume

---

[4] Initially, the flows were specified at the distal AA and SMA boundaries, and a pressure at the inlet. This lead to the breakdown of the flow field, which was likely caused by a problem with the 'upwinding' approach of the software.

between those values found at systole and diastole. In each case, velocities were specified at the two AA boundaries and pressure at the SMA unless otherwise stated.

6.2.1 – Mesh Density Convergence

As the key variable of interest was wall shear stress, this was used as the indicator of mesh convergence; it has been shown in previous studies [154] that WSS field convergence is a substantially more stringent test of mesh invariance, than flow field convergence. In order to easily monitor wall shear stresses, it was advantageous to split the WSS into two components, which could be considered separately. As vessel centrelines were available from the image registration step, it was decided that these should be the axial and transverse components of wall shear stress; this was achieved in the manner described below:

- For a chosen near-wall node (i.e. a node not on the wall but attached to an element with one face on the wall), the closest part of the centre-line was found using the algorithm described in 4.6.2.
- The vector of the centre-line at this point was found (the axial vector), along with the vector from this point to the chosen node (the radial vector), and a third vector comprising the cross-product of the radial and axial vectors (the transverse vector). By definition, these three vectors form an orthogonal set.
- The velocity time-histories for the node were resolved in the three newly defined components.
- The axial WSS is given by 6.1, and the transverse WSS by 6.2, the radial component is always small for a smooth-walled vessel, but can be used to check calculations).

$$\tau_{axial} = \frac{\partial V_{axial}\mu}{\partial r} = \frac{V_{axial}\mu}{h} \qquad 6.1$$

$$\tau_{transverse} = \frac{\partial V_{transverse}\mu}{\partial r} = \frac{V_{transverse}\mu}{h} \qquad 6.2$$

Where V_{axial} and $V_{transverse}$ are the axial and transverse velocity components respectively, μ is fluid viscosity, r is the radial co-ordinate, and h is the radial distance from the chosen node to the nearest point anywhere on the vessel wall (the algorithm used was exactly the same as that for calculating the linear displacement spectrum, as described in 4.5.1)

6.2.1.1 – Unstructured Meshes

Initially, unstructured meshes of tetrahedral elements were used to represent the model geometry. Ansys allowed control of element size by specifying a representative element edge length.

Table 6.1 shows details of the meshes used; figure 6.1 shows images of the coarsest and finest of these meshes.

Mesh Name	Edge length (mm)	Number of:				
		Nodes	Elements	AA Inlet Nodes	AA Outlet Nodes	SMA Outlet Nodes
M15	1.5	6419	31218	128	97	27
M12	1.2	10612	53188	202	145	31
M10	1.0	20295	106985	277	202	49
M8	0.8	36080	195247	438	310	79
M6	0.6	73629	406300	763	537	128

Table 6.1. Details of unstructured meshes.

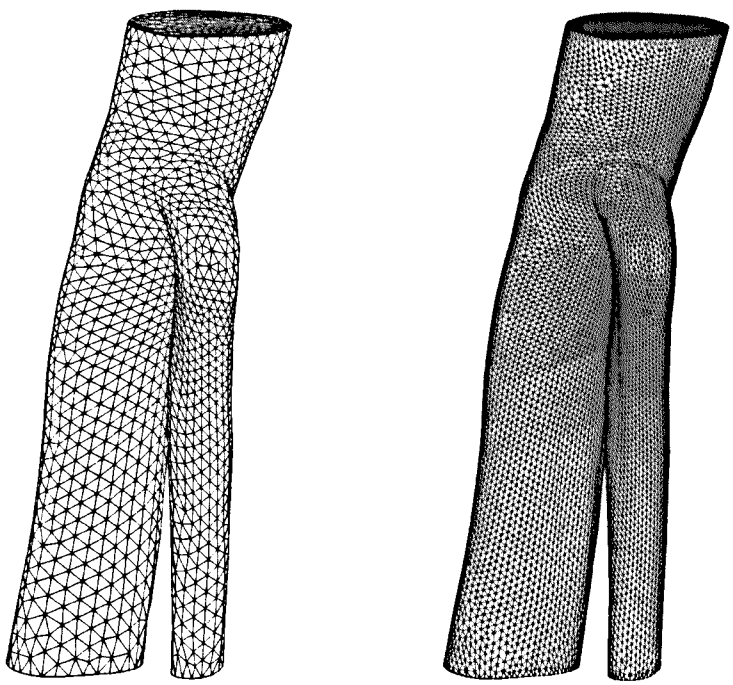

Figure 6.1. Unstructured meshes with element edge length 1.5mm (left) and 0.6mm (right).

As an initial check on mesh convergence, axial and transverse wall shear stresses were calculated at a node on the anterior aspect of the SMA as shown in figure 6.2. A wall node was chosen on the coarsest mesh, and the closest wall node to this point found for each remaining mesh. In each case, the WSS was calculated for the closest non-wall node to this point, with the distance 'h' calculated as the distance from that node to the closest point on any surface triangle. Figures 6.3 and 6.4 show time-varying WSS for the chosen node for each of the unstructured meshes.

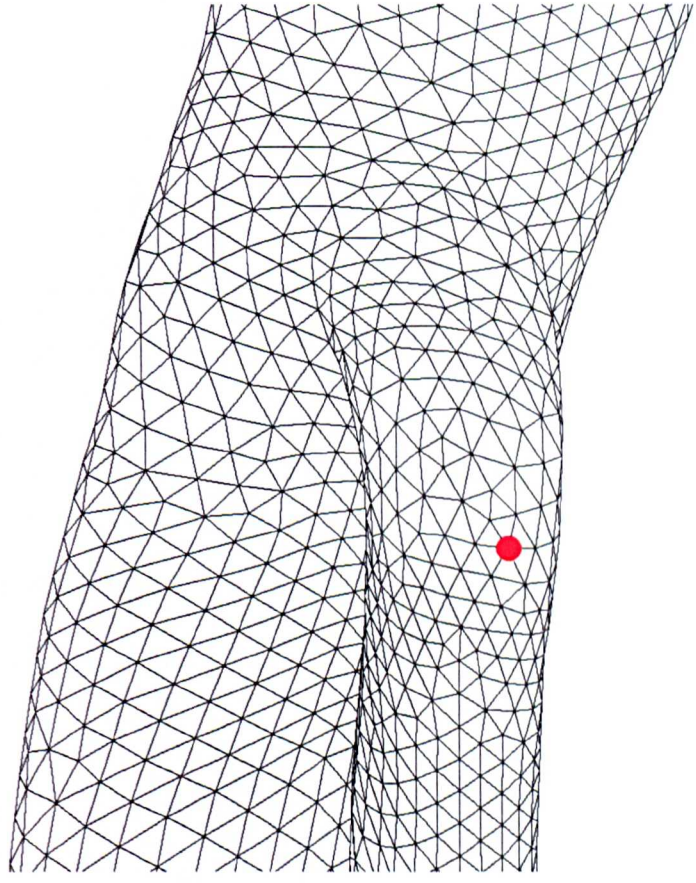

Figure 6.2. Detail of coarse mesh with node used for initial mesh invariance testing (red dot).

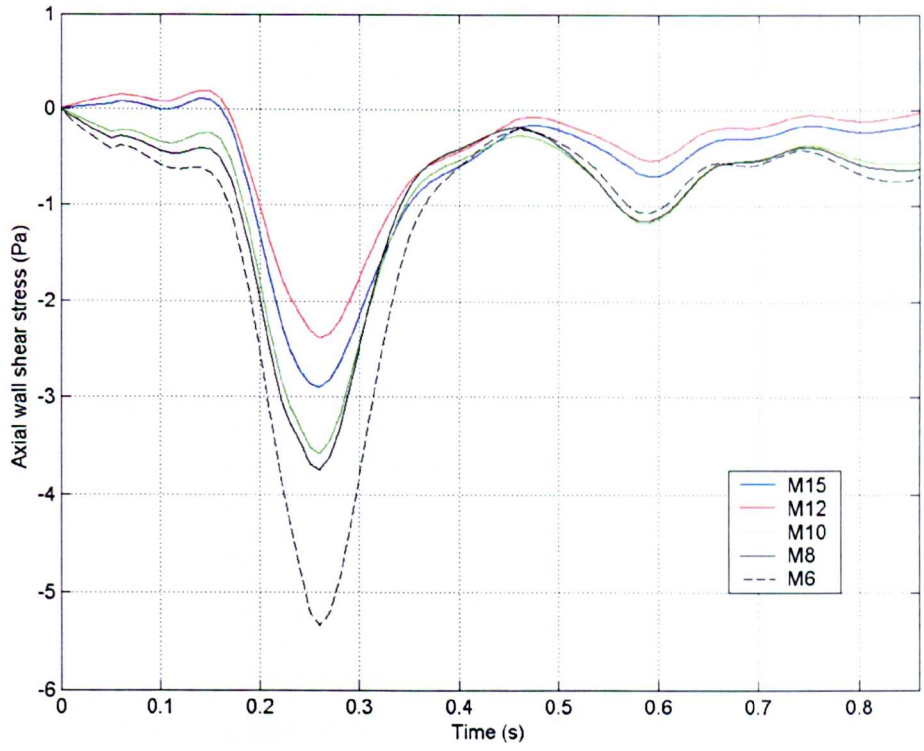

Figure 6.3. Axial wall shear stress results for node on SMA front edge (for all unstructured meshes).

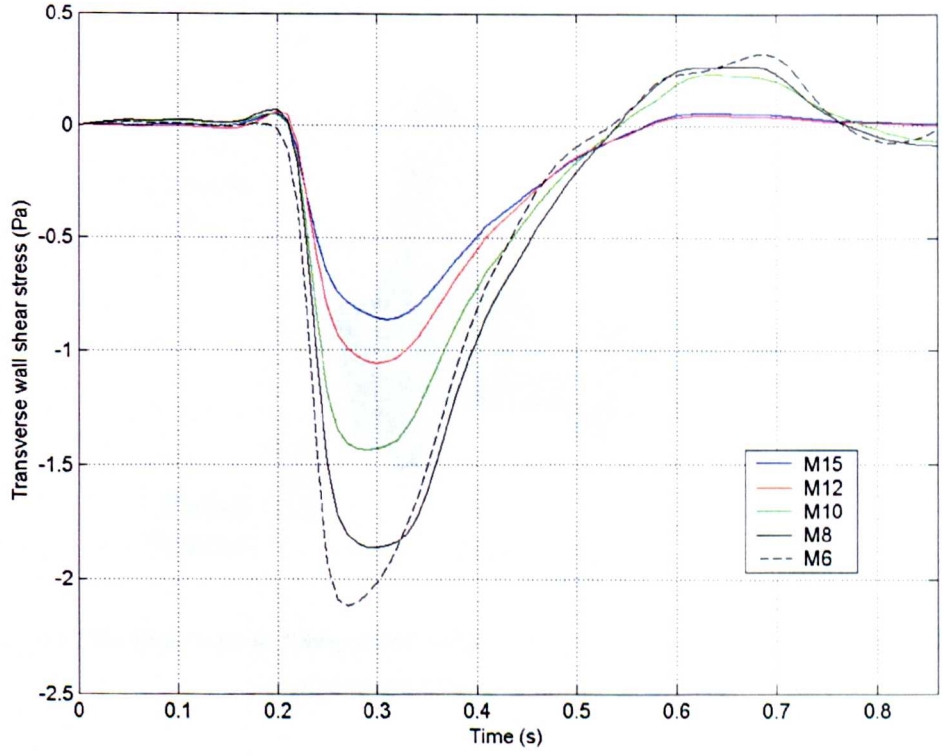

Figure 6.4. Transverse wall shear stress results for node on SMA front edge (for all unstructured meshes).

Figure 6.3 and 6.4 clearly show that mesh invariance was not being achieved using the unstructured mesh approach. The general trend was that peak wall shear stress was increasing with mesh density, suggesting that flow field was not being fully characterised by the analysis, clearly a better mesh was needed.

6.2.1.2 – Semi-structured Meshes

The finest unstructured mesh had a total of 400 000 elements; due to the 3d nature of the problem, halving the element edge length would require 8 times as many elements. Continuing with the unstructured approach to the available limit of 2 000 000 elements (governed by software licensing) would only yield an element edge length of around 0.35mm, and at great computational cost. However, the insight gained into the problem allowed for the design of an improved semi-structured mesh.

It was clear that one key characteristic of the flow was its fairly flat profile across the vessel, with a boundary layer and a central 'plug' of fluid with smooth, lower velocity gradients, this can be clearly seen in figure 6.5. Also, it was noted that the region of interest was around the bifurcation of the vessels and that the downstream portion of the aorta in particular was using substantially more elements than necessary.

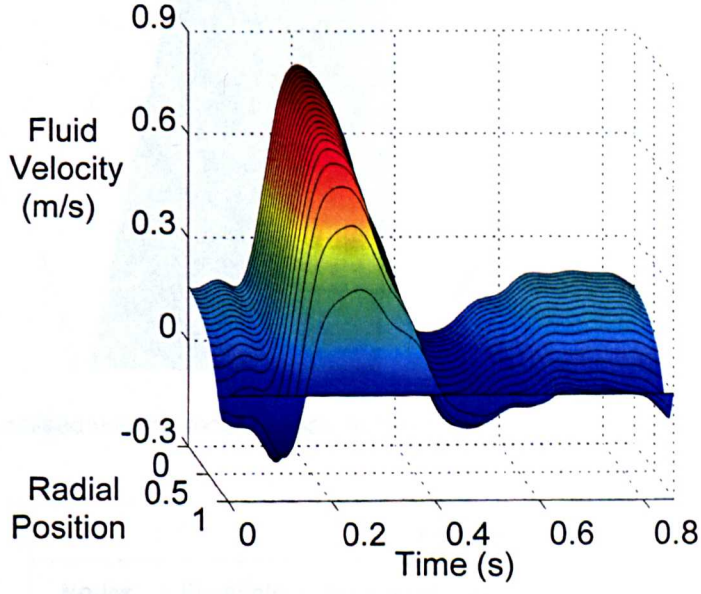

Figure 6.5. Surface map showing blood velocity magnitude at AA inlet varying with time and radial position over a single cardiac cycle.

The idealised volume model from which the mesh was built, was separated into four main volumes; upper AA, lower AA, AA transition zone, and SMA. Apart from the

axial transition zone, all of the main sections were themselves separated into 4 concentric volumes, as shown in figure 6.6. Using this structure it was now possible to have different mesh densities in different sections of the vessel, have smaller elements closer to the wall, and control the transition from the large elements in the centre of the vessel to small ones near the walls. The AA transition zone allowed for a smooth transition between the two mesh densities in the AA without elements of poor quality being generated. Three meshes were constructed using this technique. Their details are outlined in Tables 6.2a and b. Images of idealised and volunteer specific semi-structured meshes are shown in figures 6.7 and 6.8.

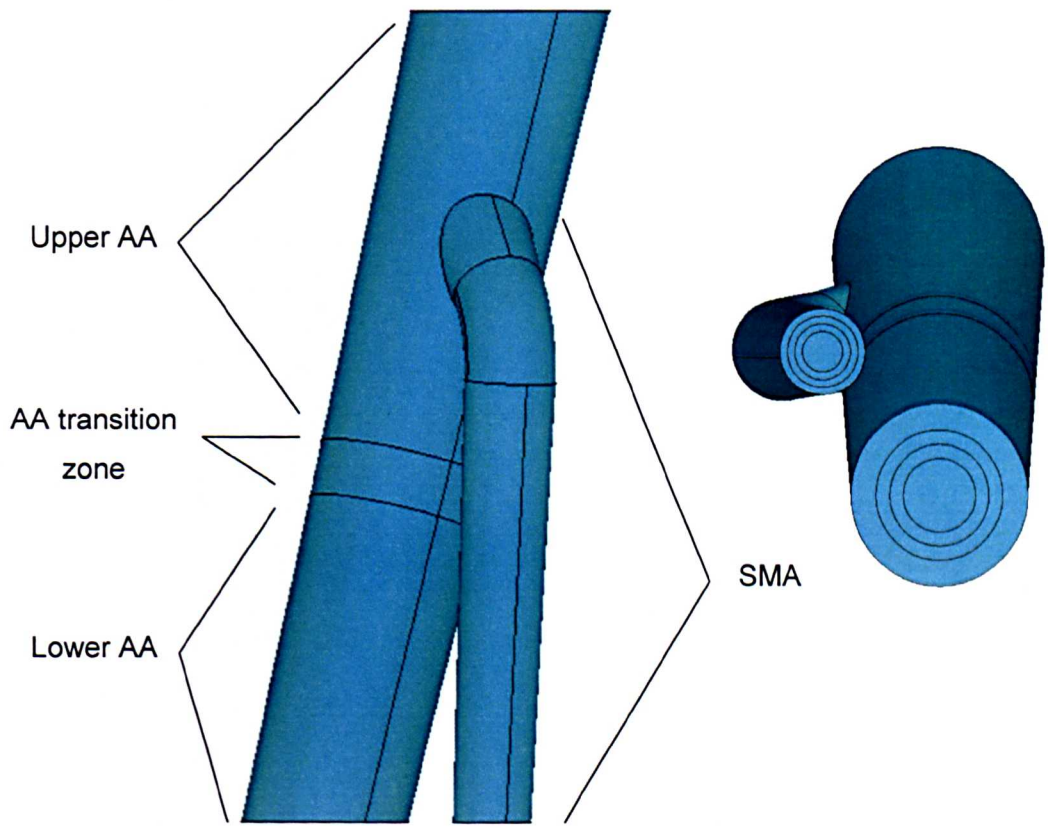

Figure 6.6. Idealised volume model separated into sections for semi-structured meshing.

Mesh Name	Number of:				
	Nodes	Elements	AA Inlet Nodes	AA Outlet Nodes	SMA Nodes
SS1	100 465	526 091	650	295	207
SS2	137 830	722 119	782	295	274
SS3	266 283	1 421 052	1227	295	416

Table 6.2a. Details of semi-structured meshes.

Mesh Name	Element size in millimetres at:					
	AA upper (centre)	AA upper (wall)	AA lower (centre)	AA lower (wall)	SMA (centre)	SMA (wall)
SS1	1.5	0.4	1.5	0.667	1	0.4
SS2	1.5	0.33	1.5	0.667	1	0.33
SS3	1.5	0.25	1.5	0.667	1	0.25

Table 6.2b. Details of semi-structured meshes.

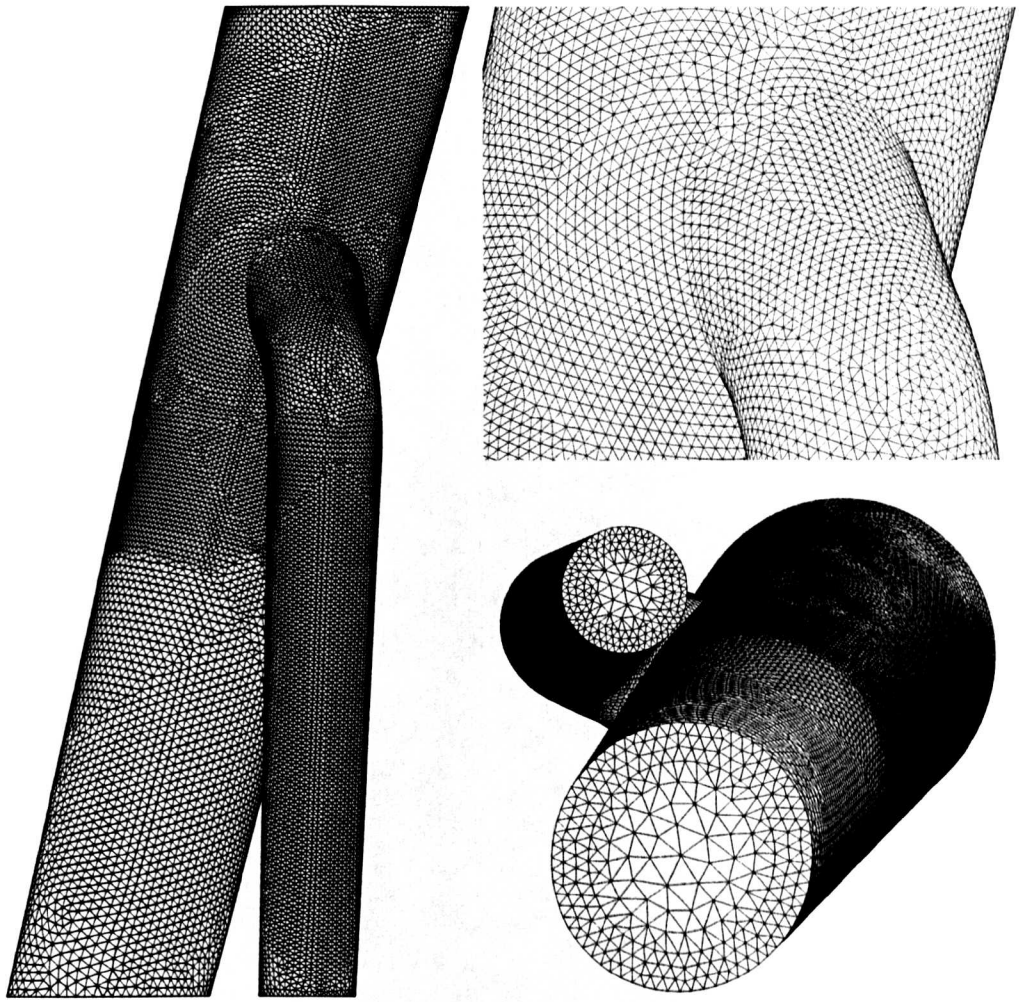

Figure 6.7. Idealised semi-structured mesh (SS1).

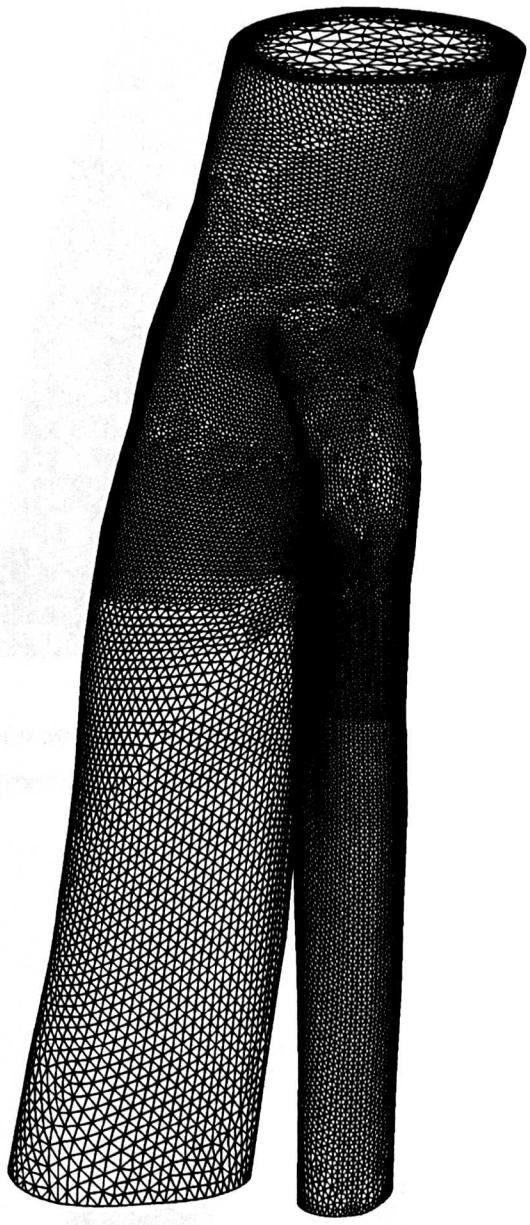

Figure 6.8. Volunteer-specific semi-structured mesh (SS1).

For these meshes, mesh invariance was considered in a wider manner. Firstly, maps of wall shear stress magnitude (WSS in the direction of the local velocity vector) were compared at different time-steps. Secondly eight points were chosen, four around the AA superior to the origin of the SMA, and four around the SMA below its curvature. Patterns of WSS, as well as Peak WSS magnitude, Time-averaged WSS and OSI (as defined in 1.5) were used to assess mesh-dependence.

Figures 6.9 to 6.11 show maps of WSS magnitude for the three meshes at three time steps, relating to peak systole, end systole (with decelerating flow) and end diastole.

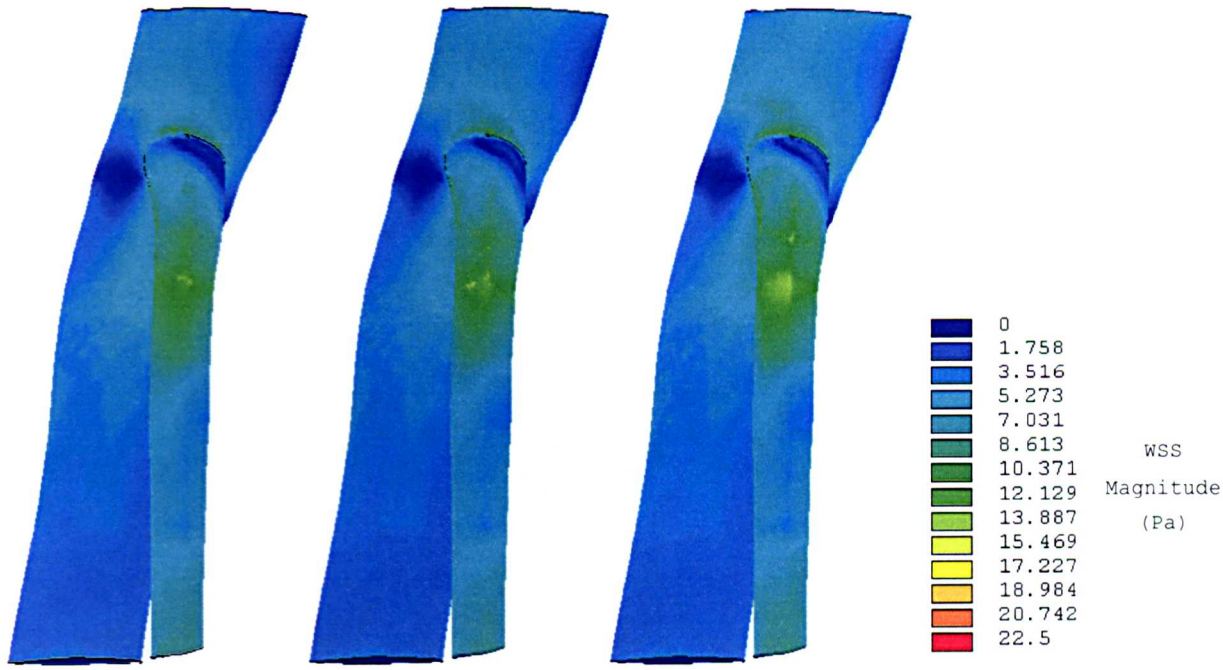

Figure 6.9. WSS magnitude maps at peak systole. Meshes SS1-SS3, left to right (In all cases peak WSS was seen in a small region on the anterior aspect of the SMA at its attachment to the AA).

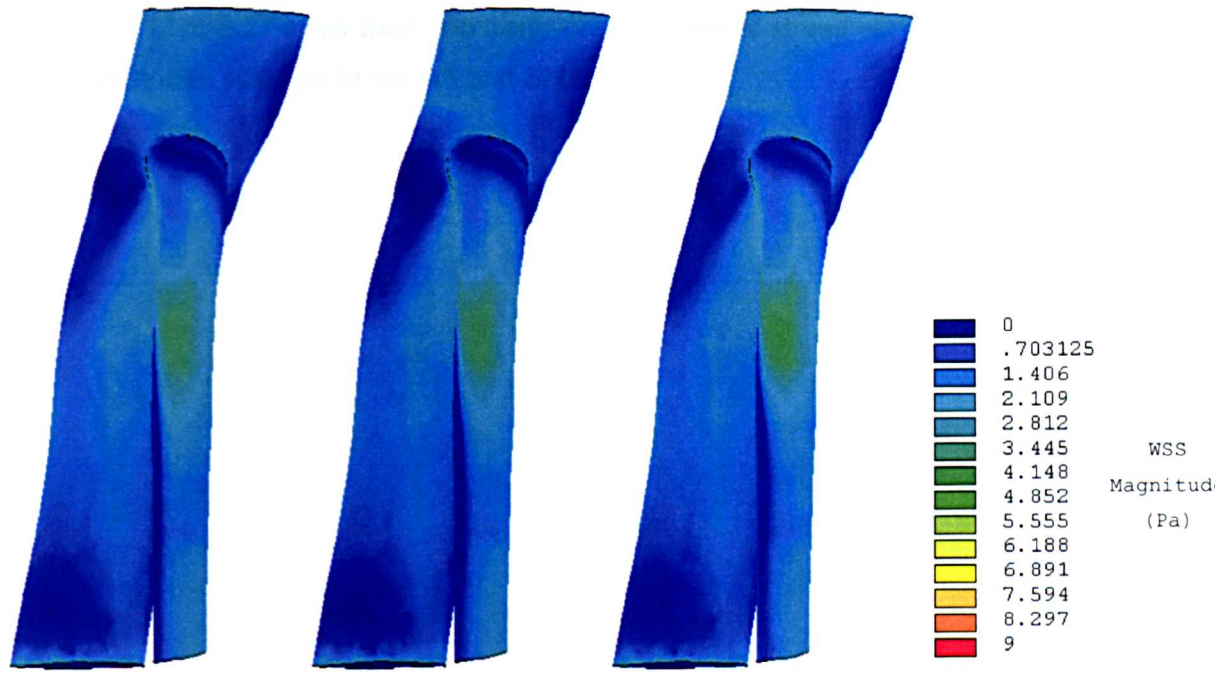

Figure 6.10. WSS magnitude maps at late systole. Meshes SS1-SS3, left to right.

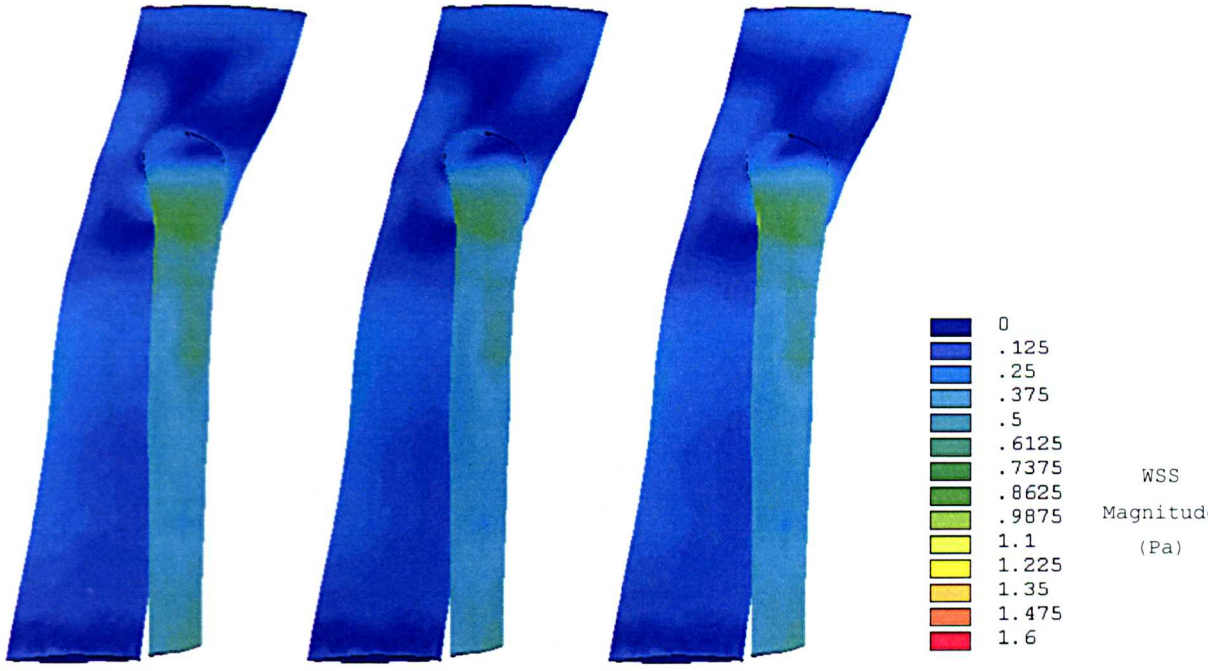

Figure 6.11. WSS magnitude maps at late diastole. Meshes SS1-SS3, left to right.

Clearly from the above figures, WSS magnitude distributions were very similar for all three models at the three timesteps chosen. There were slight variations in local values, but crucially, the same WSS (and therefore flow) patterns were predicted for all three meshes.

Figures 6.12 to 6.27 show axial and transverse wall shear stress varying with time for the eight nodes selected in the AA and SMA.

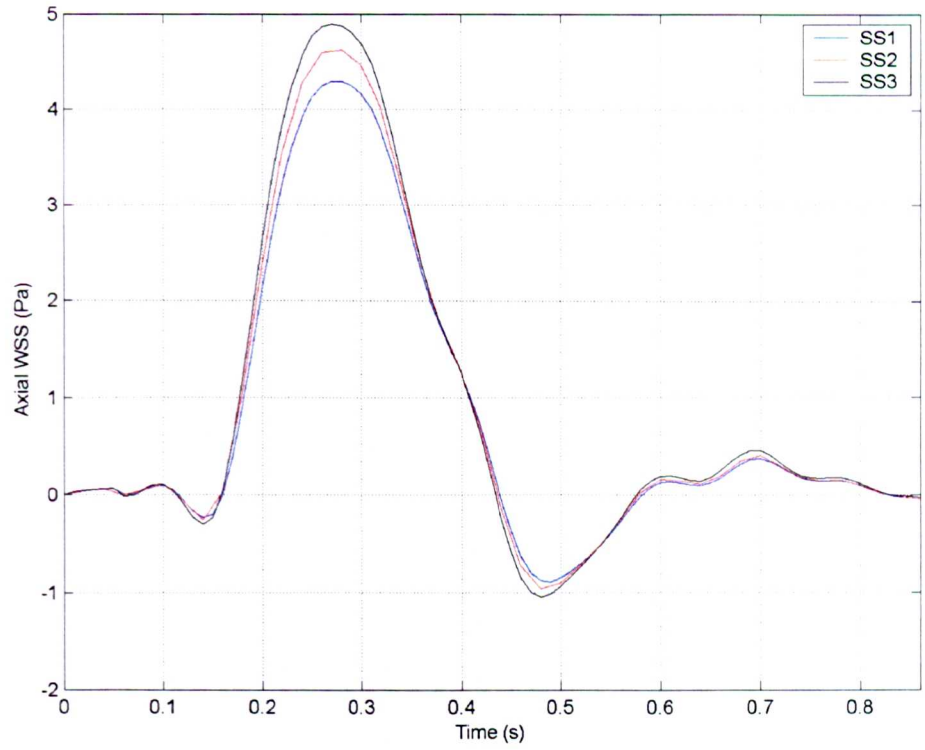

Figure 6.12. Time-varying axial WSS for node on anterior wall of aorta, superior to the SMA.

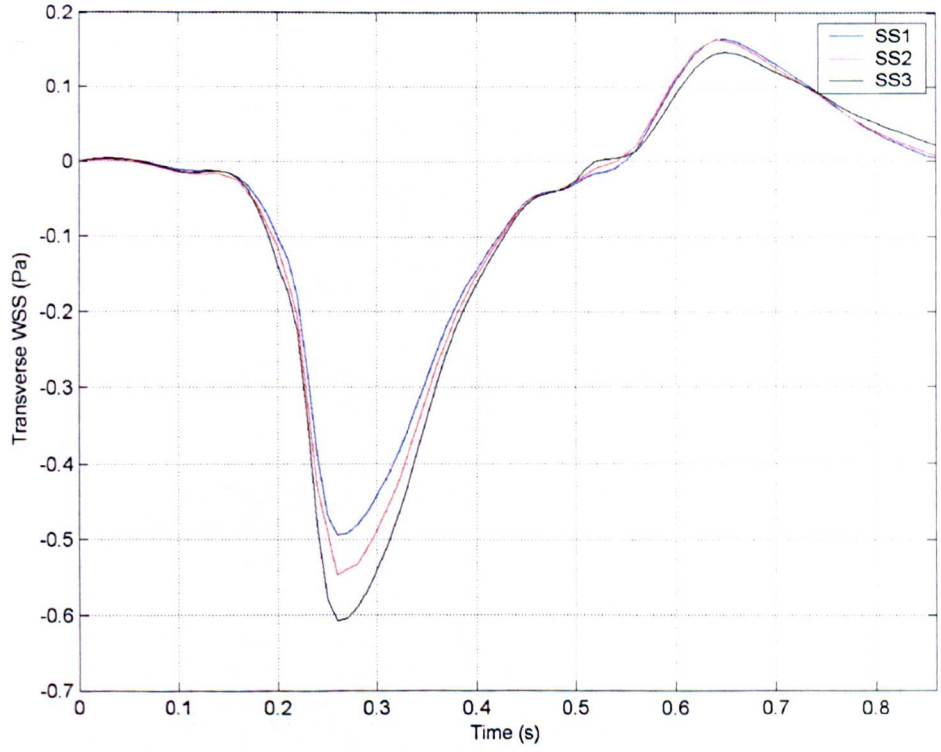

Figure 6.13. Time-varying transverse WSS for node on anterior wall of aorta, superior to the SMA.

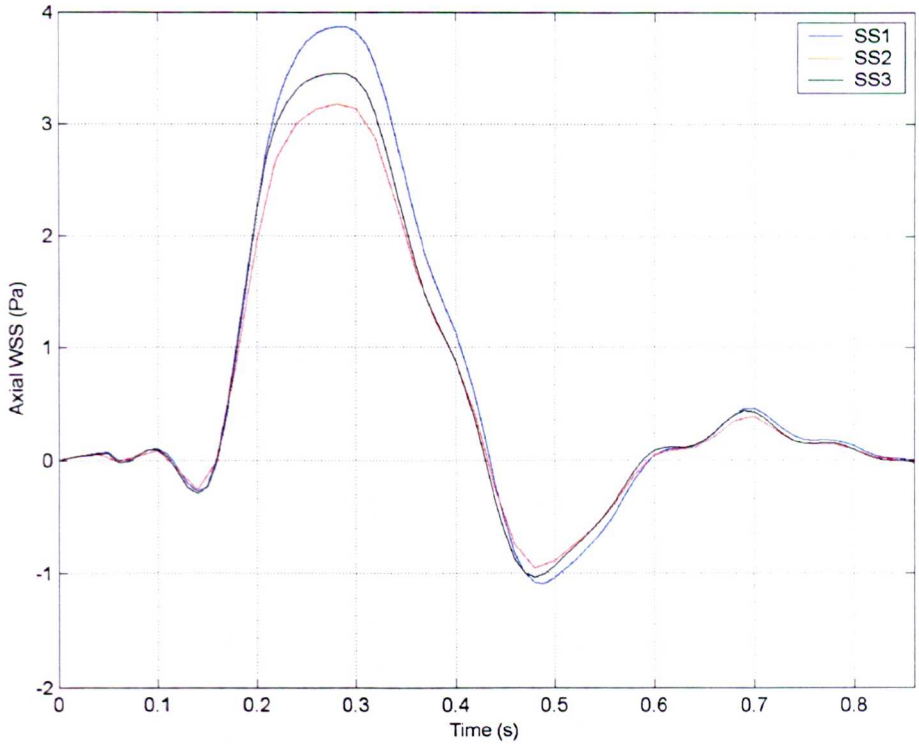

Figure 6.14. Time-varying axial WSS for node on posterior wall of aorta, superior to the SMA

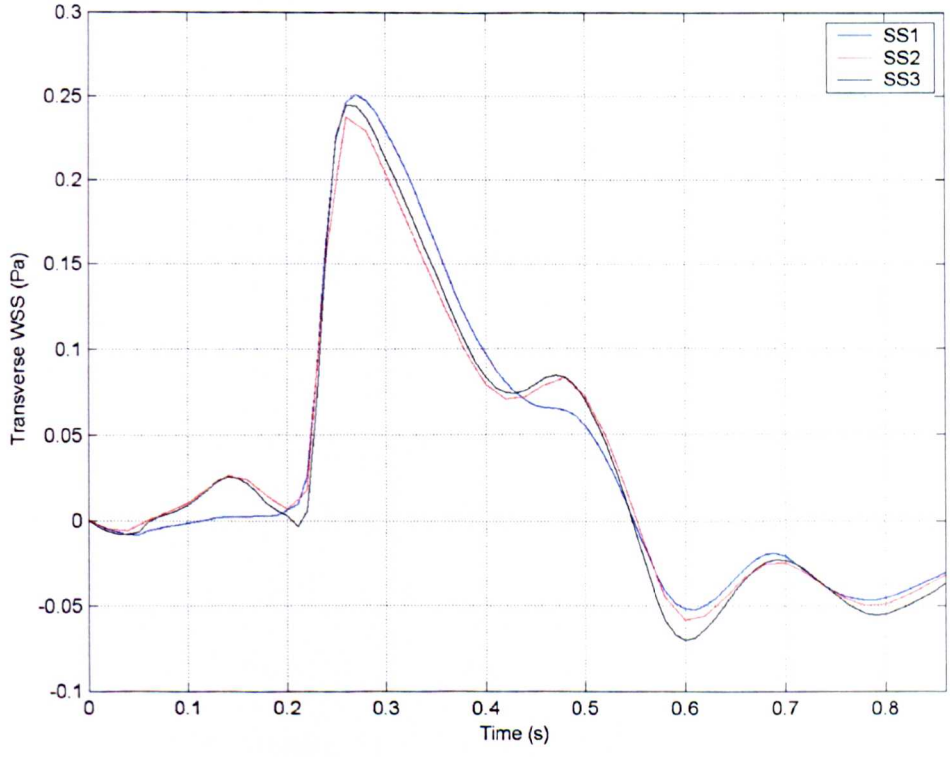

Figure 6.15. Time-varying transverse WSS for node on posterior wall of aorta, superior to the SMA.

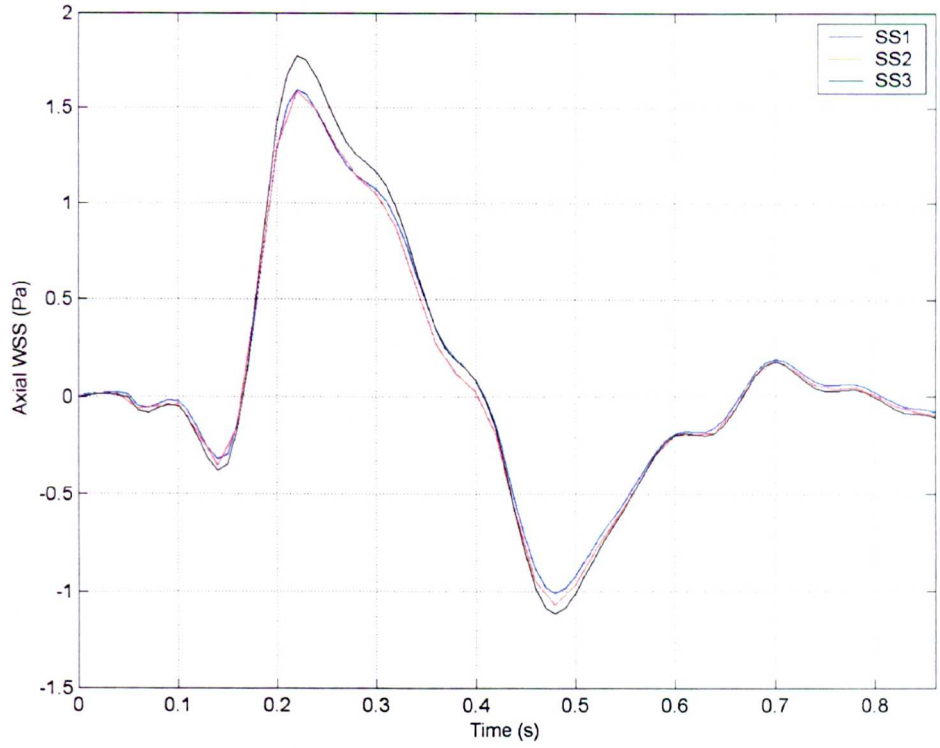

Figure 6.16. Time-varying axial WSS for node on left wall of aorta, superior to the SMA.

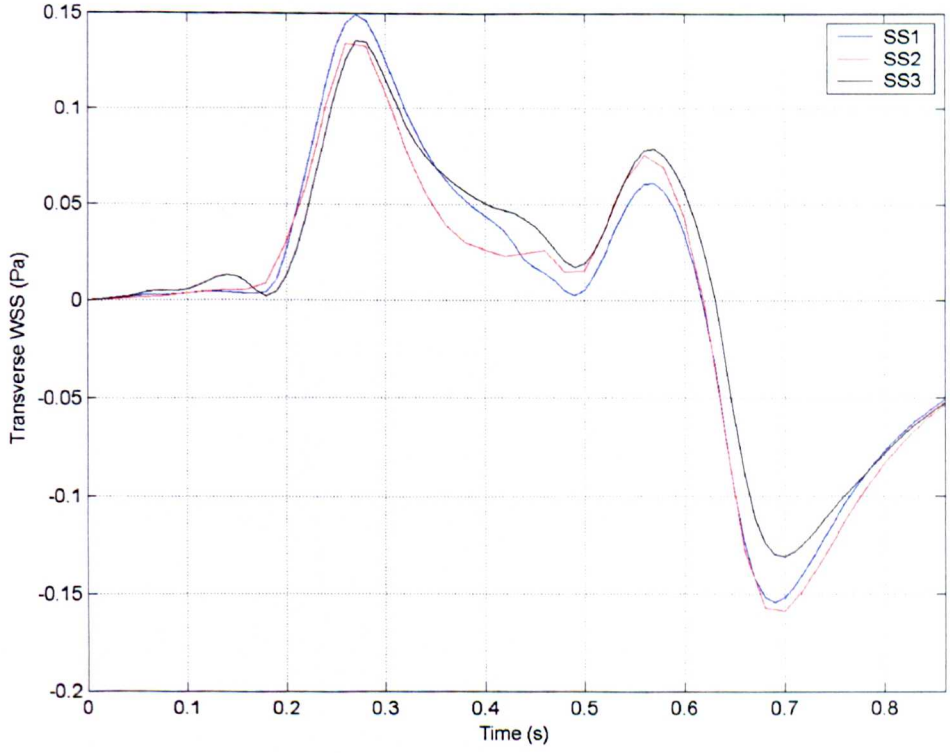

Figure 6.17. Time-varying transverse WSS for node on left wall of aorta, superior to the SMA.

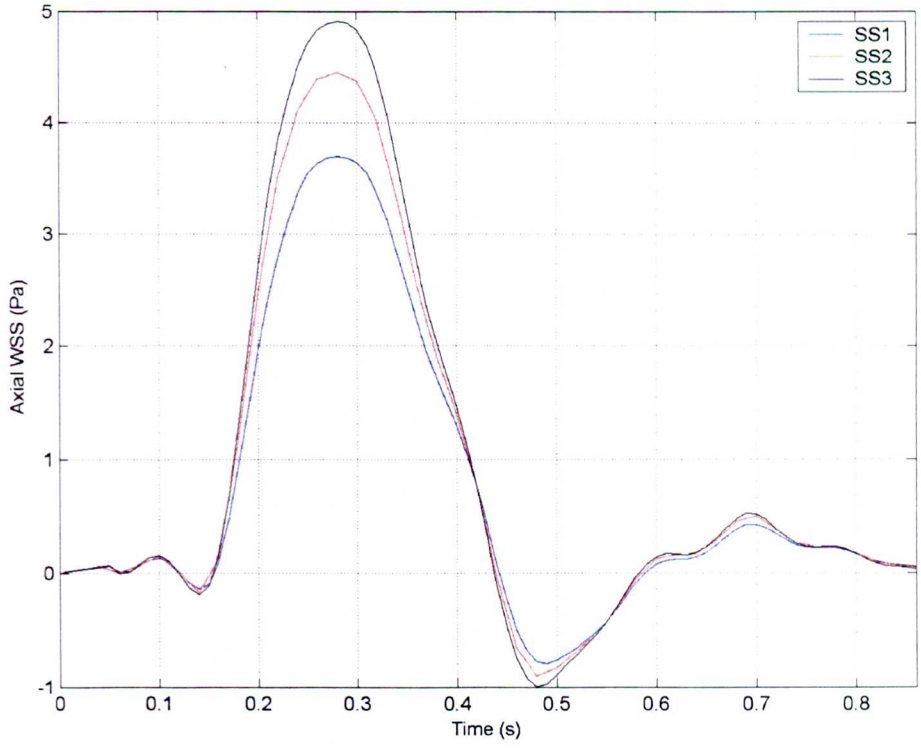

Figure 6.18. Time-varying axial WSS for node on right wall of aorta, superior to the SMA.

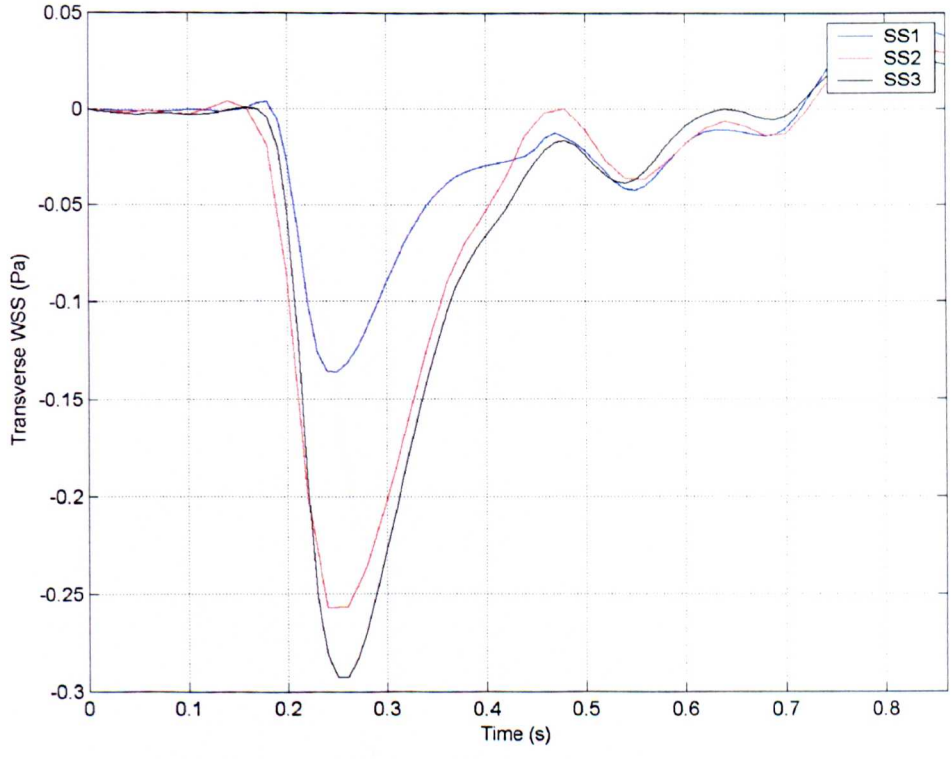

Figure 6.19. Time-varying transverse WSS for node on right wall of aorta, superior to the SMA.

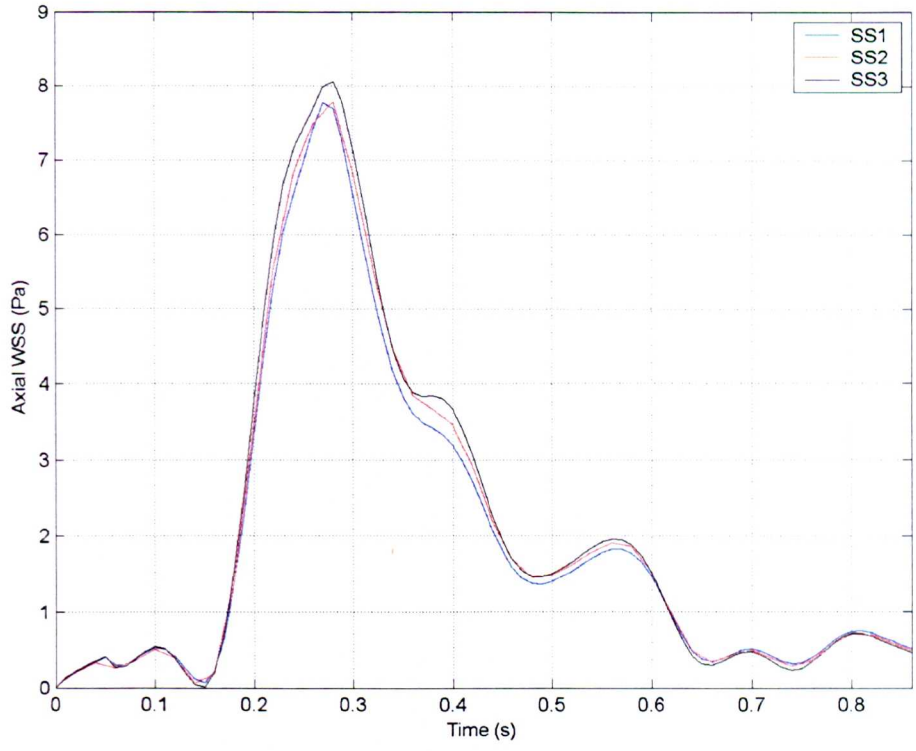

Figure 6.20. Time-varying axial WSS for node on anterior wall of SMA, inferior to its curvature.

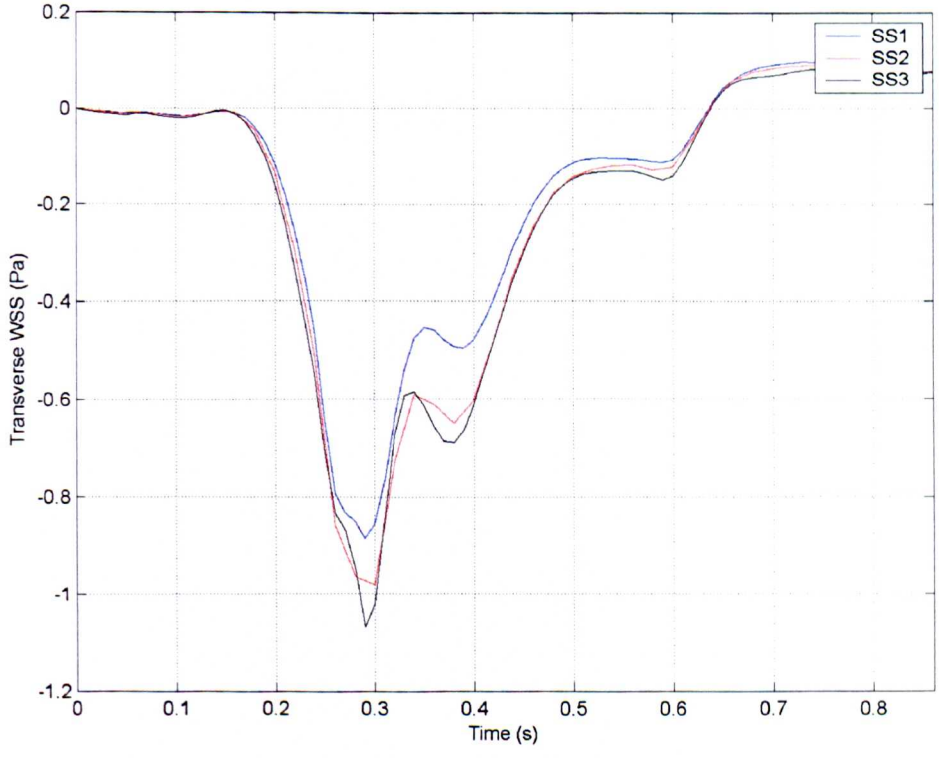

Figure 6.21. Time-varying transverse WSS for node on anterior wall of SMA, inferior to its curvature.

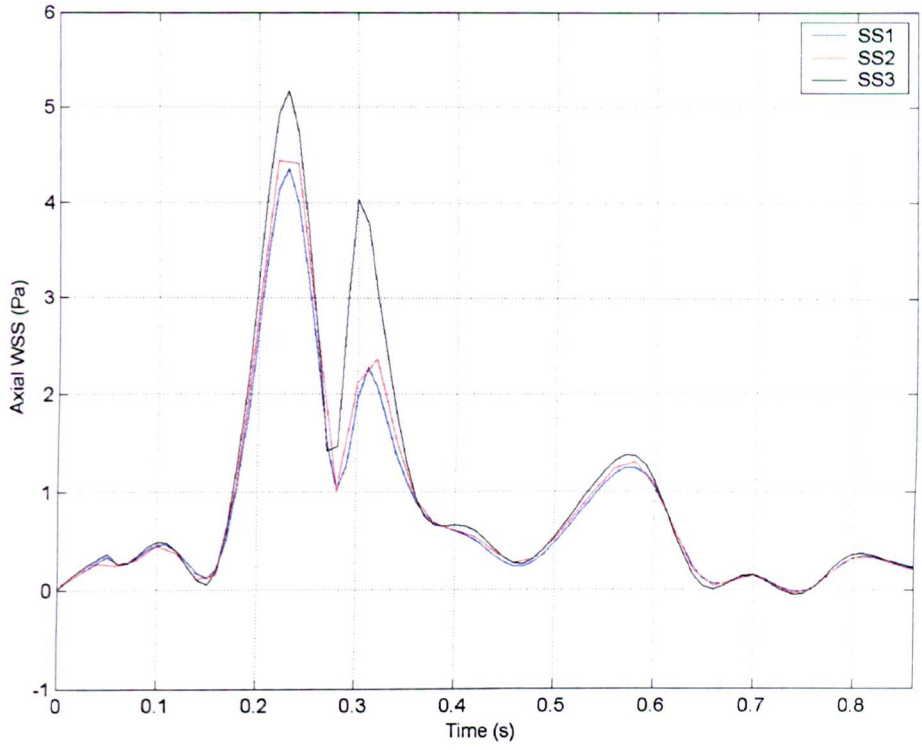

Figure 6.22. Time-varying axial WSS for node on posterior wall of SMA, inferior to its curvature.

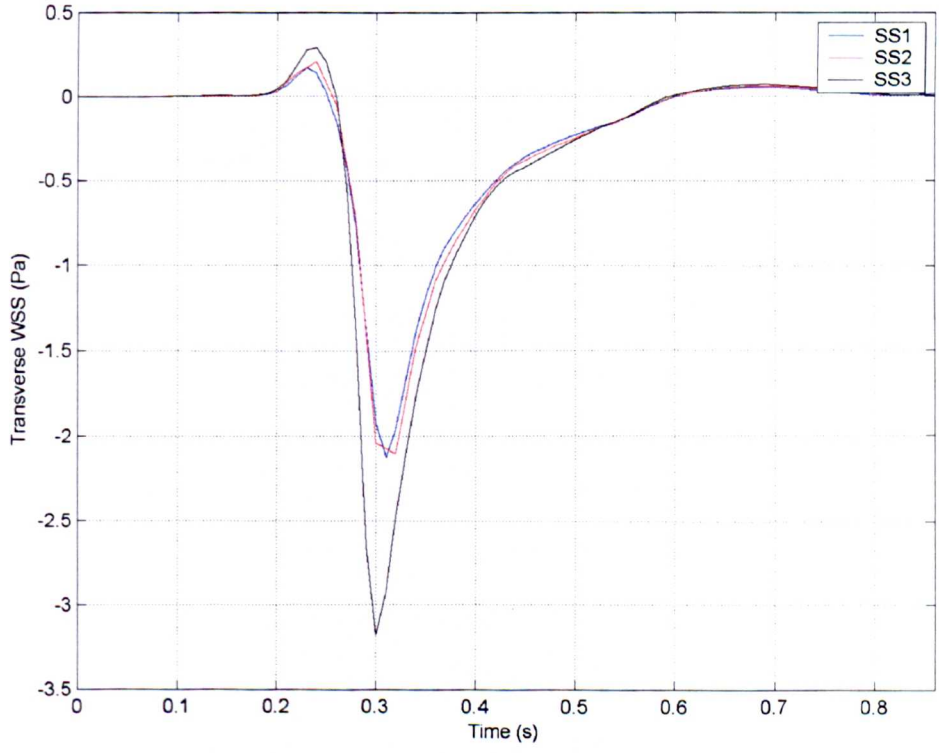

Figure 6.23. Time-varying transverse WSS for node on posterior wall of SMA, inferior to its curvature.

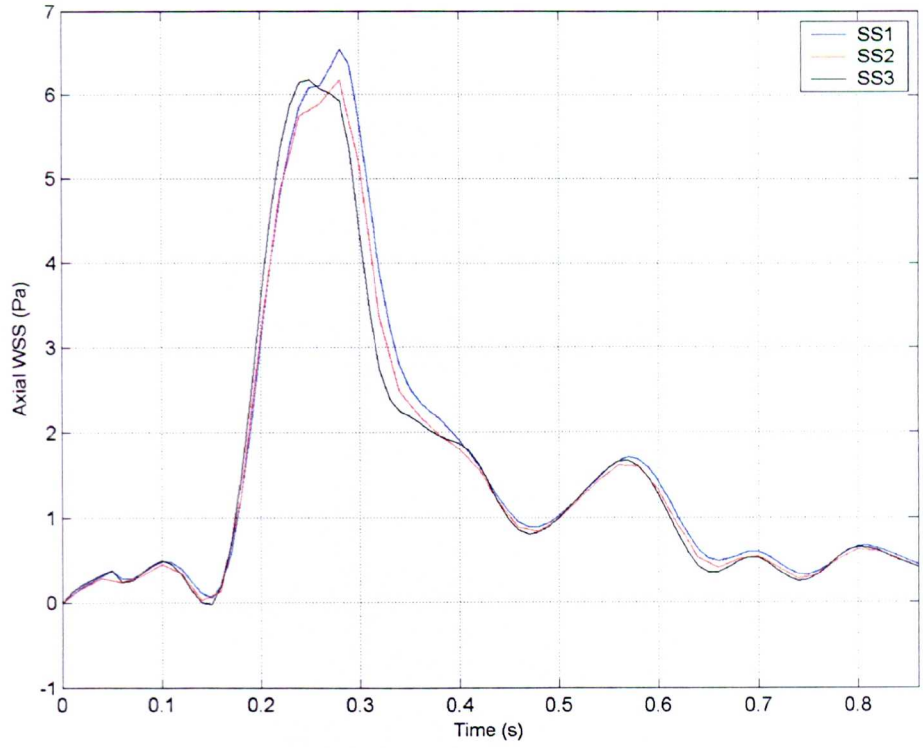

Figure 6.24. Time-varying axial WSS for node on left wall of SMA, inferior to its curvature.

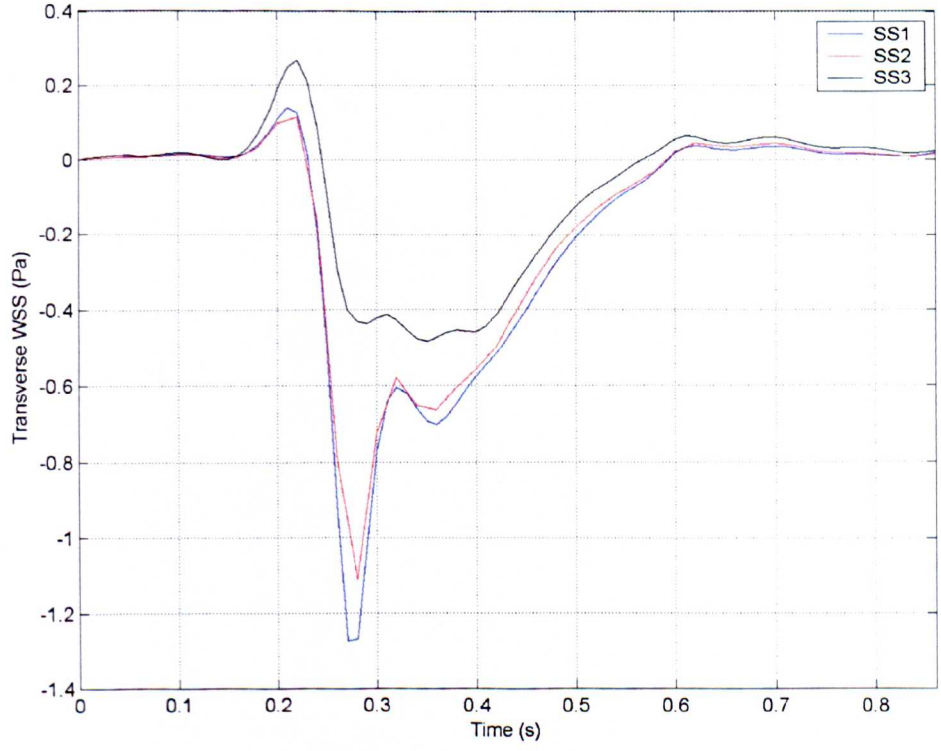

Figure 6.25. Time-varying transverse WSS for node on left wall of SMA, inferior to its curvature.

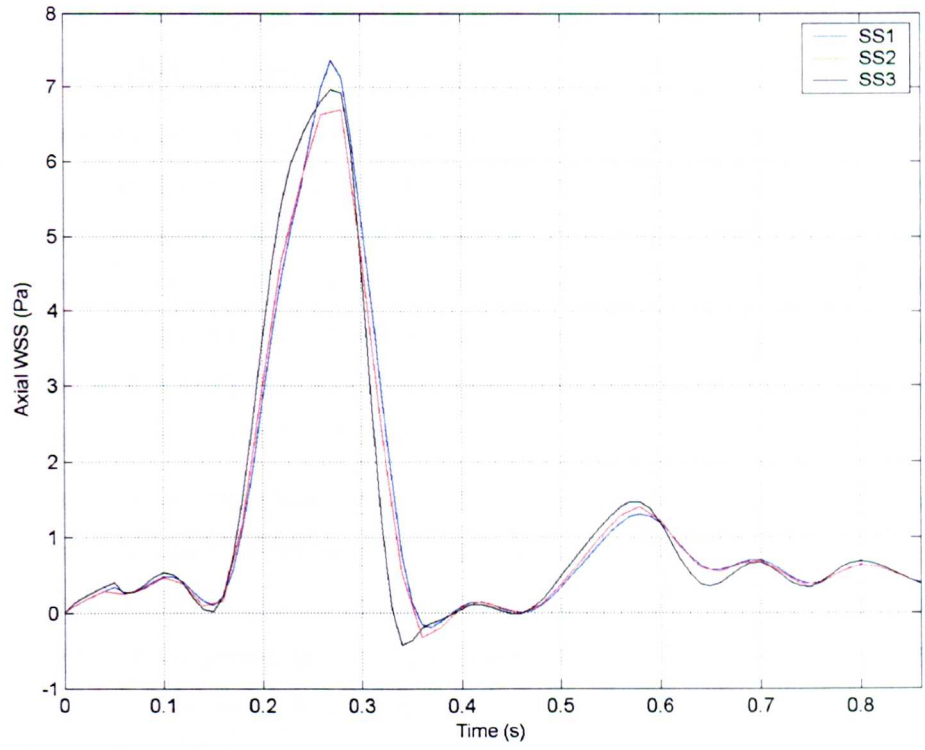

Figure 6.26. Time-varying axial WSS for node on right wall of SMA, inferior to its curvature.

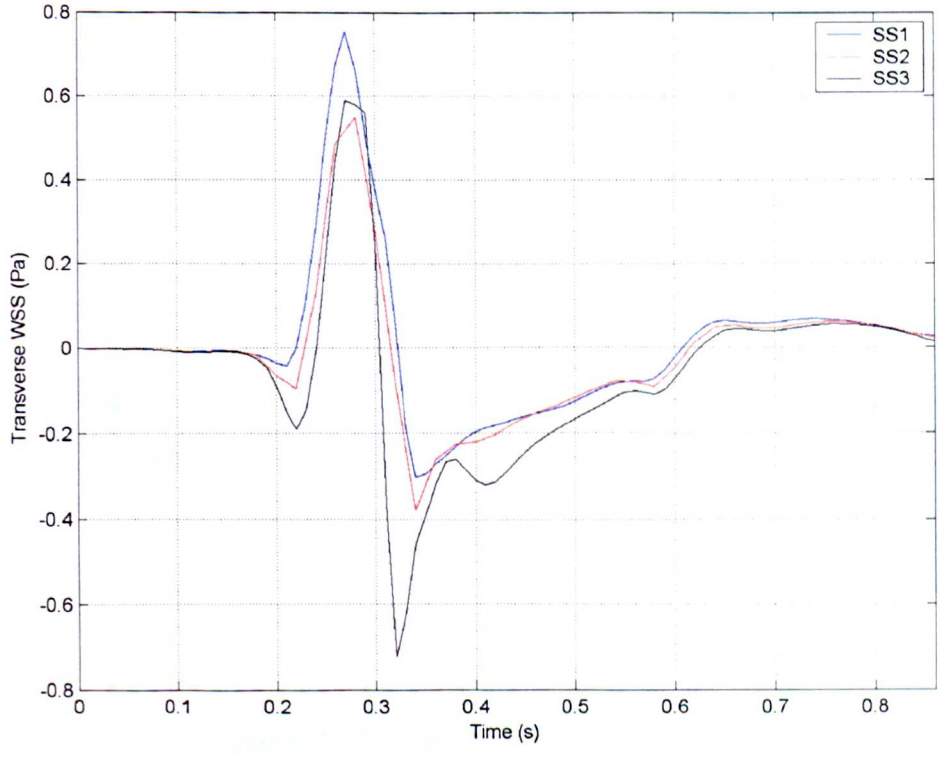

Figure 6.27. Time-varying transverse WSS for node on right wall of SMA, inferior to its curvature.

In all cases, the axial WSS results were qualitatively reproducible; the general shape of each curve did not change substantially with the mesh. Where WSS reversal did occur, this was reflected in all three meshes.

Measurements taken at the anterior, posterior and left walls of the AA showed good agreement, as did axial WSS on the right of the AA, in the one case exhibiting substantial disagreement in terms of transverse WSS, on the right wall of the aorta (as shown in figure 6.19), the transverse WSS itself was very small (approximately 6% of the axial WSS) and this difference only represents a very small change in WSS vector, so it is likely that this could have been caused by a small change in local surface normal due to the different meshes.

The differences and similarities between the two time-varying vectors can be seen by creating a plot with axial WSS on one axis and transverse WSS on the other, the WSS vector is plotted at each point in time with each vector coloured according to this time. Figure 6.28 shows an example of such a plot with axial and transverse WSS varying cosinusoidally and sinusoidally respectively over a 0.86 second heartbeat. Figure 6.29 shows equivalent plots for the node on the right wall of the SMA, clearly the overall shape of the waves is not significantly changed.

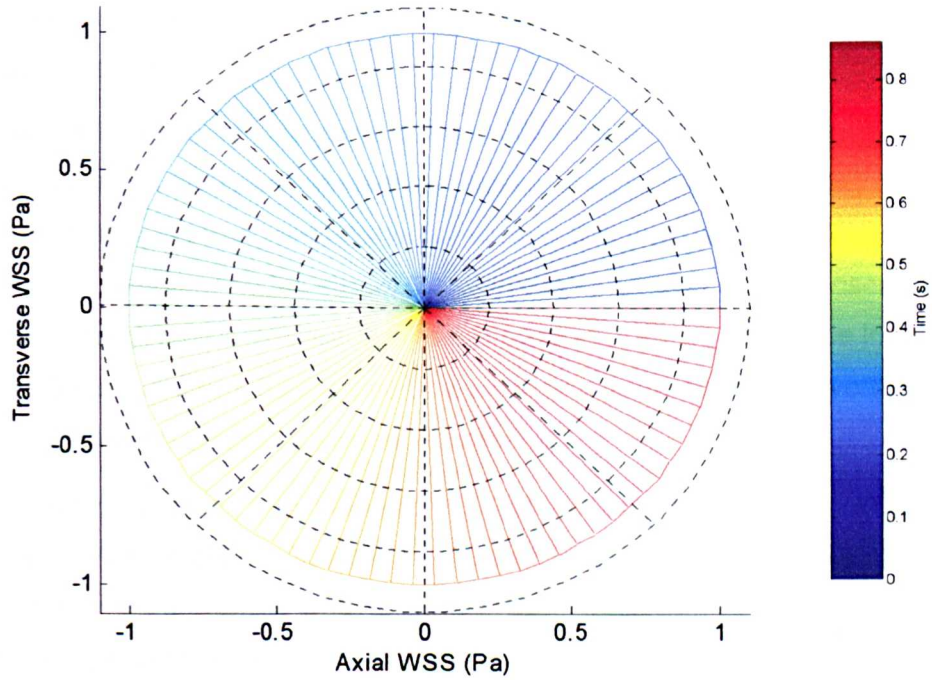

Figure 6.28. Example time-varying vector plot.

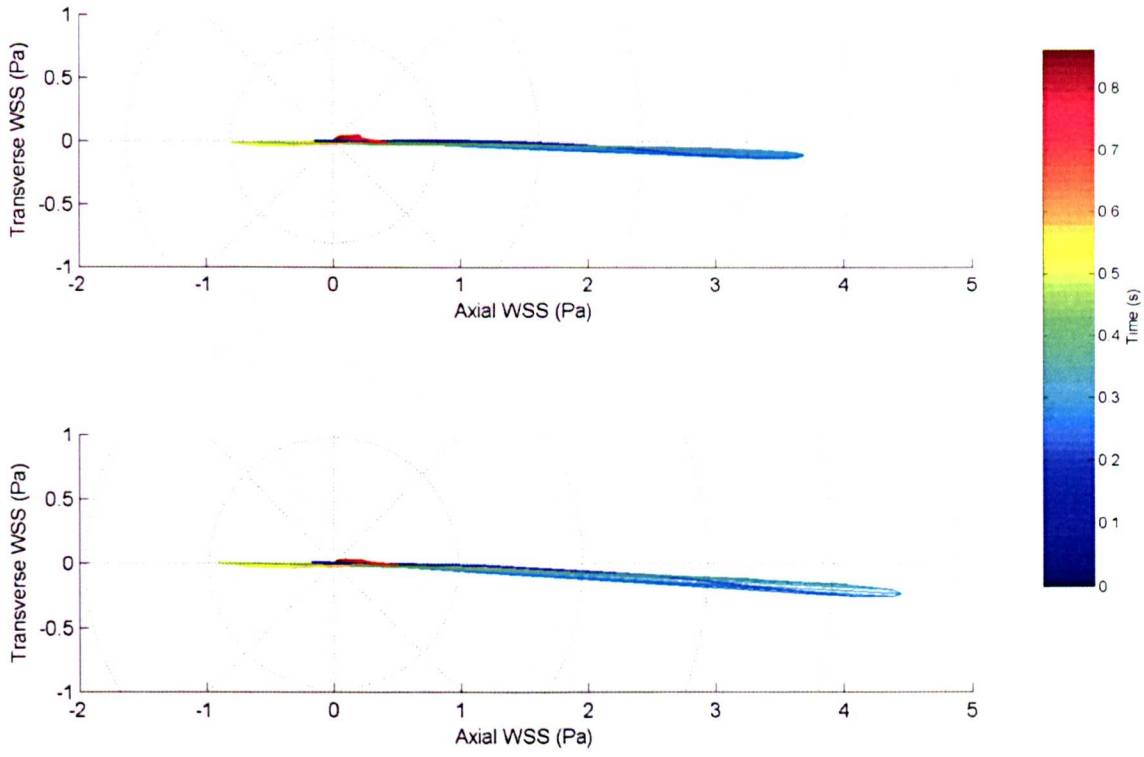

Figure 6.29. Time-varying vector plot showing WSS for node on right wall of aorta (mesh SS1 – above, mesh SS2 – below).

For the SMA, the most significant inter-mesh differences were seen in axial WSS on the posterior wall, and transverse WSS on the left wall, both during the decelerating flow, late-systole period.

Figure 6.30 shows flow through the plane of the 4 SMA nodes at the point of maximum disagreement between the meshes (looking distally along the SMA). The flow is characterised by a strong anti-clockwise vortex. The good agreement in transverse WSS at the other nodes shows that this vortex is being characterised in the same way by the different meshes. It is therefore likely that the difference in transverse WSS seen in figure 6.25 is due to a small difference in how this vortex forms and the transverse boundary layer is diminished.

Figure 6.31 shows flow through the plane of the SMA nodes at the time of peak difference in axial WSS shown in figure 6.22. A small volume of reversed flow can be seen close to the posterior wall of the SMA, this is associated with separation of the flow from the wall as seen in the posterior part of 6.30, a small change in the exact behaviour of this region is likely to have caused the difference between the results seen in figure 6.22.

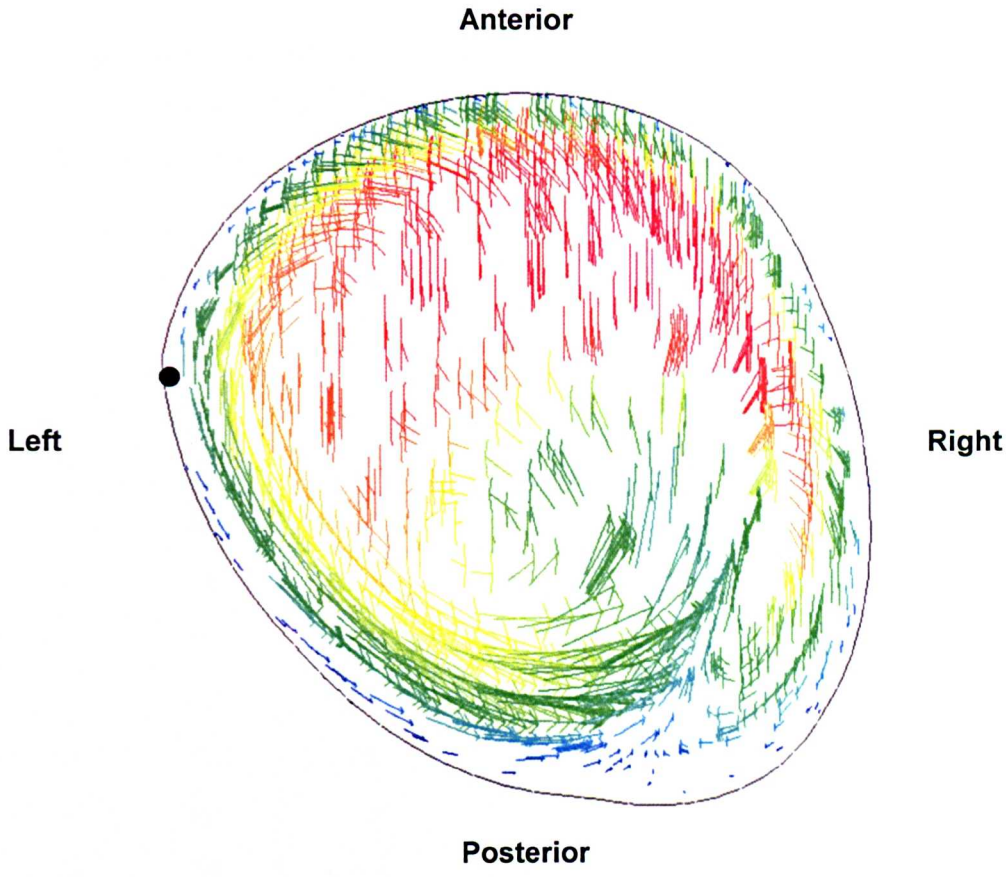

Figure 6.30. Vector plot of flow through and across plane of SMA nodes at time of peak difference between transverse shear results at left node (marked with black dot), based on mesh SS1 results.

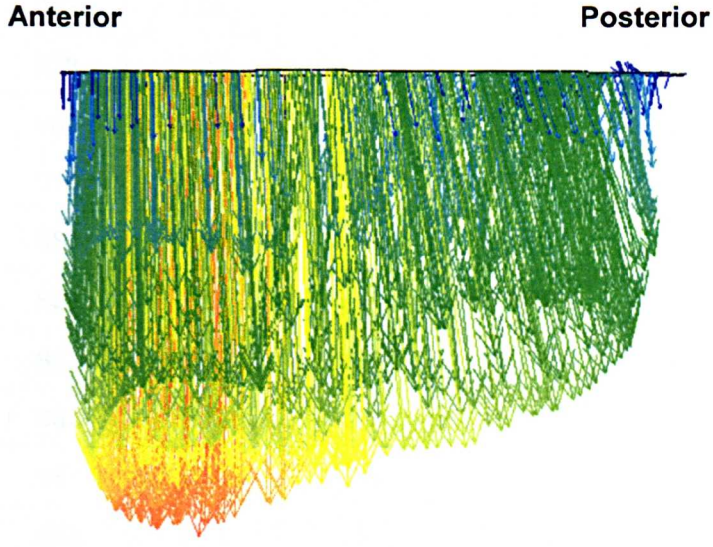

Figure 6.31. Vector plot of flow through plane of SMA nodes, at time of peak difference in axial WSS results at posterior node.

Table 6.3 presents peak and mean axial and transverse WSS, and OSI (as given by equation 1.5) for each of the eight nodes selected. Table 6.4 presents means of this data over the 3 meshes, and maximum percentage deviation from this mean.

Node	Mesh	Mean WSS (Axial)	Peak WSS Magnitude (Axial)	Mean WSS (Transverse)	Peak WSS Magnitude (Transverse)	OSI
AA Anterior	SS1	0.772	4.28	-0.0567	0.494	0.108
AA Anterior	SS2	0.821	4.62	-0.0638	0.548	0.106
AA Anterior	SS3	0.877	4.90	-0.0744	0.608	0.108
AA Posterior	SS1	0.694	3.87	0.0373	0.246	0.139
AA Posterior	SS2	0.555	3.17	0.0314	0.237	0.148
AA Posterior	SS3	0.614	3.45	0.0311	0.244	0.146
AA Left	SS1	0.092	1.59	0.0021	0.154	0.394
AA Left	SS2	0.068	1.59	-0.0013	0.159	0.423
AA Left	SS3	0.093	1.77	0.0084	0.135	0.401
AA Right	SS1	0.727	3.69	-0.0207	0.136	0.0993
AA Right	SS2	0.857	4.44	-0.0421	0.257	0.0915
AA Right	SS3	0.95	4.91	-0.0469	0.293	0.0908
SMA Anterior	SS1	1.94	7.77	-0.1582	0.886	0.0014
SMA Anterior	SS2	1.99	7.77	-0.1887	0.981	0.0015
SMA Anterior	SS3	2.08	8.05	-0.199	1.07	0.0013
SMA Posterior	SS1	0.790	4.35	-0.2358	2.13	0.0382
SMA Posterior	SS2	0.824	4.42	-0.2391	2.11	0.0394
SMA Posterior	SS3	0.958	5.18	-0.303	3.18	0.0401
SMA Left	SS1	1.58	6.55	-0.1807	1.28	0.0038
SMA Left	SS2	1.48	6.18	-0.1619	1.11	0.0038
SMA Left	SS3	1.49	6.18	-0.0862	0.484	0.0032
SMA Right	SS1	1.20	7.36	0.0115	0.750	0.0150
SMA Right	SS2	1.15	6.70	-0.0116	0.545	0.0195
SMA Right	SS3	1.19	6.96	-0.0542	0.722	0.0294

Table 6.3 Temporal peak and mean WSS, and OSI data.

Node	Measure	Mean WSS (Axial)	Peak WSS Magnitude (Axial)	Mean WSS (Transverse)	Peak WSS Magnitude (Transverse)	OSI
AA Anterior	Mean	0.823	4.60	-0.0650	0.55	0.107
AA Anterior	Variation	6.52%	6.96%	-14.5%	10.5%	0.267%
AA Posterior	Mean	0.621	3.50	0.0333	0.242	0.144
AA Posterior	Variation	11.8%	10.7%	12.1%	2.20%	1.07%
AA Left	Mean	0.0843	1.65	0.00307	0.149	0.406
AA Left	Variation	19.4%	7.27%	174%	9.60%	3.40%
AA Right	Mean	0.845	4.35	-0.037	0.229	0.0939
AA Right	Variation	13.9%	15.1%	-43.4%	40.5%	1.09%
SMA Anterior	Mean	2.00	7.86	-0.182	0.979	0.00140
SMA Anterior	Variation	3.83%	2.37%	-13.1%	9.50%	0.02%
SMA Posterior	Mean	0.857	4.65	-0.259	2.47	0.0392
SMA Posterior	Variation	11.7%	11.34%	-16.9%	28.6%	0.207%
SMA Left	Mean	1.52	6.30	-0.143	0.958	0.0036
SMA Left	Variation	4.18%	3.91%	-39.7%	49.5%	0.08%
SMA Right	Mean	1.18	7.01	-0.0181	0.672	0.0213
SMA Right	Variation	2.54%	5.04%	-199%	18.9%	1.62%

Table 6.4. Means and variations of WSS and OSI between meshes (WSS variations presented as a percentage of the mean value over the three meshes, OSI variation measured as a percentage of possible OSI range (0-0.5).

Mean and peak axial WSS were on average converged to within 9.2% and 7.8% respectively; maximum percentage variations were 19.4% and 15.1% respectively.

Due to the flow features described above and the very small transverse components in some cases (as little as 3.5% of the equivalent axial value), mean and peak transverse WSS exhibited up to 200% and 50% variations between the meshes, respectively; mean variations were 17.6% and 21.2% respectively.

The more global measure of OSI showed much better convergence with each value within 3.4% agreement between the meshes.

Although some small differences existed between meshes, investigation of the flow field, showed that these were due to subtle effects and that the key features of the flow and WSS fields were adequately captured by all three semi-structured meshes; to minimise computational time (in both the solution and post-processing phases) the coarsest mesh (SS1) was chosen to be used for all further analyses.

6.2.2 – Time-step Convergence

Once the appropriate mesh had been chosen, time-step convergence was checked by once more considering the same wall shear stress parameters and varying the timestep of the model.

Analyses were run using timesteps of 1,2 and 5 ms, wall shear stress histories at the 8 nodes used previously were once more used to measure convergence.

Peak axial WSS for all timesteps was within 6.9% of the mean value for the three timesteps at all nodes; the mean difference over all eight nodes was 0.57%.

Peak transverse WSS for all timesteps was within 7.4% of the mean value for the three timesteps at all nodes; the mean difference over all eight nodes was 0.75%.

Time-averaged axial WSS for all timesteps was within 4.2% of the mean value for the three timesteps at all nodes; the mean difference over all eight nodes was 0.15%.

Time-averaged transverse WSS for all timesteps was within 9.8% of the mean value for the three timesteps at all nodes; the mean difference over all eight nodes was 0.53%.

OSI for all timesteps was within 0.7% of OSI range at all nodes.

Figures 6.32 to 6.35 show time-varying axial and transverse WSS for all 8 nodes with the three timesteps.

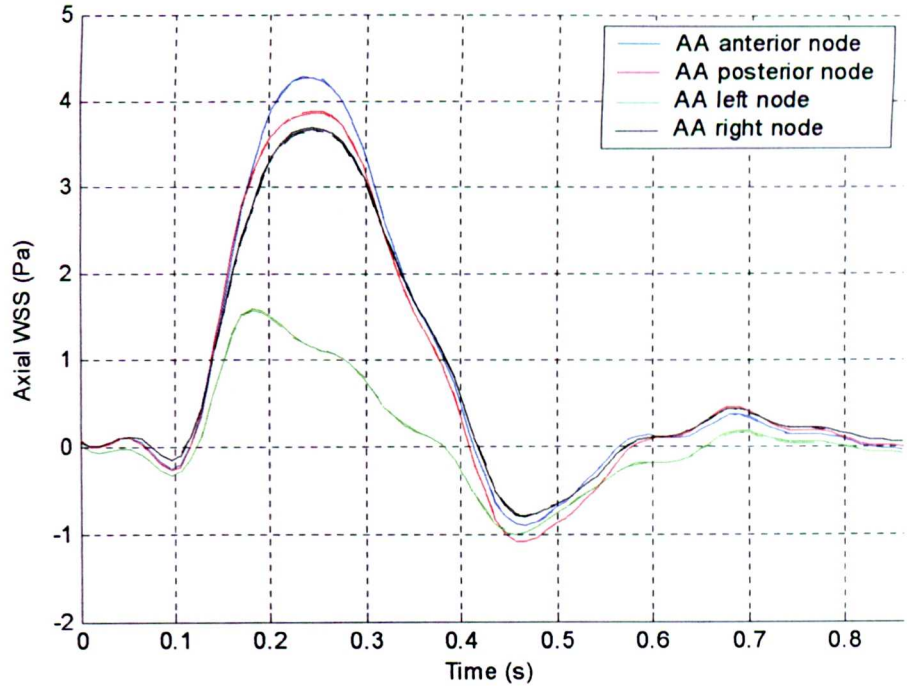

Figure 6.32. Time-varying axial WSS for 4 nodes on AA (continuous line represents 5ms timestep, dashed line represents 2ms timestep, dot/dashed line represents 1ms timestep). In each case all three lines overlap.

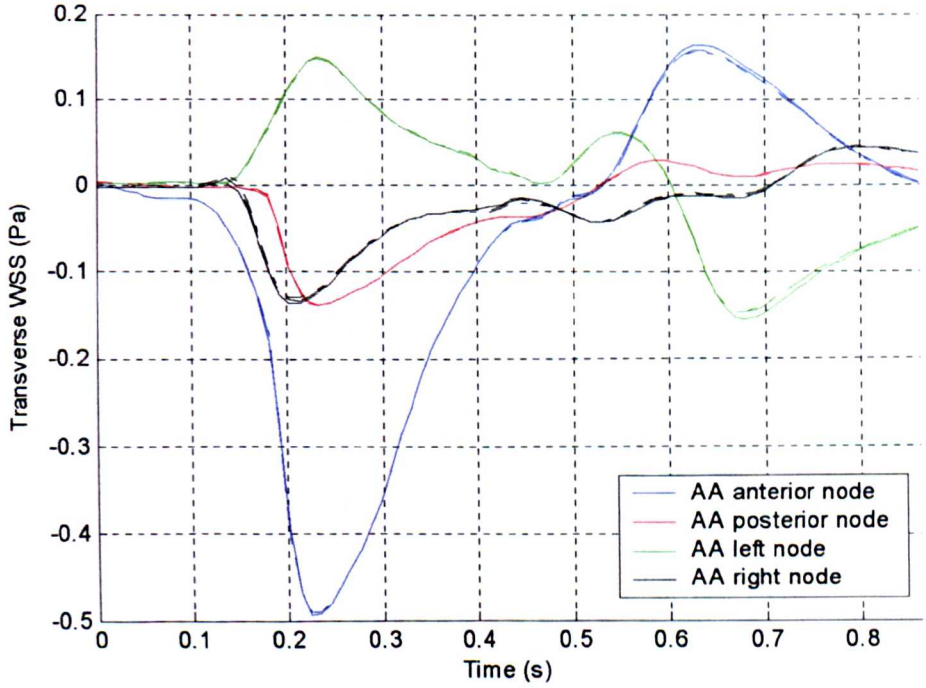

Figure 6.33. Time-varying transverse WSS for 4 nodes on AA (continuous line represents 5ms timestep, dashed line represents 2ms timestep, dot/dashed line represents 1ms timestep).

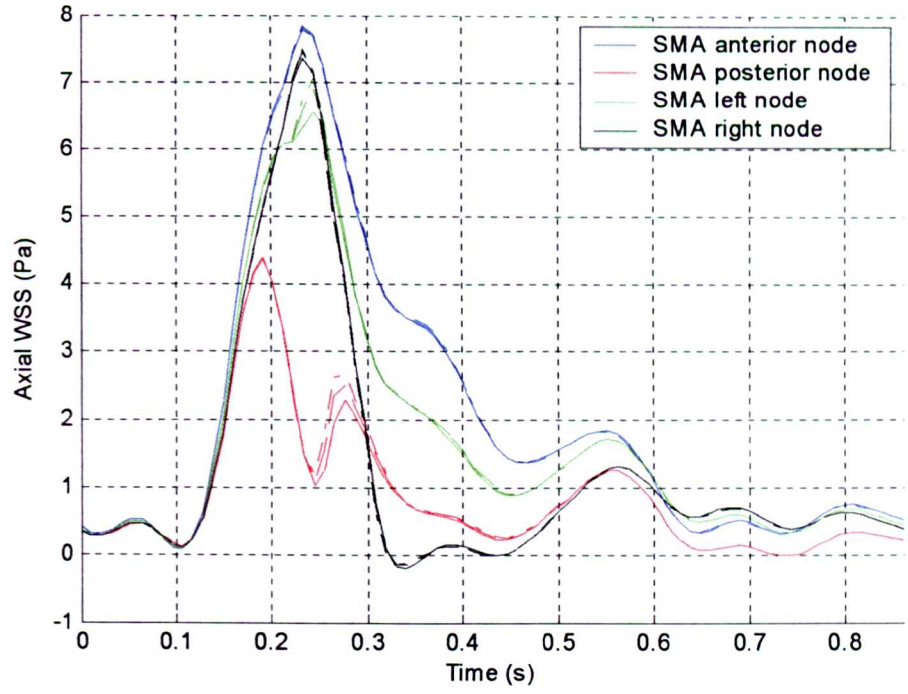

Figure 6.34. Time-varying axial WSS for 4 nodes on SMA (continuous line represents 5ms timestep, dashed line represents 2ms timestep, dot/dashed line represents 1ms timestep).

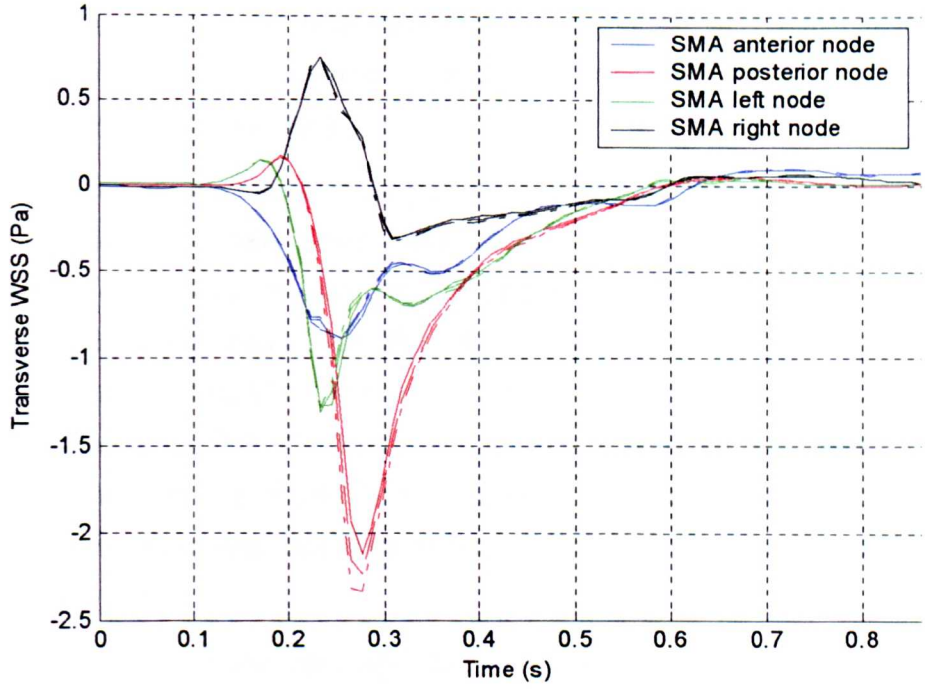

Figure 6.35. Time-varying transverse WSS for 4 nodes on SMA (continuous line represents 5ms timestep, dashed line represents 2ms timestep, dot/dashed line represents 1ms timestep).

In conclusion, there were small differences between the results for the different timesteps; these differences were smaller than those observed between the meshes. Peak and Time-averaged WSS agreed to within 10% for the different meshes. OSI agreed to within less than 1%.

The results for the different timesteps suggest that all three timesteps capture the important flow features; the results were successfully converged to within 10% in terms of peak and mean WSS for all nodes measured. Taking these results and run-time considerations into account it was decided to use a 5ms timestep for all following runs.

6.2.3 – Initial Conditions and Harmonic Convergence

Harmonic convergence of a pulsatile system is concerned with how the initial conditions in a model affect its solution, and the diminution of these effects with increasing simulation time. The key test of harmonic convergence is whether two consecutive cycles produce differing results.

The initial conditions for the analysis were zero flow and pressure everywhere in the fluid domain. For the proximal and distal AA openings (where velocity components were specified as the boundary conditions), the analysis started by ramping the nodal velocities from zero to the initial velocity values calculated in 5.3, this took place over 50ms. At the end of the ramp, the cardiac cycle started and nodal boundary conditions based on that were used.

Harmonic convergence was investigated by running the chosen mesh and time-step for three cardiac cycles. Once more, WSS at the eight chosen nodes was the parameter considered. It was found that the maximum difference in axial WSS (normalised against peak axial WSS in the second cycle) between the first and second cycles was 22.6%; the same measure between the second and third cycles gave a value of just 0.016%. Similar results were found for the transverse WSS, with a maximum difference of 24.5% for the first two cycles reducing to 0.16% for the second and third cycles. OSI likewise showed minimal variation between the second and third cycles.

It is clear that harmonic convergence had been achieved by the beginning of the second cardiac cycle. For this reason, results for the second cardiac cycle will be used throughout the following sections.

6.2.4 – Solver Convergence

Throughout the runs carried out for the previous sections, solver performance and convergence were monitored. The convergence monitor used by Flotran is the normalised change of solution variable (summed over all nodes) from one iteration to the next. The values of convergence criteria used were 1e-2 for vx, vy, and vz and 1e-6 for pressure. For all runs each timestep converged to within the set criteria within 50 iterations. For those analyses for which convergence was studied in a little more detail, it was seen that pressure was always the last variable to converge, and that tightening the pressure convergence criterion by an order of magnitude did not affect the results.

6.3 – Moving Geometry Run Details

For the moving geometry, it was assumed that the time-step and mesh-density values found for the static-wall analyses were appropriate. A fully comment copy of the input file used for the moving mesh analysis is included in appendix C.

6.3.1 – Wall Boundary Condition

The displacement boundary conditions developed in chapter 4 were applied to all nodes (both interior and wall nodes) in order to allow Flotran to take advantage of the registration algorithm's smoothness and sympathy towards mesh quality. The exact method of implementation is described in appendix D. Due to limitations in Ansys (again described in appendix D), the position for each node was linearly interpolated between the node's positions at the 16 MRI timesteps.

Once more a no-slip condition (this time in relation to the moving wall) was enforced at the wall. This was specified directly as a table of velocities at the moving wall, formed from the temporal derivative of the tables governing displacement of the wall nodes.

6.3.2 – Flow Boundary Conditions

The boundary conditions were altered to take account of the fact that the inlet and outlet boundary areas change through the cardiac cycle. The inlet boundary condition was also altered to include the extra flow into the vessel associated with the change in vessel volume.

The flow associated with the volume change, if applied in its raw form, would comprise a series of sudden steps between periods of steady flow (to match the 16-point piece-wise linear motion of the mesh). In order that this flow could go through process described in 5.3, it had to be smoothed to give a manageable number of frequencies, the smoothed and raw data are shown in figure 5.36.

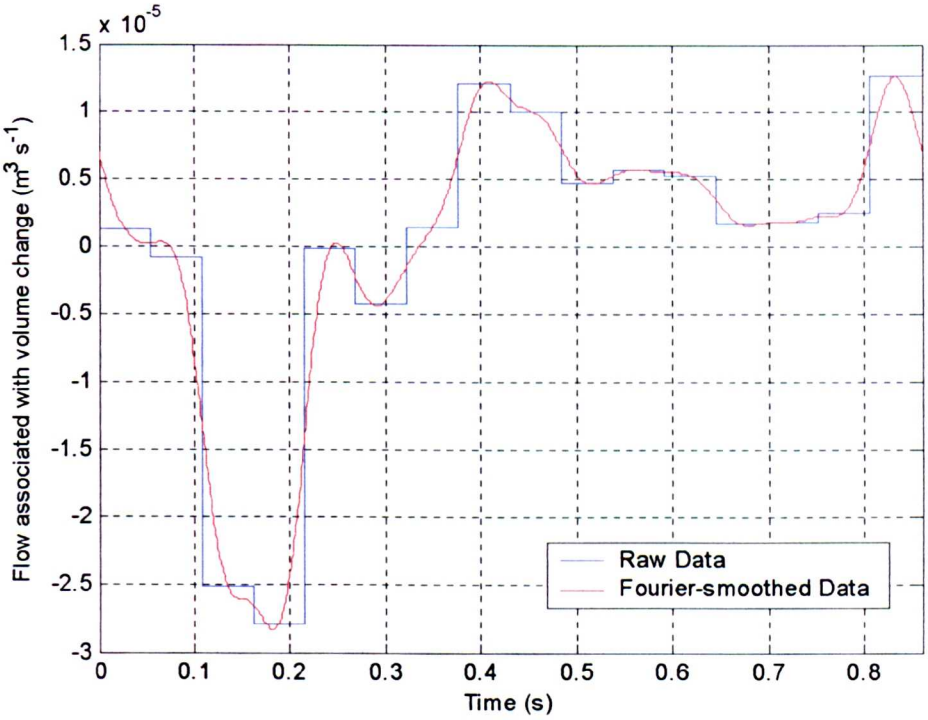

Figure 6.36. Raw and smoothed flow waveforms associated with volume change of the moving mesh model.

The difference between the raw and smoothed waveforms in figure 5.36 meant that there was a slight mass flow imbalance between the flows specified at the two opening and due to the wall motion, and the expected flow at the third opening. For this reason, the AA outlet was chosen as the outlet with the pressure boundary condition. The small spikes in velocity at AA outlet caused by this error quickly dispersed and did not cause convergence problems or propagate any visible disturbance back into the flow.

6.4 – Results: Flow Patterns and Wall Shear Stress Distributions in the SMA and AA

It was noted at this point that an error was present in the code creating the flow boundary conditions, this led to a small miscalculation of volume flow (up to 20% error) through the openings, this was corrected for the final static and moving-wall analyses. All convergence results in section 6.2 are assumed to hold for the updated boundary conditions.

6.4.1 – Key Flow Features in the Static SMA Geometry

The key flow feature in the SMA and AA as modelled, was the jet of flow into the SMA at peak systole. Associated with this jet were regions of detached flow. A crop plane was chosen to clearly show these features, the plane's position and orientation are shown in figure 6.37; velocity vector plots are shown in figures 6.38 and 6.39 (all vector plots throughout this section use the same colour scale).

Figure 6.37. Position of crop plane used to examine flow-features in SMA.

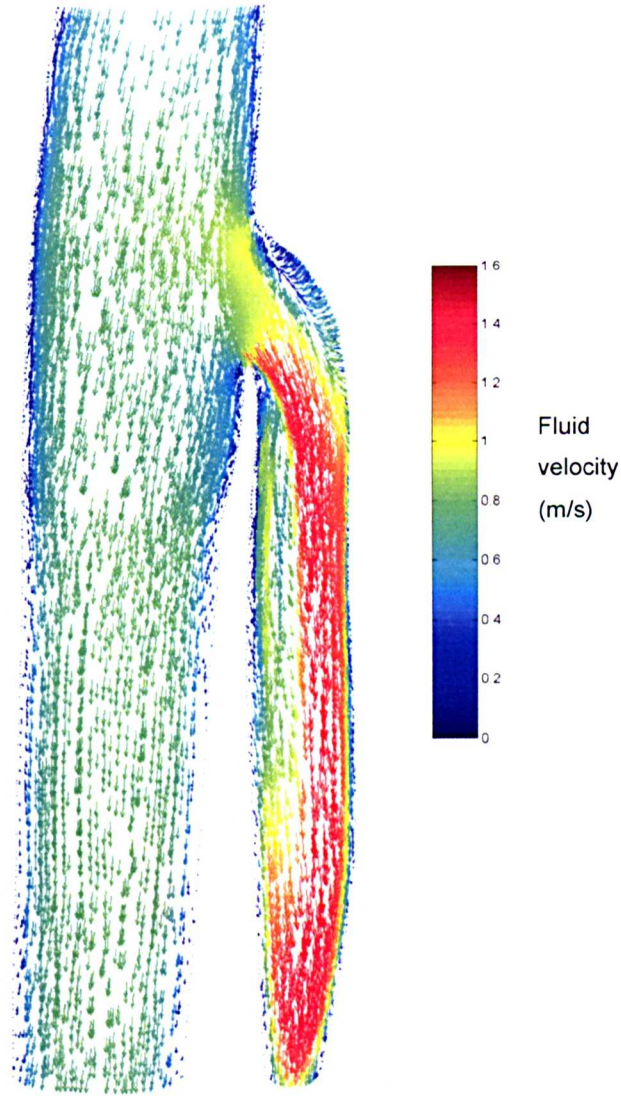

Figure.6.38. Vector map of fluid velocity at nodes on the plane shown in figure 6.36, vectors coloured according to fluid velocity magnitude (m/s), taken at peak systole.

As well as creating the areas of flow separation, it can also be seen that the jet tends to thicken the boundary layer on the posterior wall of the SMA and reduce it on the anterior wall, this explains the region of elevated WSS on the anterior wall of the SMA seen in figure 6.9. The area of reduced WSS magnitude is associated with the separated flow, whilst the impingement of the jet on the anterior wall leads to an area of increased WSS.

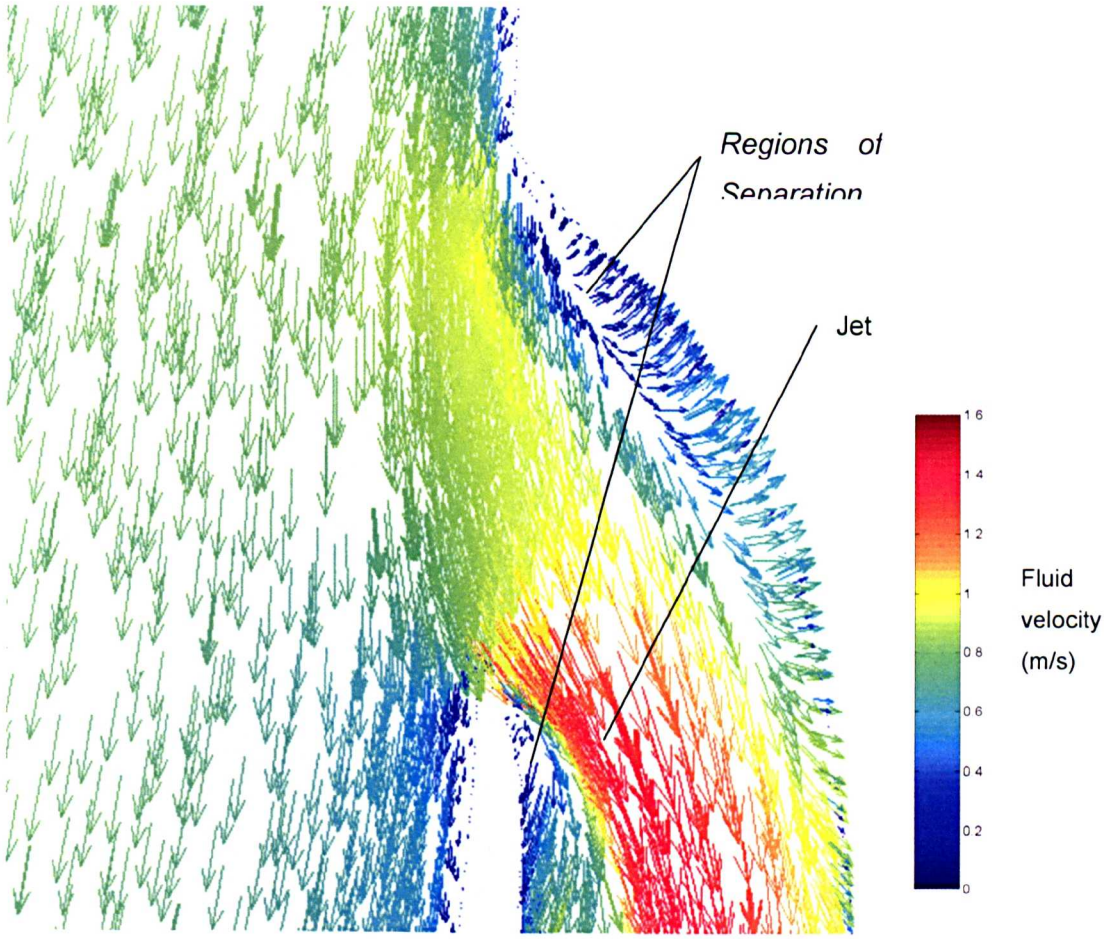

Figure.6.39. Detail from figure 6.38.

In late systole, as the flow decelerates, the jet weakens, narrows and is focused on the anterior wall of the SMA, the areas of separation increase in size, particularly on the posterior wall of the SMA. These effects can clearly be seen in figures 6.40 and 6.41, which reproduce figures 6.38 and 6.39 for late systole.

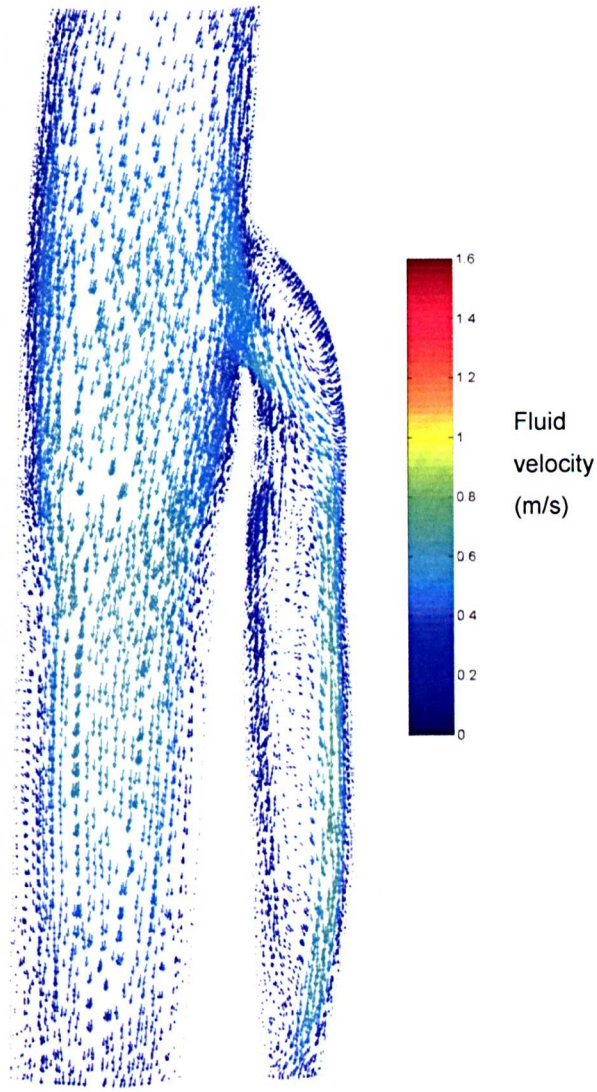

Figure.6.40. Vector map of fluid velocity at nodes on the plane shown in figure 6.37, vectors coloured according to fluid velocity magnitude (m/s), taken at late systole.

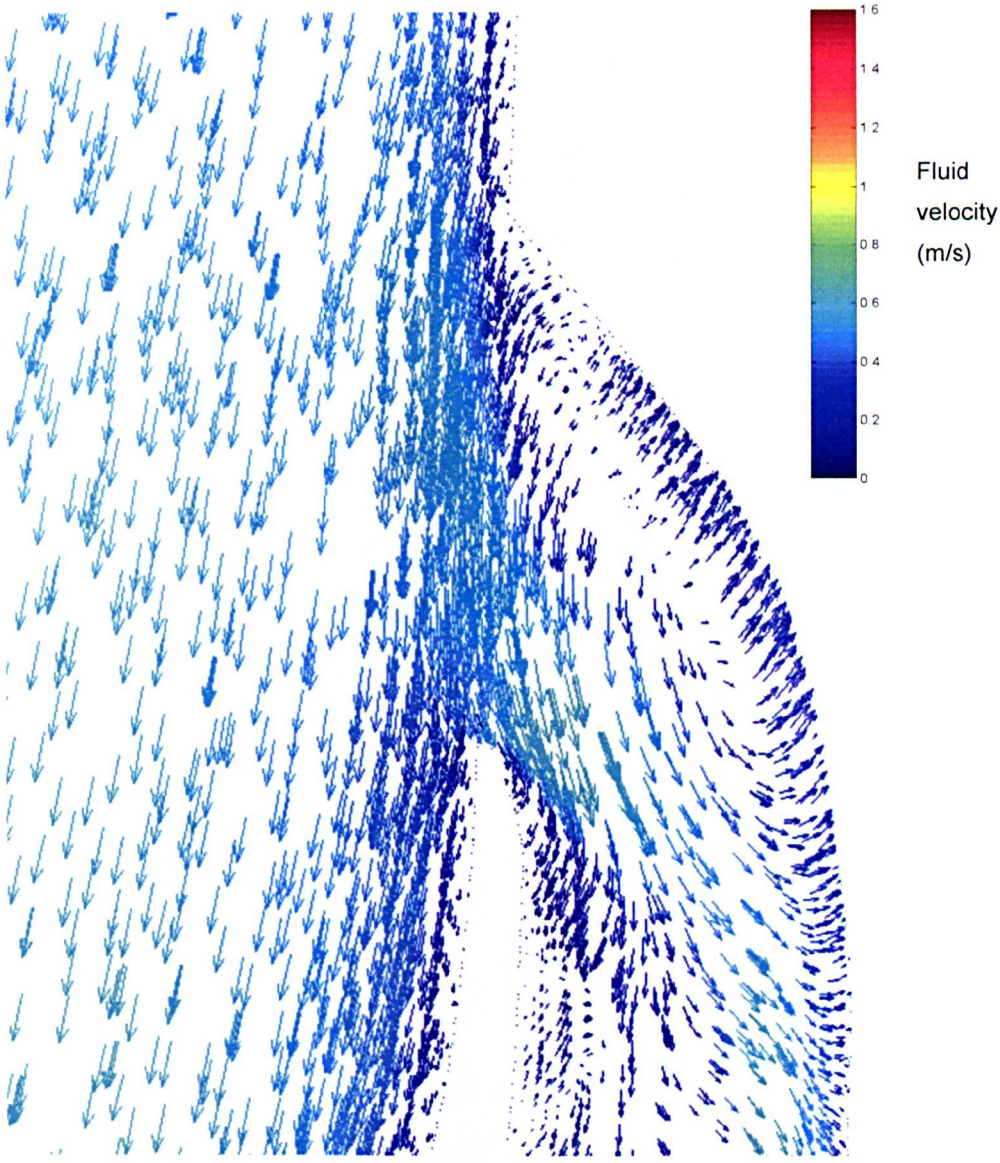

Figure.6.41. Detail from figure 6.40.

In both cases, but particularly at peak systole, the areas of separation do not appear as classical recirculation-bubbles due to the complex 3d nature of the geometry and flow. This can be better appreciated by considering a series of slices normal to the SMA centreline, the positions of three such slices are shown in figure 6.42 and velocity vector plots for each plane at peak and late systole shown in figure 6.43.

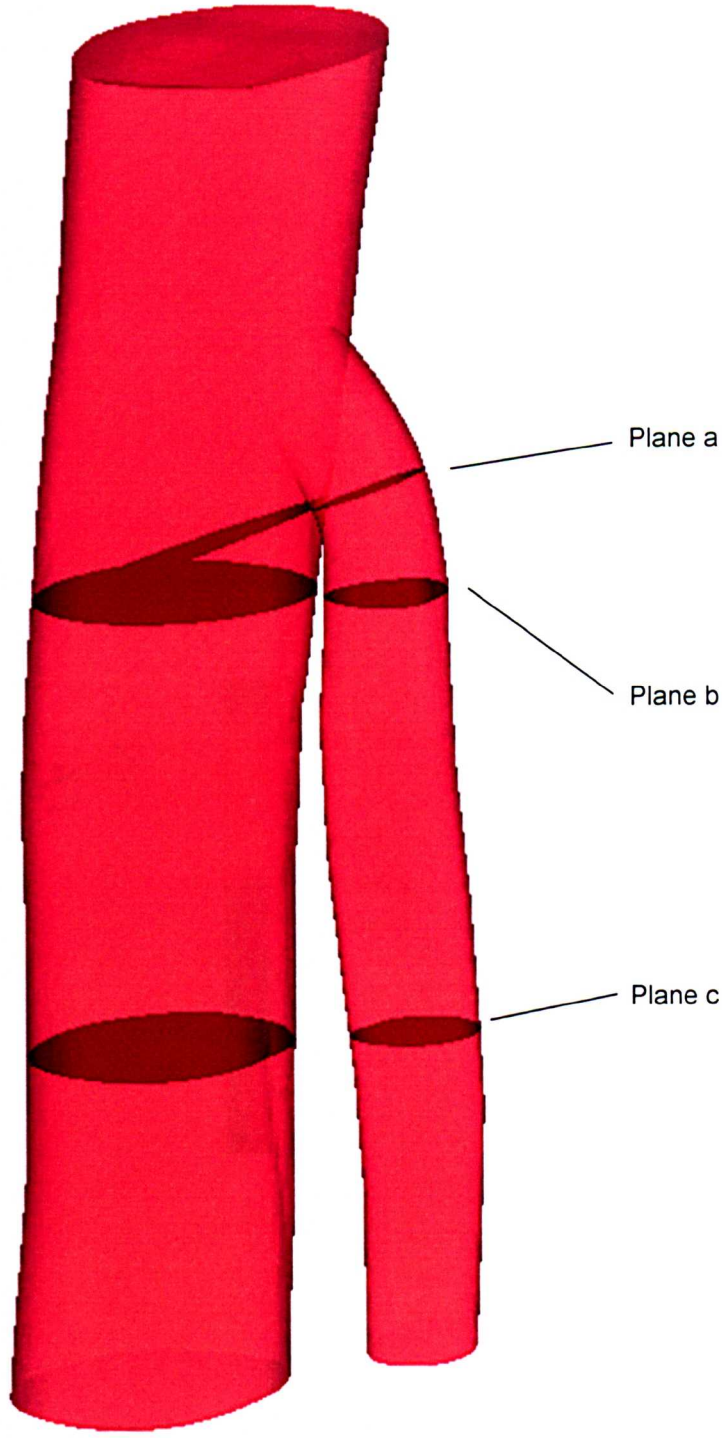

Figure 6.42. Positions of crop planes normal to SMA centre (only regions of planes on SMA were used for flow analysis).

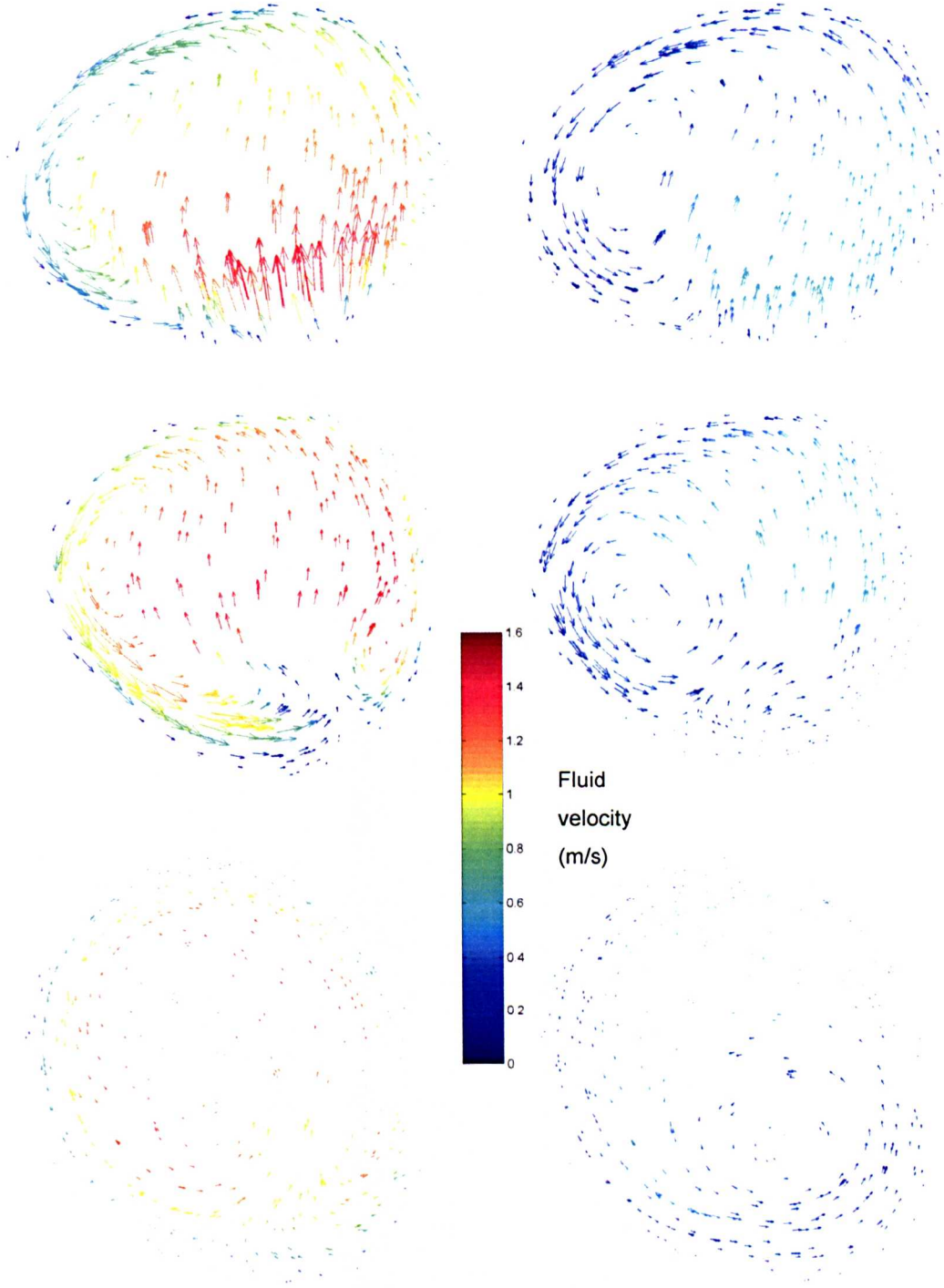

Figure 6.43. Vector flow-fields at crop-planes a, b and c (top, middle and bottom respectively) at peak systole (left) and late systole (right) – all images looking distally along the SMA.

It is clear from figure 6.43, that the key component of secondary flow in the SMA is an anti-clockwise vortex. Further analysis of the data showed that the vortex begins as one of a pair during a period of low flow, and grows to swallow its counterpart as the systolic pulse arrives; this pattern has previously been seen in the aortic arch [161]. A separate analysis with flow imposed at the distal AA boundary and pressure

at the SMA, showed that the weakening of the vortex along the SMA was not caused by the assumption of axial flow at the AA outlet.

6.4.2 – Key Flow Features in the Moving SMA and AA

The same parameters investigated for the static analysis were investigated for the moving wall case. Figure 6.44 to 6.46 repeat figures 6.38, 6.39 and 6.43 for the moving wall case (crop-planes are the same as those used for the static mesh)

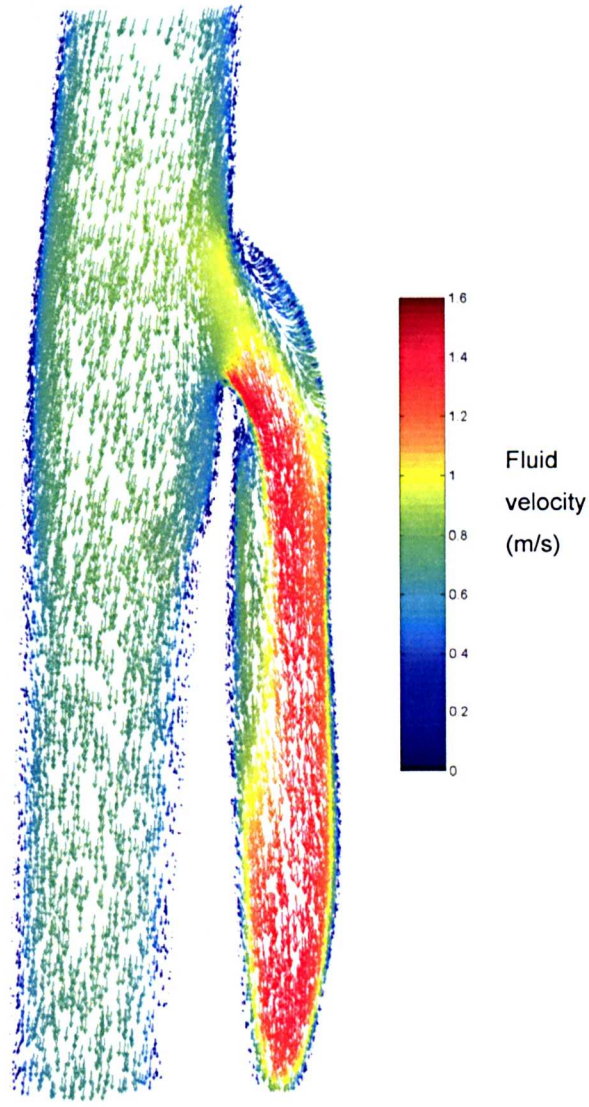

Figure 6.44. Vector map of fluid velocity at nodes on the plane shown in figure 6.36, vectors coloured according to fluid velocity magnitude (m/s), taken at peak systole.

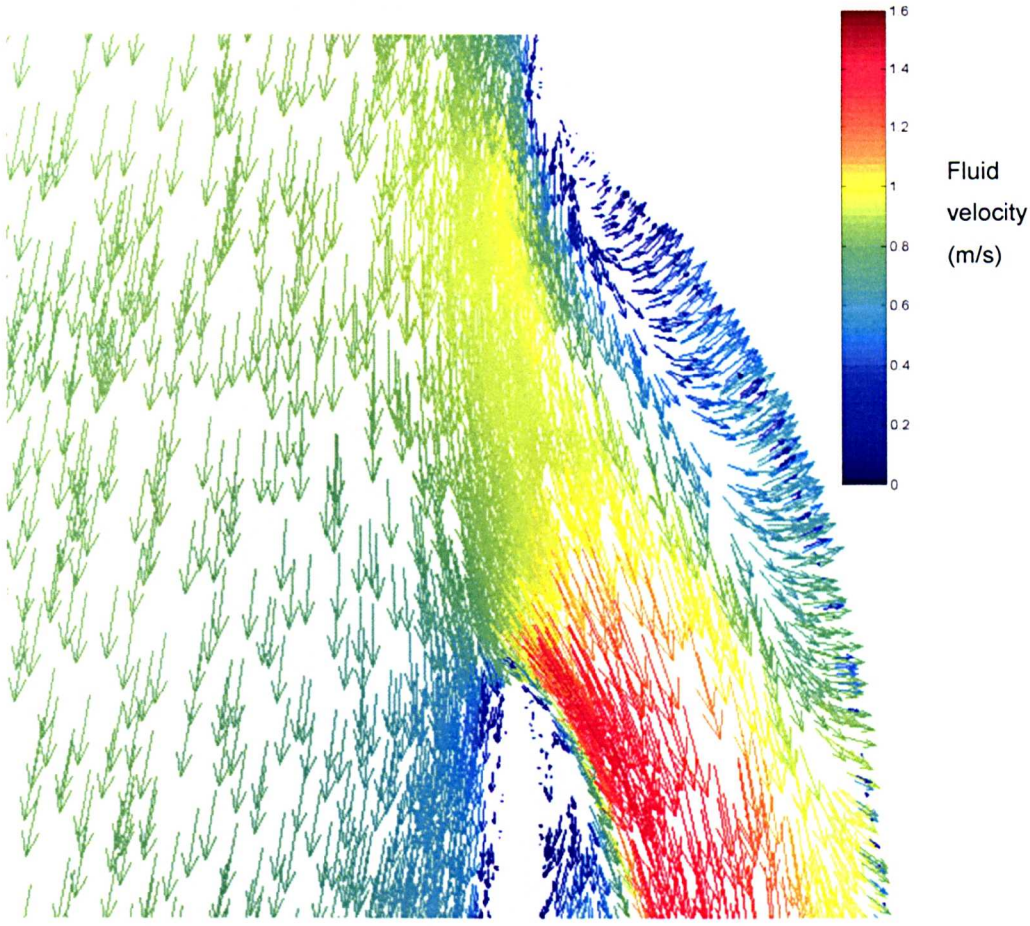

Figure 6.45. Detail from figure 6.44.

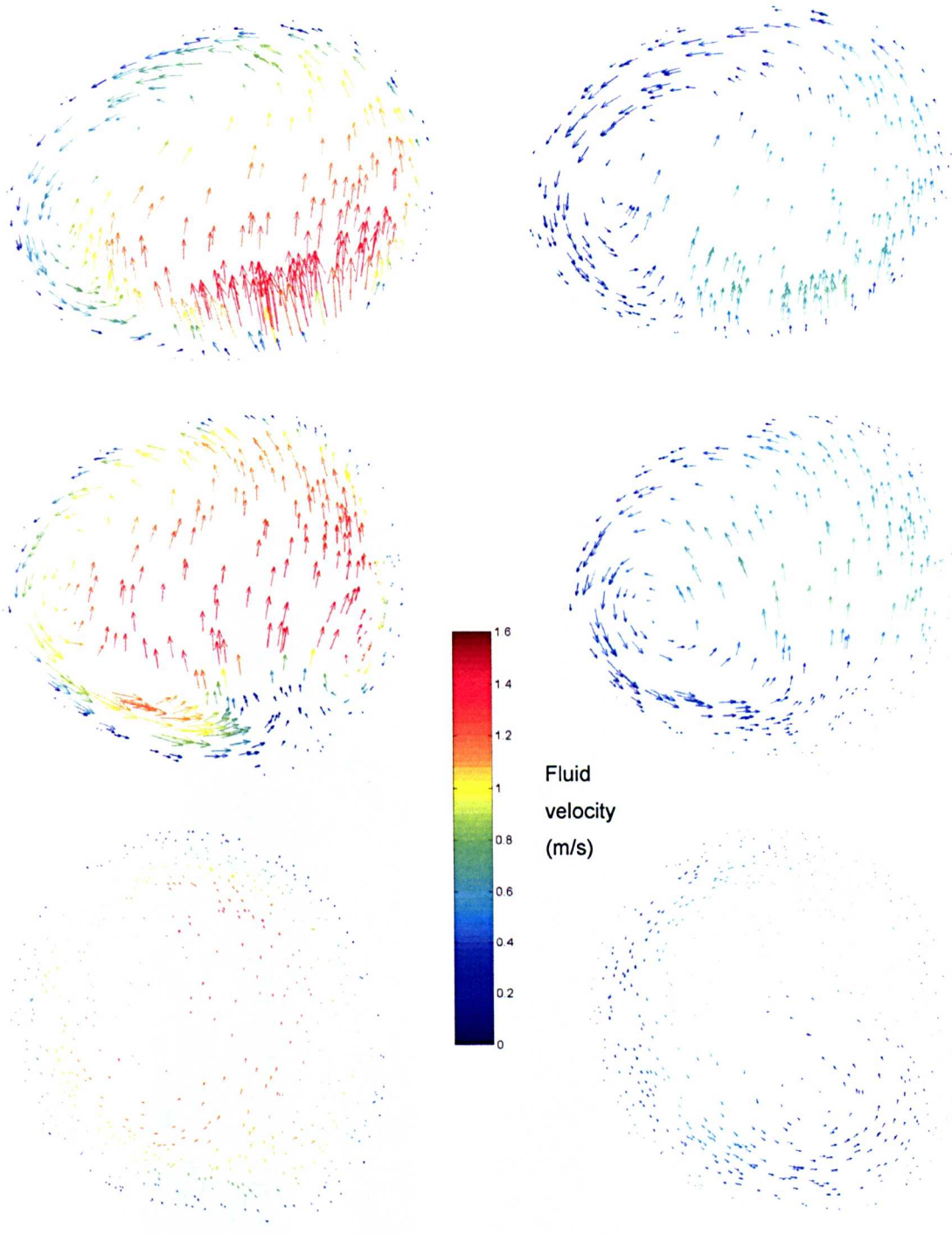

Figure 6.46. Vector flow-fields in the moving geometry at crop-planes a, b and c (top, middle and bottom respectively) at peak systole (left) and late systole (right) – all images looking distally along the SMA.

Comparing figures 6.44 to 6.46 with figures 6.38, 6.39 and 6.43, shows that there is no substantial effect of cardiac motion of the general patterns of blood flow in the

SMA. The only, minor, differences observed were in the exact shape of the vortex as it developed during systole, and in how quickly it diminished along the SMA.

6.4.3 – Wall Shear Stress in the Static and Moving SMA and AA

Figures 6.47 to 6.49 compare WSS distributions at different times in the moving and static SMA and AA models. For the moving wall analysis, wall node velocities associated with the vessel motion were small compared to near-wall fluid velocities, and were discarded in the WSS calculations.

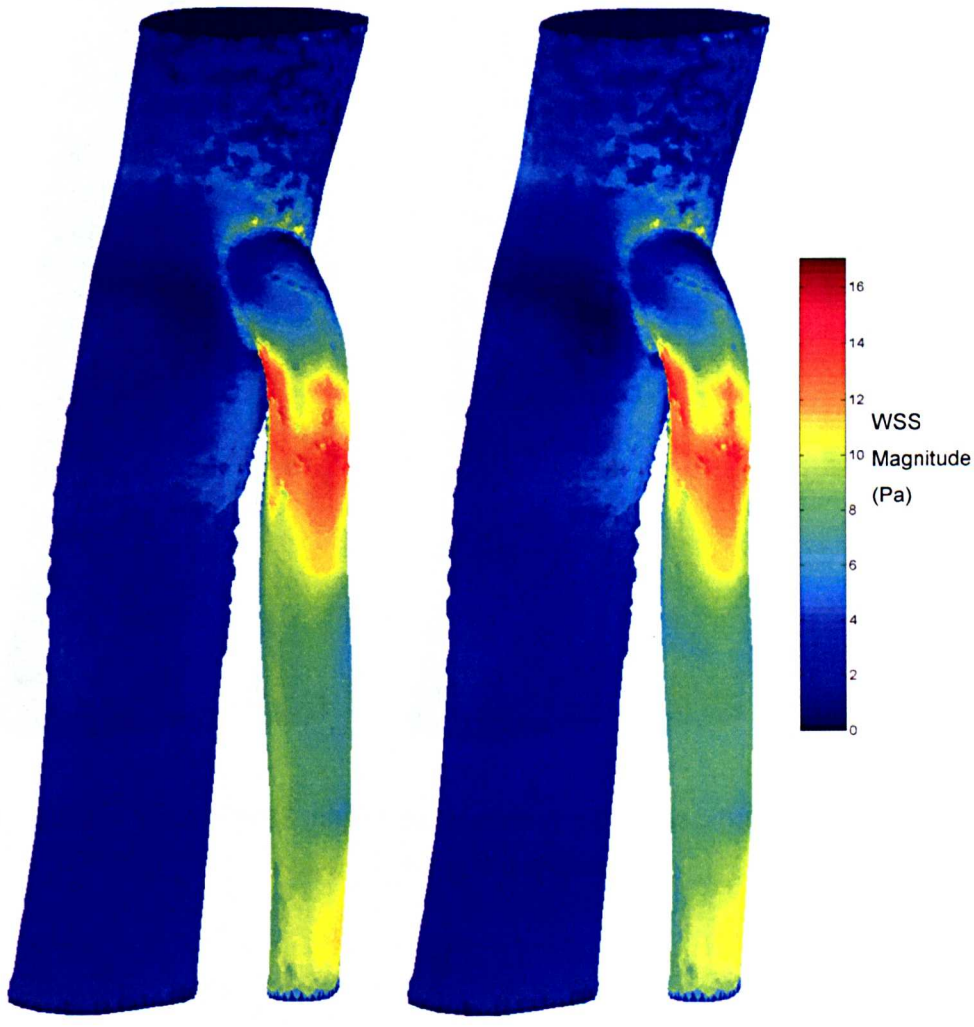

Figure 6.47. Surface maps of WSS magnitude for static mesh analysis (left) and moving mesh analysis (right) at peak systole.

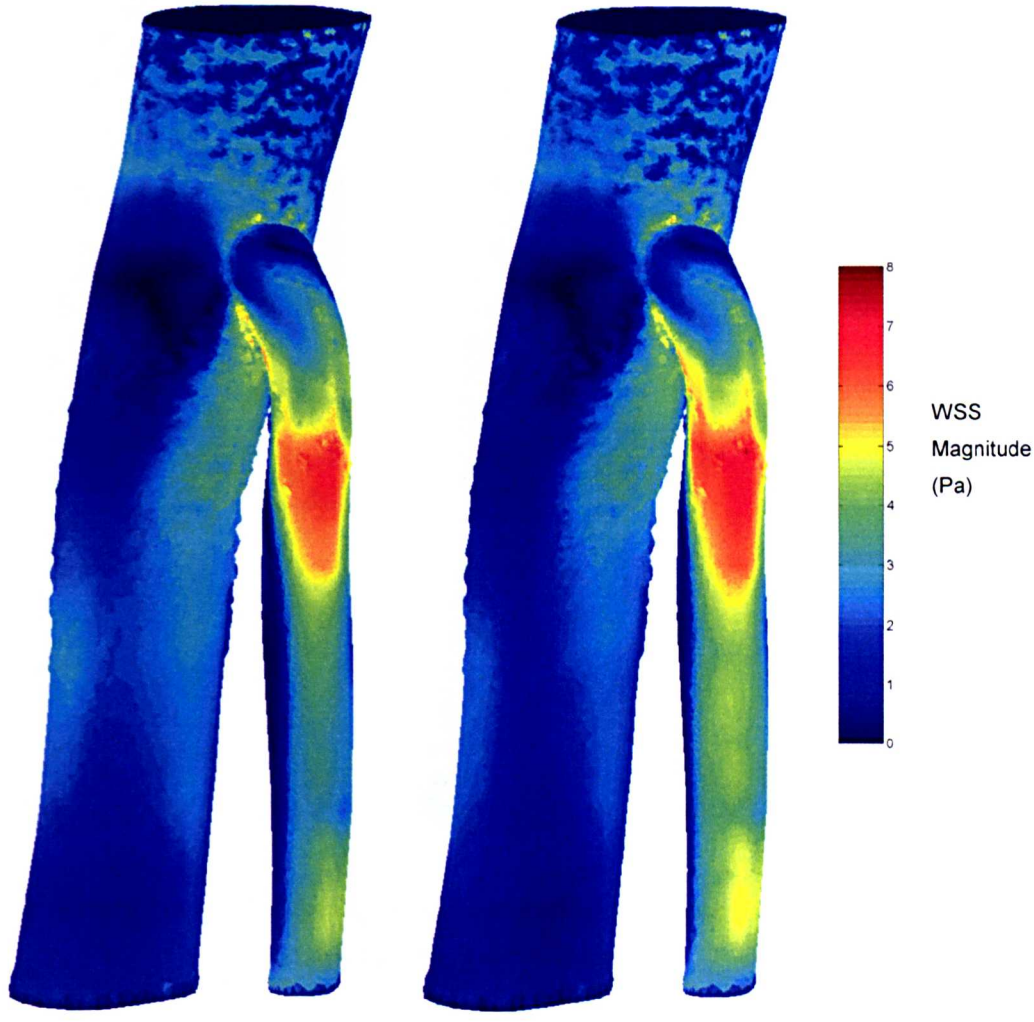

Figure 6.48. Surface maps of WSS magnitude for static mesh analysis (left) and moving mesh analysis (right) at late systole.

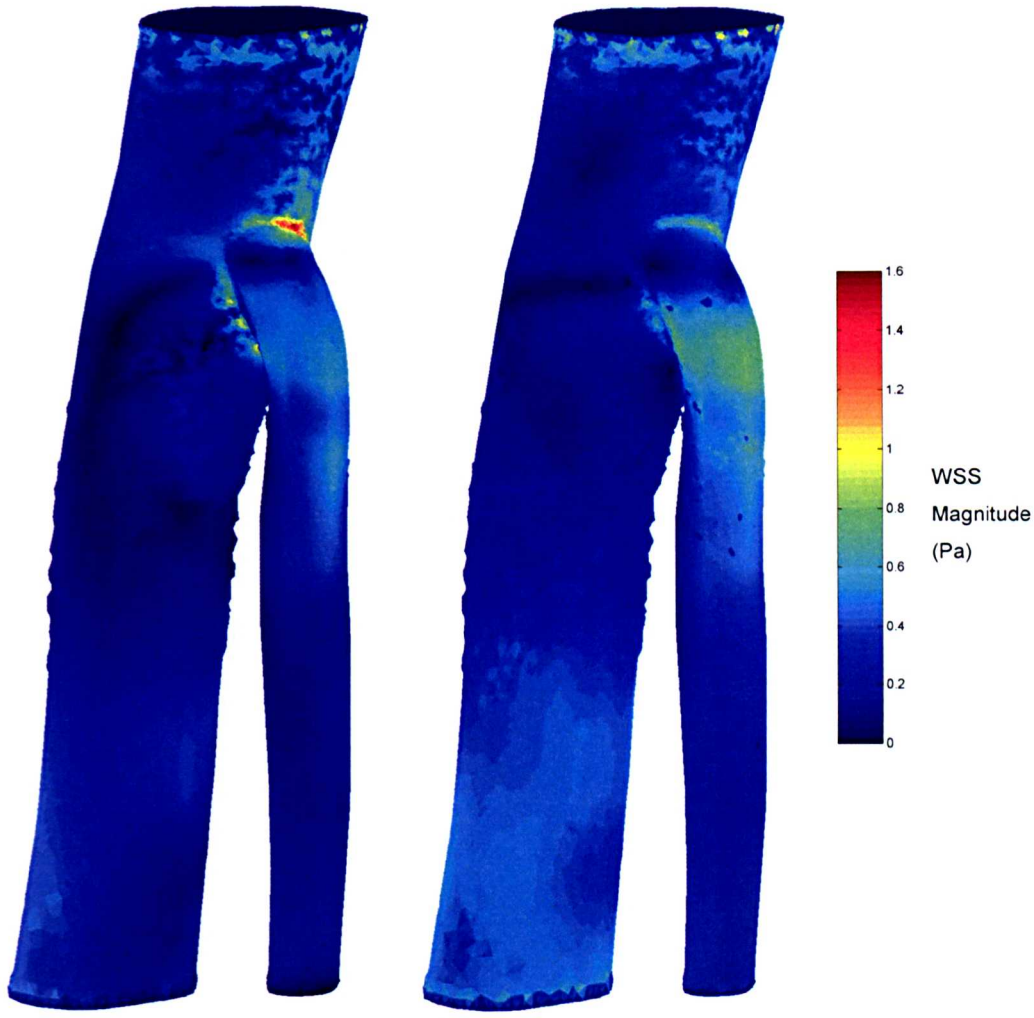

Figure 6.49. Surface maps of WSS magnitude for static mesh analysis (left) and moving mesh analysis (right) at end diastole.

In figures 6.47 to 6.49, little difference is seen in WSS distributions between the static and moving-walled models. At late systole, the area of high shear associated with the jet is larger in the moving-walled model; this is likely associated with the motion of the vessel posteriorly towards the jet, reducing the boundary layer thickness (the same effect reversed would lead us to expect lower WSS on the anterior aspect of the SMA during early systole, as the vessel expands away from the jet).

Figures 6.50 to 6.52 show peak WSS magnitude, time-averaged WSS magnitude and OSI over one cardiac cycle for the static and moving models.

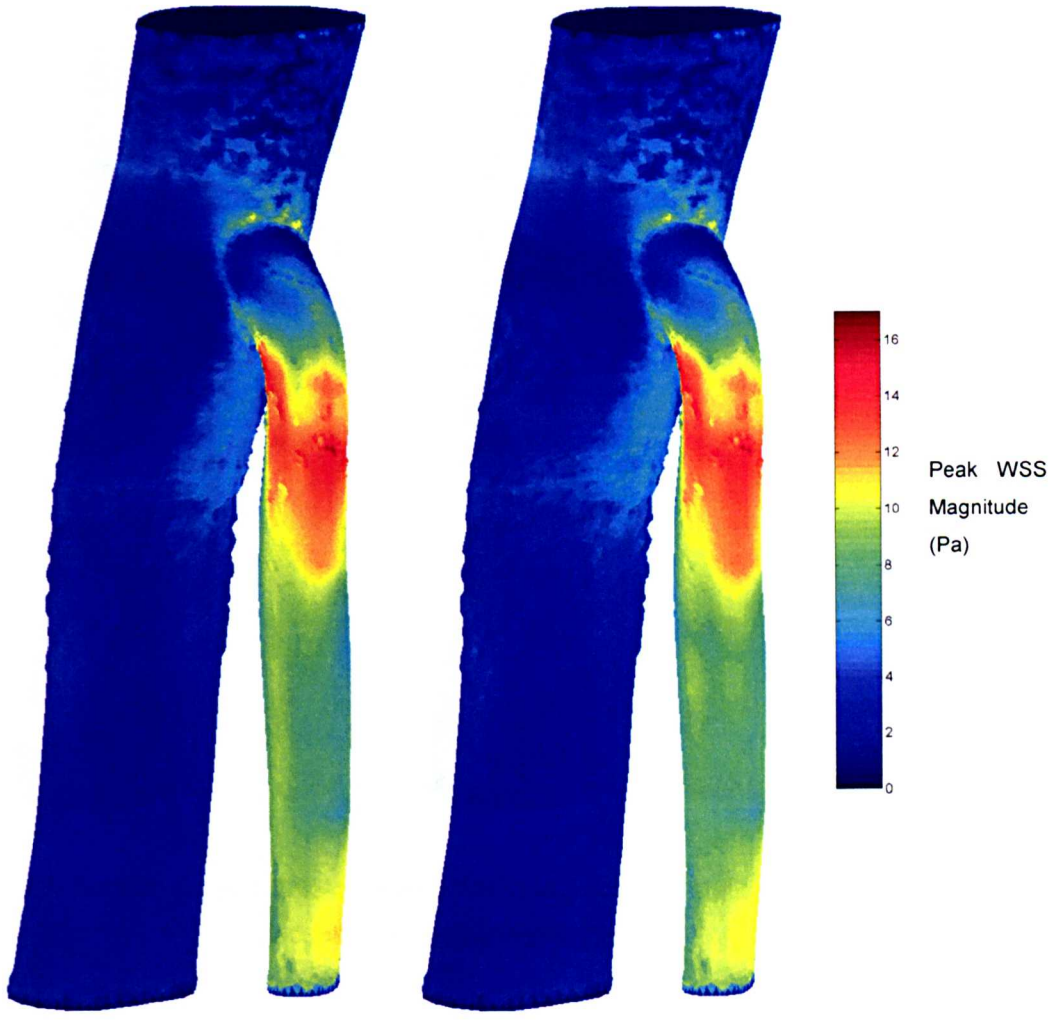

Figure 6.50. Surface maps of peak WSS magnitude for static mesh analysis (left) and moving mesh analysis (right).

Peak WSS was on average 4.6% lower in the moving case, this small difference may be associated with the fact that the moving mesh had an increased volume over the period of high flow and associated high shear.

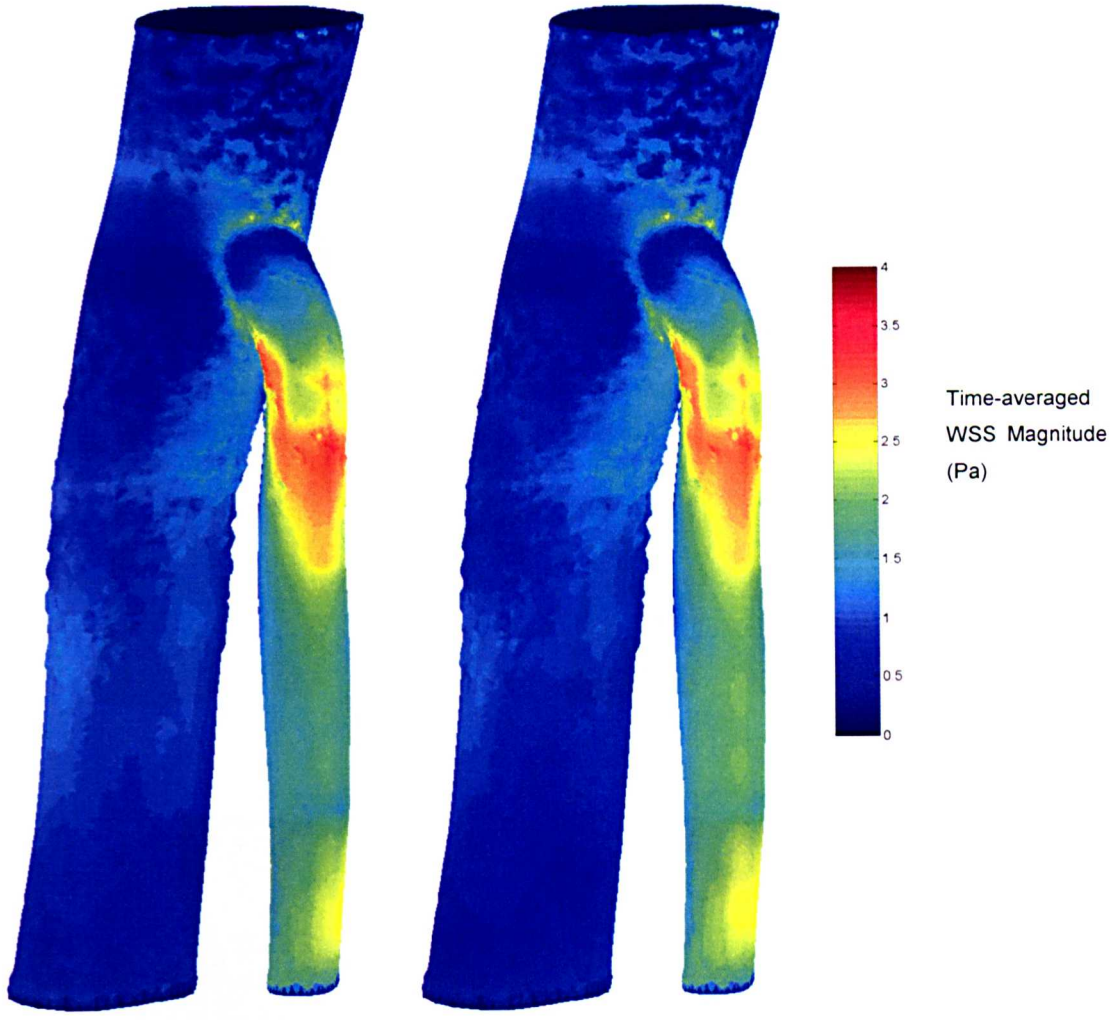

Figure 6.51. Surface maps of time-averaged WSS magnitude for static mesh analysis (left) and moving mesh analysis (right).

Figure 6.51 shows that the moving wall analysis had little effect on patterns of time-averaged WSS. Time-averaged WSS was on average the same to within 1% between the static and moving meshes.

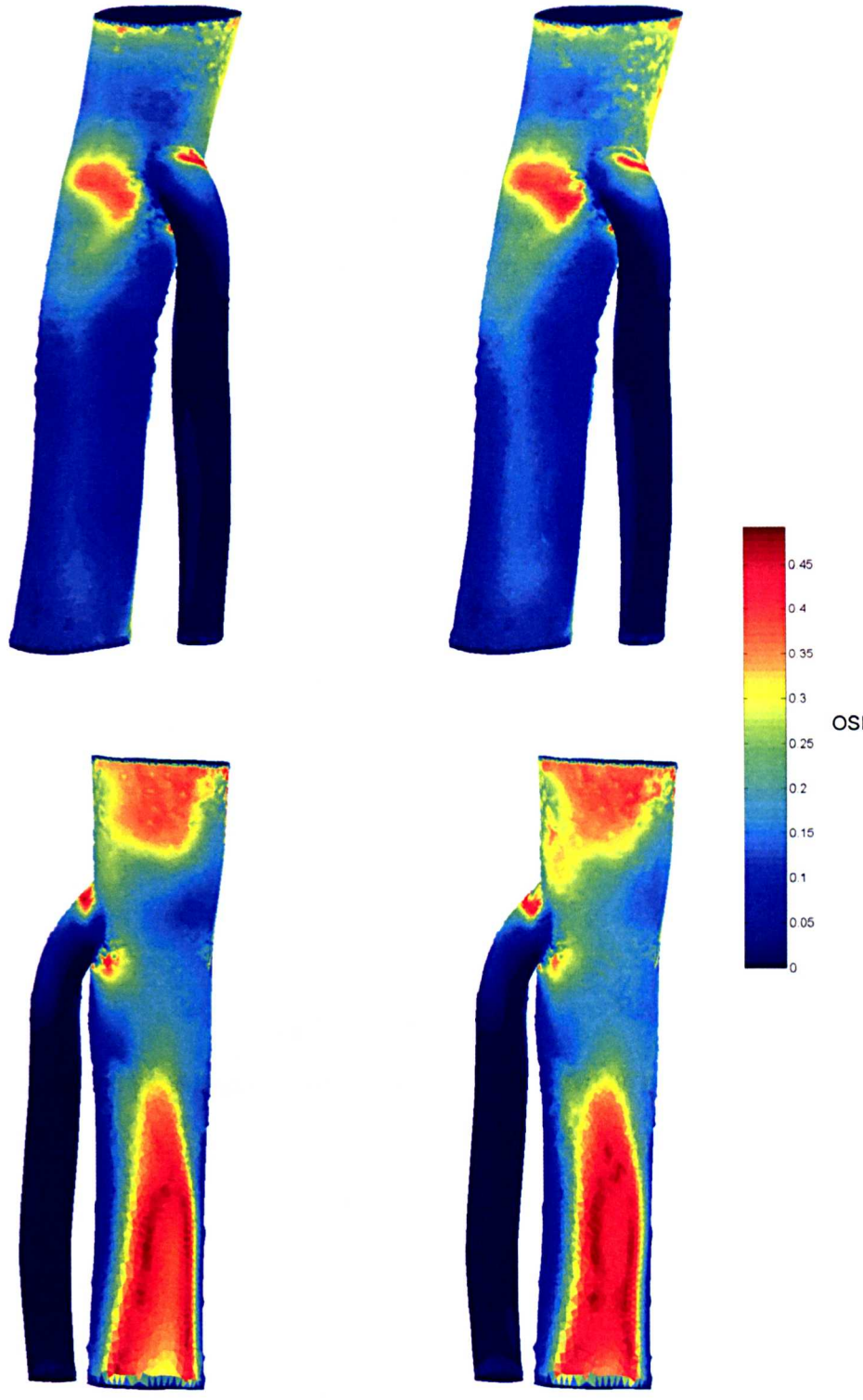

Figure 6.52. Surface maps of OSI for static mesh analysis (left) and moving mesh analysis (right).

In both the static and moving mesh cases, OSI in the SMA was seen to be substantially lower than in the AA, this agrees with the observations that, the SMA tends to be spared the effects of atherosclerosis, and that areas of with high OSI

tend to be those likely to be affected. There were no significant differences in OSI between the static and moving mesh analyses

The one region of high OSI in the SMA was the area on the anterior wall where flow separation was evident, this area diminished slightly in the moving model. The time-varying vector plots in figures 6.52 and 6.53 clearly show the wildly different time-varying WSS experienced by SMA endothelial cells in areas of low or high OSI respectively (note also the widely different scales).

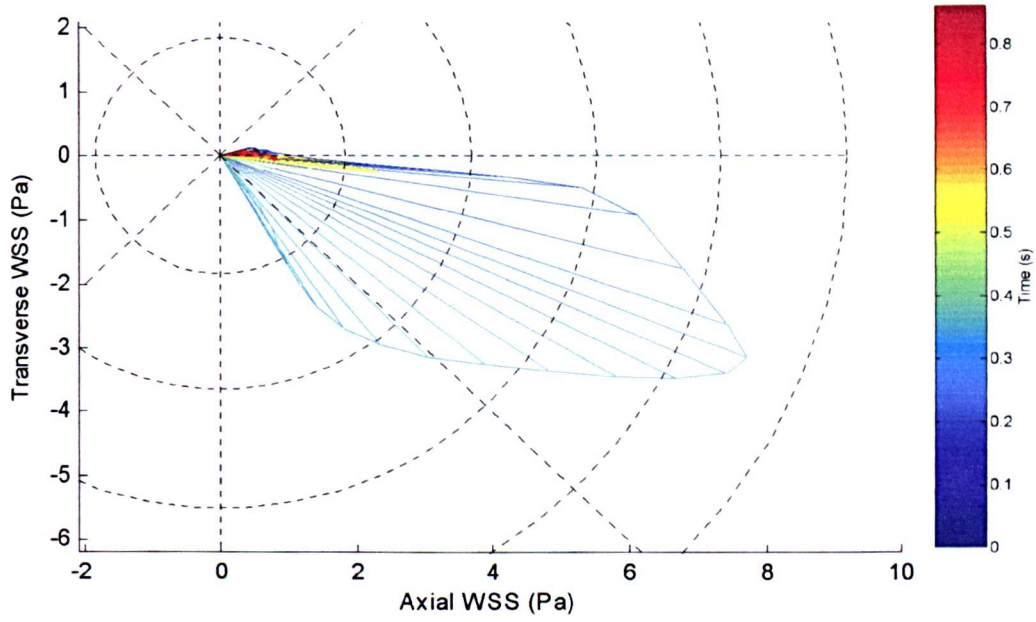

Figure 6.53. Time-varying WSS experienced by node in low OSI (0.029) region of the SMA.

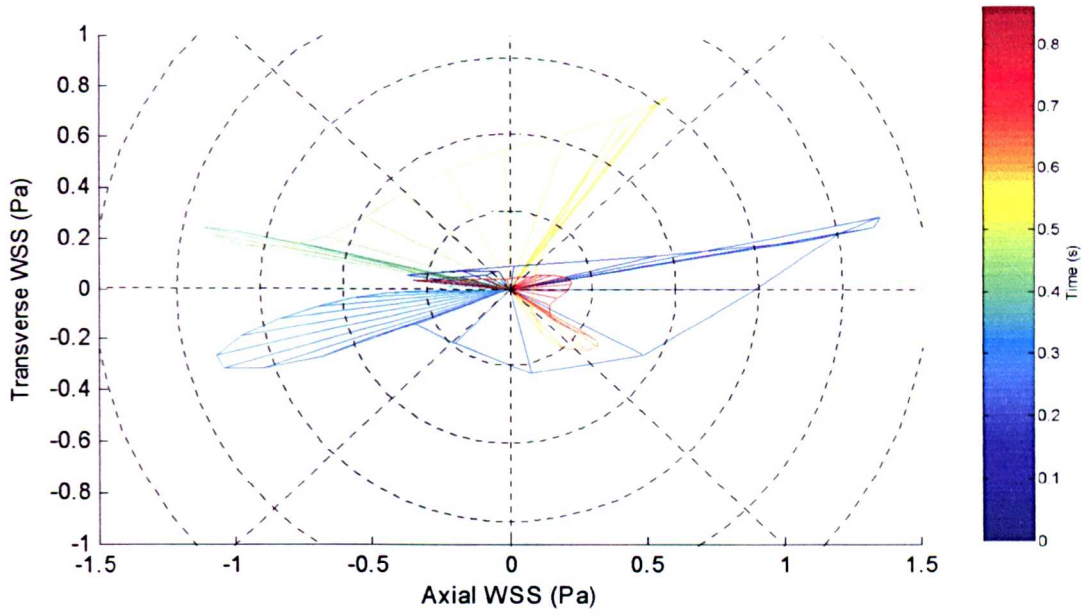

Figure 6.54. Time-varying WSS experienced by node in high OSI (0.389) region of the SMA.

6.5 – Conclusions

Based on the anatomically accurate models of SMA and AA geometry developed in chapter 4, and boundary conditions developed in chapter 5, CFD models were created representing the blood flow through the SMA and AA during a normal cardiac cycle. Results for WSS and OSI were shown to be largely independent of mesh density and timestep using meshes with more than 500 000 elements with mesh density greatest near to the wall, and timesteps of 1 to 5ms. Harmonic convergence of WSS was shown to occur within the first cycle, so only two cycles were needed to capture a developed cardiac cycle.

Only slight differences in WSS and OSI were seen between the static and moving models of the SMA and AA geometry. The SMA was seen to have generally low OSI with a band of increased OSI corresponding to the region of separated flow close to the anterior wall near its origin; this pattern was not substantially different between the static and moving mesh analyses.

Interestingly, the area of high OSI visible in figure 6.51 corresponds very closely with the position commonly associated with atherosclerotic plaques on the occasions that they are found in the SMA, as shown in the angiogram in figure 6.55.

Therefore, it can be said with some confidence, that the cardiac motion of the SMA is not the key contributing factor to its protection from development of atherosclerosis.

However, the flow regime in the SMA does offer an environment of high time-averaged WSS and low OSI that, according to current understanding, serves to protect the vessel from the development of atherosclerosis.

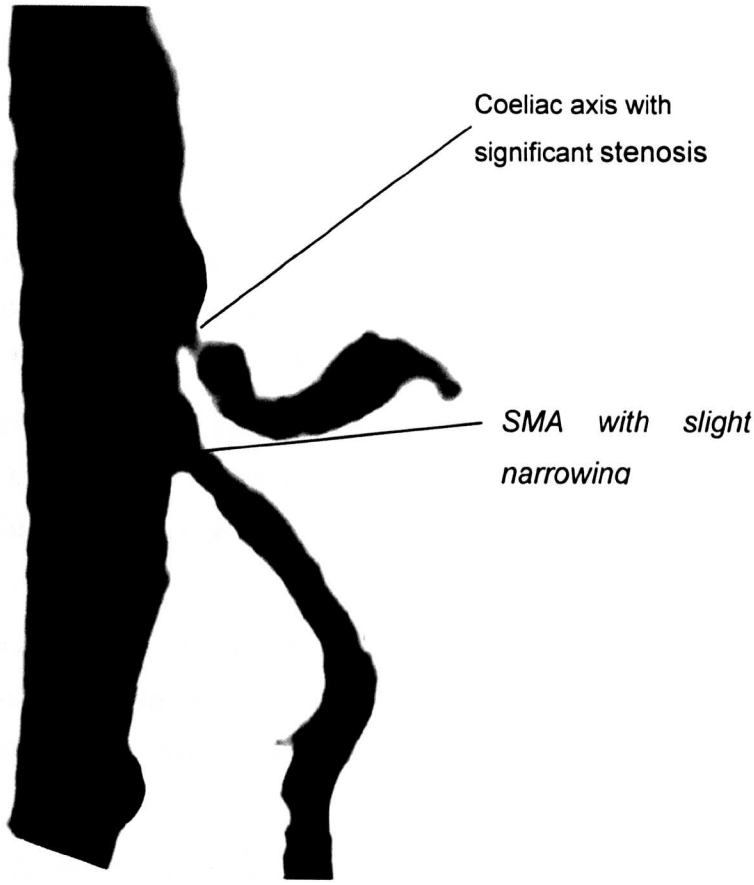

Figure 6.55. SMA Angiogram showing atherosclerotic plaque [162].

Chapter 7. Conclusions and Further Work

7.1 – Conclusions

The aim of this project was to investigate the haemodynamic factors that may be important in the protection of the SMA from the effects of atherosclerotic disease.

In order to produce accurate models of the haemodynamics, it was necessary to first acquire geometry data; this was achieved using MRI. Early results from the MRI suggested that a key feature of the SMA's anatomy was its mobility. It was postulated that this might play an important role in determining the exact haemodynamic conditions in the SMA, and therefore this motion was included in the model.

The observation and quantification of the substantial cardiac and respiratory motion of the SMA is important in its own right. At the time of printing, a paper outlining the dynamic anatomy of the SMA is in preparation with the aim of submission to an anatomy journal.

Volunteer motion proved to be a major problem in generating full sets of time-varying 3d data; fortunately, in one case there was no volunteer motion and the data could be used directly. This problem would have to be addressed to deal with larger study groups.

Due to the large number of images to be dealt with for a moving-mesh analysis, segmentation by registration was used to speed up the segmentation process and reduce the subjectivity associated with hand segmentation.

Mesh generation by registration was used to create both static and moving meshes, key benefits of this approach were:

- The absence of the 'terracing' seen in some analyses (where the mesh follows the edge of individual voxels).
- The ability to quantify the quality of fit between the mesh and the MRI data.
- The ability to produce moving meshes without altering mesh topology.
- The ability to monitor and manage mesh quality.

Much time in the project was spent in consideration and development of downstream boundary condition models. Whilst the development of the project, as well as technical considerations, meant that these were not used directly in the final analyses, this information is still important as the results hold true and can be applied to other software packages, with particular use likely to be found in FSI analyses.

The final analyses showed that whilst the cardiac motion of the SMA and AA was substantial, it did not have a significant effect on WSS and OSI distributions in the SMA; however the WSS and OSI patterns in the SMA did fall into the range regarded as protective against atherosclerosis for both the static and moving walled analyses.

Two major factors seem to contribute to this protective flow condition. First, as mentioned in chapter 6, is the rapid reattachment of the jet, which leaves only a small area of vessel wall exposed to flow with a high OSI. Second is the fact that there is no significant bulk flow reversal in the SMA (this was seen in the PCMRA results for the whole cohort of volunteers), meaning that flow reversal can only occur as a results of secondary flow structures.

7.2 – Directions for Further Work

From a clinical perspective, the significance of this work is limited by the fact that flow was modelled in only one volunteer. This aspect was largely controlled by time-constraints and by the problems in volunteer movement associated with the large number of breath-hold scans needed to acquire cine-slices.

There are two approaches available to solve the slice alignment issue. The first approach is to alter the MRI protocol either by using different sequences to capture the geometry (as they become available), or by somehow restraining the volunteer to reduce the possibility of motion (which may run into problems with volunteer comfort and acceptance). The second is to use a rigid registration approach to realign the slices (as mentioned in chapter 4). Whilst this latter approach was attempted in this project, it proved unsuccessful with the algorithms and data available. Further investigation of this, along with additional data capture and processing may possibly yield improved results.

The finding that cardiac motion does not significantly alter the WSS patterns in the SMA suggests that it would be useful to use an alternative MRI sequence to acquire vessel geometry at one point in the cardiac cycle over a single scan (with reduced time and associated reduction in volunteer movement problems), this could be the

first step towards a study with significant numbers. It is worth noting that a contrast-enhanced magnetic resonance angiography type approach would still not be appropriate to capture the geometry, as the ~15s breath-hold acquisition leads to time-averaging of the geometry which acts to smear the cardiac motion.

Cardiac motion was one of two important modes of motion observed in the SMA, the other being respiratory motion. Having investigated the effect of cardiac motion it would be interesting to extend this to consider respiratory motion (both along with cardiac motion and separately; clearly this would require substantial further MRI time.

The absence of bulk flow reversal in the SMA also merits further consideration; investigation of the features of the gut vasculature that cause this to be the case may further inform understanding of not only the gut vasculature, but also more general systemic haemodynamics.

Taking a wider outlook, whilst the link between wall shear stress and atherosclerosis is fairly well documented, the mechanisms associated with the initiation of atherosclerotic plaques are not well characterised. *In vitro* experimental work aiming to further understanding of the relationship between time-varying WSS patterns and endothelial cell function will provide insight into these mechanisms.

While FSI analysis is an attractive technique with which to model wave-propagation and dilatation effects, finding physiologically appropriate boundary conditions to control gross motion in a vessel as mobile and complexly situated as the SMA seems an intractable task. One possible approach to overcoming this is to separate the centre-line and dilatation components of the motion (as in section 4.6.2) and use this data to perform an FSI analysis where centre-line motion is specified, but the FSI is allowed to calculate the dilatation component.

References

1. Ross, R., *The pathogenesis of atherosclerosis: a perspective for the 1990s.* Nature, 1993. **362**(6423): p. 801-9.
2. Underwood, J., ed. *General and Systematic Pathology.* 1992, Churchill Livingstone.
3. Guyton, A.C. and J.E. Hall, *Textbook of Medical Physiology.* 10th ed. 2000, Philadelphia: W B Saunders Company.
4. Lawford, P.V., *MSc Lecture Notes: Anatomy of the Cardiovascular System.* 2002.
5. Cycowitz, Z.J., *Normal Blood Cells: Development and Morphology.* 1997.
6. Gray, H., *Gray's Anatomy.* 38 ed. 1995, Philadelphia: Churchill Livingston.
7. Marieb, E.N., *Human Anatomy and Physiology.* Third ed. 1995, Redwood City: Benjamin/Cummings.
8. Clarkson, T.B., K.W. Weingand, B.T. Goodwin, and L. Hulsebos, *Animal models of atherosclerosis*, in *Atherosclerosis: Biology and Clinical Science*, A.G. Olsson, Editor. 1987, Churchill Livingston: Edinburgh. p. 23-33.
9. Ross, R. and J.A. Glomset, *Atherosclerosis and the arterial smooth muscle cell: Proliferation of smooth muscle is a key event in the genesis of the lesions of atherosclerosis.* Science, 1973. **180**(93): p. 1332-9.
10. Ross, R. and J.A. Glomset, *The pathogenesis of atherosclerosis (first of two parts).* N Engl J Med, 1976. **295**(7): p. 369-77.
11. Ross, R., *The pathogenesis of atherosclerosis--an update.* N Engl J Med, 1986. **314**(8): p. 488-500.
12. Stary, H.C., A.B. Chandler, S. Glagov, J.R. Guyton, W. Insull, Jr., M.E. Rosenfeld, S.A. Schaffer, C.J. Schwartz, W.D. Wagner, and R.W. Wissler, *A definition of initial, fatty streak, and intermediate lesions of atherosclerosis. A report from the Committee on Vascular Lesions of the Council on Arteriosclerosis, American Heart Association.* Circulation, 1994. **89**(5): p. 2462-78.
13. Jonasson, L., J. Holm, O. Skalli, G. Bondjers, and G.K. Hansson, *Regional accumulations of T cells, macrophages, and smooth muscle cells in the human atherosclerotic plaque.* Arteriosclerosis, 1986. **6**(2): p. 131-8.
14. van der Wal, A.C., P.K. Das, D. Bentz van de Berg, C.M. van der Loos, and A.E. Becker, *Atherosclerotic lesions in humans. In situ immunophenotypic analysis suggesting an immune mediated response.* Lab Invest, 1989. **61**(2): p. 166-70.
15. Napoli, C., F.P. D'Armiento, F.P. Mancini, A. Postiglione, J.L. Witztum, G. Palumbo, and W. Palinski, *Fatty streak formation occurs in human fetal aortas and is greatly enhanced by maternal hypercholesterolemia. Intimal accumulation of low density lipoprotein and its oxidation precede monocyte recruitment into early atherosclerotic lesions.* J Clin Invest, 1997. **100**(11): p. 2680-90.
16. Simionescu, N., E. Vasile, F. Lupu, G. Popescu, and M. Simionescu, *Prelesional events in atherogenesis. Accumulation of extracellular cholesterol-rich liposomes in the arterial intima and cardiac valves of the hyperlipidemic rabbit.* Am J Pathol, 1986. **123**(1): p. 109-25.
17. Glagov, S., E. Weisenberg, C.K. Zarins, R. Stankunavicius, and G.J. Kolettis, *Compensatory enlargement of human atherosclerotic coronary arteries.* N Engl J Med, 1987. **316**(22): p. 1371-5.
18. Libby, P. and R. Ross, *Cytokines and growth regulatory molecules*, in *Atherosclerosis and coronary artery disease*, V. Fuster and R. Ross, Editors. 1996, Lippincott-Raven: Philadelphia. p. 585-94.

19. Raines, E.W., M.E. Rosenfeld, and R. Ross, *The role of macrophages*, in *Atherosclerosis and coronary artery disease*, V. Fuster and R. Ross, Editors. 1996, Lippincott-Raven: Philadelphia. p. 539-55.
20. Falk, E., P.K. Shah, and V. Fuster, *Pathogenesis of plaque disruption*, in *Atherosclerosis and coronary artery disease*, V. Fuster and R. Ross, Editors. 1996, Lippincott-Raven: Philadelphia. p. 492-510.
21. Falk, E., *Coronary thrombosis: pathogenesis and clinical manifestations.* Am J Cardiol, 1991. **68**(7): p. 28B-35B.
22. Zaman, A.G., G. Helft, S.G. Worthley, and J.J. Badimon, *The role of plaque rupture and thrombosis in coronary artery disease.* Atherosclerosis, 2000. **149**(2): p. 251-66.
23. Becker, A.E. and R.H. Anderson, *Cardiac Pathology: an integrated text and colour atlas.* 1st ed. 1983, Edinburgh: Churchill Livingstone.
24. www.cardioliving.com/consumer/Heart/Atherosclerosis.shtm.
25. Nowak, T. and A. Handford, eds. *Essentials of Pathophysiology: concepts and applications for health-care professionals.* 1994, William Brown Publishers: Iowa.
26. Caro, C.G., J.M. Fitz-Gerald, and R.C. Schroter, *Arterial wall shear and distribution of early atheroma in man.* Nature, 1969. **223**(211): p. 1159-60.
27. Ku, D.N., D.P. Giddens, C.K. Zarins, and S. Glagov, *Pulsatile flow and atherosclerosis in the human carotid bifurcation. Positive correlation between plaque location and low oscillating shear stress.* Arteriosclerosis, 1985. **5**(3): p. 293-302.
28. White, F.M., *Fluid Mechanics.* 5th ed. 2003: McGraw-Hill.
29. He, X. and D.N. Ku, *Pulsatile flow in the human left coronary artery bifurcation: average conditions.* J Biomech Eng, 1996. **118**(1): p. 74-82.
30. Taylor, C.A., *Finite element modeling of blood flow: Relevance to atherosclerosis*, in *Intra and Extracorporeal Cardiovascular Fluid Dynamics: Vol. 2 - Fluid Structure Interaction*, P.R. Verdonck and K. Perktold, Editors. 2001, WIT Press.
31. Zarins, C.K., D.P. Giddens, B.K. Bharadvaj, V.S. Sottiurai, R.F. Mabon, and S. Glagov, *Carotid bifurcation atherosclerosis. Quantitative correlation of plaque localization with flow velocity profiles and wall shear stress.* Circ Res, 1983. **53**(4): p. 502-14.
32. Taylor, C.A., T.J. Hughes, and C.K. Zarins, *Finite element modeling of three-dimensional pulsatile flow in the abdominal aorta: relevance to atherosclerosis.* Ann Biomed Eng, 1998. **26**(6): p. 975-87.
33. Butterfield, A.B., C.W. Miller, W.V. Lumb, F.D. McLeod, A.W. Nelson, and M.B. Histand, *Inverse effect of chronically elevated blood flow on atherogenesis in miniature swine.* Atherosclerosis, 1977. **26**(2): p. 215-24.
34. Sawchuk, A.P., J.L. Unthank, T.E. Davis, and M.C. Dalsing, *A prospective, in vivo study of the relationship between blood flow hemodynamics and atherosclerosis in a hyperlipidemic swine model.* J Vasc Surg, 1994. **19**(1): p. 58-63; discussion 63-4.
35. Oshinski, J.N., D.N. Ku, S. Mukundan, Jr., F. Loth, and R.I. Pettigrew, *Determination of wall shear stress in the aorta with the use of MR phase velocity mapping.* J Magn Reson Imaging, 1995. **5**(6): p. 640-7.
36. Oyre, S., E.M. Pedersen, S. Ringgaard, P. Boesiger, and W.P. Paaske, *In vivo wall shear stress measured by magnetic resonance velocity mapping in the normal human abdominal aorta.* Eur J Vasc Endovasc Surg, 1997. **13**(3): p. 263-71.
37. Levesque, M.J. and R.M. Nerem, *The elongation and orientation of cultured endothelial cells in response to shear stress.* J Biomech Eng, 1985. **107**(4): p. 341-7.

38. Levesque, M.J., D. Liepsch, S. Moravec, and R.M. Nerem, *Correlation of endothelial cell shape and wall shear stress in a stenosed dog aorta.* Arteriosclerosis, 1986. **6**(2): p. 220-9.
39. Okano, M. and Y. Yoshida, *Junction complexes of endothelial cells in atherosclerosis-prone and atherosclerosis-resistant regions on flow dividers of brachiocephalic bifurcations in the rabbit aorta.* Biorheology, 1994. **31**(2): p. 155-61.
40. Malek, A.M., S.L. Alper, and S. Izumo, *Hemodynamic shear stress and its role in atherosclerosis.* Jama, 1999. **282**(21): p. 2035-42.
41. Porth, C., ed. *Pathopysiology: Concepts of Altered Health States.* Fifth ed. 1998, Lippincott: New York/Philadelphia.
42. Glagov, S., C. Zarins, D.P. Giddens, and D.N. Ku, *Hemodynamics and atherosclerosis. Insights and perspectives gained from studies of human arteries.* Arch Pathol Lab Med, 1988. **112**(10): p. 1018-31.
43. Roberts, J.C., C. Moses, and R.H. Wilkins, *Autopsy Studies in Atherosclerosis 1. Distribution and Severity of Atherosclerosis in Patients Dying without Morphologic Evidence of Atherosclerotic Catastrophe.* Circulation, 1959. **20**: p. 511-519.
44. Roberts, J.C., R.H. Wilkins, and C. Moses, *Autopsy Studies in Atherosclerosis 2. Distribution and Severity of Atherosclerosis in Patients Dying with Morphologic Evidence of Atherosclerotic Catastrophe.* Circulation, 1959. **20**: p. 520-526.
45. Wilkins, R.H., J.C. Roberts, and C. Moses, *Autopsy Studies in Atherosclerosis 3. Distribution and Severity of Atherosclerosis in the Prescence of Obesity, Hypertension, Nephrosclerosis and Rheumatic Heart Disease.* Circulation, 1959. **20**: p. 527-536.
46. Shaaban, A.M. and A.J. Duerinckx, *Wall shear stress and early atherosclerosis: a review.* AJR Am J Roentgenol, 2000. **174**(6): p. 1657-65.
47. Letner, C., ed. *Geigy scientific tables.* 8th ed. Vol. 5 - Heart and circulation. 1990, Ciba-Geigy.
48. Cappell, M.S., *Intestinal (mesenteric) vasculopathy. I. Acute superior mesenteric arteriopathy and venopathy.* Gastroenterol Clin North Am, 1998. **27**(4): p. 783-825, vi.
49. van Bockel, J.H., R.H. Geelkerken, and M.N. Wasser, *Chronic splanchnic ischaemia.* Best Pract Res Clin Gastroenterol, 2001. **15**(1): p. 99-119.
50. Roobottom, C.A. and P.A. Dubbins, *Significant disease of the celiac and superior mesenteric arteries in asymptomatic patients: predictive value of Doppler sonography.* AJR Am J Roentgenol, 1993. **161**(5): p. 985-8.
51. Hansen, K.J., D.B. Wilson, T.E. Craven, J.D. Pearce, W.P. English, M.S. Edwards, J. Ayerdi, and G.L. Burke, *Mesenteric artery disease in the elderly.* J Vasc Surg, 2004. **40**(1): p. 45-52.
52. Heino, A., J. Hartikainen, M.E. Merasto, E.M. Koski, E. Alhava, and J. Takala, *Systemic and regional effects of experimental gradual splanchnic ischemia.* J Crit Care, 1997. **12**(2): p. 92-8.
53. Li, K.C., W.S. Whitney, C.H. McDonnell, J.O. Fredrickson, N.J. Pelc, R.L. Dalman, and R.B. Jeffrey, Jr., *Chronic mesenteric ischemia: evaluation with phase-contrast cine MR imaging.* Radiology, 1994. **190**(1): p. 175-9.
54. Bardhan, K.D., *Personal Communication.*
55. Vieli, A., U. Moser, S. Maier, D. Meier, and P. Boesiger, *Velocity profiles in the normal human abdominal aorta: a comparison between ultrasound and magnetic resonance data.* Ultrasound Med Biol, 1989. **15**(2): p. 113-9.
56. Nichols, W.W. and M.F. O'Rourke, *McDonald's Blood Flow in Arteries.* 3 ed. 1990: Edward Arnold.
57. Santamarina, A., E. Weydahl, J.M. Siegel, Jr., and J.E. Moore, Jr., *Computational analysis of flow in a curved tube model of the coronary*

arteries: effects of time-varying curvature. Ann Biomed Eng, 1998. **26**(6): p. 944-54.
58. Schulze-Bauer, C.A. and G.A. Holzapfel, *Determination of constitutive equations for human arteries from clinical data.* J Biomech, 2003. **36**(2): p. 165-9.
59. Bergel, D.H., *The static elastic properties of the arterial wall.* Journal of Physiology, 1961. **156**: p. 445-457.
60. Bergel, D.H., *The dynamic elastic properties of the arterial wall.* Journal of Physiology, 1961. **156**: p. 458-469.
61. Dobrin, P.B., *Biaxial anisotropy of dog carotid artery: estimation of circumferential elastic modulus.* J Biomech, 1986. **19**(5): p. 351-8.
62. Zhou, J. and Y.C. Fung, *The degree of nonlinearity and anisotropy of blood vessel elasticity.* Proc Natl Acad Sci U S A, 1997. **94**(26): p. 14255-60.
63. Love, A.E.H., *A treatise on mathematical elasticity.* 3rd ed. 1927, Cambridge: Cambridge University Press.
64. Berne, R.M. and M.N. Levy, *Cardiovascular Physiology.* 7th ed. 1997, St. Louis: Mosby.
65. Imura, T., K. Yamamoto, K. Kanamori, T. Mikami, and H. Yasuda, *Non-invasive ultrasonic measurement of the elastic properties of the human abdominal aorta.* Cardiovasc Res, 1986. **20**(3): p. 208-14.
66. Latham, R.D., N. Westerhof, P. Sipkema, B.J. Rubal, P. Reuderink, and J.P. Murgo, *Regional wave travel and reflections along the human aorta: a study with six simultaneous micromanometric pressures.* Circulation, 1985. **72**(6): p. 1257-69.
67. Luchsinger, P.C., R.E. Snell, D.J. Patel, and D.L. Fry, *Instanteous Pressure Distribution Along the Human Aorta.* Circ Res, 1964. **15**: p. 503-10.
68. Duck, F.A., *Physical properties of tissue: A comprehensive reference book.* 1990, London: Academic Press.
69. Holzapfel, G.A. and T.C. Gasser, *A new constitutive framework for arterial wall mechanics and a comparative study of material models.* Journal of Elasticity, 2000. **61**: p. 1-48.
70. Holzapfel, G.A., T.C. Gasser, and M. Stadler, *A structural model for the viscoelastic behaviour of arterial walls: Continuum formulation and finite element analysis.* European Journal of Mechanics A/Solids, 2002. **21**: p. 441-463.
71. Merrill, E.W., A.M. Benis, E.R. Gilliland, T.K. Sherwood, and E.W. Salzman, *Pressure-flow relations of human blood in hollow fibers at low flow rates.* J Appl Physiol, 1965. **20**(5): p. 954-67.
72. Chien, S., S. Usami, H.M. Taylor, J.L. Lundberg, and M.I. Gregersen, *Effects of hematocrit and plasma proteins on human blood rheology at low shear rates.* J Appl Physiol, 1966. **21**(1): p. 81-7.
73. Merrill, E.W., E.R. Gilliland, G. Cokelet, H. Shin, A. Britten, and R.E. Wells, Jr., *Rheology of human blood, near and at zero flow. Effects of temperature and hematocrit level.* Biophys J, 1963. **3**: p. 199-213.
74. Whitmore, R.L., *Rheology of the Circulation.* 1968, Oxford: Pergamon Press.
75. Fung, Y.C., *Biomechanics: Mechanical properties of living tissues.* 2nd ed. 1993, New York: Springer-Verlag.
76. Hughes, W.F. and J.A. Brighton, *Schaums Outlines: Fluid Dynamics.* 3 ed. 1999: Mcgraw Hill.
77. Witzig, K., *Uber erzw ngene Wellenbewegungen zaher, inkompressibler Flussigkeiten in elastichen Rohren.* 1914: Bern.
78. Womersley, J.R., *Method for the calculation of velocity, rate of flow and viscous drag in arteries when the pressure gradient is known.* J Physiol., 1955. **127**: p. 553-563.

79. Womersley, J.R., *Oscillatory motion of a viscous liiquid in a thin-walled elastic tube - 1: The linear approximation for long waves.* Phil. Mag., 1955. **46**: p. 199-221.
80. Womersley, J.R., *Oscillatory flow in arteries: the constrained elastic tube as a model of arterial flow and pulse transmission.* Phys. Med. Biol., 1957. **2**: p. 178-187.
81. Moens, A.I., *Die Pulskurve.* 1878, Leiden.
82. Nerem, R.M. and W.A. Seed, *An in vivo study of aortic flow disturbances.* Cardiovasc Res, 1972. **6**(1): p. 1-14.
83. Pedley, T.J., *The fluid mechanics of large blood vessels.* 1st ed. 1980, Cambridge: Cambridge University Press.
84. Nerem, R.M., W.A. Seed, and N.B. Wood, *An experimental study of the velocity distribution and transition to turbulence in the aorta.* Journal of Fluid Mechanics, 1972. **52**: p. 137-60.
85. Stein, P.D., H.N. Sabbah, and D.T. Anbe, *Blood velocity in the abdominal aorta and common iliac artery of man.* Biorheology, 1979. **16**: p. 249-55.
86. Black, M.M., D.R. Hose, and P.V. Lawford, *The origin and significance of secondary flows in the aortic arch.* J Med Eng Technol, 1995. **19**(6): p. 192-7.
87. Frazin, L.J., M.J. Vonesh, K.B. Chandran, T. Shipkowitz, A.S. Yaacoub, and D.D. McPherson, *Confirmation and initial documentation of thoracic and abdominal aortic helical flow. An ultrasound study.* Asaio J, 1996. **42**(6): p. 951-6.
88. Bogren, H.G. and M.H. Buonocore, *4D magnetic resonance velocity mapping of blood flow patterns in the aorta in young vs. elderly normal subjects.* J Magn Reson Imaging, 1999. **10**(5): p. 861-9.
89. Frank, O., *Die Grundform des arterielen Pulses erste Abhandlung: mathematische Analyse.* Z. Biol, 1899. **37**: p. 483-526.
90. Stergiopulos, N., J.J. Meister, and N. Westerhof, *Evaluation of methods for estimation of total arterial compliance.* Am J Physiol, 1995. **268**(4 Pt 2): p. H1540-8.
91. Westerhof, N., G. Elzinga, and P. Sipkema, *An artificial arterial system for pumping hearts.* J Appl Physiol, 1971. **31**(5): p. 776-81.
92. Westerhof, N., *Analog studies of human systemic arterial hemodynamics.* 1968, University of Pennslvania: Philadelphia.
93. Olufsen, M.S., *Structured tree outflow condition for blood flow in larger systemic arteries.* Am J Physiol, 1999. **276**(1 Pt 2): p. H257-68.
94. Ruan, W., M.E. Clark, M. Zhao, and A. Curcio, *A hperbolic system of equations of blood flow in an arterial network.* SIAM Journal of Applied Mathematics, 2003. **64**(2): p. 637-667.
95. Hose, D.R., P.V. Lawford, A.J. Narracott, J.M. Penrose, and I.P. Jones, *Fluid-solid interaction: benchmarking of an external coupling of ANSYS with CFX for cardiovascular applications.* J Med Eng Technol, 2003. **27**(1): p. 23-31.
96. Stergiopulos, N., B.E. Westerhof, and N. Westerhof, *Total arterial inertance as the fourth element of the windkessel model.* Am J Physiol, 1999. **276 (Heart Circ. Physiol. 45)**: p. H81-H88.
97. Segers, P., A. Qasem, T. De Backer, S. Carlier, P. Verdonck, and A. Avolio, *Peripheral "oscillatory" compliance is associated with aortic augmentation index.* Hypertension, 2001. **37**(6): p. 1434-9.
98. Westerhof, N., F. Bosman, C.J. de Vries, and A. Noordergraaf, *Analog studies of the human systemic arterial tree.* Journal of Biomechanics, 1969. **2**: p. 121-143.
99. Jones, D.M., *Westerhof Model Communications.* 2005.
100. Avolio, A.P., *Multi-branched model of the human arterial system.* Med Biol Eng Comput, 1980. **18**(6): p. 709-18.

101. Zamir, M., *Arterial branching within the confines of fractal L-system formalism.* J Gen Physiol, 2001. **118**(3): p. 267-76.
102. ANSYS, I., *Ansys Release 8.1 Documentation.* 2004.
103. Patankar, S.V., *Numerical heat transfer and fluid flow.* 1980, New York: Hemisphere.
104. Rice, J.G. and R.J. Schnipke, *A Monotone Streamline Upwind Finite Element Method for Convection-Dominated Flows.* Computer Methods in Applied Mechanics and Engineering, 1985. **48**: p. 313-327.
105. Elman, H.C., *Preconditioned Conjugate-Gradient Methods for Nonsymmetric Systems of Linear Equations*, in *Advances In Computer Methods For Partial Differential Equations IV*, R. Vichnevetsky, Editor. 1981, IMACS. p. 409-413.
106. Jones, G.T., J.A. Peacock, and R.J. Lutz. *Onset of Turbulence for Pulsatile flow within In Vitro models.* in *ASME Bioengineering.* 1991.
107. Chandran, K.B., M.J. Vonesh, A. Roy, S. Greenfield, B. Kane, R. Greene, and D.D. McPherson, *Computation of vascular flow dynamics from intravascular ultrasound images.* Med Eng Phys, 1996. **18**(4): p. 295-304.
108. Augst, A.D., D.C. Barrett, B. Ariff, A.D. Hughes, S.A. Thom, and X.Y. Xu. *CFD Modelling of Carotid Bifurcation Flow using 3D Ultrasound: Correlations of Wall Shear Stress with Intima Media Thickness.* in *Physical, Mathematical and Numerical Modelling of Blood Flow in Cardiovascular Disease.* 2003. York: IPEM.
109. Cebral, J.R., R. Lohner, P.L. Choyke, and P.J. Yim, *Merging of intersecting triangulations for finite element modeling.* J Biomech, 2001. **34**(6): p. 815-9.
110. Long, Q., X.Y. Xu, M.W. Collins, M. Bourne, and T.M. Griffith, *Magnetic resonance image processing and structured grid generation of a human abdominal bifurcation.* Comput Methods Programs Biomed, 1998. **56**(3): p. 249-59.
111. Cheong, P.L., T.M. Griffith, M. Bourne, and X. Xu. *Effect of Body Posture on Haemodynamics at the Abdominal Aorta.* in *Physical, Mathematical and Numerical Modelling of Blood Flow in Cardiovascular Disease.* 2003. York: IPEM.
112. Pittaccio, S., F. Migliavacca, G. Dubini, E. Morre-Pedersen, E.T. Frund, V. Hjortdal, X.Y. Xu, and M.R. de Leval. *CFD-MRI combined 3D study of end-to-end coarctation repair.* in *Physical, Mathematical and Numerical Modelling of Blood Flow in Cardiovascular Disease.* 2003. York: IPEM.
113. Lee, D. and J.Y. Chen, *Numerical simulation of steady flow fields in a model of abdominal aorta with its peripheral branches.* J Biomech, 2002. **35**(8): p. 1115-22.
114. Berger, S.A. and L.-D. Jou, *Flows in Stenotic Vessels.* Annual Review of Fluid Mechanics, 2000. **32**: p. 347-382.
115. Marques, P.F., M.E. Oliveira, A.S. Franca, and M. Pinotti, *Modeling and simulation of pulsatile blood flow with a physiologic wave pattern.* Artif Organs, 2003. **27**(5): p. 478-85.
116. Longest, P.W. and C. Kleinstreuer, *Computational haemodynamics analysis and comparison study of arterio-venous grafts.* J Med Eng Technol, 2000. **24**(3): p. 102-10.
117. Migliavacca, F., G. Dubini, G. Pennati, R. Pietrabissa, R. Fumero, T.Y. Hsia, and M.R. de Leval, *Computational model of the fluid dynamics in systemic-to-pulmonary shunts.* J Biomech, 2000. **33**(5): p. 549-57.
118. Zhao, S.Z., X.Y. Xu, M.W. Collins, A.V. Stanton, A.D. Hughes, and S.A. Thom, *Flow in carotid bifurcations: effect of the superior thyroid artery.* Med Eng Phys, 1999. **21**(4): p. 207-14.
119. Hyun, S., C. Kleinstreuer, and J.P. Archie, Jr., *Hemodynamics analyses of arterial expansions with implications to thrombosis and restenosis.* Med Eng Phys, 2000. **22**(1): p. 13-27.

120. Perktold, K., M. Hofer, G. Rappitsch, M. Loew, B.D. Kuban, and M.H. Friedman, *Validated computation of physiologic flow in a realistic coronary artery branch.* J Biomech, 1998. **31**(3): p. 217-28.
121. Bertolotti, C., V. Deplano, J. Fuseri, and P. Dupouy, *Numerical and experimental models of post-operative realistic flows in stenosed coronary bypasses.* J Biomech, 2001. **34**(8): p. 1049-64.
122. Weydahl, E.S. and J.E. Moore, *Dynamic curvature strongly affects wall shear rates in a coronary artery bifurcation model.* J Biomech, 2001. **34**(9): p. 1189-96.
123. Kim, T., T. Seo, and A.I. Barakat, *Numerical simulations of fluid mechanical interactions between two abdominal aortic branches.* Korea-Australia Rheology Journal, 2004. **16**(2): p. 75-83.
124. Buchanan, J.R., C. Kleinstreuer, S. Hyun, and G.A. Truskey, *Hemodynamics simulation and identification of susceptible sites of atherosclerotic lesion formation in a model abdominal aorta.* J Biomech, 2003. **36**(8): p. 1185-96.
125. Migliavacca, F., G. Pennati, E. Di Martino, G. Dubini, and R. Pietrabissa, *Pressure drops in a distensible model of end-to-side anastomosis in systemic-to-pulmonary shunts.* Comput Methods Biomech Biomed Engin, 2002. **5**(3): p. 243-8.
126. O'Brien, T. and T. McGloughlin. *The Effects of Wall Compliance on Blood Flow Patterns Through Vascular Grafts.* in *ASME Bioengineering.* 2001.
127. Klein, A. and G. Gerlach, *Simulation der Fluid-Struktur-Wechselwirkung von Mikromembranpumpen.* Informationstechnik und Technische Informatik, 1999. **4**.
128. Zhao, S.Z., X.Y. Xu, A.D. Hughes, S.A. Thom, A.V. Stanton, B. Ariff, and Q. Long, *Blood flow and vessel mechanics in a physiologically realistic model of a human carotid arterial bifurcation.* J Biomech, 2000. **33**(8): p. 975-84.
129. Zhang, H., X. Zhang, S. Ji, Y. Guo, G. Ledezma, N. Elabbasi, and H. deCougny, *Recent development of the fluid-structure interaction capabilities in the ADINA system.* Computers and Structures, 2003. **81**: p. 1071-1085.
130. Shim, E.B., J.Y. Yeo, H.J. Ko, C.H. Youn, Y.R. Lee, C.Y. Park, B.G. Min, and K. Sun, *Numerical analysis of the three-dimensional blood flow in the korean artificial heart.* Artif Organs, 2003. **27**(1): p. 49-60.
131. Verdonck, P.R. and J.A. Vierendeels. *Fluid-Structure Interaction Modelling of Left Ventricular Filling.* in *ICCS.* 2002.
132. Maurits, N.M., E. Loots, and A.E.P. Veldman. *Fluid-structure Interaction and Peripheral Resistance in the Carotid Bifurcation: a CFD Model Compared to In-vivo Ultrasound Measurements.* in *Physical, Mathematical and Numerical Modelling of Blood Flow in Cardiovascular Disease.* 2003. York: IPEM.
133. Bathe, M. and R.D. Kamm, *A fluid--structure interaction finite element analysis of pulsatile blood flow through a compliant stenotic artery.* J Biomech Eng, 1999. **121**(4): p. 361-9.
134. Lee, K.W. and X.Y. Xu, *Modelling of flow and wall behaviour in a mildly stenosed tube.* Med Eng Phys, 2002. **24**(9): p. 575-86.
135. Tang, D., C. Yang, H. Walker, S. Kobayashi, and D.N. Ku, *Simulating cyclic artery compression using a 3D unsteady model with fluid-structure interaction.* Computers and Structures, 2002. **80**: p. 1651-1665.
136. Di Martino, E.S., G. Guadagni, A. Fumero, G. Ballerini, R. Spirito, P. Biglioli, and A. Redaelli, *Fluid-structure interaction within realistic three-dimensional models of the aneurysmatic aorta as a guidance to assess the risk of rupture of the aneurysm.* Med Eng Phys, 2001. **23**(9): p. 647-55.
137. van der Heide, D., *Fluid Solid Interaction Analysis of Flow through the Abdominal Aorta.* 2000.

138. Formaggia, L., J.F. Gerbau, F. Nobile, and A. Quarteroni, *On the coupling of 3D and 1D Navier-Stokes equations for flow problems in compliant vessels.* Comput Method Appl, 2001. **M191**(6-7): p. 561-582.
139. Lagana, K., G. Dubini, F. Migliavacca, G. Pennati, R. Pietrabissa, S. Ragni, A. Veneziana, and A. Quarteroni. *Multiscale modelling as a tool to prescribe realistic boundary conditions for the study of local and global haemodynamics.* in *ASME Bioengineering.* 2001.
140. Edelman, R.R., J.R. Hesselink, and M.B. Zlatkin, *Clinical Magnetic Resonance Imaging.* 2nd ed. 1996, Philadelphia: W.B.Sauders Company.
141. Runge, V.M., *Safety of approved MR contrast media for intravenous injection.* J Magn Reson Imaging, 2000. **12**(2): p. 205-13.
142. Crowe, L., P. Gatehouse, C. Charrier, and D.N. Firmin. *A Volume Selective 3D Turbo Spin Echo Sequence for Vessel Wall and Compliance Measurement.* in *International Society of Magnetic Resonance in Medicine.* 2002. Hawaii.
143. Gill, J.D., H.M. Ladak, D.A. Steinman, and A. Fenster, *Accuracy and variability assessment of a semiautomatic technique for segmentation of the carotid arteries from three-dimensional ultrasound images.* Med Phys, 2000. **27**(6): p. 1333-42.
144. Papathanasopoulou, P., S. Zhao, U. Kohler, M.B. Robertson, Q. Long, P. Hoskins, X.Y. Xu, and I. Marshall, *MRI measurement of time-resolved wall shear stress vectors in a carotid bifurcation model, and comparison with CFD predictions.* J Magn Reson Imaging, 2003. **17**(2): p. 153-62.
145. Robertson, M.B., U. Kohler, P.R. Hoskins, and I. Marshall, *Quantitative analysis of PC MRI velocity maps: pulsatile flow in cylindrical vessels.* Magn Reson Imaging, 2001. **19**(5): p. 685-95.
146. Kohler, U., I. Marshall, M.B. Robertson, Q. Long, X.Y. Xu, and P.R. Hoskins, *MRI measurement of wall shear stress vectors in bifurcation models and comparison with CFD predictions.* J Magn Reson Imaging, 2001. **14**(5): p. 563-73.
147. Cheng, C.P., D. Parker, and C.A. Taylor. *Wall Shear Stress Quantification from MRI Data Using Lagrangian Interpolation Functions.* in *ASME Bioengineering.* 2001.
148. Katz, I.M., E.J. Shaughnessy, and B.B. Cress, *A technical problem in the calculation of laminar flow near irregular surfaces described by sampled geometric data.* J Biomech, 1995. **28**(4): p. 461-4.
149. Kramer, C.M., *Magnetic resonance imaging to identify the high-risk plaque.* Am J Cardiol, 2002. **90**(10C): p. 15L-17L.
150. Choi, C.J. and C.M. Kramer, *MR imaging of atherosclerotic plaque.* Radiol Clin North Am, 2002. **40**(4): p. 887-98.
151. Kirbas, C. and F.K. Quek. *A review of vessel extraction techniques and algorithms.* in *The 3rd IEEE Symposium on Bioinformatics and Bioengineering.* 2001. Bethesda.
152. McCarthy, A.D., I.D. Wilkinson, D.R. Hose, D.C. Barber, S. Wood, G. Darwent, D. Chan, and D.R. Bickerstaff. *Musculo-Skeletal Simulation: Finite Element Meshes Derived From Magnetic Resonance Volumes.* in *10th Scientific Meeting and Exhibition of the ISMRM.* 2002. Honolulu.
153. Barber, D.C. and D.R. Hose, *Automatic segmentation of medical images using image registration: diagnostic and simulation applications.* J Med Eng Technol, 2005. **29**(2): p. 53-63.
154. Prakash, S. and C.R. Ethier, *Requirements for mesh resolution in 3D computational hemodynamics.* J Biomech Eng, 2001. **123**(2): p. 134-44.
155. Barber, D.C., *Automatic generation of Regions Of Interest for Radionuclide Renograms.* 2002, University of Sheffield: Sheffield.

156. Piene, H. and T. Sund, *Does normal pulmonary impedance constitute the optimum load for the right ventricle?* Am J Physiol, 1982. **242**(2): p. H154-60.
157. Proakis, J.G. and D.G. Manolakis, *Digital Signal Processing: Principles, Algorithms and Applications.* 3rd ed. 1996, Upper Saddle River: Prentice-Hall.
158. Franklin, G., J.D. Powell, and M.L. Workman, *Digital Control of Dynamic Systems.* 2nd ed. 1990, Reading, Massachusetts: Addison-Wesley.
159. Sonesson, B., T. Lanne, E. Vernersson, and F. Hansen, *Sex difference in the mechanical properties of the abdominal aorta in human beings.* J Vasc Surg, 1994. **20**(6): p. 959-69.
160. Schreiner, W. and P.F. Buxbaum, *Computer-optimization of vascular trees.* IEEE Trans Biomed Eng, 1993. **40**(5): p. 482-91.
161. Kilner, P.J., G.Z. Yang, R.H. Mohiaddin, D.N. Firmin, and D.B. Longmore, *Helical and retrograde secondary flow patterns in the aortic arch studied by three-directional magnetic resonance velocity mapping.* Circulation, 1993. **88**(5 Pt 1): p. 2235-47.
162. Spencer, P.A., *Anonymised SMA and CA Angiogram*, A.D. Jeays, Editor. 2005.

Appendix A – Validation of Registration Including Centre-line Extraction

Test 1: Circles

The first validation case was the registration of a small circle onto a larger one as shown in figure A1. The images were 100*100 pixels and the circles were of radius 15 centred at pixels (50,35) and 30 pixels centred at (50,50).

The registration algorithm used was the SMW algorithm. Validation was carried out for a range of lambda values.

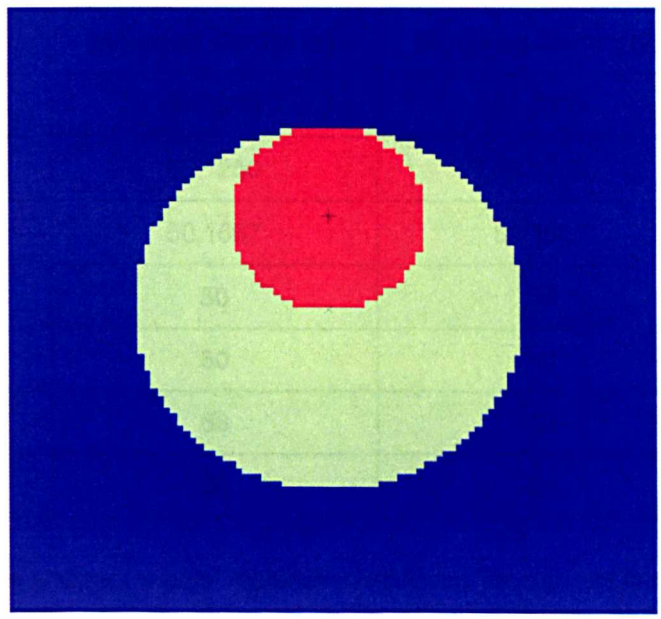

Figure A1. Image registration validation case 1: Green circle represents target image, red circle represents source image, cross and star represent respective centres.

The first test of the registration was to ensure that it recreated the circle appropriately. This is shown in figure A2. Table A1 shows quantitative measures of the quality of the registration.

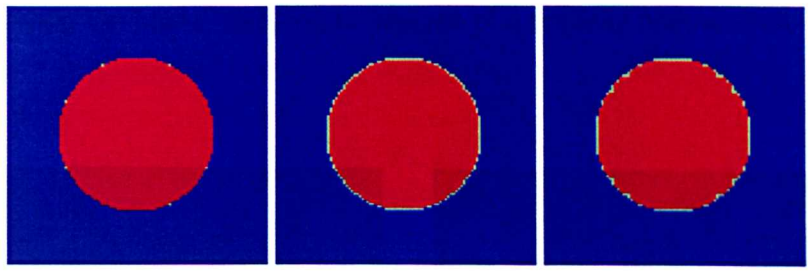

Figure A2. Target (green) and morphed (red) images, (left to right: lambda 0.01, 1000, affine-only).

Lambda	Morphed Centre (x)	Morphed Centre (y)	ALD
0.01	57.3333	57.3333	0.0307
0.1	53.1250	53.1250	0.0307
1	50.1667	50.1667	0.0511
10	50	50	0.0614
100	50	50	0.5425
1000	50	50	0.7473
Affine only	50	50	0.608

Table A1. Circle and centre point registration accuracy for different lambda values.

The registration algorithm implements an affine transform first, which in the case of a single circle produces quite a good fit to the target circle (with some error due to the fact that the pixel size is not insignificant compared to the object size). The only error in the stiffer analyses was in the form of the morphed circle being about one pixel smaller than the target, however they did not move the centre-point from where it is put by the affine transform.

Even though the affine transform performed well in this test, the less stiff transforms moved the centre-point substantially, making them unsuitable for centreline extraction from a complex geometry, futher insight may be gained by considering the

result of applying the same mapping to images of a partially hollow circle as shown in figure A3.

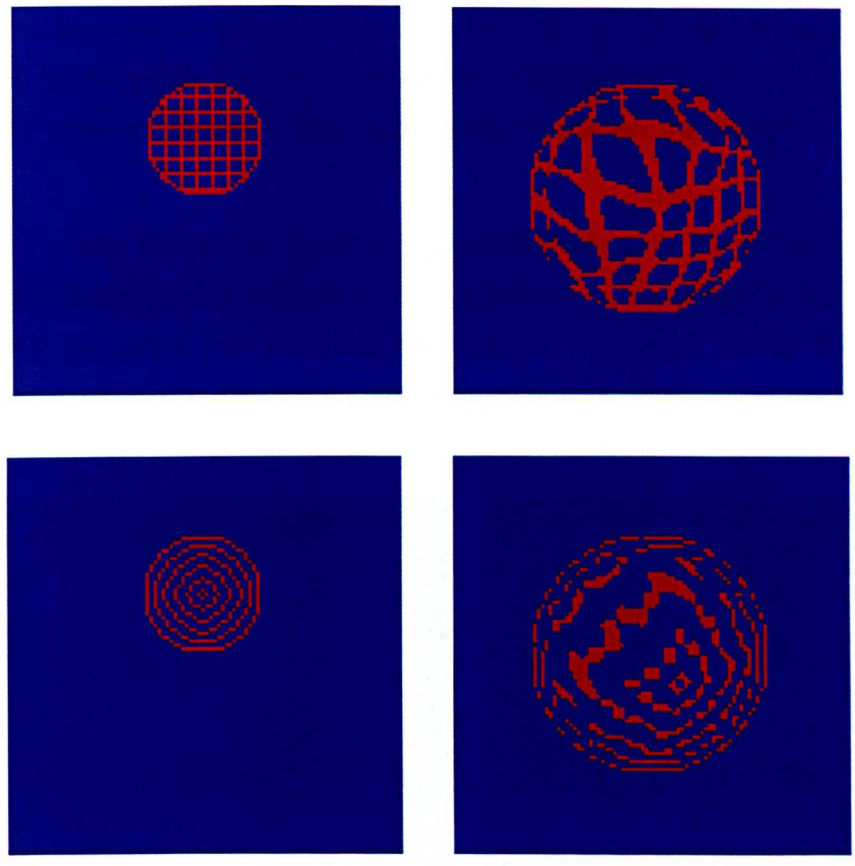

Figure A3. Two sets of source (left) and morphed (right) test images for registration (lambda = 0.01).

For this example, the registration of the circle worked well for all values of lambda especially those below 100. The correct movement of the centre-line (to within one pixel) was preserved for lambda greater than or equal to 1.

Test 2: Cylinders

The second validation case was designed to see how the algorithm coped with lengthening of a vessel. A small (radius 8 units, length 50 units) cylinder was registered onto a larger coaxial one (radius 10 units, length 100 units), figure A4 shows the relative initial positions of these two cylinders. These cylinders were created in Ansys, imported into Matlab and converted into 3d images with voxel size 0.5 units by 0.5 units by 1 unit (the long axis of the voxel being aligned with the

cylinder's axis). The registration was performed on these images but the resulting mapping can be applied to the Ansys meshes or a set of nodes representing the vessel centreline.

Registrations were run with lambdas ranging from 0.1 to 1000 as for the 2d case. All figures and values in this section are based on a lambda of 10. The ALD was found to be 0.063 units indicating a very good match between the morphed and target datasets.

The centre line was defined as a set of 100 equidistant points for both the target and source images, figures A5, A6 and A7 show the x and y (radial), and z (axial) co-ordinates for the target and morphed centre-lines. Figure A8 shows the morphed vessel surface mesh with the morphed and target centre-lines.

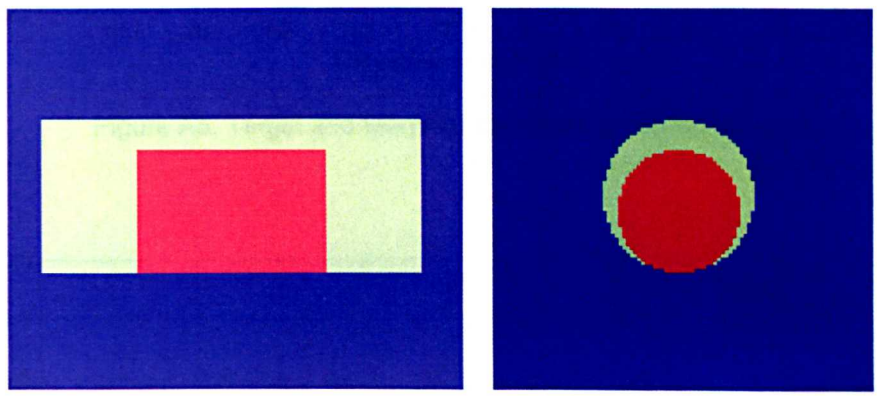

Figure A4. Axial (left) and circumferential (right) cross-sections of target (green) and source(red) cylinders.

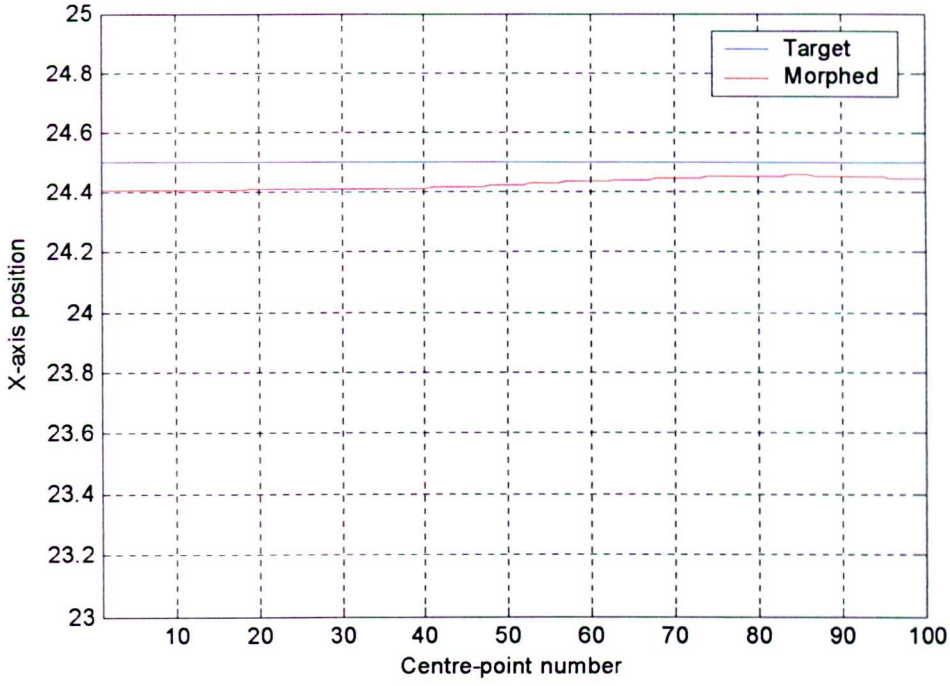

Figure A5. Target and Morphed centreline x-coordinates.

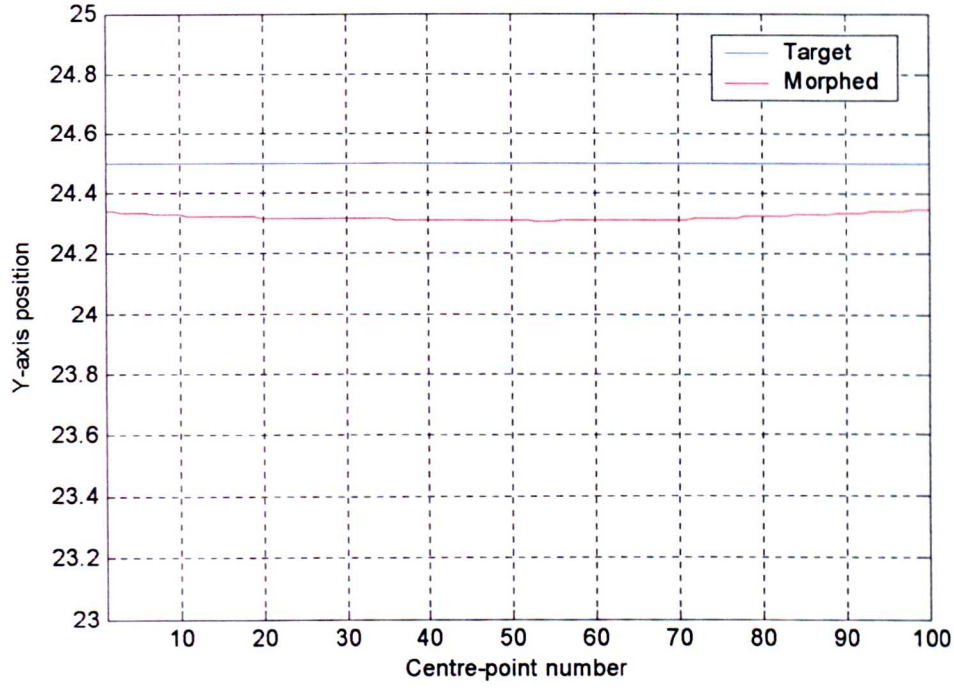

Figure A6. Target and Morphed centreline y-coordinates.

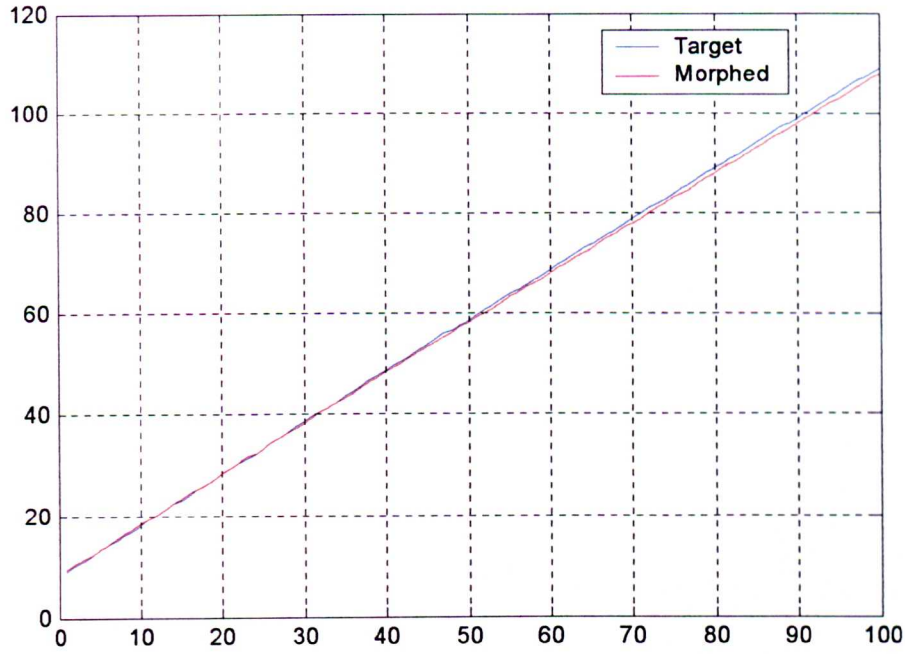

Figure A7. Target and Morphed centreline z-coordinates .

Figure A8. Section of morphed surface mesh with target(blue) and morphed(yellow) centrelines.

These validation exercises show that the registration algorithm performs well for these cases, and gives plausible centre-lines quantifiably close to the defined vessel centre-line.

Appendix B – Full Results of the Initial Registrations

Initial Idealised Mesh – SMW Algorithm only

Table B1 shows the results for the initial registration described in 4.53. During the analyses needed to complete this table it became clear that the SMW algorithm, must have some coding bug or random element, as the exact same analysis could be carried out multiple times and yield different results. At the time of writing, this was being investigated by the algorithm's author.

Lambda	Run number	Number of degenerate elements	Maximum GAR*	ALD (mm)
1	1	40	2779.9	0.6872
1	2	32	1128.4	0.666
1	3	40	2779.9	0.6872
10	1	25	1140.3	0.6874
10	2	7	65.5	0.673
10	3	25	1140.3	0.6874
100	1	12	422.1	0.6868
100	2	12	422.1	0.6868
100	3	12	422.1	0.6868
1000	1	0	69.7	0.6749
1000	2	0	69.7	0.6749
1000	3	0	69.7	0.6749
10^4	1	1	36.5	0.6628
10^4	2	1	36.5	0.6628
10^4	3	8	3477.9	0.639
10^5	1	0	33	0.6702
10^5	2	0	33	0.6702
10^5	3	0	33	0.6702
10^6	1	0	11	0.6825
10^6	2	0	11.4	0.6936

Lambda	Run number	Number of degenerate elements	Maximum GAR*	ALD (mm)
10^6	3	0	11.4	0.6936
10^7	1	0	5.49	0.9206
10^7	2	0	5.49	0.9214
10^7	3	0	5.49	0.9214

Table B1. Results of registration using SMW algorithm with different stiffness parameter (lambda) values (original idealised mesh).

Improved Idealised Mesh – SMW Algorithm

Table B2 lists the results for the SMW algorithm with improved idealised mesh outline in section 4.5.4

Figures B1 to B4 show the results for both the original and improved meshes over the full range of lambda values.

Lambda	Run number	Number of degenerate elements	Maximum GAR	ALD (mm)
1	1	6	177.9894	0.4442
1	2	6	177.9894	0.4442
1	3	6	177.9894	0.4442
10	1	3	282.1475	0.4408
10	2	2	91.5498	0.4161
10	3	3	282.1475	0.4408
100	1	3	847.2141	0.4389
100	2	3	847.2141	0.4389
100	3	3	847.2141	0.4389
1000	1	3	266.4354	0.408
1000	2	3	266.4354	0.408
1000	3	4	125.0591	0.4564
10^4	1	7	174.7437	0.4231

Lambda	Run number	Number of degenerate elements	Maximum GAR	ALD (mm)
10^4	2	1	145.9759	0.4266
10^4	3	1	145.9759	0.4266
10^5	1	0	7.3186	0.4131
10^5	2	0	7.3186	0.4131
10^5	3	0	7.3186	0.4131
10^6	1	0	5.1216	0.4489
10^6	2	0	5.2678	0.4468
10^6	3	0	5.2678	0.4468
10^7	1	0	4.805	0.5484
10^7	2	0	4.805	0.5484
10^7	3	0	4.8095	0.5558

Table B2. Results of registration using SMW algorithm with different stiffness parameter (lambda) values (improved idealised mesh).

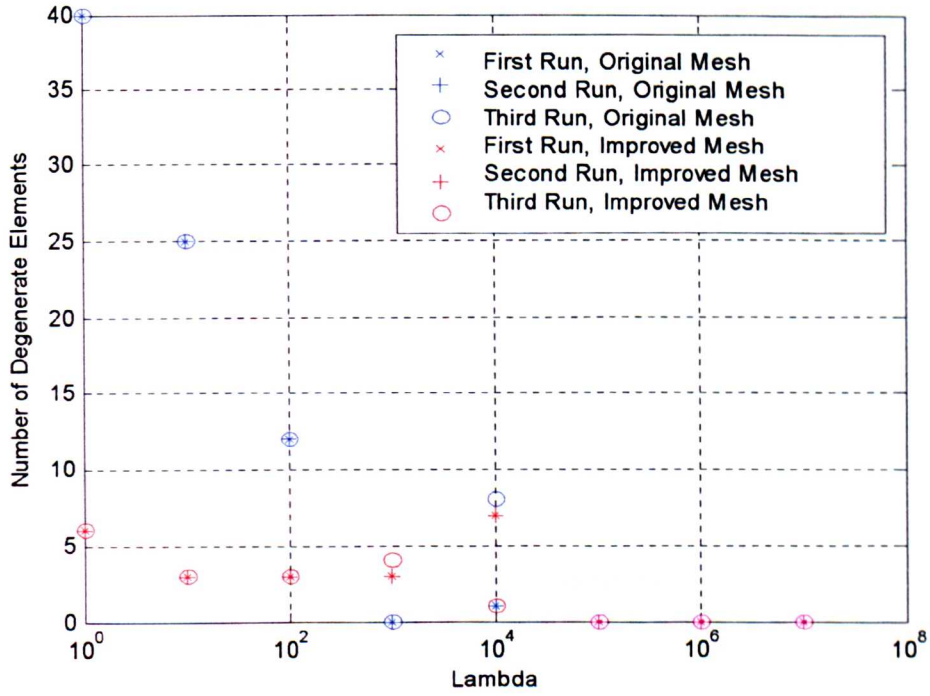

Figure B1. Number of Degenerate Elements against lambda for both meshes.

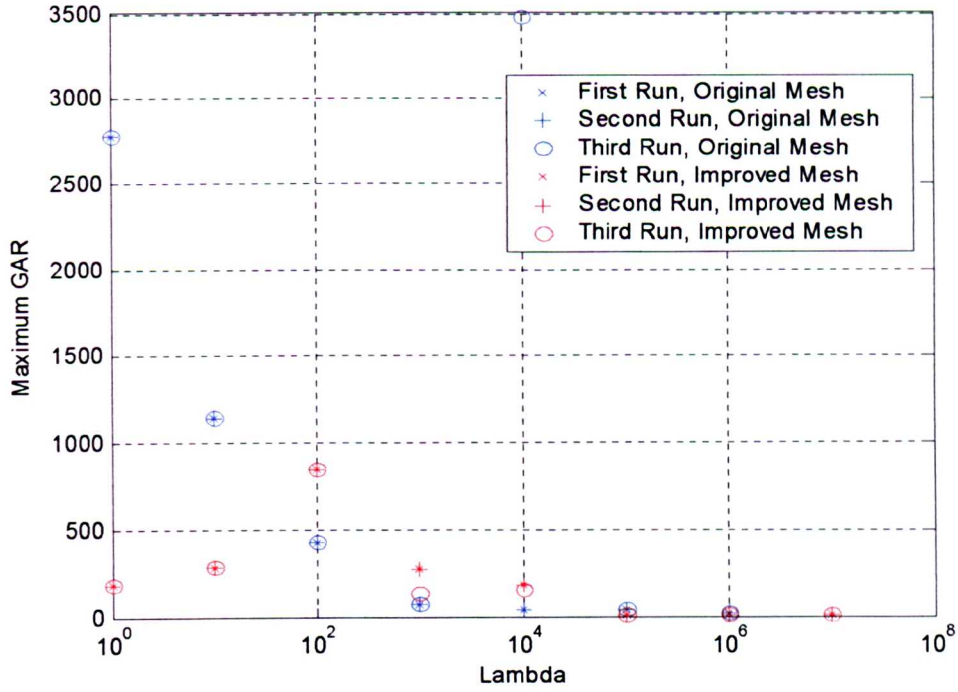

Figure B2. Maximum GAR against lambda for both meshes.

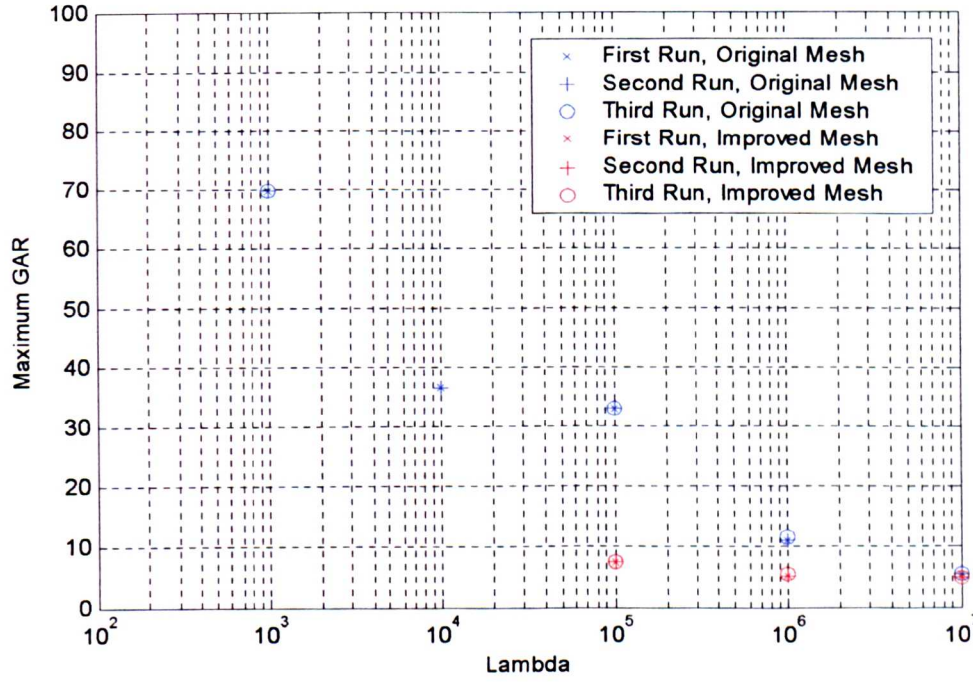

Figure B3. Detail from figure B2.

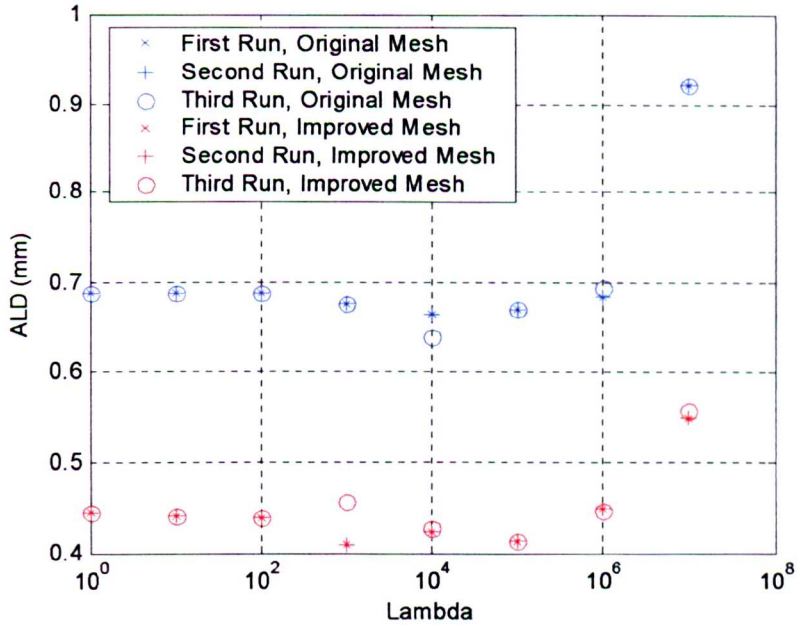

Figure B4. ALD against lambda for both meshes.

Improved Idealised Mesh – DCB Algorithm

Table B3 shows results for a range of start and end grid sizes. Figures B5 to B7 show the results from table B3 in graphical form.

Start Grid Size	End Grid Size	Number of degenerate elements	Maximum GAR	ALD (mm)
32	2	131	26475	0.77
32	4	0	35.5	0.392
32	8	0	5.09	0.315
32	16	0	4.77	0.484
32	32	0	4.27	2.69
64	2	107	54826	0.808
64	4	0	23.0	0.489
64	8	0	5.73	0.34
64	16	0	4.963	0.496
64	32	0	4.53	1.14
64	64	0	4.28	2.69

Table B3. Results of registration using DCB algorithm with different start and end grid sizes (improved idealised mesh).

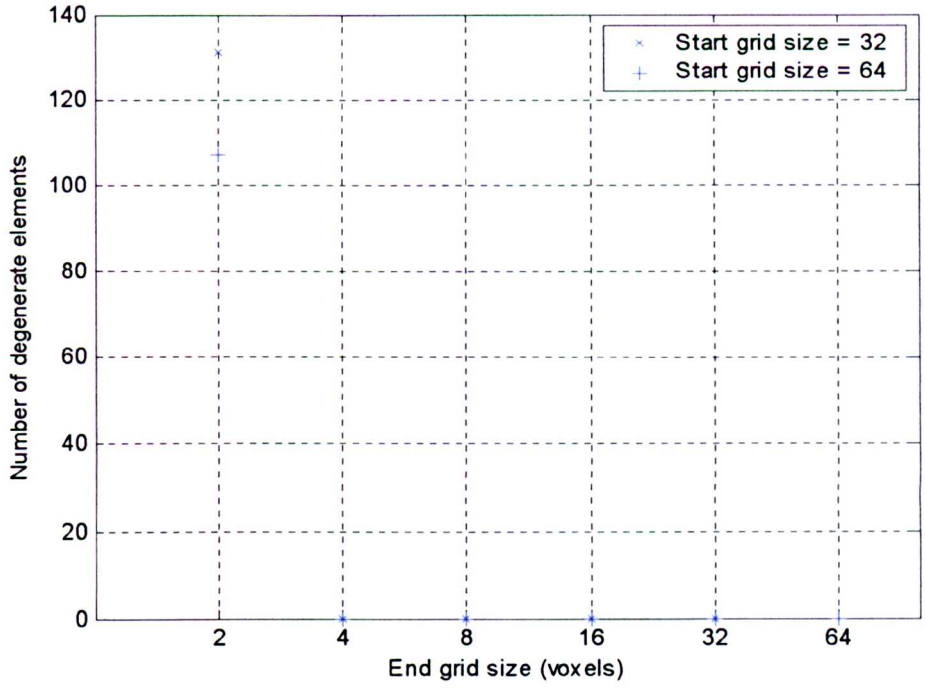

Figure B5. Number of degenerate elements against end grid size.

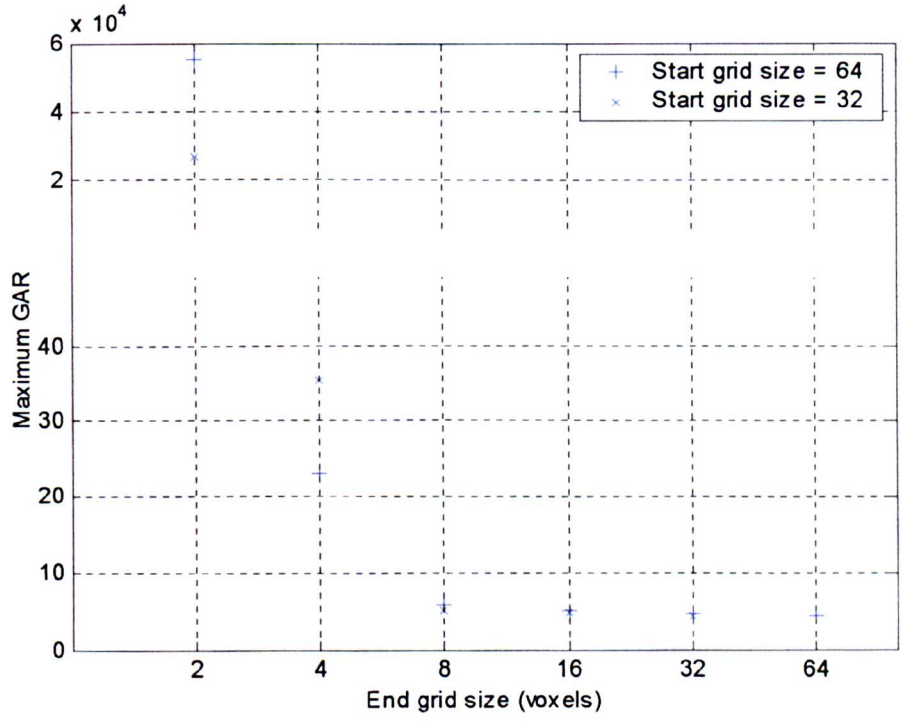

Figure B6. Maximum GAR against end grid size.

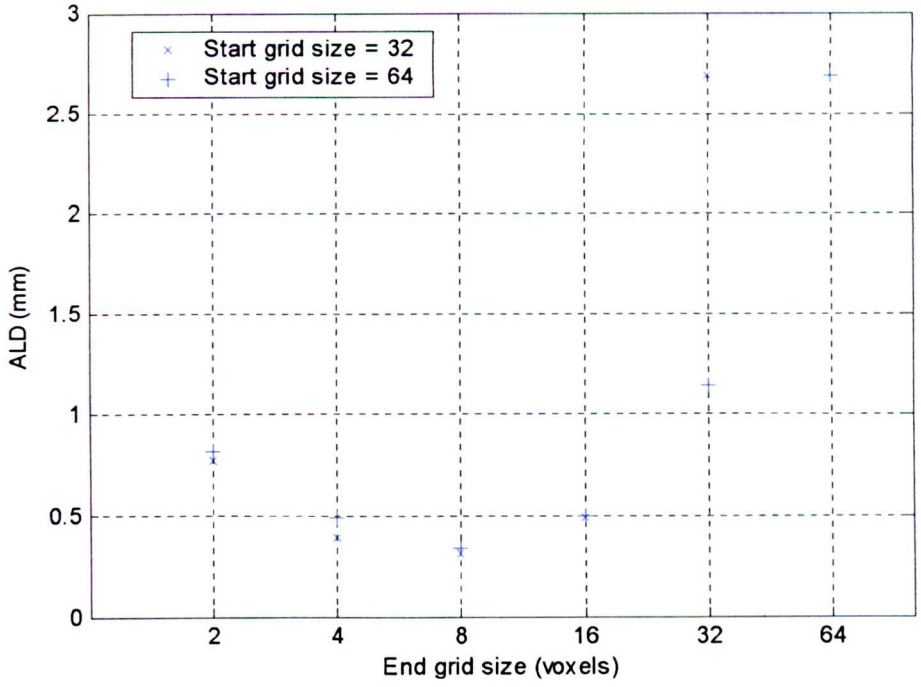

Figure B7. ALD against end grid size.

Appendix C – Commented Ansys Input File for Moving Mesh Analysis

```
/filname,moving4a,1      !set analysis filename
/outp,m4a_pre,out        !set output filename
/config,nres,7000        !allow Ansys to store more than 7000
                         !timesteps if necessary
/prep7                   !enter preprocessor

filename = 'moving4a'    !set filename variable for later use

resume,disp_vels_in,db,  !resume database which just contains the
                         !displacements and wall velocities
reindex_disp_tab,0.05,0.91     !reindex displacement table to only
                               !start displacement after the 50ms ramp
reindex_vel_tab,0.05,0.05375,0.0001       !reindex velocity tables as
                                          !well

cdread,comb,aorta_s3m_moving,cdb    !read in initial mesh

keyopt,1,4,1      !turn on ALE solver

!FLUID BOUNDARY CONDITIONS
/inp,aa_in_flow_moving,inp          !AA inlet flow
alls

/inp,sma_out_flow_moving,inp        !SMA outlet flow
alls

/inp,aa_out_pressure           !AA outlet pressure
alls

cmsel,s,wall,node              !Wall motion (velocity)
d,all,enke,-1                  !indicates moving wall
d,all,vx,%wall_vels_x%
d,all,vy,%wall_vels_y%
d,all,vz,%wall_vels_z%
alls

d,all,ux,%disps_x%             !Wall motion (displacment)
d,all,uy,%disps_y%
d,all,uz,%disps_z%


!Fluids solver setup

total_time = 0.91
tstep = 0.005

fldata1,solu,tran,t      !Solve for transient flow
fldata1,solu,ale,t       !ALE solution procedure on


fldata4,time,step,tstep        !set timestep
fldata4,time,tend,total_time   !set analysis end time
fldata4,time,pres,1e-6         !convergence criteria
fldata4,time,vx,1e-2
fldata4,time,vy,1e-2
```

```
fldata4,time,vz,1e-2
fldata4,time,meth,back  !time integration methon

fldata4,time,glob,100   !max number of fluid iterations per timestep

fldata4,time,appe,0.01  !write output every 0.01 seconds.

fldata5,outp,tauw,t     !write output including WSS values

fldata8,nomi,dens,1000        !fluid density
fldata8,nomi,visc,0.004       !fluid viscosity

/outp,m4a_main,out      !direct output to specified file

/solu             !enter solution phase
solve
save

/prep7
reindex_disp_tab,0.91,1.77    !reindex displacement table for second
                              !heartbeat
reindex_vel_tab,0.91,0.05375,0.0001 !reindex velocity table as well

!reiterate ALE boundary conditions

cmsel,s,wall,node
d,all,enke,-1
d,all,vx,%wall_vels_x%
d,all,vy,%wall_vels_y%
d,all,vz,%wall_vels_z%
allsel
d,all,ux,%disps_x%
d,all,uy,%disps_y%
d,all,uz,%disps_z%

fldata32,rest,time,0.91 !restart analysis from where we left off
fldata4,time,tend,1.77  !set new analysis end time

/solu
solve
save
```

Appendix D – Imposing Wall Movement Boundary Conditions in Ansys

Having performed the image registration steps and created a moving mesh, the movement of each node had to be described in such a way that it could be interpreted quickly by the CFD solver (in our case Ansys Flotran).

Applying Displacement Boundary Conditions in Ansys Flotran

The approach taken for the application of mesh movement boundary conditions is outlined below.

A file containing the geometry information for the first time-step is read into Ansys, all displacements stated are relative to this initial mesh. The mesh movements must then be applied as boundary conditions; this is done using the 'd' command. The general form of this command is shown below:

d,node,label,value

'node' specifies the node on which the boundary condition is to be applied, this can either be a number, or the string 'all', in which case Ansys applies the boundary condition to all selected nodes.

'label' specifies the degree of freedom to be constrained, the three components of mesh displacement are given the labels, ux,uy and uz.

'value' is the value of the degree of freedom, it can be a number, a pre-defined variable, or an Ansys table (in which case the table name must be surrounded by a pair of percentage signs).

Tables in Ansys are indexed, multi-dimensional data structures; tables support linear interpolation between available data-points. Each dimension may be named to match one of a list of primary variables, these include x, y and z positions and time. When the dimensions of a table have been named using primary variables, Ansys looks up the appropriate point in the table for each node at which a boundary condition is specified. For example, for a 4-dimensional table called 'x_displacements' with primary variables x, y, z and time, the command:

d,all,ux,%x_displacements%

will apply a different time-varying x displacement value for each selected node.

There are a number of ways of using the 'd' command to apply mesh displacement boundary conditions in Ansys:

- Apply the displacement value for each node directly at each timestep without using tables.
- Use three 1d tables per node with primary variable being time. Registration output would be used directly.
- Use three four-dimensional tables as in the above example. Primary variables would be x, y, z and time.

The first option is straightforward to program but increases computational overhead and decreases flexibility for each timestep substantially, as a new input file must be read in at for each timestep. Any change in timestep or mesh density would require the writing of new input files. Theoretically, this technique could be altered to use ramped loading and only specify the displacement at the 16 MRI timesteps; unfortunately, this approach causes Ansys to crash, even for a simple validation case.

The second option is attractive but cannot be implemented for sensible size meshes, as Ansys is limited to 5000 tables. The ideal solution to this problem would be if Ansys allowed 'node number' as a primary variable, then the displacements could be set up as a single 2d table in node number and time. The problems associated with altering mesh density would still occur, however.

The third option requires more work but allows both mesh density and timestep dependence checks to be performed without problems. The mappings must be applied to a regular grid to transfer the data into the correct format; the effect of this mapping can be easily checked to ensure that no significant degradation occurs due to the interpolation. The displacements are therefore applied as a set of three 4-dimensional tables (in x, y, z and time).

Based on the above information, the third option was selected for boundary condition implementation.

Issues Arising in Displacement Boundary Condition Implementation

Having adopted the 4d table approach to boundary condition implementation, it quickly became apparent that the displacements as understood by Ansys were not

those required. The error laid in Ansys' interpretation of the x, y and z primary variables.

At each timestep, Ansys updates the mesh with any previous displacements before applying the boundary conditions; this means that when it interrogates the table it looks at the point in space where the node has moved to for the displacement, whereas the required displacement is at the point where the node started. This can be shown by considering one node in a 2-d example.

Consider a node moving in one dimension (x) as time varies, ux=f(x,t). The required displacements are known at the mesh timesteps 0,T, 2T, and at positions, n-1, n, n+1. For this example, the CFD timestep is T/3 so at CFD timesteps, 1,2,4 and 5 linear interpolation is used to find the displacement value. At t=0 the node is at x=n. Figure D1 shows the position of the node at each timestep assuming that Ansys always checks in the node's original position for the displacement value.

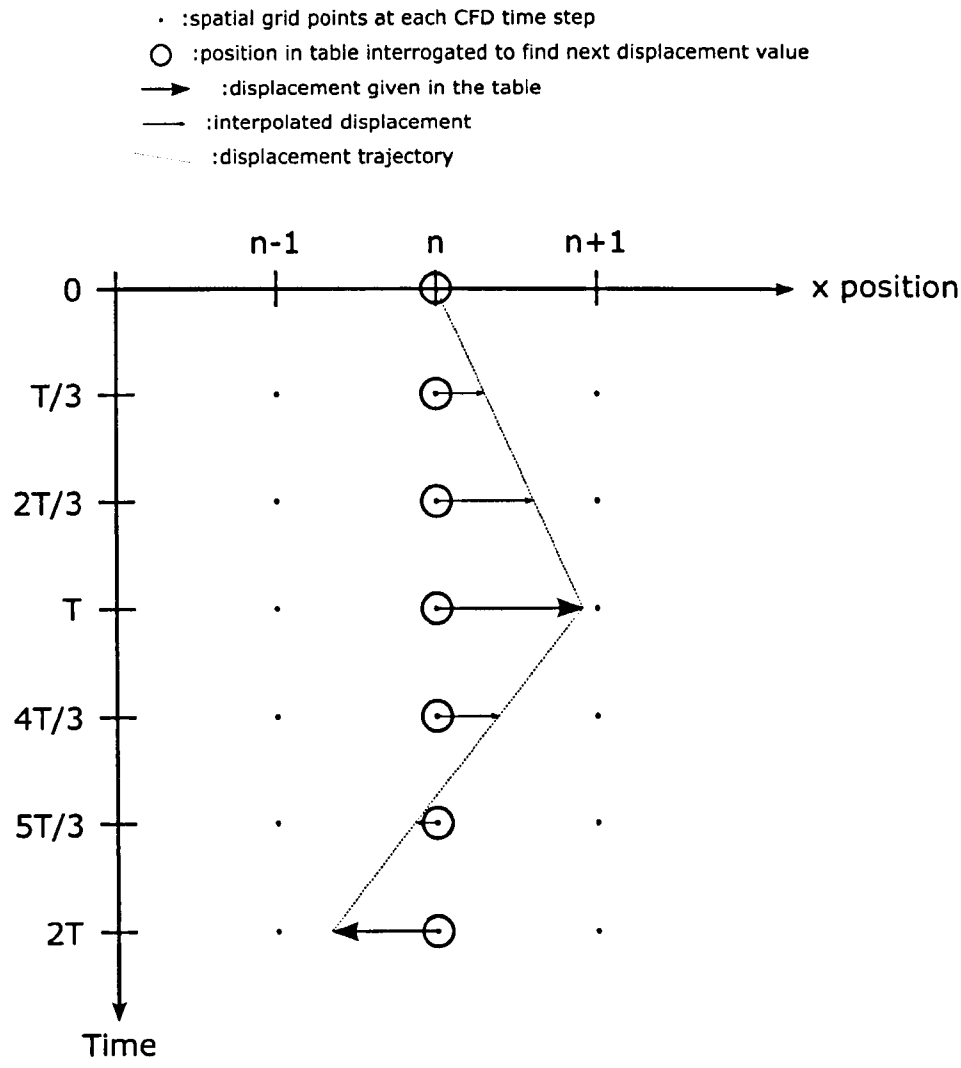

Figure D1. Nodal displacement history assuming Ansys uses original node position as index to interrogate displacement table.

In this case, the nodal displacements are as required, with linear interpolation between known values.

Figure D2 shows how Ansys actually interprets the same displacement table, displacements at x = n+1 are now included as they affect the outcome.

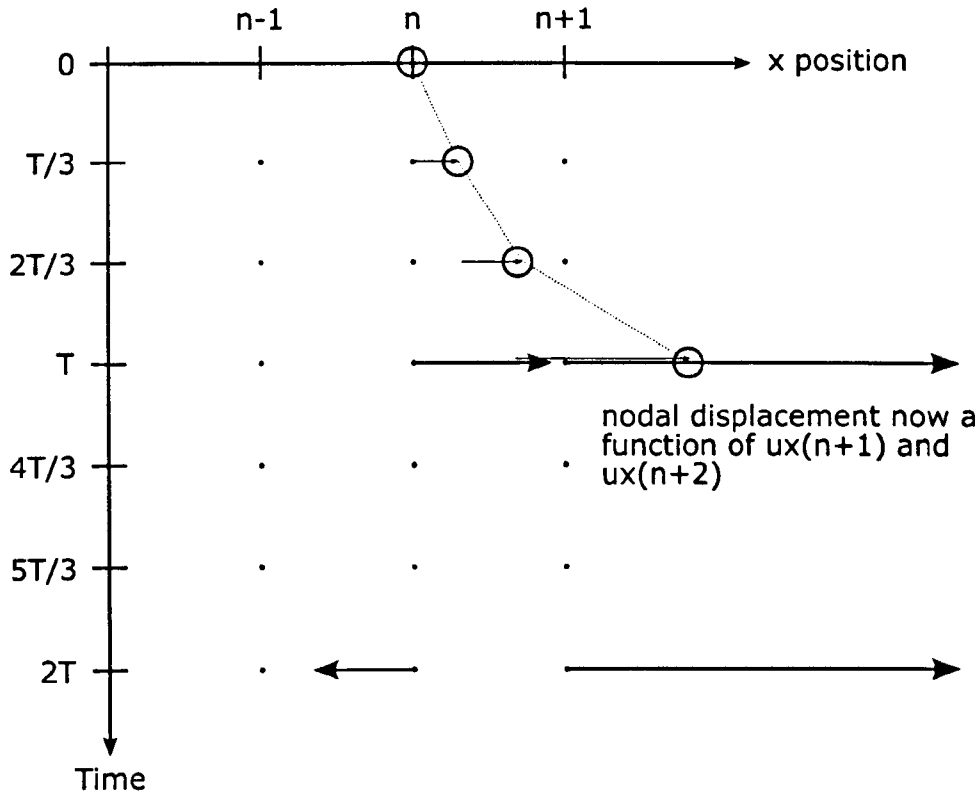

Figure D2. Example nodal displacement history assuming Ansys uses morphed node position as index to interrogate displacement table.

After the first CFD timestep, the node has moved exactly as in the first example. Ansys bases the displacement for the next timestep on the value at t=T/3 and the displaced nodal position, interpolating between ux(n,0),(n,T),(n+1,0) and (n+1,T). In this instance, the large value of ux(n+1,T) means that the node is dragged further to the right than required. The same effect occurs at t=2T/3. At T=3 the node has moved so far that it is the far side of n+1 and it's displacement is now independent of ux(n).

Modifying the Displacement Tables

The approach taken was to alter the table such that the correct nodal displacement at each mesh timestep was moved to the displaced node position.

Consider once more the 1d example, this time with a CFD timestep equal to the mesh timestep; the grid needs to be altered so the displacements in the top image are replaced by those in the bottom image, in figure D3.

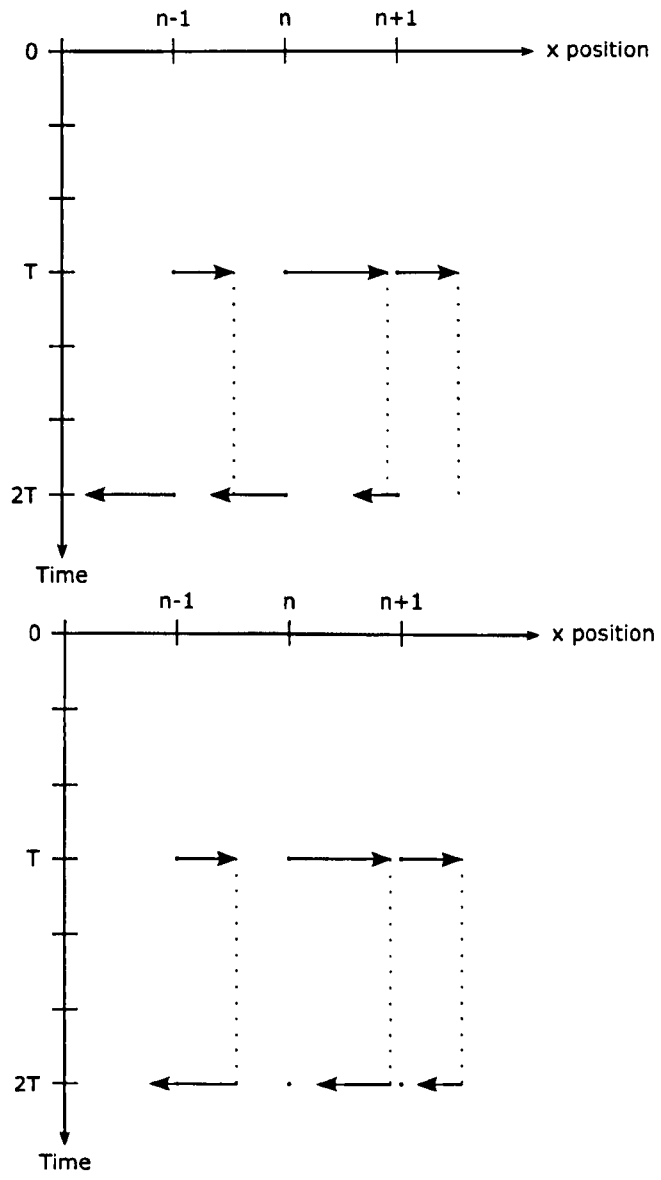

Figure D3. Original table approach (above) and updated approach (below) to match Ansys' interpretation of table.

The problem with the lower version is that the data is now not on a uniform grid. In order to find the displacement values at the grid points, the inverse mapping is needed to tell us where we have to look at t=T for the displacements that will be needed at t=2T.

Estimating the Inverse Mapping

As the mappings used are generally non-linear, they do not posses an analytical inverse. For this reason, the inverse mapping must be estimated. The simplest way of gaining such an inverse is to reverse the original registration procedure, registering

the output of the original mapping onto the source image. This was seen to produce a qualitatively acceptable inverse mapping, but when applied to the 4d table, the ALD was substantially degraded.

This approach was extended with a variety of test images other the original mapping output without great success.

It was found that the only reliable method for generating the reverse mapping was to use a series of images each containing a single pixel, and generate the reverse mapping by applying the original map to the pixel image and calculating the centre of gravity of the morphed pixel image, this allowed a reverse map to be built.

This technique was successfully implemented in Matlab and tested in Ansys; it was found that the final applied displacements represented the original moving mesh with an ALD within 0.2mm for all timesteps.